The Dissertation Committee for Priyanshu Agarwal
certifies that this is the approved version of the following dissertation:

A Hand Exoskeleton with Series Elastic Actuation for Rehabilitation: Design, Control and Experimentation

Committee:

Ashish D. Deshpande, Supervisor

Richard R. Neptune

Benito R. Fernandez

Marcia K. O'Malley

A Hand Exoskeleton with Series Elastic Actuation for Rehabilitation: Design, Control and Experimentation

by

Priyanshu Agarwal, B.TECH.; M.S.

DISSERTATION

Presented to the Faculty of the Graduate School of

The University of Texas at Austin

in Partial Fulfillment

of the Requirements

for the Degree of

DOCTOR OF PHILOSOPHY

THE UNIVERSITY OF TEXAS AT AUSTIN

May 2017

Dedicated to my supportive parents, loving wife and to all those who inspired me not to quit when it was difficult, not to yield when it was tough.

Acknowledgments

I would like to thank all those who made the accomplishment of this work possible.

First of all, I would like to express my gratitude to my thesis advisor and mentor Prof. Ashish Deshpande, who provided me the opportunity to pursue research in the ReNeu Robotics Lab at University of Texas (UT) at Austin. The countless discussions I had with him significantly shaped the way my research evolved during the course of this work. At times the discussions motivated me to think in new directions, which helped me explore new research areas and interests. Apart from providing valuable guidance, he also provided personal support during my stay at UT without having to worry about my funding situation.

I would also like to thank my thesis committee members. I am obliged to Prof. Richard Neptune for his course on musculoskeletal biomechanics, which equipped me with the tools needed to model coupled human exoskeleton systems. I really appreciate the class discussions, which helped me build an understanding of the subject and provided me the skills required to analyze such systems. I am also grateful to Prof. Benito Fernandez for the courses on nonlinear control and applied intelligence, which provided me the background to develop advanced controllers for the device. Several controllers developed

for the device were a result of the projects I pursued in these courses. I would also like to express my thanks to Prof. Marcia O'Malley, whose group also collaborated on this project. The combined group discussions we had on the hand-wrist exoskeleton project significantly shaped the design and development of the hand exoskeleton.

I am indebted to the members of the hand exoskeleton team for being excellent teammates and supporting the development of the device over several years. Youngmok Yun for working on the electronics and software aspect of the system. Jonas Fox for modeling and designing the hand exoskeleton system. Kaci Madden for developing solutions for the thumb attachment. It was though several thoughtful discussions that the development of the device could be made possible. Also, thanks to the several undergraduate researchers who supported the development of the device over the years.

I would also like to express my special thanks to the members of the ReNeu Robotics Lab who provided the much needed support throughout my stay at UT. I am also thankful to all those who volunteered to be the subjects for my experiments without worrying about the discomfort these experiments brings.

Furthermore, I would like to acknowledge the staff members in the Mechanical Engineering department, Mark Phillips, who provided us access to the selective laser sintering facility at UT and helped us print the parts for the exoskeleton. Also, I would like to thank the staff members of machine shop who provided us the resources and the guidance to machine parts for the

device.

It is through the constant love, support and patience of my family that this work could be accomplished. My parents were always by my side whenever I needed them. This work would have been impossible without their support. I would forever be indebted to my wife, who always encourage me to follow my heart and pursue my dreams.

I would also like to thank the funding agencies National Science Foundation (NSF grant # CNS-1135949) and National Aeronautics and Space Administration (NASA grant # NNX12AM03G) and The University of Texas at Austin for supporting this research and helping me pursue my research endeavors.

Finally, I would like to reiterate what kept me going through all these years

Be the flesh of your flesh,
Be the soul of your soul,
Be someone you have always praised,
Be a man with infinite traits.

And soon you will be out of this mess,
This mess of forgetfulness,
Of much oblivion that we possess,
About the world of success,
And the knowledge we possess.

This world is not enough, I confess,

At times why, I can't guess.

This is the only reason I depress,

Why we don't suppress such sort of ambivalence,

Of mixed emotions that we possess.

But one thing I can state with sureness,

The restlessness within me will one day relax,

For I'll achieve what I manifest,

And on that day I have attained success.

A Hand Exoskeleton with Series Elastic Actuation for Rehabilitation: Design, Control and Experimentation

Publication No. _____

Priyanshu Agarwal, Ph.D.
The University of Texas at Austin, 2017

Supervisor: Ashish D. Deshpande

Rehabilitation of the hands is critical for restoring independence in activities of daily living for individuals with upper extremity disabilities. Conventional therapies for hand rehabilitation have not shown significant improvement in hand function. Robotic exoskeletons have been developed to assist in therapy and there is initial evidence that such devices with force-control based strategies can help in effective rehabilitation of human limbs. However, to the best of our knowledge, none of the existing hand exoskeletons allow for accurate force or torque control. In this dissertation, we design and prototype a novel hand exoskeleton that has the following unique features: (i) Bowden-cable-based series elastic actuation allowing for bidirectional torque control of each joint individually, (ii) an underlying kinematic mechanism that is optimized to achieve large range of motion and (iii) a thumb module that allows for independent actuation of the four thumb joints.

To control the developed hand exoskeleton for efficacious rehabilitation after a neuromuscular impairment such as stroke, we present two types of subject-specific assist-as-needed controllers. Learned force-field control is a novel control technique in which a neural-network-based model of the required torques given the joint angles for a specific subject is learned and then used to build a force-field to assist the joint motion of the subject to follow a trajectory designed in the joint-angle space. Adaptive assist-as-needed control, on the other hand, estimates the coupled digit-exoskeleton system torque requirement of a subject using radial basis function (RBF) and on-the-fly adapts the RBF magnitudes to provide a feed-forward assistance for improved trajectory tracking. Experiments with healthy human subjects showed that each controller has its own trade-offs and is suitable for a specific type of impairment.

Finally, to promote and optimize motor (re)-learning, we present a framework for robot-assisted motor (re)-learning that provides subject-specific training by allowing for simultaneous adaptation of task, assistance and feedback based on the performance of the subject on the task. To train the subjects for dexterous manipulation, we present a torque-based task that requires subjects to dynamically regulate their joint torques. A pilot study carried out with healthy human subjects using the developed hand exoskeleton suggests that training under simultaneous adaptation of task, assistance and feedback can module challenge and affect their motor learning.

Table of Contents

List of Tables

List of Figures

Chapter 1

Introduction[1]

1.1 Motivation and Goals

Over 19.9 million people in the US exhibit a disability of physical function of the upper body and have difficulty lifting or grasping [18]. Rehabilitation using robots has the potential to provide effective therapy to individuals with disabilities while also allowing for quantitative assessment of recovery. Clinical trials have shown that robot-aided hand therapy results in improved hand motor function after chronic stroke with increased sensorimotor cortex activity for practiced tasks [67, 152]. However, several technical challenges in areas including hand biomechanics, rehabilitation, actuators, sensors, physical human-robot interaction, and control based on the user intent [62] need to be overcome for designing an effective, small, and light weight robotic hand exoskeleton. Development of these exoskeletons requires physical hardware design (mechanism synthesis, human-robot interaction interface, optimal design parameters) and software-based control algorithms (subject specific kinemat-

[1]Portions of this chapter has previously been published in the following article–P. Agarwal, J. Fox, Y. Yun, M. K. OMalley and A. D. Deshpande, "An Index Finger Exoskeleton with Series Elastic Actuation for Rehabilitation: Design, Control and Performance Characterization", International Journal of Robotics Research, 34(14), pp.1747-1772, 2015. The author carried out the literature review of the existing hand exoskeletons, and developed and tested the presented hand exoskeleton in the cited work.

ics estimation, position or torque control), to ensure desirable coupled system performance.

Research over the past decade has shown initial evidence that force-control based strategies (e.g. impedance, admittance, assist-as-needed [23]) can be more effective for rehabilitation of both the upper [16, 33, 117] and lower limbs [102] than pure position-based control [58]. Force-control based strategies can be designed to encourage an active effort from the subject during therapy, which is shown to be more effective than passive motor training even for a longer duration [98] and is thought to be essential for provoking motor plasticity [119]. On the other hand, position-control based strategies physically guide the movement of the impaired limb to strictly follow a predefined trajectory without enabling the subject to actively participate in the task [15] or allowing for any subject-specific customization of the assistance [104]. The guidance hypothesis in motor control research suggests that such a physically guided movement may decrease motor learning for some tasks due to the reduction in burden (motor output, effort, energy consumption or attention) on the subject's motor system to discover the principles necessary to perform the task successfully [132]. Furthermore, some hand disabilities (e.g. spasticity) lead to uncertain motion of the digits. This uncertainty requires that during rehabilitation therapy appropriate forces are applied on the digits rather than simply moving them through some predetermined positions, which can lead to the application of large forces and further harm the hand.

The introduction of passive compliance in the form of Bowden-cable-

based series elastic actuator (SEA) has been identified as a good force or torque source with low inertia for impedance controlled exoskeletons, especially for the lower extremity [163]. It has been suggested for the lower extremity exoskeletons that the interaction between a therapist and a patient's limb can be simulated by applying forces corresponding to virtual springs and dampers [161]. In addition, introducing appropriate compliance in actuation can also ensure safe and comfortable interaction with the human hand. However, the role of compliance and series elastic actuation has not yet been explored in hand exoskeletons. Thus, the existing hand exoskeletons suffer from two major limitations. Firstly, none of them allow for accurate torque or impedance control at individual finger joints for effective therapy. Secondly, none of them decouples the inertia and nonlinear actuator gearing effects from the human finger for kinematically and dynamically transparent [160] interaction with the device to ensure comfort and safety.

Our goal is to design a robotic device that can provide therapeutic exercises that can lead to quicker recovery of the hand digits. Toward this goal, we set the following objectives for the design of our hand exoskeleton: (i) the device should allow for accurate and stable bidirectional torque control with high backdrivability and low reflected inertia, (ii) the design should be kinematically and dynamically compatible with the human finger and be quickly adjustable for a specific subject and (iii) the device should be light in weight and allow for free motion of the hand with low movement resistance. We use the following design goals for the actuator for our application of hand rehabili-

tation: (i) a required bidirectional peak torque of at least 0.3 Nm based on the torques applied by experienced therapists for hand rehabilitation as measured through a torque measuring device [157], (ii) torque bandwidth of at least 2 Hz based on the fact that the bandwidth of the human force compliance control loop is 1–2 Hz [28, 141]. Also, typically rehabilitation exercises for the finger are carried out at angular velocities of less than 50°/s i.e. full range of motion frequencies below 0.5 Hz [1, 79].

Physical assessment studies of hand function have shown that the loss of finger adduction or abduction motion has minimal effect on the activities of daily living [47]. Furthermore, abduction-adduction motion is not important for achieving the critical hand functions including tip pinch, key pinch, pulp pinch, power grasp, briefcase grip, holding glass etc. and therefore is not considered during the ergonomic evaluation of biomechanical function of the hand [90]. In addition, the index finger has limited range of motion (20 to 30 degrees) at the metacarpophalangeal (MCP) abduction-adduction joint [9, 47]. Also, incorporation of an active abduction-adduction joint significantly increases the complexity of the design of our finger exoskeleton without much additional benefit. Considering all these factors, we do not include active rehabilitation of the abduction-adduction joint as the design goal for our index finger exoskeleton. The rationale behind providing passive degree of freedom (DOF) is that the device should allow for free movement at this joint while the subject performs flexion-extension motion at the other finger joints.

The thumb provides more than 40% of the entire hand function and is

given first priority for replantation [145]. Studies on understanding and classifying the human hand use in activities of daily living has shown that apart from thumb flexion-extension at the carpometacarpal (CMC), metacarpophalangeal (MCP) and interphalangeal (IP) joints, thumb abduction-adduction at the CMC joint plays a significant role in accomplishing different types of grasps including power, tripod, precision, palmar, tip pinch and lateral pinch [40, 96]. Thumb opposition, which is vital for normal hand function, is achieved via coordinated flexion-extension and abduction-adduction motion at the CMC joint [94]. Furthermore, thumb abduction-adduction at the CMC joint has large range of motion (40 to 45 degrees) [34, 144]. Considering all these factors, we aim for the active rehabilitation of thumb flexion-extension at the CMC, MCP and IP joints and abduction-adduction at the CMC joint as the design goal for our thumb exoskeleton.

In this dissertation, we present a novel hand exoskeleton with series elastic actuation capable of achieving bidirectional and independent joint torque control and introduce compliance in the mechanism to make it safe and comfortable. From the robot design and controls perspective, this dissertation makes the following contributions: (i) presents a mechanism that inherently induces low joint reaction forces at the joints of the hand digits during the articulation of the digits, while providing large ranges of motion, (ii) implements a miniature Bowden-cable-based SEA, which is small enough to fit on a hand exoskeleton and is capable of achieving accurate torque control, (iii) presents a method to use the redundant sensor information to estimate the unknown

kinematic model parameters for accurate control, and (iv) demonstrates the implementation of torque controllers for accurately applying torques both at the exoskeleton and finger joints. From the rehabilitation perspective, we present a fully developed prototype, a control system for the device, and experimental results with human subjects, that demonstrate the capabilities of the device that are critical for delivering physical therapy.

The rest of the dissertation is organized as follows. A background of the existing hand exoskeletons, series elastic actuators and controls along with their limitations are presented in Chapter 1. The SEAs developed for bidirectional torque control and the details of the index finger and thumb exoskeleton prototypes along with their system model and experimentation are described in Chapter 2. The details of the two subject-specific advanced controllers developed for the hand exoskeleton are described in Chapter 3. The details of the proposed rehabilitation framework are presented in Chapter 4. Finally, the dissertation is concluded with a summary of the contributions of this work along with the possible future research avenues.

1.2 Literature Review

1.2.1 Hand Exoskeletons

A number of hand exoskeletons have been designed to date, and these can be categorized into passive (with no actuators) [19] and active (with actuators) devices. Within the active category, devices can either provide continu-

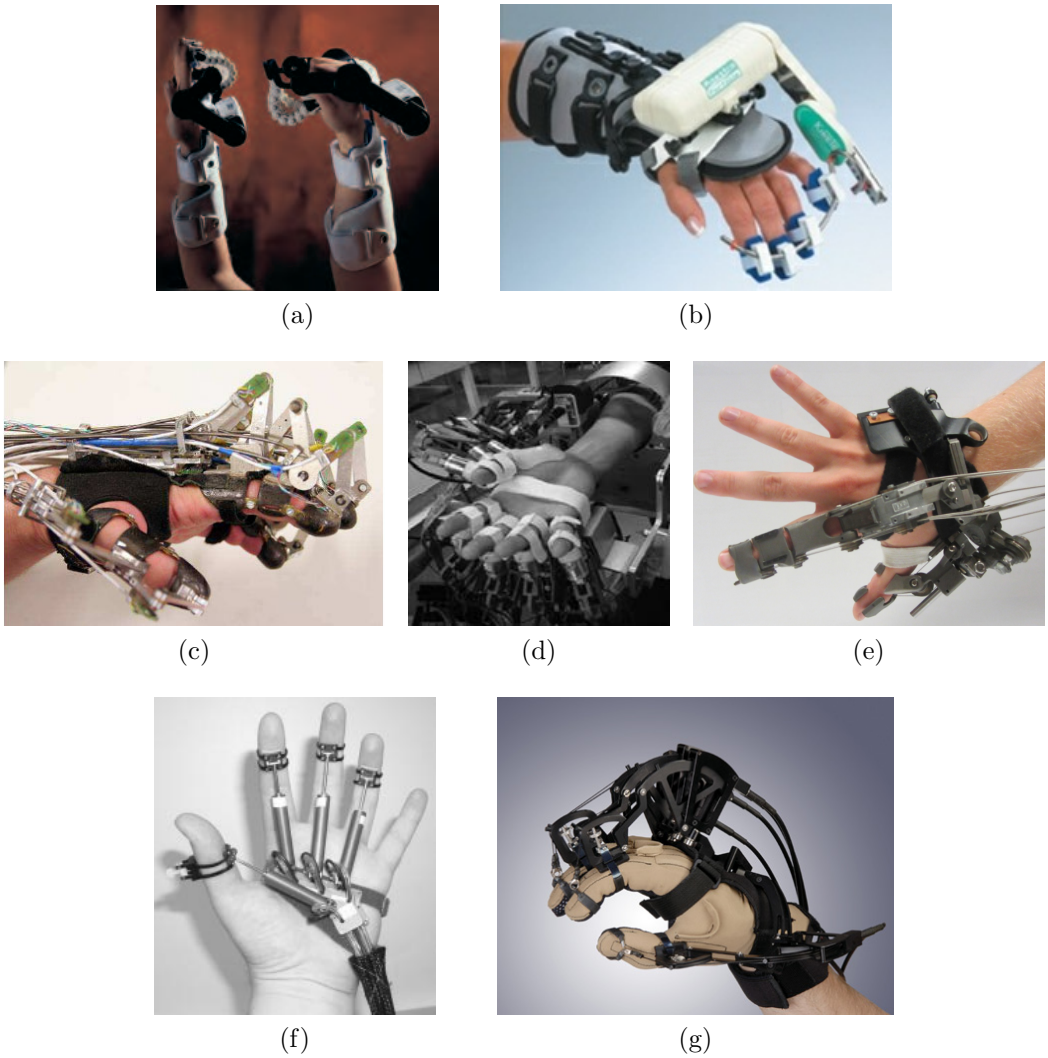

Figure 1.1: Some of the existing hand exoskeletons designed for rehabilitation and virtual reality applications. (a) Waveflex, (b) Kinetec Maestra Portable Hand CPM, (c) Wege et al., (d) Ueki et al., (e) HX, (f) Rutger's Master II and (g) Cybergrasp.

ous passive movement (CPM) (e.g. Waveflex CPM[2], Kinetec Maestra Portable

[2]http://www.remingtonmedical.com/product/detail/A1

Hand CPM[3], Ren et al. [121]) (Figs. 1.1a,b) or active assistance, where the human hand actively interacts with the device and the device reacts as per the interaction based on a feedback (e.g. position sensing) [73, 128, 157]. There are devices that use geared servomotors either directly mounted at the exoskeleton joints [150, 157] or connected through tendons [73]. However, this makes the device bulky, restricts the hand to a stationary device and makes it difficult to achieve torque control due to losses in the gearing or routing pulleys without using explicit force feedback for controlling the device. The hand is restricted in such designs as it is attached to a stationary device on a bench top due to the fact that the forces from the transmission mechanism needs to be transferred to the ground through the structure of the device.

A Bowden-cable-based mechanism allows the subject to freely orient and translate their hand within a reasonably large range for physical therapy. This is important for rehabilitation as some impairments of the upper limb make it difficult to fix the hand in certain positions. In addition, a device that would allow for free movement of the hand during operation can be used to perform activities of daily living in a rehabilitation setting both for therapy and assessment. Bowden-cable-based transmission has been employed with electric motors to make devices portable, however, these devices focus only on the position control of the digits [27, 93, 166] and use force measurements from peizoresistive force sensors or strain gages, either to roughly compensate

[3]http://orthoplusinc.com/index.php/products/continuous-passive-motion/kinetec-maestra-portable-hand-cpm

for the combined resistance due to friction in the Bowden cable and moment of inertia during only finger flexion motion (no contact force information was available during extension motion) [165] or to limit the tension in the Bowden cable for safe operation [32] or some altogether ignore the losses in the Bowden cable transmission [127] (Figs. 1.1c,d,e). Also, experimentation with a hand exoskeleton has shown that the force measurement using force sensing resistors is inaccurate due to the nature of the sensors, inability to mount the sensors to cover the entire contact area between the device and the finger, and change in the angle of application of force to the sensor [167].

A few devices use pneumatic cylinders for actuation and estimate the force applied on the finger tips by measuring the pressure inside the cylinder [17, 20] (Fig. 1.1f). However, these could not be used to control interaction force or torque at the individual phalanges or joints of the finger as their mechanism had only one DOF for each finger and is controlled by attaching the linear pneumatic actuator to only a specific phalanx. Thus by design, any force that is applied on the distal phalanx is propagated to all the joints without any means to control it individually. In addition, the mechanism on these devices is located on the palmar side, which makes it difficult to perform grasping tasks using physical objects for rehabilitation. [151] developed a system to aid in grasping, without any explicit position or force control, using air cylinders, which are pressurized or depressurized based on the output from a bending sensor. [156] developed a power-assist glove that provided some assistance using pneumatic actuators by recognizing the type of grasp based

on the angle information from angle sensors. Some of the devices also used EMG to control the motion of the device. These devices had a single actuator for each digit and controlled only the hand opening and closing using the EMG signal [37, 99, 112, 154] or had multiple actuators to apply some assistive force for grasping based on EMG signal [59]. However, none of them could accurately control the torque applied on the finger or its position.

Hand exoskeletons have also been developed for virtual reality applications. However, these devices are designed to apply only unidirectional forces or torques to simulate contacts in a virtual environment [54]. Rehabilitation exoskeletons, on the other hand, are required to apply bidirectional forces on hand during therapy. A commerically available device, CyberGrasp, is also only capable of exerting unidirectional forces to oppose the finger flexion motion with one actuated DOF for each digit (does not allow for control of torque applied at the individual finger joints) at a limited sampling rate of 90 Hz [95], which was improved to 2 kHz with an external ExHand box in [8] (Fig. 1.1g).

Several thumb exoskeletons have also been developed to date for rehabilitation, virtual reality or teleoperation applications that allow for active actuation of the thumb (Table 1.1). For this review, we consider the devices (total 15) that could actively actuate the thumb and are published in the literature with some experimental results. We compare the devices based on the following 8 criteria, which are important for a thumb exoskeleton for rehabilitation: (i) whether the device supports each thumb joint individually (exoskeletal type) or connects to the distal phalanx of the thumb (end-effector

type), (ii) the number of active DOFs in the device, (iii) the type of actuators used, (iv) whether the actuators are situated locally or remotely, (v) the type of sensors in the device, (vi) weight of the device, (vii) what physical quantities could be controlled using the device and (viii) what are the peak achievable forces or torques on the device.

Exoskeletal type devices allow for controlling the position or torque applied at each joint explicitly as compared to end-effector type devices, which could only control the position or force at the distal phalanx. The number of active DOFs in a device determines the variety and complexity of assisted motions it could provide. Individual support of thumb joints is important to provide targeted therapy to a specific joint, which may be necessary for certain thumb pathologies (e.g. spasticity). Ensuring natural coordinated motion at pathological thumb joints require that the device be exoskeletal type with each DOF actuated individually. The type of actuator and its placement determine whether the device would be bulky or light and therefore, whether it will allow for free movement of the hand while in operation. It is important for certain hand pathologies where the upper extremity could not be oriented in a certain manner. The type of sensors on the device determines what physical quantities the device could control. The weight of the device determines how easy or cumbersome it is for use. The controller on the device governs what physical quantities (position or force) the device could control, which in turn decides what robotic rehabilitation control paradigms (e.g. force-field control, assist-as-needed control [102]) the device is capable of rendering. Finally, the

peak achievable forces or torques determine for what kind of impairments the device could be used. One of the limitations of the exoskeletons developed for virtual reality applications is that they only allow to apply unidirectional forces on the thumb. Rehabilitation exoskeletons, are however, required to apply bidirectional forces on the thumb based on the nature of the impairment. A comparison of the weight of the proposed thumb exoskeleton with the existing ones shows that it has the least weight for the number of degrees of freedom it offers. The weight per DOF for our device is about 34 g including the weight of the exoskeleton base on hand (Table 1.1).

There have been five main types of actuation mechanism used for thumb exoskeletons: (i) linkage-based actuation with locally situated motor [49, 89, 128, 157], (ii) tendon-based actuation with locally situated motor [10, 59], (iii) cable and sheath transmission with remotely located motor [8, 27, 56, 93, 127], (iv) flexible shaft transmission with remotely located motor [164] and (v) pneumatic actuation [17, 151]. None of these mechanisms allow for accurate and stable torque control of the digit joints individually. Furthermore, these mechanisms have poor backdrivability and results in high reflected inertia. In addition, the transmission and actuator gearing in some of these mechanisms suffer from nonlinear friction and stiction, which makes it difficult to control actuator force or torque accurately.

The actuator mechanism of our thumb exoskeleton lies in category (iii) and so we discuss the designs in that category in more detail. Commercially available system, CyberGrasp [8, 17], supports only 1 DOF motion of the

Table 1.1: A comparison of the characteristics and specifications of the actuated thumb exoskeletons.

	Physical Characteristics						Specifications		
Thumb Exoskeleton	**Type**	**Active Independent DOFs**	**Actuator Type**	**Actuation** [6]	**Sensors**	**Weight** (g)	**Control**[2]	**Peak Force/ Torque**	**Remarks**
Rutger's Master II [17]	End-effector	1[1] (CMC E, MCP E)	Pneumatic actuators with compressed air source	Remote, Pneumatic tubes	infrared reflective sensor for position, hall-effect angle sensor, pressure sensor	80[4]	Unidirectional phalanx force using pressure	16 N[5]	Designed for virtual reality applications
[151]	exoskeletal	1 (MCP F/E)	Air cylinder with compressed air source	Remote, Pneumatic tubes	Bend sensor, electric pressure regulator	-	Grasping on-off	-	Experimental evaluation with a wooden hand model is presented
CyberGrasp [8, 17]	End-effector	1[1] (CMC E, MCP E, IP E)	Servo motor	Remote, Cable + Sheath	position	539[4]	Unidirectional phalanx force using motor current	12 N[5]	Losses in the transmission are neglected

[1] coupled actuation of DOFs present in design [2] missing control represents that only mechanical design has been presented so far [3] combined weight of index finger and thumb exoskeleton [4] total weight of the hand exoskeleton [5] only allows for unidirectional force [6] actuation refers to whether the actuator was located at the joint (local) or remotely (remote) and the transmission mechanism

Table 1.1: A comparison of the characteristics and specifications of the actuated thumb exoskeletons. (contd.)

	Physical Characteristics						Specifications		
Thumb Exoskeleton	**Type**	**Active Independent DOFs**	**Actuator Type**	**Actuation** [6]	**Sensors**	**Weight** (g)	**Control**[2]	**Peak Force/ Torque**	**Remarks**
[59]	Exoskeletal	2[1]	DC motor + Gear drive	Local, Tendon	Potentiometer, Encoder, EMG	–	Position or Grasping on-off	–	Thumb opposition and IP + MP joint are each actuated by one actuator.
HEXORR [128]	End-effector	1 (CMC F/E)	AC servo motor + Harmonic drive (100:1)	Local, Linkage	Encoder, Torque sensor	–	–	–	Hand is fixed in the device. CMC A/A angle is adjustable
iHandRehab [93]	Exoskeletal	4 (CMC F/E, CMC A/A, MCP F/E, IP F/E)	DC motor + Capstan drive (8:1)	Remote, Cable + Sheath	Potentiometer, Force sensor	250[3]	–	–	Significant losses (∼ 95 %) were observed in the transmission

[1] coupled actuation of DOFs present in design [2] missing control represents that only mechanical design has been presented so far [3] combined weight of index finger and thumb exoskeleton [4] total weight of the hand exoskeleton [5] only allows for unidirectional force [6] actuation refers to whether the actuator was located at the joint (local) or remotely (remote) and the transmission mechanism

Table 1.1: A comparison of the characteristics and specifications of the actuated thumb exoskeletons. (contd.)

	Physical Characteristics						Specifications		
Thumb Exoskeleton	**Type**	**Active Independent DOFs**	**Actuator Type**	**Actuation** [6]	**Sensors**	**Weight** (g)	**Control**[2]	**Peak Force/ Torque**	**Remarks**
[164]	Exoskeletal	5 (CMC F/E, CMC A/A, MCP F/E, MCP A/A, IP F/E)	RC servo motor	Remote, Flexible shafts	Potentiometer, strain gage	200	Position	±2.5 Nm	Significant losses were observed in the transmission
[157]	Exoskeletal	4 (CMC F/E, MCP F/E, IP F/E, Opposition)	DC servo motor	Local, Linkage	Encoders, 3-axis Force sensors	–	Position	±3.72 Nm	Hand is fixed in the device
[10, 49]	End-effector	3[1]	–	Local, Linkage	–	510	3D tip force	5 N	Distal and middle exoskeleton phalanx are coupled
[89]	Exoskeletal	1[1] (CMC A/A)	Linear servo motor	Local, Linkage	Single axis force sensor	126	Position	10 N[5]	

[1] coupled actuation of DOFs present in design [2] missing control represents that only mechanical design has been presented so far [3] combined weight of index finger and thumb exoskeleton [4] total weight of the hand exoskeleton [5] only allows for unidirectional force [6] actuation refers to whether the actuator was located at the joint (local) or remotely (remote) and the transmission mechanism

Table 1.1: A comparison of the characteristics and specifications of the actuated thumb exoskeletons. (contd.)

	Physical Characteristics						Specifications		
Thumb Exoskeleton	**Type**	**Active Independent DOFs**	**Actuator Type**	**Actuation**	**Sensors**	**Weight** (g)	**Control**[2]	**Peak Force/ Pressure**	**Remarks**
IOTA [56]	End-effector	2 (CMC A/A, MCP F/E)	Servo motor	Remote, Cable + Sheath	Encoder, Bend sensor	230	Position	±0.384 Nm	Pediatric disorders
[101]	Exoskeletal	1[1] (CMC F/E, MCP F/E, IP F/E)	Fluidic actuator + compressor	Remote, Pneumatic tubing	–	200	Grasping on-off	345 kPa	No CMC A/A motion is supported
[52]	End-effector	1[1]	–	Local, Linkage	–	–	Unidirectional force	3 N [3]	No experiments with thumb module are presented
[72]	Exoskeletal	1[1] (CMC F/E, MCP F/E, IP F/E)	Linear SEA with linear motor	Local, Linkage	Potentiometer	298[4]	Grip force (Only preliminary SEA testing presented so far)	9 N[3]	No CMC motion is supported

[1] coupled actuation of DOFs present in design [2] missing control represents that only mechanical design has been presented so far [3] only allows for unidirectional force [4] total weight of the hand exoskeleton [5] weight of the index finger and thumb exoskeleton (only moving parts) [6] force at thumb tip [7] includes the weight of the hand base which is 30 g

Table 1.1: A comparison of the characteristics and specifications of the actuated thumb exoskeletons.[8] (contd.)

	Physical Characteristics						Specifications		
Thumb Exoskeleton	**Type**	**Active Independent DOFs**	**Actuator Type**	**Actuation**	**Sensors**	**Weight** (g)	**Control**[2]	**Peak Force/ Pressure**	**Remarks**
HX [27]	Exoskeletal	2[1] (MCP F/E, IP F/E, Opposition)	DC motor + Gear drive (14:1)	Remote, Cable + Sheath	–	270[6]	–	–	No experiments with thumb module are presented
BRAVO [91]	Exoskeletal	1[1] (MCP F/E, IP F/E)	DC motor + Gear drive	Local, Linkage	EMG, Sensorized object pressure	950[4]	Position	±30 N	Designed for grasping of cylindrical objects
Proposed	Exoskeletal	4 (CMC F, MCP F, IP F)	SEA with DC motor + Gear drive (14:1)	Remote, Cable + Sheath	Magneto-resistive angle sensor, Potentiometer, Encoder	136[7]	Torque	±0.3 Nm	Accurate torque control of individual thumb joint can be achieved

[1] coupled actuation of DOFs present in design [2] missing control represents that only mechanical design has been presented so far [3] only allows for unidirectional force [4] total weight of the hand exoskeleton [5] weight of the index finger and thumb exoskeleton (only moving parts) [6] force at thumb tip [7] includes the weight of the hand base which is 30 g [8] There is also a commercially available hand exoskeleton system, Festo ExoHand, with a thumb module having 2 DOFs. However, limited published information is available on the device. Regardless, it cannot control the flexion-extension motion at the CMC, MCP and IP joints independently.

thumb, control unidirectional phalanx force using motor current and cannot be used to control the position or forces of the thumb phalanges individually. iHandRehab [93] is another hand exoskeleton with a thumb module that supports 4 DOF of the thumb. However, experiments with their device showed that significant friction (percentage of friction torque accounting for the driving torque is up to 95%) was present in their transmission. In addition, no control experiments were presented with their device. [56] introduced a 2 DOF thumb exoskeleton, called IOTA (isolated orthosis for thumb actuation), for unidirectional actuation of the thumb. However, their device was designed to only control position of the joints. HX is another hand exoskeleton with a 2 DOF thumb module [27]. However, the flexion-extension motion at the MCP and IP joints is under-actuated in their design and their device is designed to be position controlled. Also, so far they have only presented the design of the thumb module. Recently, [72] designed a hand exoskeleton having a thumb module with a linear series elastic actuator (SEA) to control the grip force. However, their design has only 1 DOF for thumb with no allowable abduction-adduction motion at the CMC joint. Also, they have presented only preliminary testing of the SEA and no experiment with human subjects have been conducted with the device so far.

1.2.2 Series Elastic Actuators

A number of robotics applications demand a miniature actuation system that can deliver precise control of force or torque. Examples include an

exoskeleton for hand rehabilitation, a haptic interface and miniature robotic manipulator. [4]In most miniature robots, electromagnetic actuators (e.g. DC motors) are most suitable given the small form factor, ease of use and clean design. For electromagnetic actuators precise control of torque (or force) can be achieved either with a torque (or force) sensor and feedback controls, or with an arrangement of a spring in series with the actuator and hierarchical controls with position feedback. Adding a torque (or force sensor), e.g. a load cell, is costly and also requires significant space, which makes this option infeasible, especially for miniature robots, when compared to the series elastic actuators (SEA). An SEA also adds an inherent mechanical compliance in the system which is shown to be advantageous in the robotic systems that physically interact with the human body [35]. While SEAs are suitable for actuation with precise force controls, there is a lack of miniature, compact and bidirectional SEAs for the robotics applications.

An SEA consists of a motor, an elastic element and accurate position sensors on either side of the spring, and by measuring the deflection of the spring, torque (or force) is determined [120]. SEAs have been successfully implemented in a number of robotics applications to precisely control torque, including in a few exoskeletons for the lower extremity [148, 163] and upper extremity [138], humanoids[136] and bipeds [44]. Table 1.2 presents a survey of important SEAs for robotics applications. For the miniature robotics appli-

[4]Our broad definition of miniature or small-scale robot is a robot whose size is in the centimeter scale.

cations, we set the requirements on SEAs stiffness to be small (< 1 Nm/rad) and peak torque to be ($\sim$0.5 Nm), and we want the actuator to fit in the space of 45 x 35 x 20 mm. None of the existing SEAs are designed to satisfy these requirements.

We present two designs for miniature and compact SEAs that meet the requirements for small-scale robotics applications including maximum torque, torque tracking accuracy and torque tracking bandwidth. To reduce the size of SEA for miniature robots, we decided to locate electric motors remotely and use Bowden-cable transmission to connect motor to the springs and joint to be actuated. Similar idea has been implemented in larger SEAs [148, 163], but when applied to small size SEAs, it results in unique challenges. Our designs address these challenges. The choice of type of spring configuration and the choice of spring stiffness values are critical in successful functioning of an SEA. There are three different possibilities for type of spring elements: i) linear compression springs, ii) helical torsion springs, and iii) structural torsion springs. Design of the elastic elements within limited space itself poses distinct challenges for each configuration: (a) for linear compression springs - how to achieve high stiffness while avoiding buckling of the spring, (b) for helical torsion springs - how to achieve high stiffness in limited outer diameter and width while maintaining linear bidirectional nature of the torque and (c) for structural torsion spring - how to achieve large angular deflection with relatively high stiffness of such springs without material failure [24]. Also, to ensure a compact design small angular sensor is required to sense the joint angular

Table 1.2: A comparison of the characteristics and specifications of the existing rotary SEAs with the proposed ones. Actuator location refers to whether the actuator was located at the joint (local) or remotely (remote).

	Physical Characteristics						Performance Specifications			
SEA	**Spring Type**	**Actuator Type**	**Actuator Location**	**Spring Stiffness**[5] (Nm/rad)	**Size** (mm)	**Weight** (kg)	**Peak Torque**[3] (Nm)	**Bandwidth** (Hz)	**Torque Fidelity** (%)	**Dynamic Range**
[120, 170]	Structural Torsion	DC motor + Gear drive (66:1)	Local	34	–	–	±4	–	–	–
[163]	Linear Compression	Servo motor + Gear drive (8:1)	Remote	393.60	–	–	±30	11 @ 60 Nm	>95	–
[174]	Linear Compression	Brushed DC motor + Gear drive (156:1)	Local	138	–	–	–	–	–	–
[134]	Structural Torsion	Brushless DC motor + Harmonic drive (160:1)	Local	327	70 (diameter) ×70	–	±50	–	–	23
[148]	Helical Torsion	Brushless DC motor + Gear drive (5:1)	Remote	24	–	–	±41	8 @ 6 Nm, 4 @ 15 Nm	–	–
[82]	Helical Torsion	Brushless DC motor + Gear drive (113:1)	Local	13.17	–	–	±6	10	–	–
[13]	Linear Tension	Servo motor + Harmonic drive (160:1)	Local	8.75	–	–	0.06–1.38	12 @ 0.354 Nm	–	–

[3]Peak torque refers to the maximum achievable instantaneous torque at the SEA joint; [5]Spring stiffness refers to the effective torsional stiffness at the joint.

Table 1.2: A comparison of the characteristics and specifications of the existing rotary SEAs with the proposed ones. Actuator location refers to whether the actuator was located at the joint (local) or remotely (remote).[2] (contd.)

	Physical Characteristics						Performance Specifications			
SEA	**Spring Type**	**Actuator Type**	**Actuator Location**	**Spring Stiffness**[5] (Nm/rad)	**Size** (mm)	**Weight** (kg)	**Peak Torque**[3] (Nm)	**Bandwidth** (Hz)	**Torque Fidelity** (%)	**Dynamic Range**
[88]	Structural Torsion	Brushless DC motor + Harmonic drive (50:1)	Local	219	109 (diameter) × 185	3.175	±100	6.9 @ 100 Nm	–	–
[147]	Structural Torsion	Hydraulic	Local	150	70 (diameter) × 100	1.5	±50	18 @ 20 Nm	–	–
[137]	Structural Torsion	Brushless DC motor + Harmonic drive	Local	150	120 (diameter) × 165	1.8	±10	5.3 @ 10 Nm	–	–
[124]	50 A durometer natural rubber	Brushed DC motor + Gear drive (349:1)	Local	5.78	50 (diameter) ×–	–	±6	–	–	–
[26]	Linear Compression	Brushed DC motor + Harmonic drive (50:1)	Remote	26	–	–	±78[4]	–	–	–
LC-SEA	Linear Compression	Brushed DC motor + Gear drive (295:1)	Remote	0.31	44 × 36 × 17	0.03	±0.5	2.5 @ 0.2 Nm	>97	7–84
HT-SEA	Helical Torsion	Brushed DC motor + Gear drive (295:1)	Remote	0.53	38 × 38 × 24	0.04	±0.3	4.5 @ 0.2 Nm	>97	7.5-27.5

[2]There are also rotary SEAs in humanoid robot Dreamer[135] and Robonaut II[38], however, specifications have not been published for these SEAs. Regardless those are not suitable for small scale applications.; [3]Peak torque refers to the maximum achievable instantaneous torque at the SEA joint; [4]calculated; [5]Spring stiffness refers to the effective torsional stiffness at the joint.

position, which typically have relatively poor resolution. This requires the angular deflection of the elastic element to be sufficiently large for it to be properly resolved by the sensor and in turn achieve a desirable torque resolution. A stiffer spring allows to achieve higher peak torques and torque bandwidths, however, at a poorer resolution. Thus, a trade-off is involved in choosing the stiffness of the spring while addressing all the aforementioned challenges.

Bowden cables introduce elasticity and nonlinear friction in the transmission [75, 165]. To achieve good torque control with Bowden-cable transmission, estimation of the effective stiffness of the Bowden cable and sheath combination is necessary. In addition, the effective stiffness also changes with the configuration of the design, which affects how the load is transferred through the sheath. This requires explicit testing of SEAs having different configuration even when the stiffness of the metallic elastic element is known a priori. In the large-scale robotics applications, the problems due to Bowden-cable elasticity and friction are overcome with explicit sensors to measure the deflection of the elastic element. In the small-scale robotic application these problems lead to more severe effects and the small size makes it difficult to mount additional sensors.

We present two SEA designs: one design is with a linear compression springs (LC-SEA) and other is with a helical torsional spring (HT-SEA) (Sections 2.1.1, 2.1.2 and 2.1.3). We carried out experiments on a test rig to assess the accuracy and fidelity of torque tracking, torque bandwidth, dynamic range,

performance under various torque magnitude requirements and under various disturbances (Sections 2.1.5 and 2.1.6).

1.2.3 Controls

Robotic rehabilitation has gained increasing attention in the past decade due to the possibility of providing repetitive and intensive training with reduced manual labor and the potential to quantitatively assess recovery progress [6, 11, 41, 100]. However, understanding what control algorithms are best suited for these robotic devices in order to leverage neural plasticity and achieve best possible functional recovery has been a challenge. Our focus in this work is on developing controllers for a hand exoskeleton.

Research has shown some evidence that force-control based strategies can be more effective for rehabilitation than position-based control alone [102]. However, basic force control requires an estimate of the subject-specific limb joint torques and fails to produce an accurate movement without any error correction at the exoskeleton joints. As a result, impedance [63] or admittance control [103, 125] has been adopted, which are capable of providing compliant interaction with the human limb, while assisting in tracking the desired reference trajectory [7, 33]. Impedance control requires high stiffness to create accurate movement, especially at the finger joints, as the finger joint stiffness varies considerably in its range of motion [85], in the absence of accurate subject-specific model of the finger joint stiffness. However, a high exoskeleton impedance could lead to uncomfortable or unsafe interactions. For example,

it leads to the application of increased torques at the finger joints in case of occasionally stalled joint [2], which is possible during therapy due to the nature of impairment (e.g. spastic catch phenomena and changing nature of spasms in spastic finger muscles [42], accidental locking of finger joints due to inflammatory joint disease such as rheumatoid arthritis [31]). In addition, with impedance control there is a tendency to slack as the users rely on the assistive force to a great extent, which reduces patient involvement in the task and inhibits learning [64]. Thus, there is a need to learn subject-specific models for the finger joint torques. Also, a means to adapt to the changing requirements of a subject is an inherent control requirement.

To address the aforementioned challenges, we develop two assist-as-needed controllers for a hand exoskeleton system. Learned force-field control learns a subject-specific model of the required joint torques using a neural network and use this model to build a force-field to assist the finger joint motion of the subject. Adaptive assist-as-needed control, on the other hand, varies the amount of assistance based on online estimation of the subject performance using measurements, to encourage active participation. A force-field control has been developed for a lower limb exoskeleton, which provided only a constant assistance along the task trajectory [71, 176], was not subject-specific and did not have any learning aspect. Such a controller is not appropriate for a hand exoskeleton. This is because for finger joints where the joint stiffness changes considerably within the range of motion, accurate force-field assistance for the specific subject is needed along the task trajectory to achieve the task at de-

sired velocities. Also, the previous force-field control did not take into account the fact that the nature of assistance can vary in the workspace due to the non-homogeneous residual motor capabilities of a subject [116]. A few upper and lower limb exoskeletons have also implemented adaptive assist-as-needed control [117, 172]. However, such controllers have never been developed and implemented for a hand exoskeleton system.

1.3 Research Goals

This work has the following three research goals:

1. Goal I: Design, Development and Testing - The first goal entails designing, developing and testing the series elastic actuators, finger and thumb modules of the hand exoskeleton.

2. Goal II: Advanced Control - The second goal involves developing two subject-specific assist-as-needed controllers for the designed hand exoskeleton.

3. Goal III: Development of a Framework for Rehabilitation - The third goal consists of developing a framework for rehabilitation that gradually adapts the task, assistance and feedback to keep the task optimally challenging for a subject based on the performance on the task.

1.4 Contributions

This work makes the following novel contributions:

1. Presents the first hand exoskeleton with a series elastic actuator that allows for: (i) accurate bidirectional torque control of each actuated joint, (ii) large workspace with hand and (iii) independent torque control of the four thumb joints.

2. Presents the design of two miniature Bowden-cable based rotary series elastic actuators with linear and torsional springs. Compares and contrasts the performance of the two SEAs through experiments. Shows accurate torque tracking performance (RMSE<12% and fidelity>97%) with torque controllers that estimate the deflection of the elastic element using the motor and joint position measurements for the Bowden-cable-based SEAs.

3. Presents a novel neural-network-based learned force-field control that allows to (a) perform tasks under significant joint stiffness variation at desired velocities, which is present in hand digits and (b) capture the non-homogeneity in residual motor capabilities of a specific subject, while providing assistance.

4. Develops the learned force-field and adaptive assist-as-needed controls for the hand exoskeleton and compare and contrast the two assist-as-needed controllers.

5. Presents a framework for robot-assisted motor (re)-learning that provides subject-specific training by allowing for simultaneous adaptation of task,

assistance and feedback based on the performance of the subject on the task.

6. Presents a learning from demonstration approach to model a continuous and coordinated multi-joint task in a generative manner such that the challenge-level of the task could be modulated in an online manner.

7. Presents a torque-based task that requires subject to dynamically regulate their joint torques capturing the essence of dexterous manipulation.

1.5 Selected Publications

This work has resulted in the following publications:

Journal Articles

1. **P. Agarwal**, J. Fox, Y. Yun, M. K. O'Malley, and A. D. Deshpande, "An Index Finger Exoskeleton with Series Elastic Actuation for Rehabilitation: Design, Control and Performance Characterization", International Journal of Robotics Research, 34(14), pp.1747-1772, 2015.

2. **P. Agarwal**, R. Neptune, and A. D. Deshpande, "A Simulation Framework for Virtual Prototyping of Robotic Exoskeletons", ASME Journal of Biomechanical Engineering, 138(6), pp. 061004(1–15), 2016.

3. **P. Agarwal**, Y. Yun, J. Fox, K. Madden and A. D. Deshpande, "Design, Control and Testing of a Thumb Exoskeleton with Series Elastic Actua-

tion", International Journal of Robotics Research, 2016. (conditionally accepted)

4. **P. Agarwal** and A. D. Deshpande, "Series Elastic Actuators for Small-scale Robotics Applications", ASME Journal of Mechanisms and Robotics, 2016. (under review)

5. **P. Agarwal** and A. D. Deshpande, "Simultaneous Adaptation of Task, Assistance and Feedback affects Motor Learning", Journal of NeuroEngineering and Rehabilitation, 2016. (in preparation)

6. **P. Agarwal**, B. Fernandez and A. D. Deshpande, "Subject-specific Assist-as-needed Controllers for a Hand Exoskeleton for Rehabilitation", ASME Journal of Dynamic Systems, Measurement, and Control, 2016. (in preparation)

Patents

1. A. D. Deshpande and **P. Agarwal**, "Robotic Finger Exoskeleton", United States Patent, Application No. PCT/US2014/071049, Filed: December 18, 2014. (pending)

Conference Papers

1. **P. Agarwal**, P. Kuo, R. Neptune, and A. D. Deshpande, "A Novel Framework for Virtual Prototyping of Rehabilitation Exoskeletons", IEEE International Conference on Rehabilitation Robotics (ICORR), 2013.

2. **P. Agarwal**, A. Hechanova, and A. D. Deshpande, "Kinematics and Dynamics of a Biologically Inspired Index Finger Exoskeleton", ASME Dynamic Systems and Control Conference (DSCC), 2013.

3. **P. Agarwal** and A. D. Deshpande, "Impedance and Force-field Control of the Index Finger Module of a Hand Exoskeleton for Rehabilitation", IEEE International Conference on Rehabilitation Robotics (ICORR), 2015.

4. **P. Agarwal**, B. Fernandez, and A. D. Deshpande, "Assist-as-needed Controllers for Index Finger Module of a Hand Exoskeleton for Rehabilitation", Dynamic Systems and Control Conference (DSCC), 2015.

5. **P. Agarwal** and A. D. Deshpande, "A Novel Framework for Optimizing Motor (Re)-learning with a Robotic Exoskeleton", IEEE International Conference on Robotics and Automation, 2016. (under review)

Extended Abstracts

1. **P. Agarwal**, P. Kuo, R. Neptune, and A. D. Deshpande, "Integration of Musculoskeletal Analysis with Engineering Design for Virtual Prototyping of Exoskeletons", American Society of Biomechanics (ASB), 2013.

2. **P. Agarwal**, J. Fox, Y. Yun, M. K. OMalley, and A. D. Deshpande, "Additive Manufacturing and Series Elastic Actuation for Hand Exoskeletons", Workshop on Assistive Robots for Individuals with Disabilities:

HRI Issues and Beyond at International Conference on Intelligent Robots and Systems (IROS), 2014.

3. **P. Agrawal** and A. D. Deshpande, "A Novel Framework for Optimizing Motor (Re)-learning with a Robotic Exoskeleton", Biomechanics and Neural Control of Movement Conference, 2016.

Chapter 2

Design, Development and Testing of the Hand Exoskeleton[1]

This chapter describes the design, control and experimentation of the SEAs, index finger and thumb exoskeleton modules developed for the hand exoskeleton.

2.1 Series Elastic Actuation

In this section, we will describe the details of the two SEA prototypes developed for the hand exoskeleton, along with the experiments conducted to validate their performance.

2.1.1 Mechanical Design

We first describe the details of the design of the Bowden-cable-based SEAs including their design requirement, two configurations and modeling.

[1]Portions of this chapter has previously been published in the following article–P. Agarwal, J. Fox, Y. Yun, M. K. OMalley and A. D. Deshpande, "An Index Finger Exoskeleton with Series Elastic Actuation for Rehabilitation: Design, Control and Performance Characterization", International Journal of Robotics Research, 34(14), pp.1747-1772, 2015. The author carried out the literature review of the existing hand exoskeletons, and developed and tested the presented hand exoskeleton in the cited work.

2.1.1.1 Design Requirements

The design of the actuator for small-scale robotic applications require the size of the actuator to be small. Considering our application of a hand exoskeleton, we chose the required size to be smaller than $45 \times 35 \times 20$ mm including sensors, to accommodate several such actuators on the exoskeleton. Also, the torque bandwidth of at least 2 Hz is required based on the fact that the bandwidth of the human force compliance control loop is 1–2 Hz [28, 141]. In addition, an appreciable angular deflection ($\sim 15°$) is required for the elastic element at the maximum torque to provide sufficient torque resolution under the noisy angle sensor measurements. We aim for our hand exoskeleton to have a weight of under 300g and a total of 10 SEAs to actuate the joints of all the digits. To meet this criterion on weight, each SEA is required to weigh less than 30 g excluding the Bowden cables. Finally, we chose the required bidirectional peak torque of at least 0.3 Nm for the SEA based on the torques applied by experienced therapists for hand rehabilitation as measured through a torque measuring device [157].

2.1.1.2 Two Design Configurations

We designed two different prototypes of the SEAs using linear and torsion springs (Fig. 2.2). To achieve linear bidirectional torque characteristics, we used two elastic elements in each SEA.

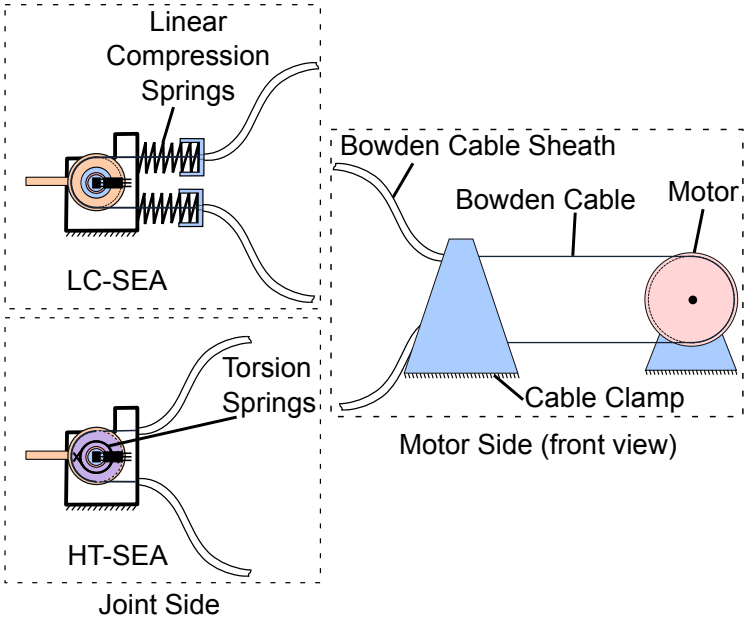

Figure 2.1: Schematic for the two SEA designs–linear compression spring SEA (LC-SEA) and helical torsion spring SEA (HT-SEA).

2.1.1.3 Linear Compression Spring SEA (LC-SEA)

In this SEA, we introduced a compression spring between the sheath and the exoskeleton base at the exoskeleton side (Fig. 2.2a). Since Bowden cable has the same tension as the compressive force acting on the sheath, the estimation of the compressive force using spring deflection gives a measure of the tension in the two cables and hence, torque acting at the joint. Also, since one end of the compression spring rests on the exoskeleton base, there is no translation of the compression spring. In addition, the compression spring reduces in length as the device operates, thus avoiding any possible interference with other components during operation. The linear compression spring for this SEA should be sufficiently stiff, have small outer diameter (<10mm) to

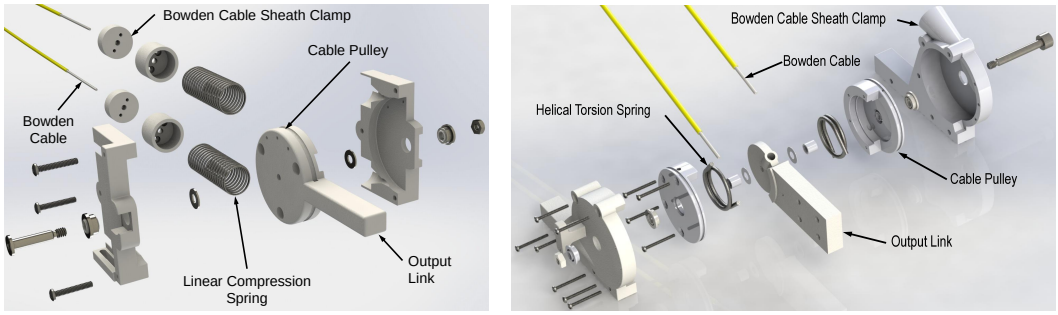

(a) (b)

Figure 2.2: Two Bowden-cable-based SEA designs: (a) LC-SEA and (b) HT-SEA.

meet the requirement on width including the sensor and not buckle at the same time (Free length $< 5\times$ Mean diameter) [122].

2.1.1.4 Helical Torsion Spring SEA (HT-SEA)

In this SEA, two helical torsion springs were introduced between the Bowden cable pulley at the joint side and the output link (Fig. 2.2b). However, since the cable pulley and output link need to be separate in this design, it had more components and was wider (24 mm) than the LC-SEA (17 mm). The torsional springs were installed in a pre-stressed state in opposite directions to achieve linear bidirectional nature of the torque.

2.1.1.5 Sensing

Typically SEAs employ explicit sensors (e.g. potentiometer) to directly measure the deflection of the elastic element. However, the considerable size of off-the-shelf sensors makes it difficult to mount these in the limited space on

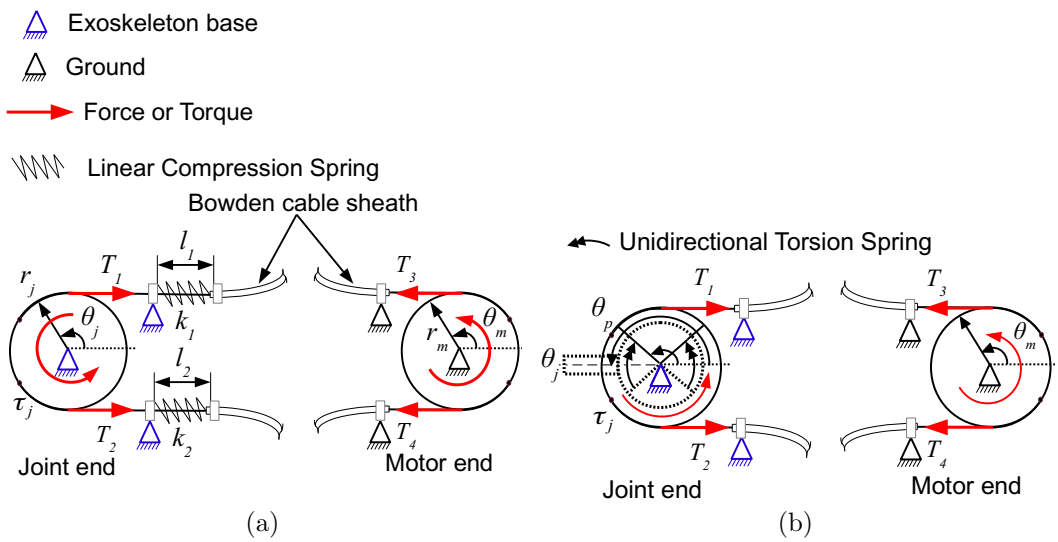

Figure 2.3: Schematic of different miniature Bowden-cable-based SEA mechanisms. (a) LC-SEA and (b) HT-SEA.

a hand exoskeleton. Instead, we estimated this deflection by using the motor and joint position measurements for both the SEAs.

2.1.2 System Modeling

The dynamics of the joint end of the two SEAs is given by Eqn. (2.1).

$$I_j\ddot{\theta}_j + b_j\dot{\theta}_j + \tau_j = (T_2 - T_1)r_j \tag{2.1}$$

The equations for the tensions in cable at the joint and motor end with $k_1 = k_2 = k$ are given by Eqn. (2.1.2).

$$\begin{aligned} T_1 &= T_{10} + k\Delta l_1 \\ T_2 &= T_{20} + k\Delta l_2 \end{aligned} \tag{2.2}$$

$$T_3 = T_1 \beta^{-\sigma(\Delta \dot{l}_1)}$$

$$T_4 = T_2 \beta^{\sigma(\Delta \dot{l}_2)}$$

β is the Bowden cable coefficient for the selected friction model [129].

2.1.2.1 LC-SEA Model

The kinematic relationship for the LC-SEA with two springs of same stiffness values ($k_1 = k_2 = k$) is given by Eqn. (2.3). (Fig. 2.3(a))

$$\Delta l_1 = -\Delta l_2 = r_j \theta_j - r_m \theta_m \tag{2.3}$$

The torque acting at the SEA joint is given by Eqn. (2.4).

$$(T_2 - T_1) r_j = 2k \left(r_m \theta_m - r_j \theta_j \right) r_j \tag{2.4}$$

The feed-forward motor position with a given reference torque (τ_r) is given by Eqn. (2.5).

$$\theta_{m,ff} = \frac{1}{r_m} \left(\frac{\tau_r}{2k r_j} + r_j \theta_j \right) \tag{2.5}$$

2.1.2.2 HT-SEA Model

For the HT-SEA, the kinematic relation with $k_1 = k_2 = k_j$ is given by the relative deflection of the pulley with respect to the joint as expressed in Eqn. (2.6).

$$\Delta \theta = \theta_p - \theta_j = \frac{r_m \theta_m}{r_j} - \theta_j \tag{2.6}$$

The torque due to the deflection of the springs at the joint is then given by Eqn. (2.7).

$$2k_j\Delta\theta = 2k_j\left(\frac{r_m\theta_m}{r_j} - \theta_j\right) \tag{2.7}$$

The feed-forward motor position with a given reference torque (τ_r) is given by Eqn. (2.8).

$$\theta_{m,ff} = \frac{r_j}{r_m}\left(\frac{\tau_r}{2k_j} + \theta_j\right) \tag{2.8}$$

It can be seen that the feed-forward terms in Eqns. (2.5) and (2.8) are mathematically equivalent when $k_j = kr_j^2$. However, in practice the effective stiffness and friction acting in the system is significantly affected by the design configuration and hence, the performance of the two SEAs needs to be experimentally validated.

2.1.3 Controller Design

Once a model of the torque output from each SEA is derived, a controller is designed for the SEA. The goal of this controller is to track the reference torque at the SEA joint using feed-forward PID control. The controller consists of an inner position control loop at the actuator level and an outer force control loop at the SEA level (Fig. 2.4). The output of the system is the torque generated at the output joint through SEA. The PID controller with the corresponding feed-forward term is then given by Eqn. (2.9).

$$u = \theta_{m,ff} + k_p e + k_d\dot{e} + k_i\int edt \tag{2.9}$$

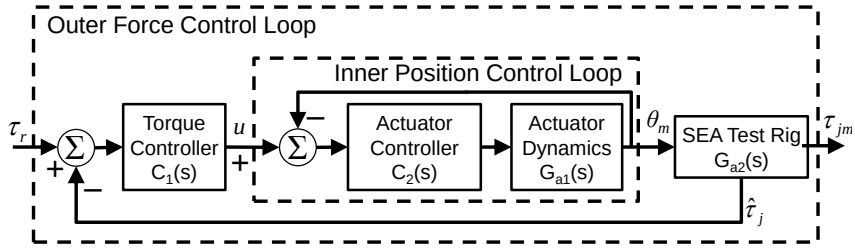

Figure 2.4: The schematic of the torque controller implemented for the SEAs. The inner position control loop represents the position control implemented in the motor driver. The outer force control loop refers to the control loop implemented for output torque tracking.

where $e = \tau_r - \hat{\tau}_j$ is the SEA joint torque error, $\hat{\tau}_j$ is the estimated torque and u is the position control command for the actuator. The open-loop transfer function of the linearized system from control command u to output torque τ_j is given by Eqn. (2.10).

$$G_{\mathrm{OL}}(s) = \frac{\tau_j}{u} = \frac{C_2(s)G_{a1}(s)G_{a2}(s)}{1 + C_2(s)G_{a1}(s)} \tag{2.10}$$

The closed-loop transfer function of the linearized system from reference torque τ_r to the output torque τ_j with transport delay in input is given by Eqn. (2.11).

$$G_{\mathrm{CL}}(s) = \frac{\tau_j}{\tau_r} = \frac{e^{-Ts}C_1(s)C_2(s)G_{a1}(s)G_{a2}(s)}{1 + C_2(s)\left(G_{a1}(s) + C_1(s)G_{a1}(s)G_{a2}(s)\right)} \tag{2.11}$$

where T is the sampling time of the overall control loop. Since inner position control loop ran at several kHz, we do not account for the transport delay in that loop.

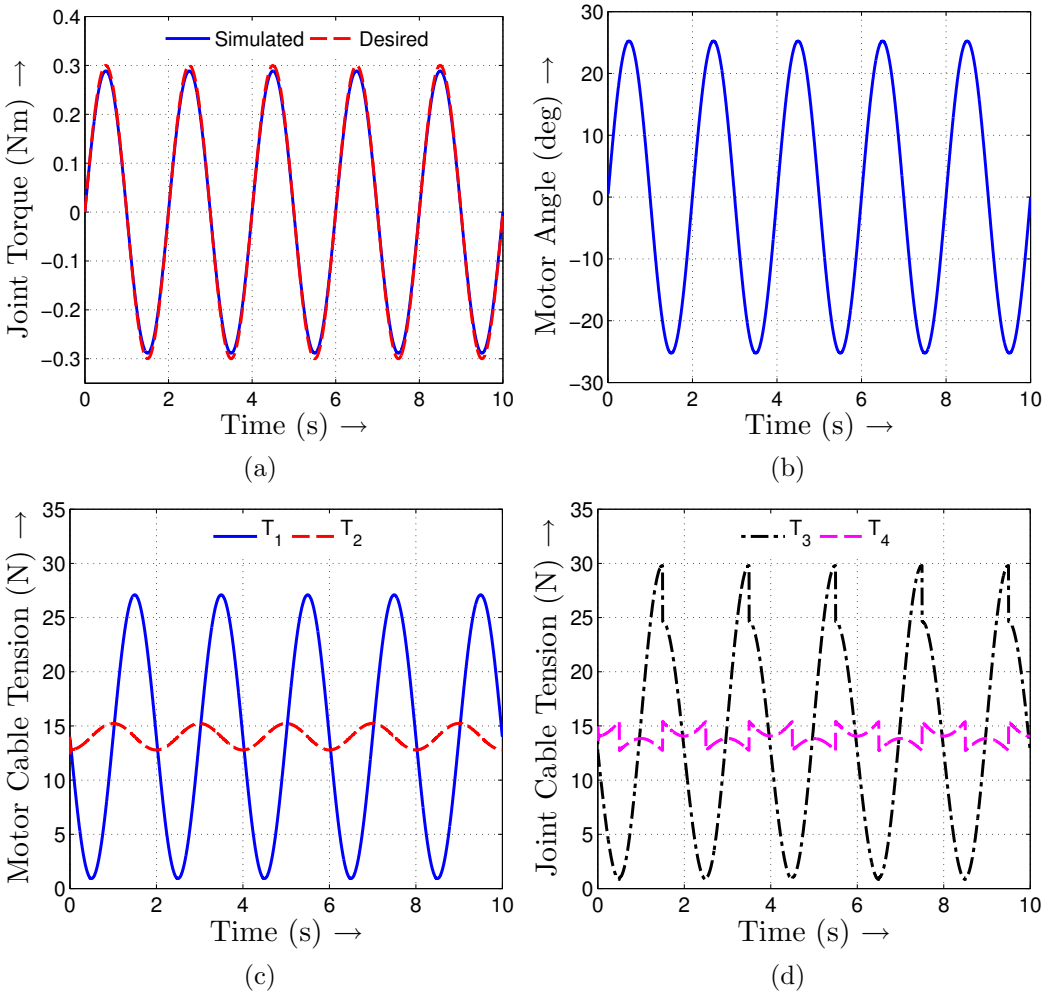

Figure 2.5: The joint torque tracking performance for the PID controller with sinusoidal torque input in simulation: (a) Output joint torque trajectory, (b) motor angle trajectory, (c) motor side cable tension, and (d) joint side cable tension. An effective spring stiffness of 2000N/m or 0.3 Nm/rad is used for these simulations.

2.1.4 Simulation

We carry out simulation of the SEA on the test rig (described in Section 2.1.5) for tracking a desired torque trajectory with sinusoidally varying torque output. Since, the two SEAs are equivalent theoretically, we only simulate the Bowden-cable-based SEA with an elastic element. The goal of the simulation is to obtain estimates of the peak tension in the cable for choosing the appropriate Bowden cable and sheath pair and required spring stiffness to achieve peak torques of at least 0.3 Nm, which is needed for our application of a hand exoskeleton. We model the load cell connected to the output link as a high stiffness torsional spring. We simulate the system dynamics using the model presented in Section 2.1.2 and the controller presented in Section 2.1.3. A sinusoidal joint torque is used as reference for the torque controller (Eqn.).

$$\tau_r = \tau_A \sin(2\pi f t + \phi) \tag{2.12}$$

where τ_r is the reference torque, τ_A is the peak torque amplitude, f and ϕ are the sinusoidal torque frequency and phase, respectively and t is simulation time.

The following values for the various parameters in the system model are used for the simulation: $I_j = 3.4 \times 10^{-5}$ kgm^2, $r_j = 12$ mm, $r_m = 28$ mm, $k = 1103$ N/m, $T_{i0} = 14N$, $\beta = 1.1$, $\tau_A = 0.3$ Nm, $f = 0.5$ Hz, $\phi = 0°$. Since, the SEA joint has a bearing, we do not consider the damping at the joint for the simulation.

The simulation results show that the PID control with a feed-forward

term is able to track the desired torque trajectory with a root mean square error (RMSE) of 2.67% (0.008 Nm). Small deviation from the desired torque was observed at the peaks of the sinusoid (Figure 2.5a). The motor angle stays within safe bounds for the system to achieve bidirectional torque control with a peak torque of 0.3 Nm (Figure 2.5b). The tension in the cable on joint side shows a sudden change due to the nature of the model that captures the change in the direction of friction as the motion reverses (Figure 2.5d). The peak tension in the Bowden cable is observed to be 30 N, which ensures that the stretch in the cable is negligible and that good spring deflection estimates could be obtained using the joint and motor position measurement. We chose a commercially available low friction Polytetrafluoroethylene (PTFE) coated sheath (1mm inner diameter, 3mm outer diameter) and Fluorinated ethylene propylene (FEP) coated cable (0.66 mm diameter) with a rated load capacity of 35.6 N and design safety factor of 5:1 compared to breaking strength for the SEAs. A quick test by hanging 10 kg load on the cable showed that it stretched less than 1 mm. The simulations also showed that an effective spring stiffness of around 2000 N/m or 0.3 Nm/rad is needed to achieve the required peak torque with a motor angle of above 20°.

2.1.5 Experiments with SEAs

A test rig was developed for testing the performance of the proposed SEAs (Fig. 2.6). On the joint side a six-axis load cell was mounted to measure the output joint torque. A compact magneto-resistive angle sensor (KMA210,

NXP Semiconductors) similar to the one installed on the index finger exoskeleton was used to measure the joint angle and provide feedback to the torque controller to take into account the effect of sensor noise on the control. We used a geared brushed DC motor (20 W) from Maxon Inc. as the actuator for the SEAs. The experiments with the SEA test rig and the developed exoskeleton were aimed at characterizing the following: (i) accuracy and fidelity of torque tracking; (ii) torque bandwidth (iii) dynamic range; (iv) performance at different peak torque magnitudes and (v) performance under disturbance. Experiments (iv) and (v), which are carried out for detailed testing of the SEA, are conducted with LC-SEA only, since the results showed that it is better suited for our application.

The effective stiffness acting in the system differs from the catalog value of the stiffness of the off-the-shelf springs. This is due to the fact that there are several factors that contribute to the effective stiffness in the system. These include the compression of the sheath and the interface in which the spring rests for LC-SEA, which is designed to have a tight fit with the spring for it to act as a built-in support for reducing sideways bending of the spring, leading to reduction in the effective length of the spring and friction. This requires explicit estimation of the effective stiffness acting in the system. Also, for the miniature SEA with 3D printed parts the joint inertia is very small and also for our application of hand rehabilitation the system is required to operate at relatively low accelerations and velocities. In addition, the damping at the joint is small as the joints are supported with miniature ball bearings. Thus,

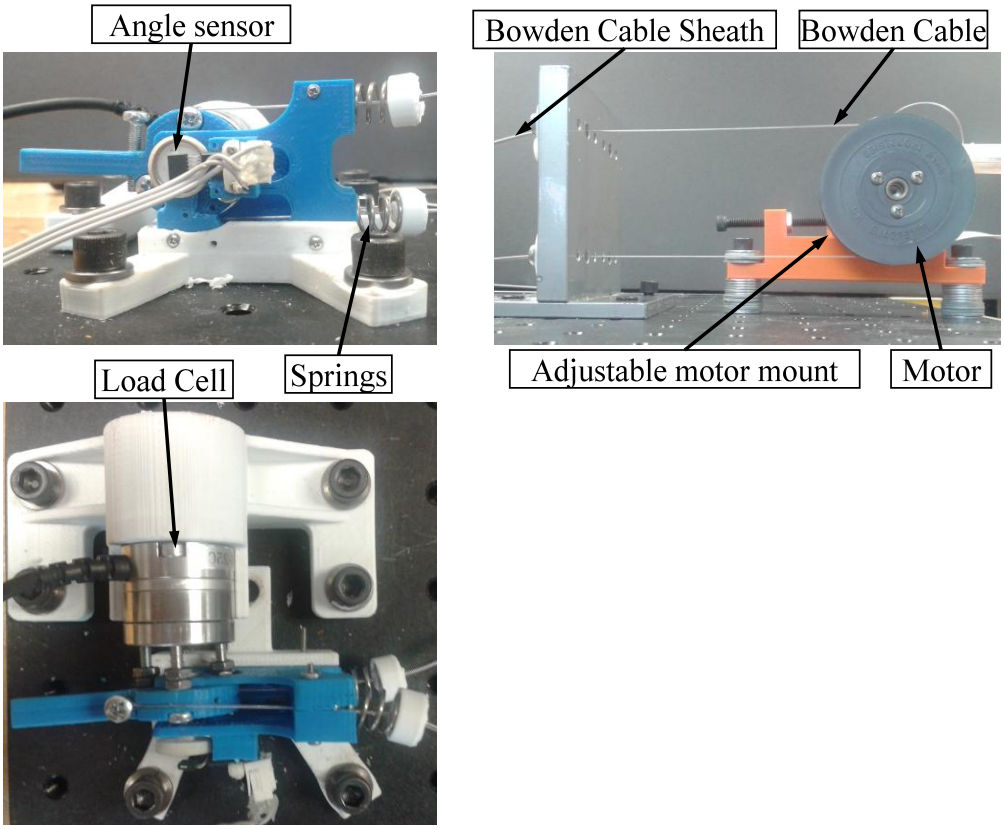

Figure 2.6: The test rig developed to assess the torque tracking performance of the SEAs. A one meter long Bowden cable sheath separated the motor side and joint side, which were mounted on two different mechanical breadboards.

the contribution of the inertial and damping terms is much smaller and the torque applied using the Bowden cables is transmitted to the joint without significant reduction.

To identify the effective stiffness, we first run the system using open-loop feedforward control with a sinusoidal torque trajectory as the desired torque and record the motor position, joint position and desired and measured

joint torques. The effective stiffness is then identified using the torque output models (Eqns. (2.4) and (2.7)) with least squares minimization [97] of the error between the estimated and measured joint torque. The system is then run with the identified stiffness for the same desired torque trajectory and the process is iterated a few times to ensure that the identified effective stiffness does not vary significantly. This identified stiffness is kept constant throughout the experiments for each SEA. Finally, the PID gains of the torque controller are manually tuned to achieve a stable and accurate control of the joint torque.

2.1.5.1 Accuracy and Fidelity of Torque Tracking

The goal of this experiment was to track a sinusoidal joint torque on the SEA test rig and verify the tracking accuracy and fidelity of the output torque using the measurements obtained through the load cell. Torque output fidelity has been defined in the past to quantify the distortion of the output due to the nonlinearities present in the system for SEAs [60, 110, 163]. We use the measure defined in Eqn. (2.13) to quantify the torque tracking fidelity.

$$F = \left(1 - \frac{var(\tau_{jm} - \tau_r)}{var(\tau_{jm})}\right) \times 100\% \tag{2.13}$$

where F represents the force fidelity, τ_{jm} and τ_d are the measured and the desired torque output, respectively, and $var(.)$ is the variance.

2.1.5.2 Torque Bandwidth

Torque bandwidth is the maximum frequency at which an SEA can deliver torque. Torque bandwidth of the proposed SEAs was evaluated by using a linear chirp signal (Eqn. (2.14)) as the desired torque for the system.

$$\tau_d = \tau_A \sin\left(2\pi(f_0 + f_1 t)t\right) \tag{2.14}$$

We evaluate the magnitude ($|G_{CL}|(j\omega)$) of the frequency response of the SEAs using the measured torque data using Eqn. (2.15) before fitting any model to capture the response with the nonlinearities present in the system. This helps in avoiding any approximation which is typically introduced when the response is obtained by using a linear model fitted to the data.

$$|G_{CL}(j\omega)| = \frac{|\tau_{jm}(j\omega)|}{|\tau_r(j\omega)|} \tag{2.15}$$

where $|\tau_{jm}(j\omega)|$ and $|\tau_r(j\omega)|$, represent the single-sided amplitude spectrum of the measured and reference torque data obtained using fast Fourier transform. We also identified the closed-loop system model Eqn. (2.11) from the sampled frequency response data by fitting continuous-time systems of different orders [53, 97] to obtain the model that best describes our system and then used the identified models to obtain the frequency response.

2.1.5.3 Dynamic Range

The dynamic range of an SEA is a measure of how sensitive the actuator is to small torques with respect to its full torque output range [123] and

is typically defined as in Eqn. (2.16). However, for the Bowden cable based SEAs, the torque resolution is not uniform throughout the force range, especially due to nonlinear friction in the Bowden cable. Thus, we define a bound on the dynamic range by evaluating minimum resolvable output torque using the measured joint angle sensor resolution (upper bound) and the maximum error observed during torque tracking (lower bound). The actual dynamic range of the SEA varies between the upper and the lower bound.

$$DR = \frac{\text{Maximum output torque}}{\text{Minimum resolvable output torque}} \tag{2.16}$$

2.1.5.4 Performance at Different Peak Torque Magnitudes

Since the torque tracking accuracy and fidelity of the SEA varies with the change in the peak torque magnitude, we carry out the tests to verify the change in performance. We apply torques with different peak torque magnitudes and separately evaluate these metrics. In addition, we identify the effective stiffness that best explains the output torque.

2.1.5.5 Performance under Disturbance

Since the index finger exoskeleton will be moved around while the device is actuating a subject's hand, assessing the performance of the device under varying degree of disturbance was important. To assess the performance under disturbance, three different levels of disturbances were applied to the joint side setup while the torque tracking experiment is carried out. For mild dis-

turbance, the joint side base is moved up and down in a plane. For medium disturbance, the joint side base was carried up and moved up and down as well as sideways such that the cable is bent by 90 degrees both ways. For the severe case, the base is carried and moved so that the Bowden cable is bent by over 180 degrees both ways. For our application, we anticipate a medium degree of disturbance during the operation of the device. Moving the configuration of the cable during the experiment helped in determining if significant error would be introduced in torque tracking during the operation of the device.

2.1.6 Results

2.1.6.1 Accuracy and Fidelity of Torque Tracking

The controller was able to track the desired torque trajectory with high fidelity for a 0.2 Nm peak torque sinusoid for both the actuators (Fig. 2.7, Table 2.1). The measured, best fit, desired, and estimated refers to the torque measured using the load cell, torque obtained by fitting the best curve to the measured torque, desired torque trajectory as available to the real-time controller and the torque trajectory as estimated by the real-time controller using SEA based torque evaluation, respectively. All the trajectories show small errors (< 11 % of peak torque) with respect to the desired torque trajectory (Table 2.1). The measured curve shows some deviation from the estimated values especially near the peak of the sinusoid. This is due to the error in torque estimation introduced due to the load and configuration dependent effective backlash [75] in the Bowden cable when the motor changes direction. Also, the effective

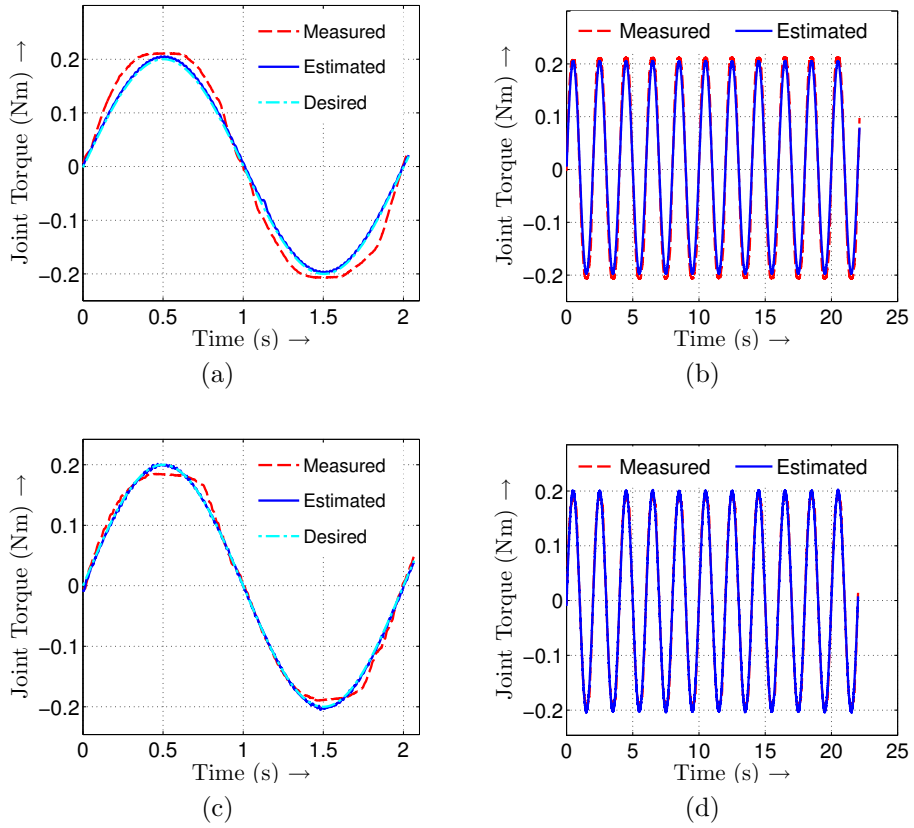

Figure 2.7: The joint torque tracking performance of the proposed SEAs with sinusoidal desired torque trajectory: (a), (b) Output joint torque trajectory comparison for LC-SEA and (c), (d) Output joint torque trajectory comparison for HT-SEA. The identified stiffness value used for evaluating the estimated torque for LC-SEA and HT-SEA was $k = 1103$ N/m and $k = 0.265$ Nm/rad, respectively.

stiffness was a result of the combined stiffness due to the springs and the Bowden cable sheath compliance.

Table 2.1: Joint torque root mean square error (RMSE) for the best fit, estimated and actual torque trajectories for the proposed SEAs at a peak torque of 0.2 Nm. The percent error represents the percentage of RMS error with respect to the peak torque.

SEA	**Best fit**		**Estimated**		**Actual**		**Fidelity**	**Catalog Stiffness**	**Identified Stiffness (k or k_j)**
	Nm	%	Nm	%	Nm	%	(%)		
LC-SEA	0.0134	6.33	0.0231	10.92	0.0229	10.86	97.94	5630 N/m	1082 N/m
HT-SEA	0.0101	5.45	0.0101	5.47	0.0102	5.49	99.47	0.43 Nm/rad	0.26 Nm/rad

2.1.6.2 Torque Bandwidth

The frequency response results showed that both the actuators satisfy the torque bandwidth criterion (> 2 Hz). The LC-SEA and HT-SEA have closed-loop bandwidths (-3 dB magnitude) of 2.5 and 4.5 Hz, respectively, for a 0.2 Nm peak torque (Figs. 2.8 and 2.9). LC-SEA has a more damped frequency response as compared to HT-SEA. The fitting results showed that LC-SEA and HT-SEA showed the best fit for a fifth and fourth order system, respectively (Tables 2.2) A comparison of the system response from the identified model that best explains the system with the measured and the desired torque trajectory shows that there is low phase angle between the trajectories even at relatively higher frequencies of > 2 Hz for LC-SEA and > 3 Hz for HT-SEA (Fig. 2.10). However, the fitting percentage shows that the non-linearity in the system (possibility due to nonlinear friction in Bowden cable) is not completely explained by these models (Table 2.2).

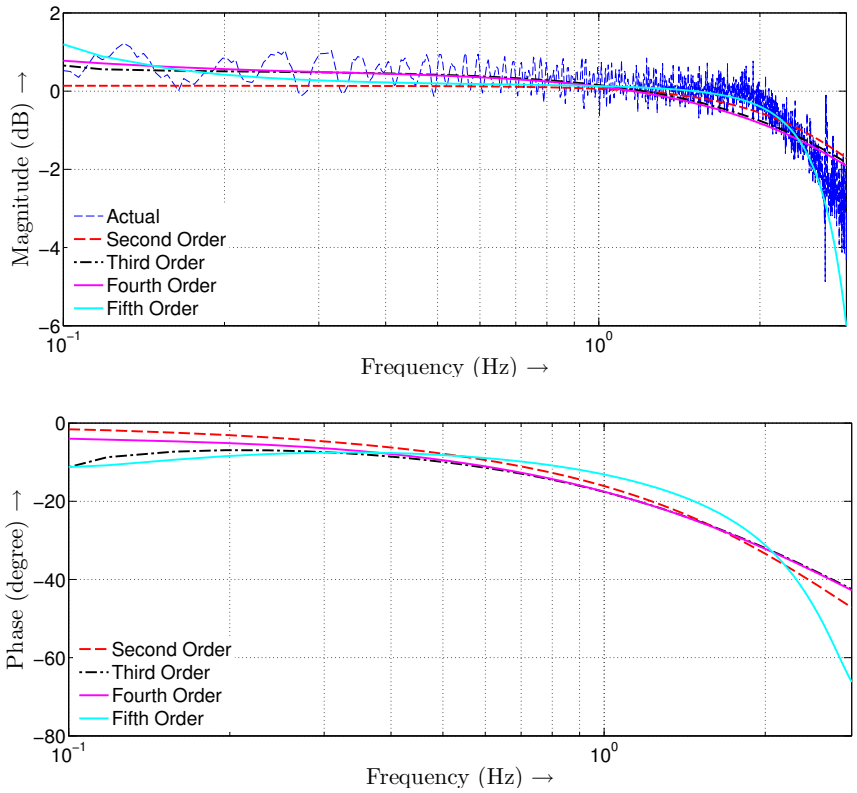

(a)

Figure 2.8: Bode plot of the proposed SEAs: (a) magnitude and phase of LC-SEA and (b) magnitude and phase of HT-SEA.

2.1.6.3 Dynamic Range

The dynamic range of LC-SEA was found to be about three times higher than HT-SEA (Table 1.2). This is because of the higher effective stiffness of HT-SEA as compared to LC-SEA. Also, gradually increasing the desired peak torque for the HT-SEA showed that the achievable peak torque was limited to 0.3 Nm with off-the-shelf torsion springs (Fig. 2.11). In addition, the torque was found to scale more non-linearly for HT-SEA as compared to LC-SEA.

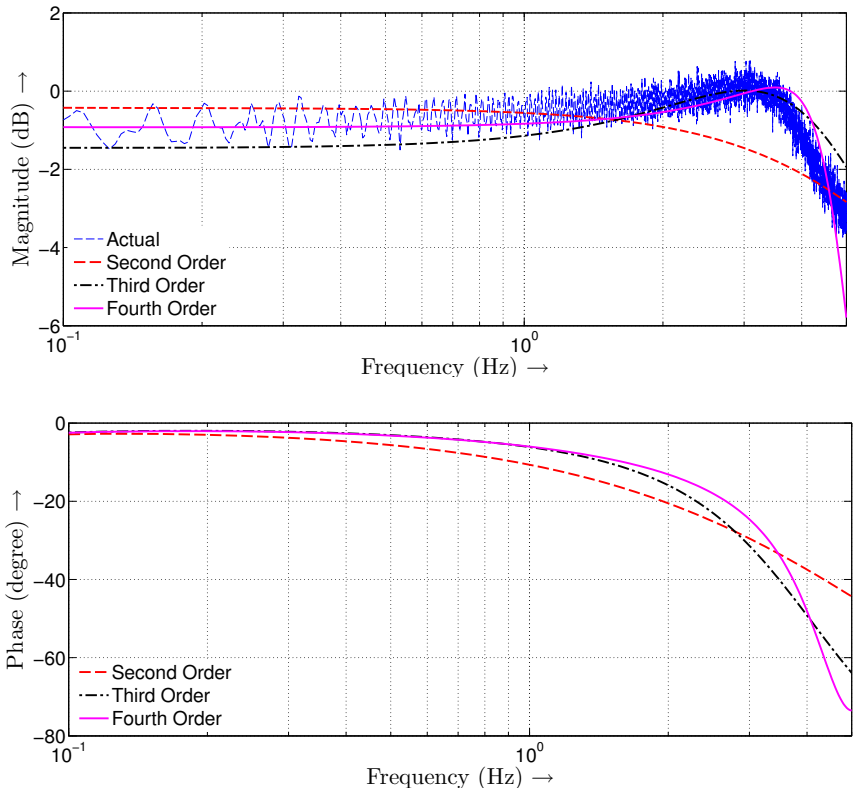

(b)

Figure 2.9: Bode plot of the proposed SEAs: (a) magnitude and phase of LC-SEA and (b) magnitude and phase of HT-SEA.

2.1.6.4 Performance at Different Peak Torque Magnitudes

LC-SEA can be controlled to achieve good tracking performance (RMSE < 12 % and fidelity > 97 %) for torques of peak magnitudes between 0.15 - 0.3 Nm (Fig. 2.12, Table 2.3). In addition, the identified stiffness was found to be fairly constant at all peak torque magnitudes. Thus, LC-SEA can be used as a good torque source for the hand exoskeleton.

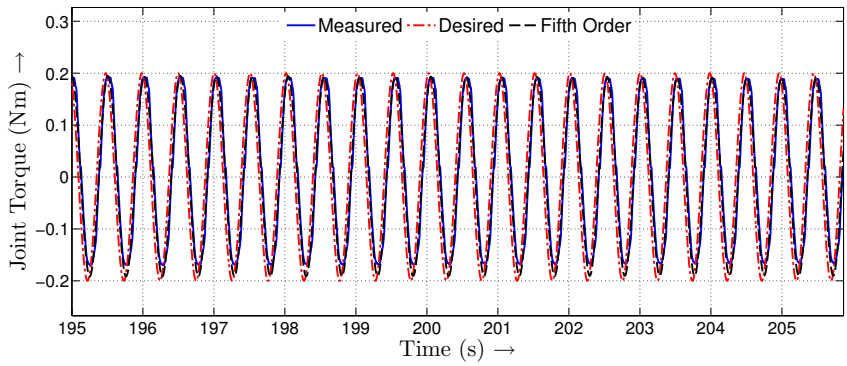

(a)

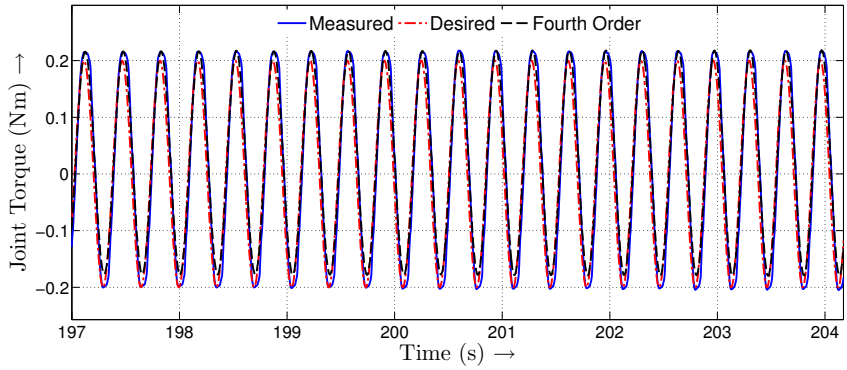

(b)

Figure 2.10: Comparison of the identified system response with the measured and desired torque trajectories for a portion of the applied chirp signal: (a) fifth order system response for LC-SEA and (b) fourth order system response for HT-SEA.

Table 2.2: Model fitting statistics for closed loop systems of different orders. The missing values in the table show that the estimation algorithm failed to converge. FPE refers to the Akaike's Final Prediction Error criterion, which is a measure of the fitted model quality [97].

	LC-SEA			**HT-SEA**		
System Order	Fit (%)	FPE	MSE	Fit (%)	FPE	MSE
2nd	85.06	0.01067	0.01067	77.58	0.02010	0.02010
3rd	85.51	0.01006	0.01004	82.59	0.01213	0.01212
4th	85.32	0.01048	0.01030	**87.47**	**0.00629**	**0.00628**
5th	**88.56**	**0.00634**	**0.00626**	–	–	–
6th	87.82	0.00882	0.00709	86.14	0.01188	0.00767

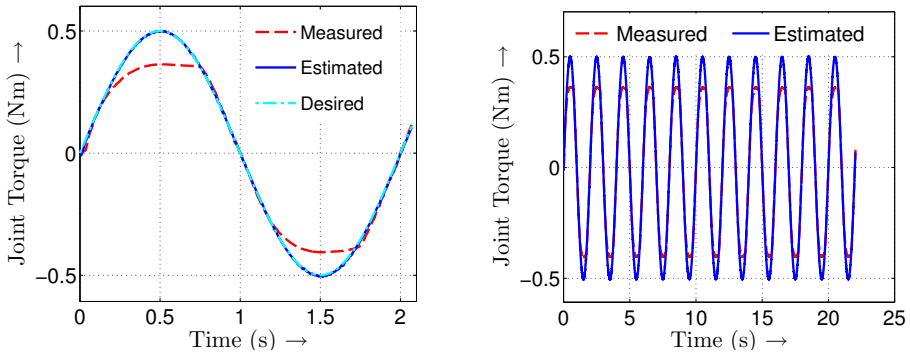

(a) (b)

Figure 2.11: The joint torque tracking performance of HT-SEA with sinusoidal desired torque trajectory. Output joint torque trajectory comparison for: (a) one cycle and (b) several cycles.

Table 2.3: Joint torque root mean square error (RMSE) for the best fit, estimated and actual torque trajectories for the LC-SEA. The percent error represents the percentage of RMS error with respect to the peak torque. The catalog stiffness of the compression spring used for LC-SEA is 5630 N/m

Peak Torque Magnitude	**Best fit**		**Estimated**		**Actual**		**Fidelity**	**Identified Stiffness (k)**
Nm	Nm	%	Nm	%	Nm	%	%	N/m
0.15	0.0128	8.76	0.0132	9.00	0.0136	9.28	98.58	984
0.20	0.0134	6.33	0.0231	10.92	0.0229	10.86	97.94	1082
0.30	0.0179	5.54	0.0379	11.76	0.0374	11.59	97.70	1103

2.1.6.5 Performance under Disturbance

The results show that the tracking performance did not deteriorate significantly even when severe disturbance was applied at the output end for the LC-SEA (Fig. 2.13). However, the torque output showed increasing error as the severity of the disturbance was increased. We anticipate a mild to medium disturbance during the operation of our device. Thus, LCSEA ensures good torque tracking performance during the operation of the device.

2.1.7 Discussion

The higher bandwidth of HT-SEA is because the effective stiffness for LC-SEA was found to be much smaller than the catalog stiffness as compared to HT-SEA (Table 2.1). This may be due to the difference in the way sheath is clamped in the two SEAs. In LC-SEA, the sheath interfaced with the linear compression spring directly, whereas in HT-SEA the sheath interfaced with the housing and the cable is attached to the pulley, which housed the

springs. Also, the springs in LC-SEA show some sideways deflection, which might contribute to the reduction in effective stiffness. In addition, in LC-SEA there is some friction between the spring and the interface where the linear compression spring rests, which reduces the effective stiffness. No such friction is present in HT-SEA.

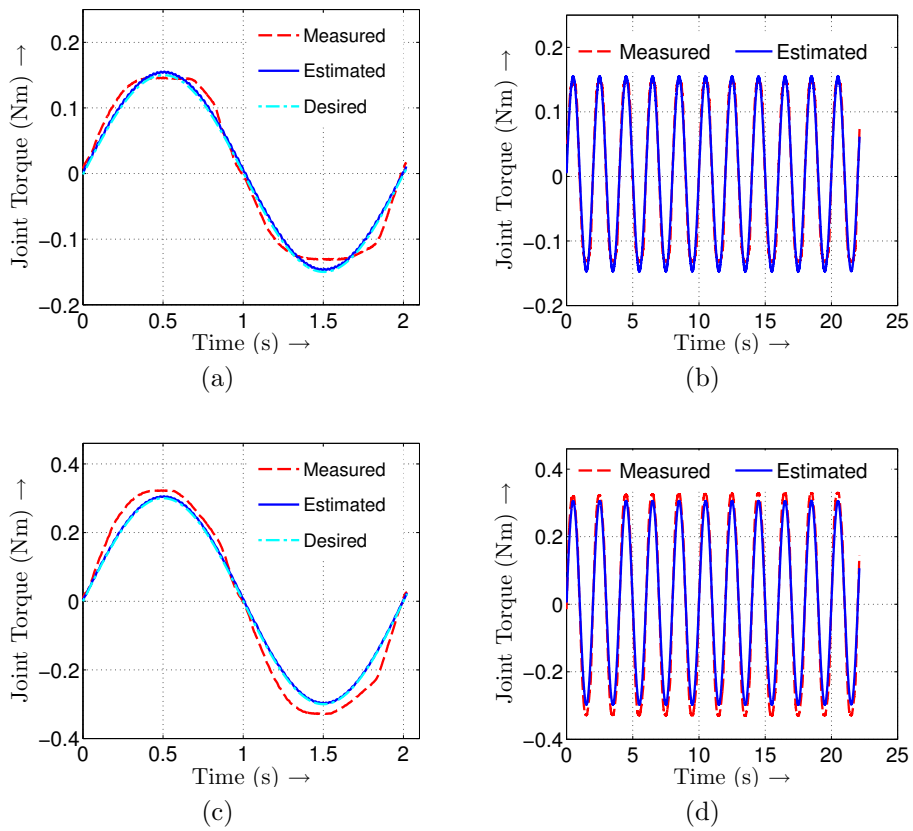

Figure 2.12: The joint torque tracking performance of LC-SEA with sinusoidal torque input. Output joint torque trajectory comparison for peak torque of magnitude: (a), (b) 0.15 Nm and (c), (d) 0.3 Nm. The identified stiffness value of $k = 1103$ N/m was used to evaluate the estimated torque for the controller for all torque trajectories.

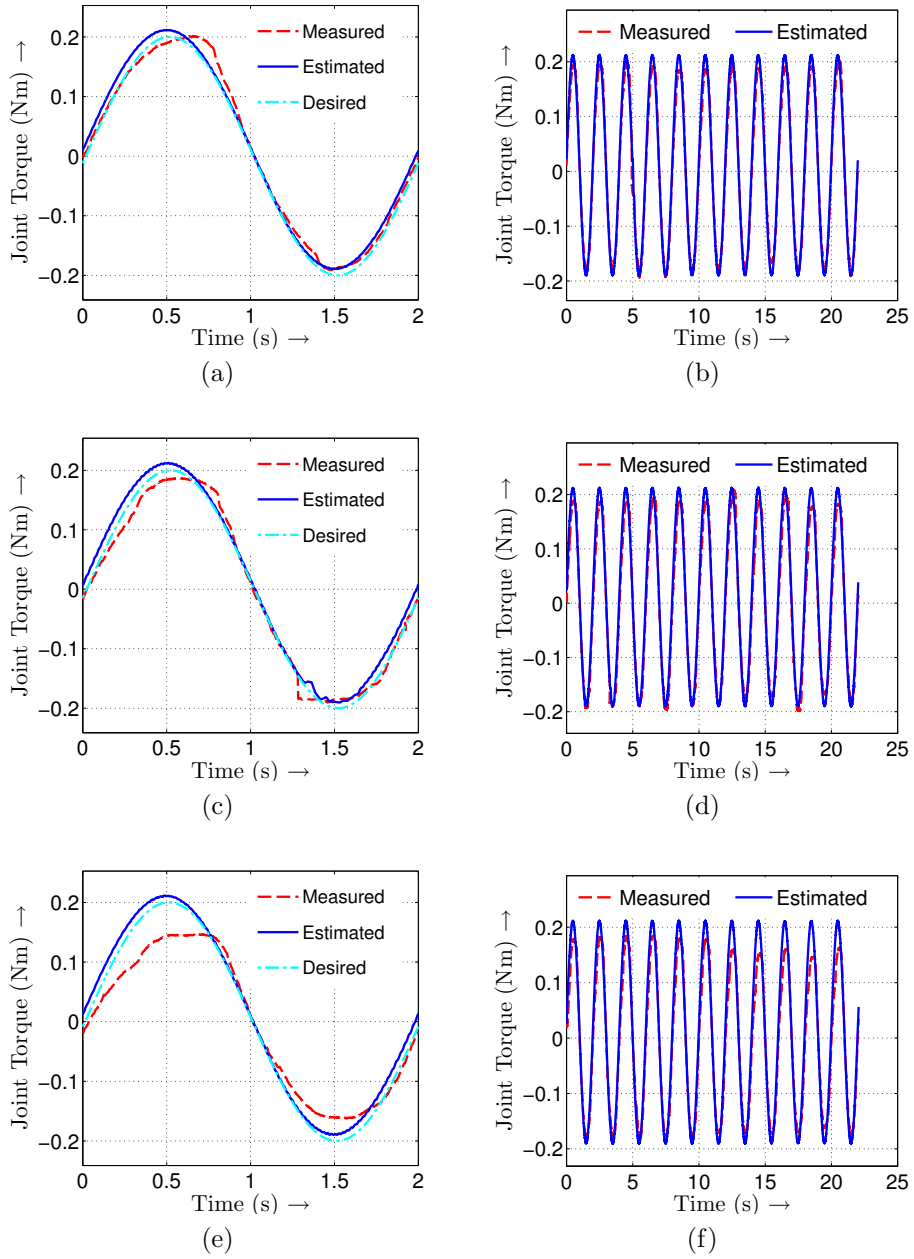

Figure 2.13: The joint torque tracking performance of LC-SEA under varying degrees of disturbance: (a), (b) mild; (c), (d) medium and (e), (f) severe. The plots in the left and right columns represent the tracking performance for one and several cycles, respectively.

The output torque range of the SEAs can be adjusted as per the application by choosing the appropriate spring stiffness. However, the design with helical torsional springs is limited by the availability of off-the-shelf springs. Good performance of the SEA requires appropriate pretension of the Bowden cable to ensure that the cable is not slack throughout the output torque range. Both highly stiff and highly compliant springs deteriorate the performance of the actuator. A very stiff spring reduces the torque resolution due to the noise in the angle sensor measurements at the joint, whereas a very compliant spring limits the maximum achievable torque at the joint. Despite the nonlinear friction in the Bowden cables, the performance of the actuator was satisfactory with feed-forward PID control. Also, it was observed during the experiments that the major contribution of the elasticity was due to the compression of the sheath rather than the elongation of the Bowden cable.

2.2 Index Finger Module of the Exoskeleton

In this section, we present the details of the design, modeling, control, simulation and experimentation of the index finger exoskeleton module of the hand exoskeleton.

2.2.1 Design

In this section, we describe the details of the mechanism of the index finger exoskeleton and the prototype developed using additive manufacturing technique.

2.2.1.1 Mechanism

Our goal is to design an index finger exoskeleton mechanism that leads to low reaction forces at the finger joints, while achieving maximum range of motion at the finger joints. Index finger consists of three joints, namely, metacarpophalangeal (MCP), proximal interphalangeal (PIP) and distal interphalangeal (DIP) (Fig. 2.15(a)). The MCP joint has two DOFs, namely, flexion-extension (up-down motion) and abduction-adduction (sideways motion). The PIP and DIP joints have only flexion-extension motion. The three finger phalanges are called proximal, middle and distal phalanx, respectively.

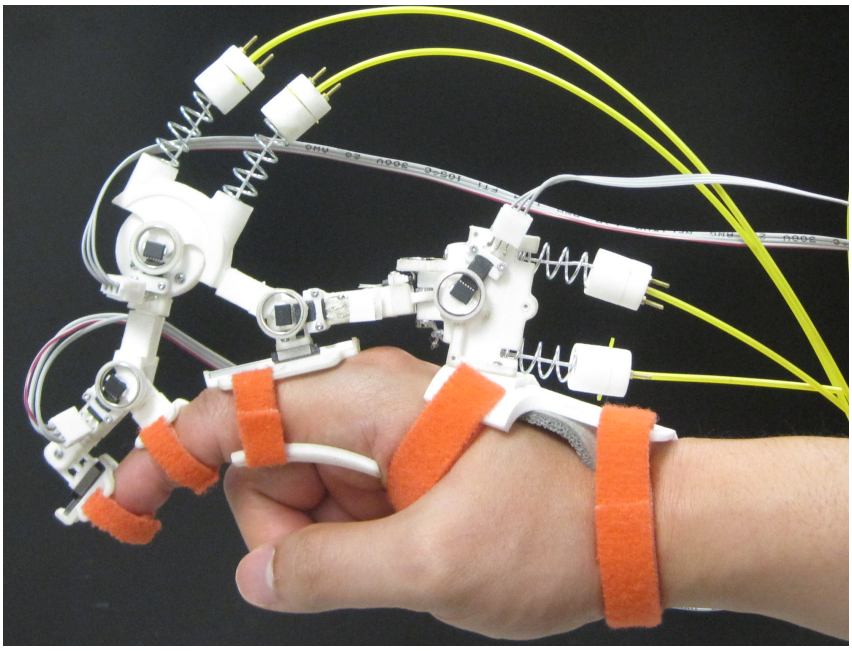

Figure 2.14: Index finger exoskeleton prototype mounted on a subject's hand for experimentation.

Simulation studies and experiments with existing index finger exoskele-

ton prototypes have shown significant loading of the finger joints when exo-tendons (tendons actuating the exoskeleton) are attached to links directly connected to the finger phalanges [5, 6, 70]. To avoid this loading, we first designed a mechanism in which the robotic kinematic chain is in parallel to the finger kinematic chain to ground the actuation reaction forces and form closed loops with the finger to avoid joint axes misalignment (Fig. 2.15(a)). A study has shown that mechanical stress correlates well with clinically observed patterns of frequency of degeneration and degenerative joint disease and suggests that it is among the factors responsible for initiating and propagating joint diseases in finger joints [109]. We introduced sliding joints as the interface between the finger phalanx and the exoskeleton link to ensure that only normal reaction forces are applied on the finger phalanges in all configurations (Fig. 2.15(b)). Any lateral force would result in the translation of the slider until only the normal reaction force exists between the two. The normal reaction force component contributes to generating a moment at the joint while the lateral component simply loads the joint without resulting in any joint moment.

Some studies of the arm have shown that anatomical breakdown (independent motion of different joints) is better than complex arm movement for rehabilitation [81]. The complexity of the task is determined by the number of anatomical joints involved in performing the task rather than the neurological effort needed. It has been shown that breaking down a simultaneous movement of the shoulder in abduction-adduction, flexion-extension, internal-

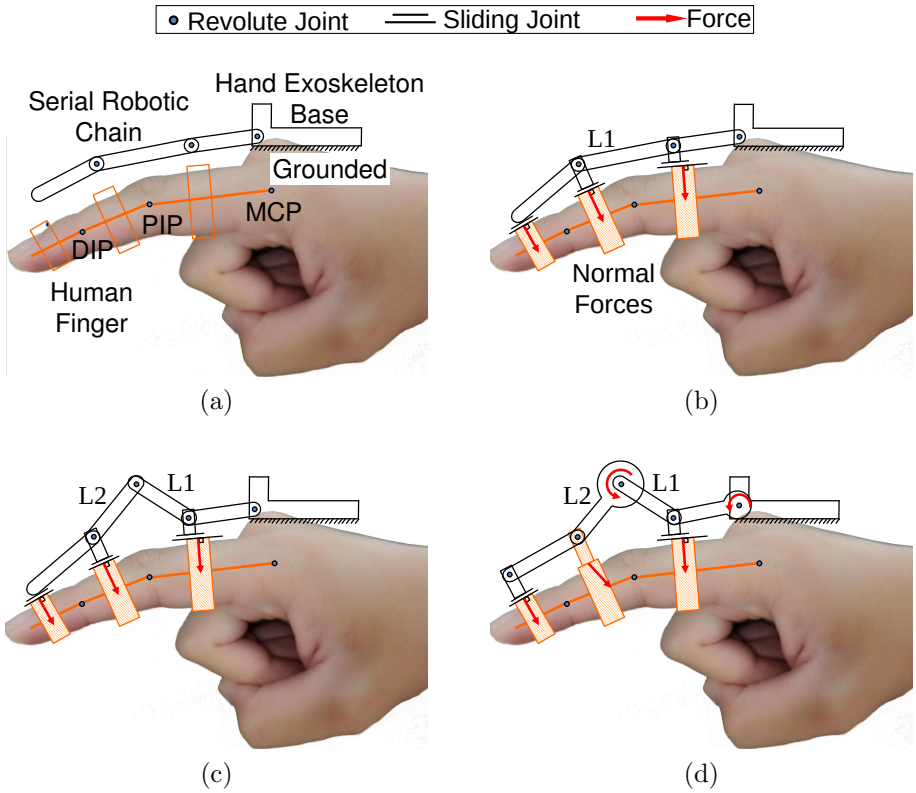

Figure 2.15: Kinematic schematic of various chains in the hand exoskeleton system. (a) Kinematic chains in the system, (b) sliding joints connecting the finger and the exoskeleton kinematic chain, (c) DOF analysis of the three closed loops in the coupled system, and (d) actuated mechanism schematic. The proximal, middle and distal chains are referred to as MCP, PIP and DIP chains, respectively.

external rotation and elbow in flexion-extension along sinusoidal trajectories into parts improve motor learning. A possible suggested hypothesis to explain this is that the motor system has trouble determining where the problems lie in making accurate, complex movements and breaking the movement into individual joint movements may allow for better identification and more focused

practice on the key problems.

For the finger motion, breaking the simultaneous movement of both the MCP and PIP joints into motion of each joint individually could improve motor learning. In addition, a device that would enable independent motion at the MCP and PIP joint would be more versatile in rehabilitating targeted joints more effectively and assessing recovery progress. Thus, we aim for independent DOF at the finger MCP and PIP joints. We do not aim to actively actuate the DIP joint, as the PIP and DIP joints are anatomically coupled in a human hand [92]. However, connecting the MCP chain with the PIP chain using a single link (L1) results in a significantly low range of motion (ROM) at the finger PIP joint due to the limited range of the available sliding length. To overcome this problem, we introduced two links (L1 and L2) connected through a revolute joint to connect the MCP chain with the PIP chain (Fig. 2.15(c)). This resulted in one DOF in the MCP chain and a coupling between the PIP and DIP finger joints whose effects can be adjusted based on the link lengths in the two chains. However, the PIP chain has two DOF and for full actuation requires two actuators. The system can be controlled with one actuator by introducing a stiffness element in the chain [32]. However, the problem of underactuation in this design became more difficult to address as the stiffness requirement in the PIP chain varies based on the configuration of the MCP chain. We decided to remove the sliding joint in the PIP chain and fix the link to the PIP phalanx rest (exoskeleton link connected to the middle phalanx). With this configuration the PIP chain can be controlled with one actuator but

also results in increased finger joint reaction forces.

In the final design (Fig. 2.15(d)), the robotic chain was parallel to the finger which ensured that all the actuation forces are grounded. There were three phalanx-exoskeleton closed-loop kinematic chains to avoid the joint axes misalignment problem. The MCP chain consisted of four links with three rotational and one translational joint resulting in one DOF. The PIP chain consisted of four links with four rotational joints (assuming the first chain was fixed) resulting in one DOF. The DIP chain consisted of four links with three rotational and one translational joint leading to one DOF.

2.2.1.2 Additive Manufacturing

We chose to manufacture various components of our prototype using Selective Laser Sintering (SLS)[2] with Nylon 12 (Fig. 2.14). This additive manufacturing method allowed us to print small and intricate components, while keeping them strong and light in weight. Since size, rather than complexity, determines the cost for SLS (as opposed to complexity more than size, for conventional machining), SLS was a particularly effective manufacturing solution for our prototype. SLS was also advantageous in that it allowed us to design components that serve multiple functions (e.g. housing for the angle sensor magnets and SEA springs were integrated with the links). This helped us in reducing both the number and size of components in the design. Also, since this method allowed for quick manufacturing of the parts, it significantly

[2] http://en.wikipedia.org/wiki/Selective_laser_sintering

reduced the development time of the prototype, leading to quick iterations of design and testing. Furthermore, the printed components were highly machinable allowing for post-processing needed for accurate dimensioning of critical parts and also for required subject specific customization (if any).

2.2.1.3 Prototype

We implemented the proposed mechanism in the form of an overall design for the index finger exoskeleton (Fig. 2.16(a)). In addition to the various joints mentioned in Section 2.2.1, a passive DOF for finger adduction-abduction motion in the MCP chain was also implemented in the design. The sliding and revolute joints were realized using ultra-miniature linear and rotary ball bearings. For components with significant loading, we used off-the-shelf steel parts (e.g. shafts) to reduce size and avoid excessive deformation. The entire chain is grounded on the exoskeleton base, which is attached on the wearer's hand with a velcro strap. In addition, a high-density rubber foam is attached on the base for comfort to the wearer. Slots are provided on the base such that the attachment of the entire chain can be adjusted both in longitudinal and lateral directions as well as in angular position to adapt to the index finger size and natural position of the wearer.

Each link consists of two segments which can slide with respect to each other and can be locked in a specific position using a screw (Fig. 2.16(b)). This allows for length adjustment of the links as per the requirement of the wearer's phalanx lengths. A magneto-resistive angle sensor module (KMA210,

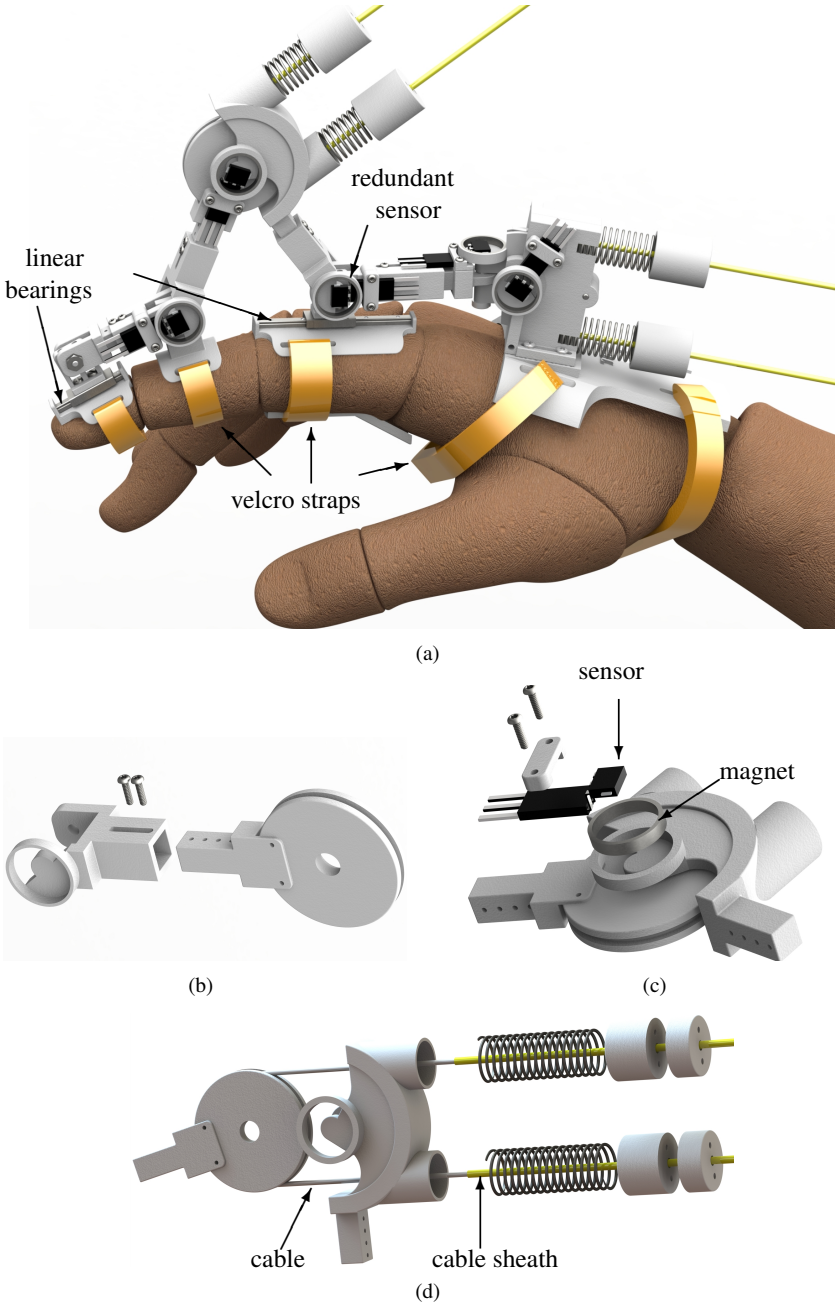

Figure 2.16: CAD model of the designed index finger exoskeleton prototype. (a) Overall design of the exoskeleton, (b) adjustable link length assembly, (c) angle sensor and ring magnet assembly for joint angle sensing, and (d) Bowden-cable-based compression spring SEA design.

NXP Semiconductors) with a diametrically magnetized ring magnet is used as a joint angle sensor (Fig. 2.16(c)). The ring magnet casing is built into the corresponding link with the sensor attached to the link moving relative to the previous one. The device has five angle sensors to collect data from five joint angles with one redundant sensor (Fig. 2.16(a)). This redundant measurement is used to estimate the kinematic parameters of the coupled finger exoskeleton system *in situ*.

We implemented a Bowden-cable-based compression spring SEA in the prototype (Fig. 2.16(d)). Each actuated joint consists of a pulley with a cable attached on the circumference of the pulley. The Bowden cable consists of an MFA (modified fluoroalkoxy) coated Nylon sheath (0.125 inch outer diameter) with an FEP (fluorinated ethylene propylene) coated stainless steel (0.026 inch diameter) wire rope to reduce the friction between the cable and the sheath. For each end of the Bowden cable connected to the joint-pulley, there is a compression spring attached to the Bowden cable sheath. When the motor actuates the joint-pulley, it first compresses the spring. The introduction of the passive series elastic element in the transmission mechanism provides a means for accurately estimating the cable tension using the joint displacement measurements obtained using the magnetic angle sensor mounted at the joint and the motor encoder. We used DC motors (RE-max 29, 22 W, Maxon Precision Motors Inc.) with planetary gearheads as the actuators for the device. The motors are mounted on a stationary platform and the Bowden cable acts as the transmission mechanism in the current design. Sufficiently long Bow-

den cables allow for moving the hand around without significantly affecting the curvature of the Bowden cables. The cable tension is maintained using a cable tensioning mechanism. The mechanism consists of a sliding platform on which the motor is mounted and the position of the platform can be fixed using a lead screw mechanism that gradually builds tension in the cable.

The entire kinematic chain is actuated in the center plane of the mechanism to ensure that no sideways forces are applied on the finger while the device is actuated. Remote actuation along with SLS using Nylon 12 significantly reduces the overall weight (hand base (30 g) + finger exoskeleton (50 g) $\approx$ 80 g) of the device compared to other exoskeletons (110 g for HANDEXOS [32], 140 g for CAFE [73]). The design also allows for the possibility of replacement of the stiffness element (for adjusting the achievable torque range specific to a subject) without having to remove the cables.

2.2.2 System Modeling

Control of the developed device requires good estimates of the joint angles of the wearer and the forces acting in the system. Thus, we developed the kinematic and statics model of the mechanism to estimate the finger joint angles and static torques of the wearer. We assumed small abduction-adduction joint angles for the index finger and thus, analyze the mechanism for planar motion.

2.2.2.1 Kinematics

The loop-closure equation for the proximal (MCP) chain of the index finger exoskeleton (Fig. 2.17) is given by (2.17).

$$l_{BC}e^{i\theta_1} + l_{CD}e^{i\theta_2} + x_3e^{i(\theta_4-\pi)} = x_A + iy_A \tag{2.17}$$

where l_{BC}, l_{CD} are the lengths of the links BC and CD, respectively. x_3 represents the sliding length in MCP chain at a given configuration, θ's represent the various angles (Fig. 2.17). (x_A, y_A) represent the coordinate of the human MCP joint (point A) in the coordinate frame located at the exoskeleton joint at B. Similarly, the loop closure equations for the middle (PIP) and distal (DIP) chains were expressed.

The forward kinematics deals with evaluating the finger MCP and PIP joint angles (θ_4, θ_8) and the exoskeleton passive joint displacements (x_3, θ_5) given the exoskeleton relative joint angles (θ_{1r}, θ_{6r}). The relative joint angle is the angle between the links connected at the joint as measured by the sensors mounted at the joint. Since, each chain can be treated as a four-bar mechanism (by fixing the remaining DOFs), we solved for the kinematics of the system using the standard four-bar kinematics solution [113]. In addition, we evaluated the least-squares solution for the closed-form kinematics when the system failed to evaluate the exact kinematics solution due to error in geometric parameters. Thus, the solution can be expressed as in (2.18).

$$\mathbf{X} = \mathbf{X}(\mathbf{\Theta_r}) \tag{2.18}$$

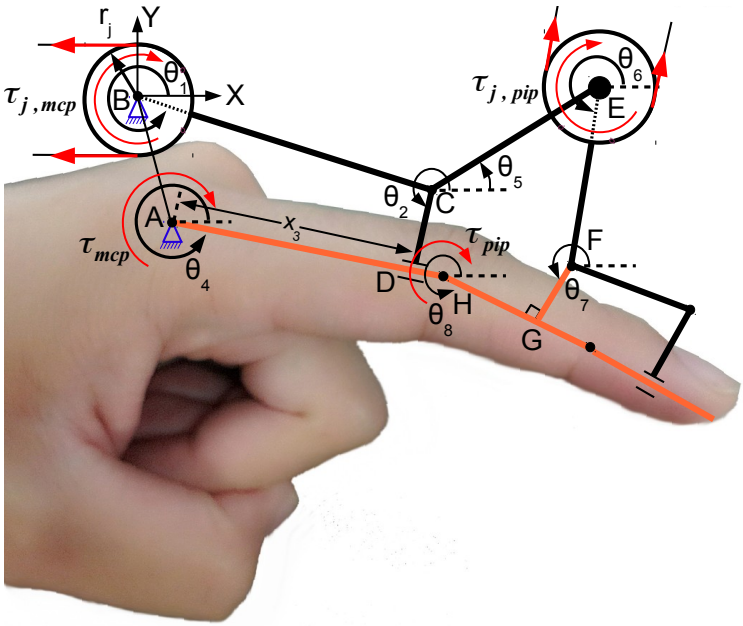

Figure 2.17: Nomenclature for the kinematic model of the designed index finger exoskeleton. All angles are measured in counterclockwise direction. The arrows in red color depict forces or torques acting on the system. The arrows in black represent kinematic variables. (Best viewed in color)

where $\mathbf{X} = \begin{bmatrix} x_3 & \theta_4 & \theta_5 & \theta_8 \end{bmatrix}^T$ and $\Theta_r = \begin{bmatrix} \theta_{1r} & \theta_{6r} \end{bmatrix}^T$.

The velocity level kinematics (2.19) can then be obtained by differentiating the position kinematics equations for the MCP (2.17) and the PIP chains. We used symbolic computation in MATLAB to evaluate the Jacobian of the system.

$$\left[\dot{\mathbf{X}}\right]_{4\times1} = \left[\mathbf{J}(\mathbf{\Theta_r})\right]_{4\times2} \left[\dot{\mathbf{\Theta}}_\mathbf{r}\right]_{2\times1} \tag{2.19}$$

where $\left[\dot{\mathbf{X}}\right]_{4\times1}$ represents the velocity vector, $\left[\dot{\mathbf{\Theta}}_\mathbf{r}\right]_{2\times1}$ represents the exoskeleton joint relative velocity vector and $\left[\mathbf{J}(\mathbf{\Theta_r})\right]_{4\times2}$ represents the Jacobian of the system.

2.2.2.2 Statics

An experimental study has shown that the human hand dynamics is dominated by the intrinsic passive viscoelastic torques at the finger joints [36]. In addition, the velocities for a rehabilitation task are relatively small. Thus, we consider only a statics model of the coupled finger exoskeleton system for developing a torque controller. The static forces/torques acting in the system can be related using the Jacobian as in (2.20).

$$\begin{bmatrix} \tau_{j,mcp} \\ \tau_{j,pip} \end{bmatrix} = \mathbf{J}(\mathbf{\Theta_r})^T \begin{bmatrix} f_3(=0) \\ \tau_{mcp} \\ \tau_5(=0) \\ \tau_{pip} \end{bmatrix} \tag{2.20}$$

where $\tau_{j,mcp}$ and $\tau_{j,pip}$ represent the torques applied at the actuated exoskeleton MCP and PIP joints, respectively. τ_{mcp} and τ_{pip} represent the torques applied at the finger MCP and PIP joints, respectively. The force or torque acting at the linear or rotary passive joint, respectively, was assumed to be zero as each joint had a bearing which made the friction at the joint small.

2.2.3 Controls

We developed two types of torque controllers for the device: exoskeleton and finger joint torque controllers. The exoskeleton joint torque controller is a basic controller implemented to test the torque control performance of the two SEAs on the device. The finger joint torque controller, on the other hand, is a more complex controller which controls the torque being applied at the individual finger joints based on a subject specific kinematics and statics model.

In addition, accurate operation of these controllers required estimation of the kinematic parameters for a specific subject. We implemented an optimization based technique to estimate the kinematic parameters of the coupled finger exoskeleton system for a specific subject.

2.2.3.1 Exoskeleton Joint Torque Control

The goal of this controller was to track the desired torque trajectories at the exoskeleton SEA joints (Fig. 2.18). The output of the system was considered to be the torque generated at the exoskeleton joints through SEA as expressed in (2.21).

$$\hat{\mathbf{y}} = \begin{bmatrix} \tau_{j,mcp} \\ \tau_{j,pip} \end{bmatrix} = 2\mathbf{K}r_j\left(r_m\mathbf{\Theta_m} - r_j(\mathbf{\Theta_r} - \mathbf{\Theta_{r0}})\right) \tag{2.21}$$

where

$$\mathbf{K} = \begin{bmatrix} k_{j,mcp} & 0 \\ 0 & k_{j,pip} \end{bmatrix},\ \mathbf{\Theta_m} = \begin{bmatrix} \theta_{m,mcp} \\ \theta_{m,pip} \end{bmatrix}$$

$k_{j,mcp}$ and $k_{j,pip}$ represent the magnitude of the effective stiffness at the exoskeleton MCP and PIP joints, respectively. $\theta_{m,mcp}$ and $\theta_{m,pip}$ are the MCP and PIP motor angles, respectively. The PID controller with the corresponding feed-forward term is then given by (2.35).

$$\begin{aligned} \mathbf{e} =& \mathbf{y}_d - \hat{\mathbf{y}} \\ \dot{\mathbf{e}} =& \dot{\mathbf{y}}_\mathbf{d} - \dot{\hat{\mathbf{y}}} \\ \mathbf{u} =& \frac{1}{r_m}\left(\frac{\mathbf{K}^{-1}\mathbf{y_d}}{2r_j} + r_j\left(\mathbf{\Theta_r} - \mathbf{\Theta_{r0}}\right)\right) + \mathbf{K_p}\mathbf{e} + \mathbf{K_d}\dot{\mathbf{e}} + \\ & \mathbf{K_i}\int \mathbf{e}dt \end{aligned} \tag{2.22}$$

where $\mathbf{e}$ is the vector containing exoskeleton joint torque errors, $\mathbf{y}_d$ is the vector containing the desired torque at the two exoskeleton joints and $\mathbf{u}$ is the control input vector for the two exoskeleton joints. The gain matrices for the controller are given by

$$\mathbf{K_p} = \begin{bmatrix} k_{p,mcp} & 0 \\ 0 & k_{p,pip} \end{bmatrix}, \mathbf{K_d} = \begin{bmatrix} k_{d,mcp} & 0 \\ 0 & k_{d,pip} \end{bmatrix}$$
$$\mathbf{K_i} = \begin{bmatrix} k_{i,mcp} & 0 \\ 0 & k_{i,pip} \end{bmatrix}$$

2.2.4 Finger Joint Torque Control

The two actuated exoskeleton joints contributed to the torque applied on the two finger joints due to the mechanical coupling caused by the exoskeleton mechanism. The goal of this controller was to track the desired torque trajectories at the two finger joints (MCP and PIP) by applying appropriate torques through the exoskeleton SEAs (Fig. 2.18). Since, the contribution of the inertial effects to the dynamics of the index finger exoskeleton system is small [36], we evaluated the output finger joint torques based on the applied SEA joint torques as given by (2.23).

$$\hat{\mathbf{y}} = \mathbf{J_n}^{-T} 2\mathbf{K} r_j \left(r_m \mathbf{\Theta_m} - r_j (\mathbf{\Theta_r} - \mathbf{\Theta_{r0}}) \right) \tag{2.23}$$

where J_n represents the Jacobian relating the exoskeleton joint torque to the finger joint torque and is given by (2.24).

$$\mathbf{J_n} = \begin{bmatrix} J_{21} & J_{22} \\ J_{41} & J_{42} \end{bmatrix} \tag{2.24}$$

where J_{ij} represents the (i,j)th entry in the Jacobian matrix $\mathbf{J}$ (see (2.19)).

The PID controller is developed considering the corresponding feed-forward term is then given by (2.25).

$$
\begin{aligned}
\tau_{\mathbf{fe}} =& \mathbf{y}_d - \hat{\mathbf{y}} \\
\mathbf{e} =& \mathbf{J_n}^T \tau_{\mathbf{fe}} \\
\dot{\mathbf{e}} =& (\dot{\mathbf{J}}_{\mathbf{n}}^T \tau_{\mathbf{fe}} + \mathbf{J_n}^T \dot{\tau}_{\mathbf{fe}}) \\
\mathbf{u} =& \frac{1}{r_m} \left(\frac{\mathbf{J_n}^T \mathbf{K}^{-1} \mathbf{y_d}}{2r_j} + r_j(\mathbf{\Theta_r} - \mathbf{\Theta_{r0}}) \right) + \\
& \mathbf{K_p e} + \mathbf{K_d \dot{e}} + \mathbf{K_i} \int \mathbf{e} dt
\end{aligned}
\tag{2.25}
$$

where $\tau_{\mathbf{fe}}$ is the vector containing finger torque errors, $\mathbf{y}_d$ is the vector containing desired torque at the two finger joints, $\mathbf{e}$ is the vector containing exoskeleton torque errors and $\mathbf{u}$ is the desired motor position vector used as control input for the two exoskeleton joints. The derivative of the Jacobian ($\dot{\mathbf{J}}_{\mathbf{n}}$), which is used to evaluate the error derivative ($\dot{\mathbf{e}}$), is computed numerically.

2.2.4.1 Parameter Estimation

Since the relative attachment of the exoskeleton on the wearer's hand changed the geometric parameters of the system, estimating the correct geometric parameters was essential for the controller to function. Also, it was difficult to measure the exact geometric parameters that were dependent on the hand of the wearer [178], since the exact locations of the finger joint axes were difficult to determine. In order to deal with these problems, we used the redundant sensor data (Fig. 2.16(a)) to estimate the uncertain geometric parameters. We collected the data from the redundant sensor for certain duration so that the full joint range of motion was traced at least once (e.g. 2

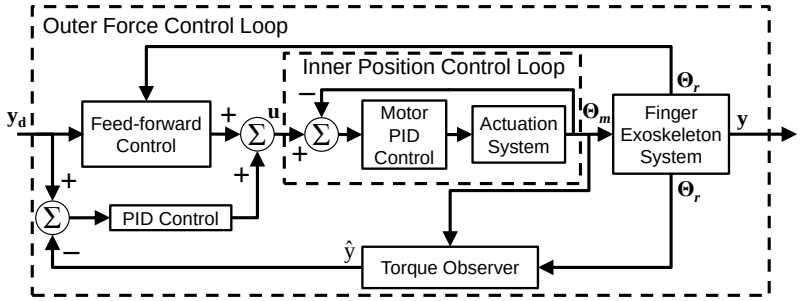

(a)

Figure 2.18: The torque controllers implemented on the index finger exoskeleton. For the exoskeleton joint torque controller, the feed-forward control and torque observer refers to the exoskeleton joint torque feed-forward control and SEA-based exoskeleton joint torque estimation. For finger joint torque controller, the feed-forward control and torque observer refers to the finger joint feed-forward torque control and finger joint torque estimation using the system statics model.

seconds for a 0.5 Hz sinusoid torque trajectory) and then used an optimization based technique to estimate all the uncertain parameters in the system offline. We formulated the following optimization problem to estimate the parameters

$$\begin{aligned} \hat{\mathbf{P}}_{\mathbf{min}} &= \arg\min_{\hat{\mathbf{P}}} \sum_{i=1}^{N} (y_k - y_{m,k})^2 \\ \mathbf{P} &= \begin{bmatrix} x_A & y_A & l_{BC} & l_{CD} & l_{AH} & l_{FG} & l_{GH} \end{bmatrix}^T \end{aligned} \tag{2.26}$$

where y_k and $y_{m,k}$ are the measured and the model-based redundant joint angle data, respectively and N is the number of measurements. The interior-point algorithm, described in [22] was used for solving the optimization problem.

2.2.5 Simulation

The proposed controller was first implemented in simulation to verify its effectiveness, before implementation on the prototype. We developed a dynamics model of the coupled finger exoskeleton system and controlled it using the proposed finger joint torque controller. In addition, simulations helped in choosing the correct magnitude of stiffness at the two SEA joints and an appropriate Bowden cable and sheath combination for the exoskeleton.

2.2.5.1 Dynamics Model

We developed a dynamics model (2.27) of the coupled finger exoskeleton system.

$$\mathcal{I}_{\mathbf{j}}\ddot{\mathbf{\Theta}}_{\mathbf{j}} + \mathcal{B}_{\mathbf{j}}\dot{\mathbf{\Theta}}_{\mathbf{j}} + \mathbf{J_n}^T\tau_{\mathbf{f}} = \tau_{\mathbf{j}} \tag{2.27}$$

$$\tau_{\mathbf{f}} = \begin{bmatrix} \tau_{mcp} \\ \tau_{pip} \end{bmatrix}, \tau_{\mathbf{j}} = \begin{bmatrix} \tau_{j,mcp} \\ \tau_{j,pip} \end{bmatrix},$$

where I_j is the inertia matrix and B_j is the damping matrix. Since the exoskeleton links were prototyped using SLS, the link mass and inertia was low and hence, we did not consider the configuration dependent change in the inertial and Coriolis terms in the dynamics (2.27). We used the human finger phalanges inertia values available in the literature [173] and estimated the exoskeleton link inertia from the CAD model (Fig. 2.16). We also assumed a linear viscous damping at the exoskeleton joints to take into account the damping due to the Bowden cable and the damping at the human joints [12].

The motion of finger joints causes passive tissues such as tendons, ligaments, skin and inactive muscles to be deformed. This deformation manifests in the form of a passive resistance or stiffness at the joint. A lumped passive torque model can be built by combining the contributions from all the constitutive factors. Experimental studies have shown that this passive torque at the finger joints exhibits double exponential nature [39, 46, 85]. We use this biomechanically consistent joint torque model (2.28) for the MCP (τ_{MCP}) and PIP (τ_{PIP}) joints [5, 85] for simulation.

$$\tau_x(\theta_x) = A_x(e^{-B_x(\theta_x - E_x)} - 1) - C_x(e^{D_x(\theta_x - F_x)} - 1) \tag{2.28}$$

where τ_x is the passive torque offered by the joint, θ_x is the joint angle, and A_x, B_x, C_x, D_x, E_x, F_x are the model coefficients. The finger joint torque controller (Section 2.2.4) was implemented on the device using the developed dynamics model of the coupled finger exoskeleton system to verify the effectiveness of the controller.

2.2.5.2 Simulation Results

The simulation results showed that the controller developed was able to track the desired sinusoidal torque trajectories with a normalized RMS error of 1.6% (0.0032 Nm) and 9.2% (0.0037) at the finger MCP and PIP joint, respectively (Figs. 2.19a and 2.19b). Also, better torque tracking was observed at the MCP joint as compared to the PIP joint as the system became more non-linear down the exoskeleton chain. This is due to the fact that both the kinematics and dynamics of the PIP chain is affected by the MCP chain and

hence, the system becomes more non-linear as one moves away from the base. The fluctuations at the peaks in the PIP joint torque did not result in large oscillations of the exoskeleton joint angles (Fig. 2.19c) and were a result of the large changes in torque with small changes in angle at the extreme angles for the double exponential torque model (2.28). The required motor angles were well within the safe limits (Fig. 2.19d) and so actuator saturation was not explicitly modeled in the controller. Also, the torque requirement for the MCP joint is higher than the PIP joint. The simulation also provided estimates of the appropriate stiffness values for the SEA springs at the MCP ($k_{j,MCP} =$ 2816 N/m) and the PIP ($k_{j,PIP} = 744$ N/m) joint, which were commercially available. The stiffness values were chosen so that the requirement of the peak torque from the coupled system dynamics (2.27) and joint torque model (2.28) could be met while ensuring sufficient torque resolution under noisy joint angle sensing (motor angle >20 degrees at peak torque) along with the availability of off-the-shelf compression springs. In addition, motor angle should be in safe limits for bidirectional torque control (motor angle lies within ±60 degrees at peak torque). Also, a smaller motor angle to achieve the peak torque allows for a higher bandwidth of the SEA. In addition, estimates of the tension in the Bowden cable also helped in choosing the appropriate Bowden cable and sheath combination.

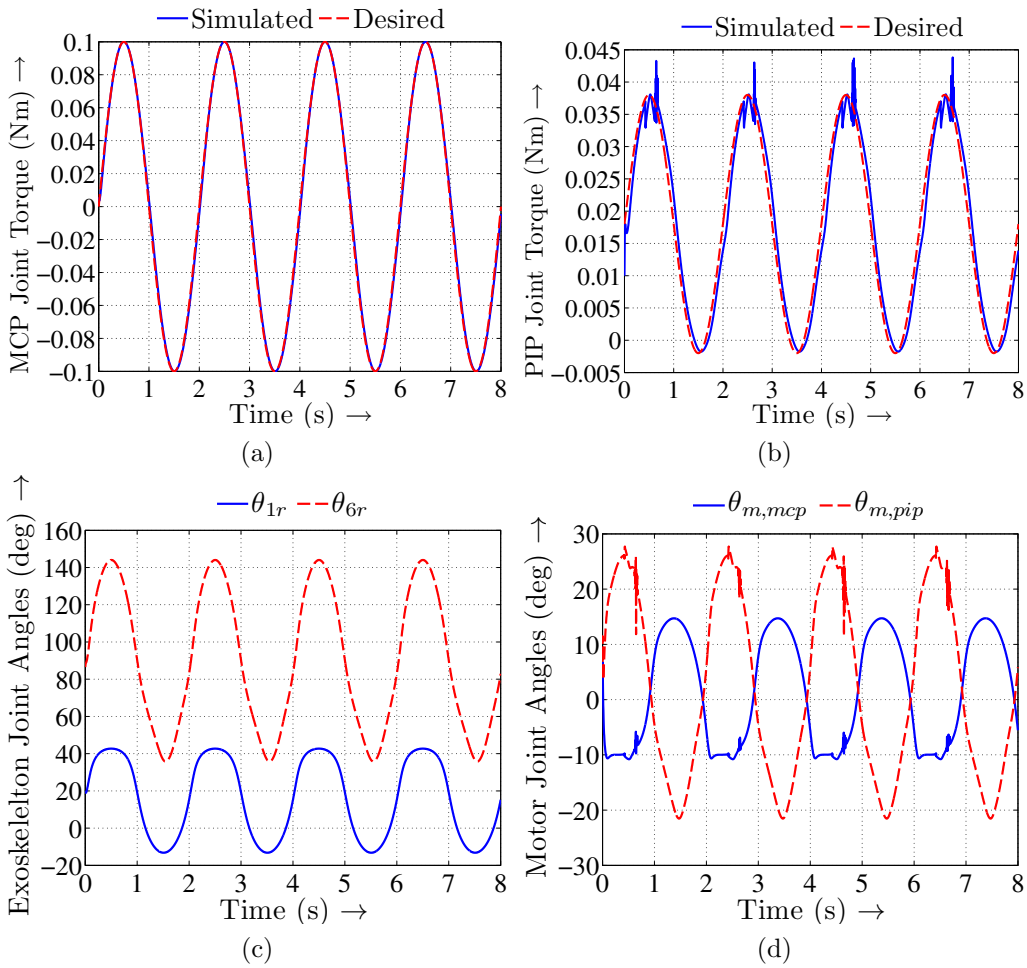

Figure 2.19: The finger joints torque tracking performance for the feed-forward PID controller with sinusoidal torque input in simulation. (a) Finger MCP joint torque trajectory, (b) finger PIP joint torque trajectory, (c) exoskeleton relative joint angle trajectories and (d) motor joint angle trajectories.

2.2.6 Experimentation

The experiments with the SEA test rig and the exoskeleton prototype were aimed at characterizing the following: (i) the torque tracking performance and bandwidth of the SEA; (ii) the kinematic transparency of the device, i.e.

how did the device affect natural motion of the finger joints; (iii) active range of motion with and without the device; (iv) validate the kinematic model, which was employed for the control of the device; (v) exoskeleton joints torque tracking performance; (vi) finger joints torque tracking performance; and (vii) dynamic transparency of the device, i.e. how did the device resist natural motion of the finger joints.

2.2.6.1 Kinematic Transparency

Since the index finger exoskeleton will be the basis for the exoskeleton modules for the other fingers, kinematic transparency tests are carried out to quantify the similarity of motion with and without the exoskeleton. Two healthy subjects (both males, ages 20-24 years) voluntarily participated in this pilot study, after they provided their informed consent (The University of Texas at Austin institutional review board study number 2013-05-0126). We used the following protocol to perform the kinematic transparency experiments. During experimentation, first the motion capture markers were placed on the various joints of the subject. The markers were placed on the side of the finger both with and without the exoskeleton to avoid any possible interference with the device and assess the performance under similar conditions (Fig. 2.20). The subjects were asked to perform the following four different motions: (i) MCP joint articulation through full active range of motion (AROM) in flexion-extension while maintaining zero flexion angle at the PIP and DIP joints, (ii) full AROM flexion-extension at the PIP and DIP joints while maintaining zero

flexion angle at the MCP joint, (iii) full AROM flexion-extension at the MCP, PIP and DIP joints, and (iv) MCP joint full AROM while maintaining full flexion at the PIP and DIP joints. The subjects were then asked to wear the device and the link lengths were adjusted so that they can comfortably reach their full AROM with the device. The motion capture markers were again placed on the various joints and the subjects were asked to perform the four different motions with the device. The subjects were allowed to practice each motion for a certain duration ($\sim$ 2 min) after which the actual experiment was conducted. In addition, the subjects were asked to keep the motion limited to the flexion-extension plane with no abduction-adduction motion. We do not carry out motions for explicit testing of the MCP abduction-adduction motion, since in our design the joint is not actuated and its role is to allow for free finger motion sideways while performing the flexion-extension motion at the other finger joints.

The experiments were performed at three different speeds–low (0.4 Hz), medium (0.8 Hz), and high (1.2 Hz). An audio cue was provided to the subjects to help them maintain the required finger frequency using GTick metronome. During all the experiments, the motion capture data was recorded using a motion capture system (PhaseSpace Inc.) at 480 Hz. For experiments with the exoskeleton, synchronized data from the angle sensors were also recorded at 1000 Hz. All the data acquisition subroutines were coded in C++ with the motion capture data acquisition task and the sensor data acquisition task running on two parallel threads to ensure hard-real-time performance. The

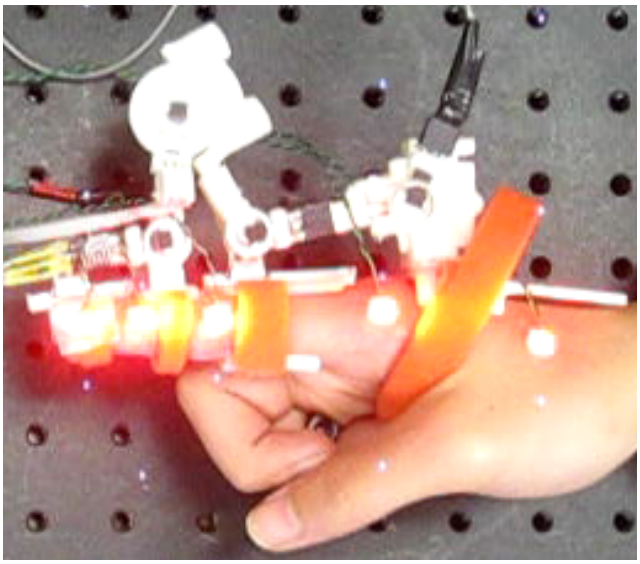

Figure 2.20: The experimental setup for the hand exoskeleton system with the motion capture markers.

motion capture data was post-processed to reconstruct any missing data [97], smoothed using a moving average filter, and resampled at 1/10 frequency (48 Hz) to filter out the noise. The angle sensor data was resampled at 1/10 frequency (100 Hz) to filter out the noise. Note that since these experiments were aimed at characterizing only the kinematics of device, the Bowden-cable-based SEAs were not connected during this experimentation.

2.2.6.2 Active Range of Motion

The subjects were asked to move their fingers at a specified frequency for the kinematic transparency tasks. However, it was difficult for the subjects to reach their full AROM while performing the task. Thus, to accurately evaluate the AROM, we separately measured the AROM for each joint with

and without the device. The subjects were asked to voluntarily move their fingers to the extreme positions for each joint. An image was captured with an overhead camera to ensure that the finger plane is parallel to the image plane of the camera for accurate measurement of the angles.

2.2.6.3 Kinematic Model Validation

Since the data from the motion capture system and the magnetic angle sensor were collected synchronously, the former was used to validate the estimates obtained using the kinematic model with the latter. The estimates of the various kinematic parameters for the kinematic model were obtained using the measurements obtained from an image of the coupled hand exoskeleton system. The sensor data from the MCP joint was first used to solve for the kinematics of the MCP chain. The obtained solutions along with the sensor data from the PIP chain were then used to solve for the kinematics of the PIP chain. Finally, using the PIP chain solutions and the DIP chain sensor data, the kinematics of the DIP chain was solved.

2.2.6.4 Exoskeleton Joint Torque Tracking

The exoskeleton joint torque control was implemented on the actual prototype to test the exoskeleton joint level torque tracking performance. We used the phase and mean shifted sinusoidal trajectories as the desired torque input to the system (2.29).

$$\tau_{jd} = \tau_{jA} \sin\left(2\pi f t + \phi_j\right) + \tau_{j\mu} \tag{2.29}$$

where τ_{jd} is the desired joint torque, τ_{jA}, f, ϕ_j and $\tau_{j\mu}$ is the amplitude, frequency, phase and mean of the sinusoidal torque trajectory. The values of various parameters in the desired trajectories were determined experimentally for a subject by gradually increasing the desired torque amplitudes at the two exoskeleton joints within the user's comfort level. All the experiments with the actuated device are carried out with one healthy human subject who has no history of any neuromuscular disorder.

2.2.6.5 Finger Joint Torque Tracking

The goal of the finger joint torque tracking test was to verify if the SEAs at the two exoskeleton joints can coordinate to generate desired torques at the two finger joints using the estimated system parameters. We experimentally determined the parameters of the desired torque trajectories (2.29) for a subject by gradually increasing the desired torque amplitudes at the two finger joints within the user's comfort level. In addition, we evaluated the finger joint reaction forces both at the MCP and PIP joints by analyzing the joint reaction forces in the two four-bar chains [113] to ensure that the human joints are not loaded significantly.

2.2.6.6 Dynamic Transparency

Finally, experiments were carried out to test dynamic transparency of the device while a subject interacts with the device. The goal was to test if the device can be controlled to offer least resistance to the finger joints. A subject

wore the device and generated fast random motions. The device is controlled to render zero torque at the exoskeleton joints which in turn should lead to zero applied torque at the finger joints.

2.2.7 Results

2.2.7.1 Kinematic Transparency

For the kinematic transparency experiments, the MCP, PIP and DIP joint angles were evaluated using the motion capture data with and without the device (Fig. 2.21). We used Pearson's product moment correlation coefficient averaged over 3 repetitions to quantify the level of similarity between the joint angle trajectories with and without the exoskeleton. We use correlation as a measure of transparency instead of RMS error as it is difficult for the subject to exactly replicate the same motion over and over again with or without the device.

Results from the kinematic transparency tests showed that in general there is strong correlation between the joint angle trajectories without and with the exoskeleton (Table 2.4). The results for motions (ii) and (iii) showed that the exoskeleton preserved the nature of motion at the MCP, PIP and DIP in flexion-extension and MCP in abduction-adduction (Figs. 2.21(c), (d), (e) and (f)). For motion (i), higher PIP joint angle variation was observed with the device ($< 20°$) than without it ($< 10°$)(Figs. 2.21(a) and (b)). This might be due to the coupling that exists between the exoskeleton MCP and PIP chains, which makes some motion at the PIP joint while moving the MCP

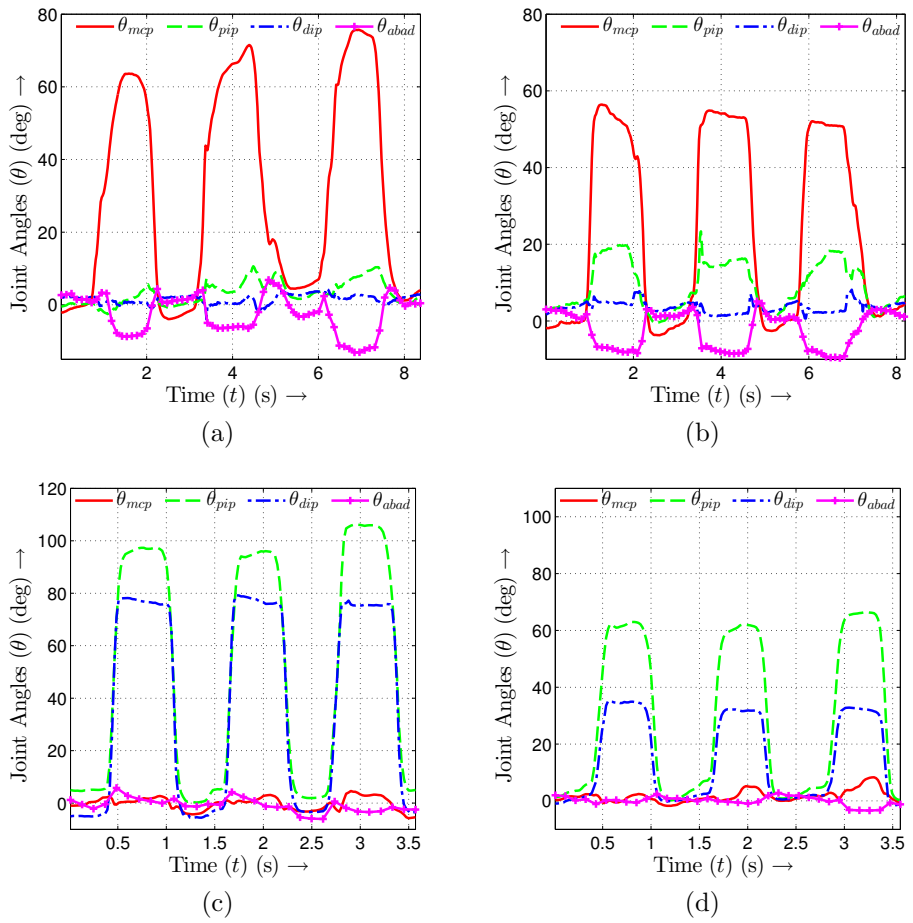

Figure 2.21: Kinematic transparency results without and with the exoskeleton for one subject. The left and right columns represent the plots of the various finger joint angles without and with the hand exoskeleton for the different experiments, respectively. (a) and (b) represent the motion (i) at low speed, (c) and (d) represent the motion (ii) at medium speed, (e) and (f) represent the motion (iii) at high speed, and (g) and (h) represent the motion (iv) at low speed.

joint relatively more comfortable for the subject. Also, higher motion was observed at the PIP joint for motion (iv) without the exoskeleton ($< 30°$) than with the exoskeleton ($< 10°$). This shows that some deviation might be

Table 2.4: Pearson's product moment correlation coefficient averaged over 3 repetitions as obtained from the kinematic transparency tests. The p-value was coumputed using a Student's t distribution.

Motion type	MCP	PIP	DIP
(i)	0.9002 ($p < 0.01$)	–	–
(ii)	–	0.9723 ($p < 0.01$)	0.9209 ($p < 0.01$)
(iii)	0.8937 ($p < 0.01$)	0.9852 ($p < 0.01$)	0.9892 ($p < 0.01$)
(iv)	0.7888 ($p < 0.01$)	–	–

observed due to a subject's inability to maintain constant finger joint angles for certain tasks rather than solely the kinematics of the device. In addition, some MCP abduction-adduction joint motion ($< 12°$) was observed even when the subject's were instructed to maintain a constant angle at that joint both without and with the exoskeleton. For motion (i), similar MCP abduction-adduction motion is observed without and with the device, which shows that the device allows for the natural abduction-adduction motion while performing flexion-extension motion at the other joints. Thus, the overall nature of the motion at the MCP, PIP and DIP joints is similar without and with the device at all speeds. In addition, at low speeds the joint angles at the PIP joint were higher when the subject was wearing the device as compared to without the exoskeleton (Fig. 2.21(a) and (b)). Also, the plots showed that at high speed, the angle range of the subject was significantly reduced both without and with the exoskeleton as the task was demanding (Fig. 2.21(e) and (f)).

The current design with adjustable link lengths supports hand sizes with index finger lengths in the range of 60 to 80 mm which corresponds to

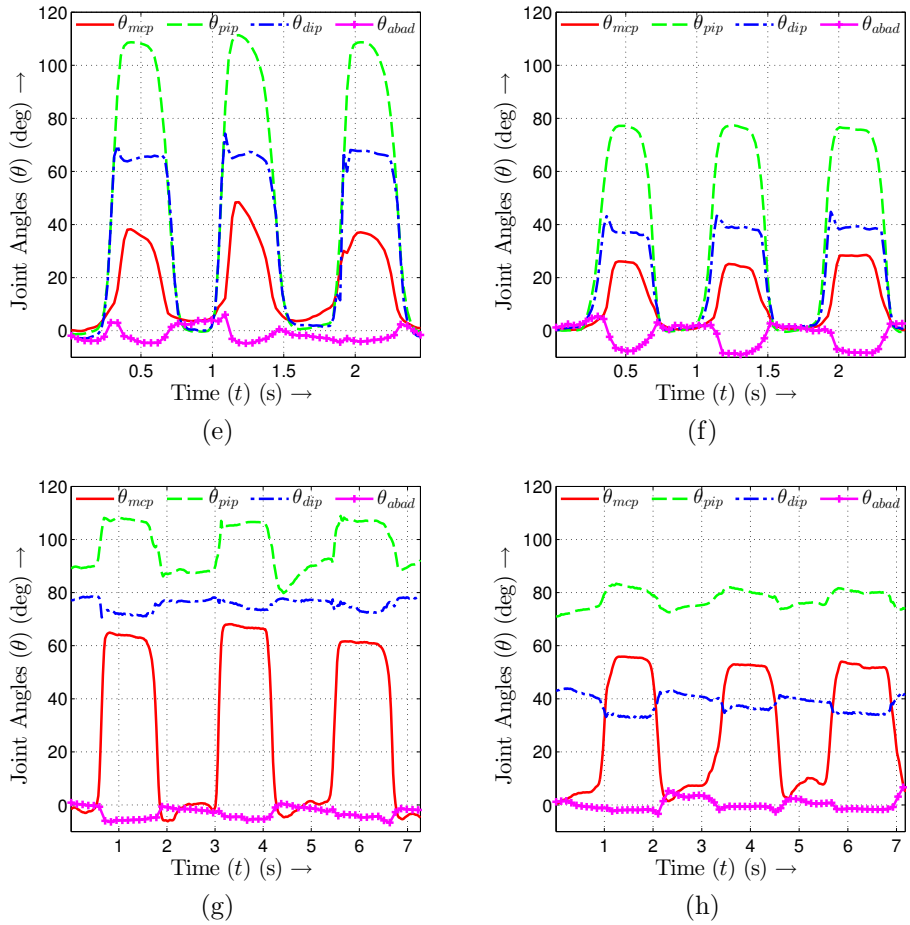

Figure 2.21: Kinematic transparency results without and with the exoskeleton for one subject. The left and right columns represent the plots of the various finger joint angles without and with the hand exoskeleton for the different experiments, respectively. (a) and (b) represent the motion (i) at low speed, (c) and (d) represent the motion (ii) at medium speed, (e) and (f) represent the motion (iii) at high speed, and (g) and (h) represent the motion (iv) at low speed. (contd.)

95th percentile of the British adult population (both males and females) aged between 19 and 65 years [45, 48]. All ranges of middle and distal phalanx thickness could be accommodated as a velcro strap is used to connect the

Table 2.5: Active Range of motion results for the different subjects without and with the index finger exoskeleton.

		Active Range of Motion			
		Without Exoskeleton		**With Exoskeleton**	
Subject	**Joint**	Flexion	Extension	Flexion	Extension
Subject 1	MCP	94°	5.2°	72.1°	2.2°
	PIP	113.4°	0.2°	92.4°	0°
	DIP	88°	10°	64.13°	8°
Subject 2	MCP	84.1°	2.5°	68.4°	0.5°
	PIP	125.9°	0.5°	89.6°	0°
	DIP	83.3°	5.9°	56.2°	1.1°

device at these phalanges. In addition, we have three different sizes for the proximal phalanx rest (link that connects to the proximal phalanx) and hand base to allow for ergonomic fit to hands of different sizes. The design allows for quick replacement of these parts to reduce the donning time of the device.

2.2.7.2 Active Range of Motion

The AROM with the exoskeleton was affected by the relative attachment of the device to the subjects' fingers. Table 2.5 presents the results of the AROM for the two subjects. Results showed that the AROM of the subject was reduced when the device is attached to the hand. The reduction in AROM was larger for PIP and DIP joints as compared to the MCP joint.

2.2.7.3 Kinematic Model Validation

Normalized RMS differences of 5.8% (1.6878°), 7.5% (5.9485°) and 19.7% (8.6929°) are observed between the finger joint angle estimates obtained using the sensor data with the kinematic model and the motion capture data at the MCP, PIP and DIP joint, respectively (Fig. 2.22(a) and (b)). Box plot of the differences also show increasing difference median and spread from MCP to PIP to DIP joint (Fig. 2.23). This is because the estimates in the MCP chain affect the estimates of both the PIP and DIP chains and the estimates in the PIP chain affect the estimates of the DIP chain. This increasing model uncertainty down the exoskeleton chain leads to increased finger joint angle differences.

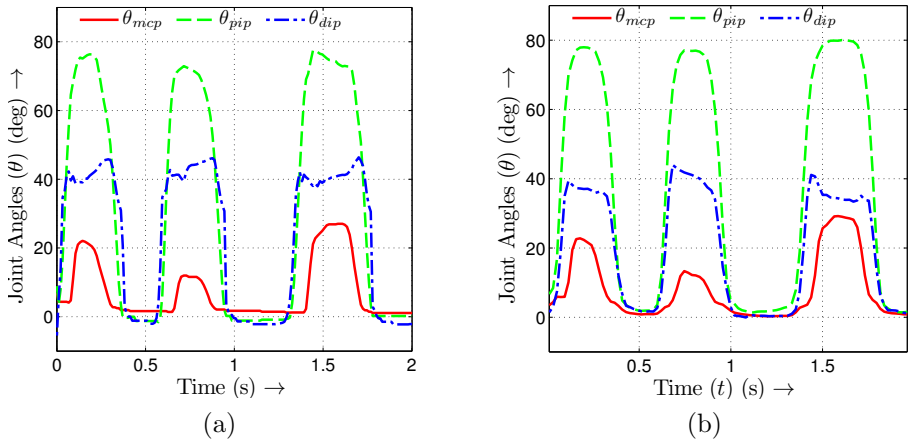

Figure 2.22: A comparison of the finger joint angle estimates obtained using: (a) angle sensor data with kinematic model and (b) motion capture data.

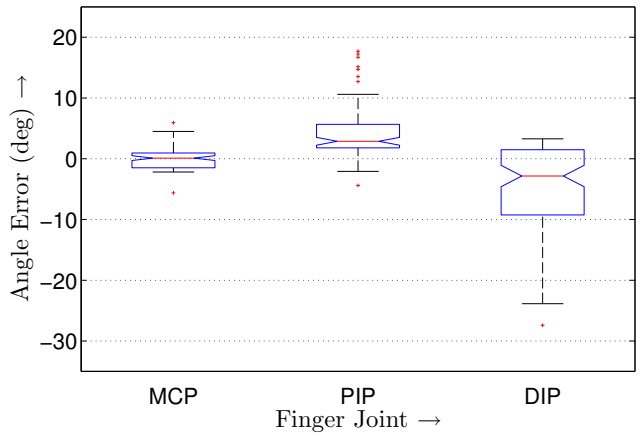

(a)

Figure 2.23: Box plot of the differences between the finger joint angle estimates obtained using the sensor data with kinematic model and motion capture data. The central mark represents the median, the edges of the box are the 25th and 75th percentiles, the whiskers extend to the most extreme data points not considered outliers and the outliers are plotted individually.

2.2.7.4 Exoskeleton Joint Torque Tracking

The controller was able to track the desired torque with normalized RMS error of 2.7% (0.0061 Nm) and 14.7% (0.0064 Nm) at the exoskeleton MCP and PIP joint, respectively (Fig. 2.24a and 2.24b). Limited noise was observed after filtering the exoskeleton joint angle sensor data (Fig. 2.24c). However, some noise was observed in the exoskeleton joint velocity estimates due to numerical differentiation (Fig. 2.24d). The residual noise in the filtered data also shows up in the estimated joint torque trajectories.

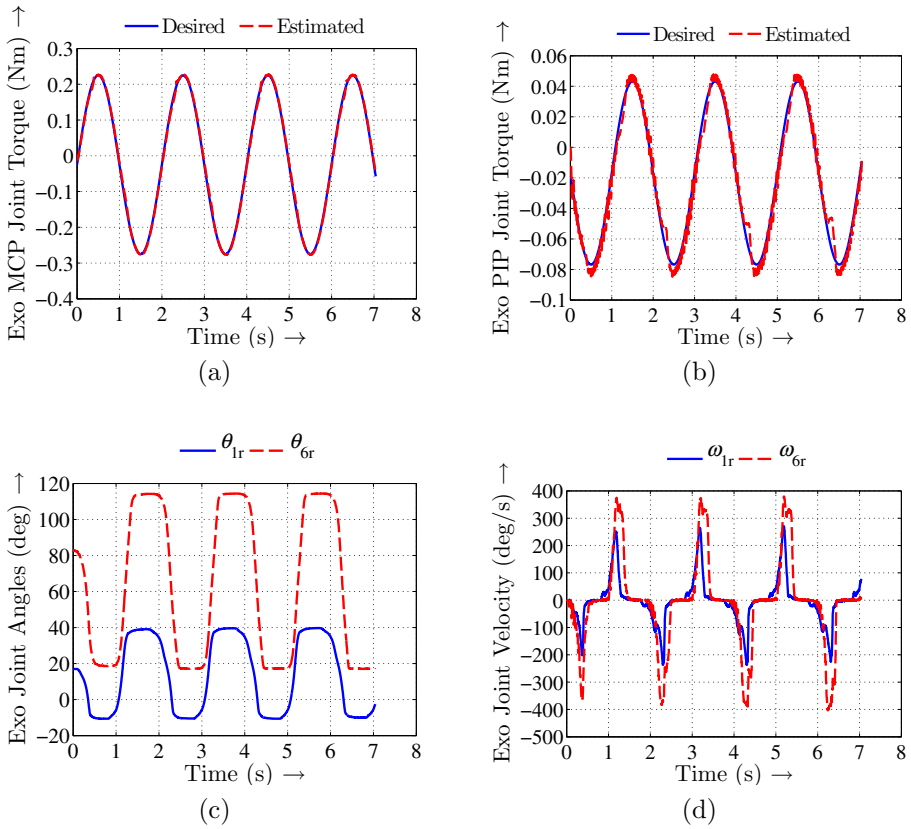

Figure 2.24: The exoskeleton joints torque tracking results from the index finger exoskeleton prototype. (a) Exoskeleton MCP joint torque trajectories, (b) exoskeleton PIP joint torque trajectories, (c) exoskeleton joint angle trajectories and (d) exoskeleton joint velocity trajectories.

2.2.7.5 Finger Joint Torque Tracking

The off-line parameter estimator was able to estimate the system parameters, which lie within the reasonable range based on typical hand sizes for these parameters (Table 2.6). The results showed that the system was able to track the desired finger torque trajectory satisfactorily well with a normalized RMS error of 1.7% (0.0041 Nm) and 3.4% (0.0012 Nm) at the finger

MCP and PIP joint, respectively (Fig. 2.25a and 2.25b). Also, better tracking is observed at the MCP joint as compared to the PIP joint as the system exhibits more non-linear and uncertain behavior (due to error in parameter values) down the exoskeleton chain compared to the MCP joint. The obtained Jacobian estimates were relatively noise free (Fig. 2.25c), however, some noise was observed in the Jacobian derivative estimates (Fig. 2.25d) as these are obtained using the noisy velocity estimates. Also, the terms $J_{n,11}$ and $J_{n,22}$ had much more significant contribution in the control input as compared to the other terms. However, at the derivative level the term $\dot{J}_{n,11}$ had much more significant contribution to the control input as compared to the other terms. Also, the kinematics estimator was able to estimate the various joint displacements in the coupled system using the obtained parameter estimates (Fig. 2.25e). The estimates of the reaction forces at the MCP and PIP joints (Fig. 2.25f) showed that the forces ($<$ 12.5 N both at the finger MCP and PIP joints) were well below that experienced by the human finger joints while performing activities of daily living ($\sim$ 86.6 N and $\sim$ 58.5 N at MCP and PIP joint, respectively) [109].

Table 2.6: The offline parameter estimation results ($\hat{\mathbf{P}}$) along with the initial parameter values ($\mathbf{P_0}$) used for optimization.[3]

$\mathbf{P}$	x_A	y_A	l_{BC}	l_{CD}	l_{AH}	l_{FG}	l_{GH}
$\mathbf{P_0}$ (m)	0.008	-0.030	0.047	0.025	0.047	0.018	0.015
$\hat{\mathbf{P}}$ (m)	0.000	-0.036	0.042	0.035	0.040	0.029	0.029
LB (m)	-0.002	-0.029	0.040	0.024	0.038	0.016	0.014
UB (m)	0.010	-0.039	0.050	0.037	0.052	0.030	0.030

2.2.7.6 Dynamic Transparency

The exoskeleton was able to maintain small torques both at the MCP (RMSE = 0.0029 Nm) (Fig. 2.26c) and PIP joints (RMSE = 0.0092 Nm) (Fig. 2.26d) throughout the arbitrary motion generated by the wearer (Fig. 2.26b). Some transient residual torques were observed when the wearer performed fast movements which settled down to zero subsequently. Residual torques generated at the exoskeleton joints were due to the error in tracking the desired motor joint angle trajectories (Figs. 2.26e and 2.26f).

2.2.8 Discussion

The control experiments showed that the device actuated the finger with good bidirectional torque control. However, since it was difficult to directly measure the joint torques on the actual prototype using a load cell while a subject was wearing the device, the estimates from the SEA were compared to the desired torque trajectory (Figs. 2.24a, 2.24b, 2.25a, 2.25b, 2.26c, 2.26d). We anticipate that the actual torques would show some deviation from the desired torques, especially at the peaks, as observed on the SEA test rig (Figs. 2.12c, 2.12d). Also, there were several simplifications made during the simulation: (i) the finger passive joint torque model is an approximation of the torque offered by the human finger and varies among subjects, (ii) the human joint also offers some non-linear damping torque [46] which was modeled as

[3]LB and UB represent the lower bound and upper bound, respectively, of the parameter as measured using a caliper for typical hand sizes.

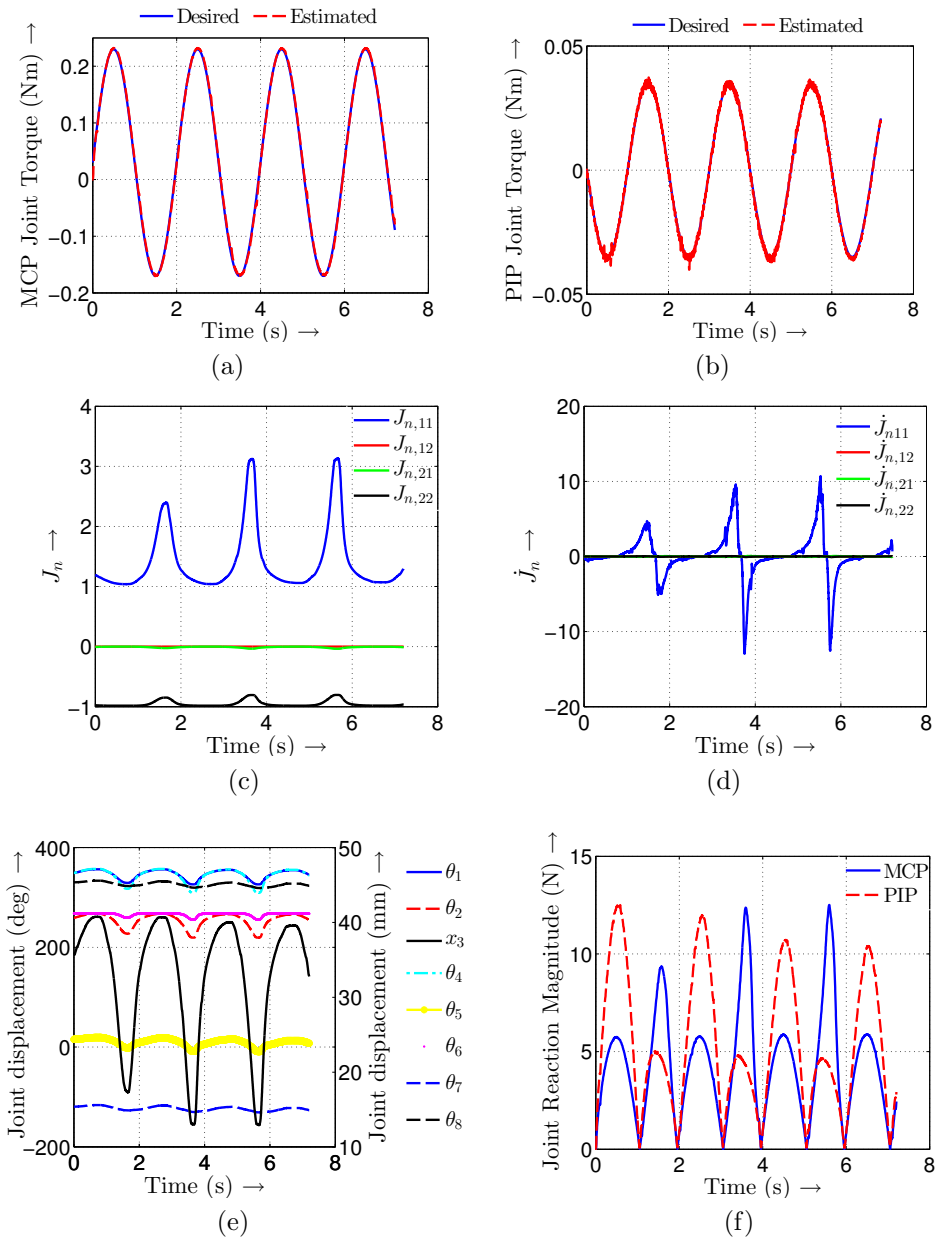

Figure 2.25: The finger joints torque tracking results from the index finger exoskeleton prototype. (a) MCP finger joint torque trajectory, (b) PIP finger joint torque trajectory, (d) Jacobian estimates, (e) Jacobian derivative estimates, (c) estimated joint displacements for the various joints in the MCP and PIP chain (x_3 is plotted on the right Y-axis) and (f) finger joint reaction forces. (Best viewed in color)

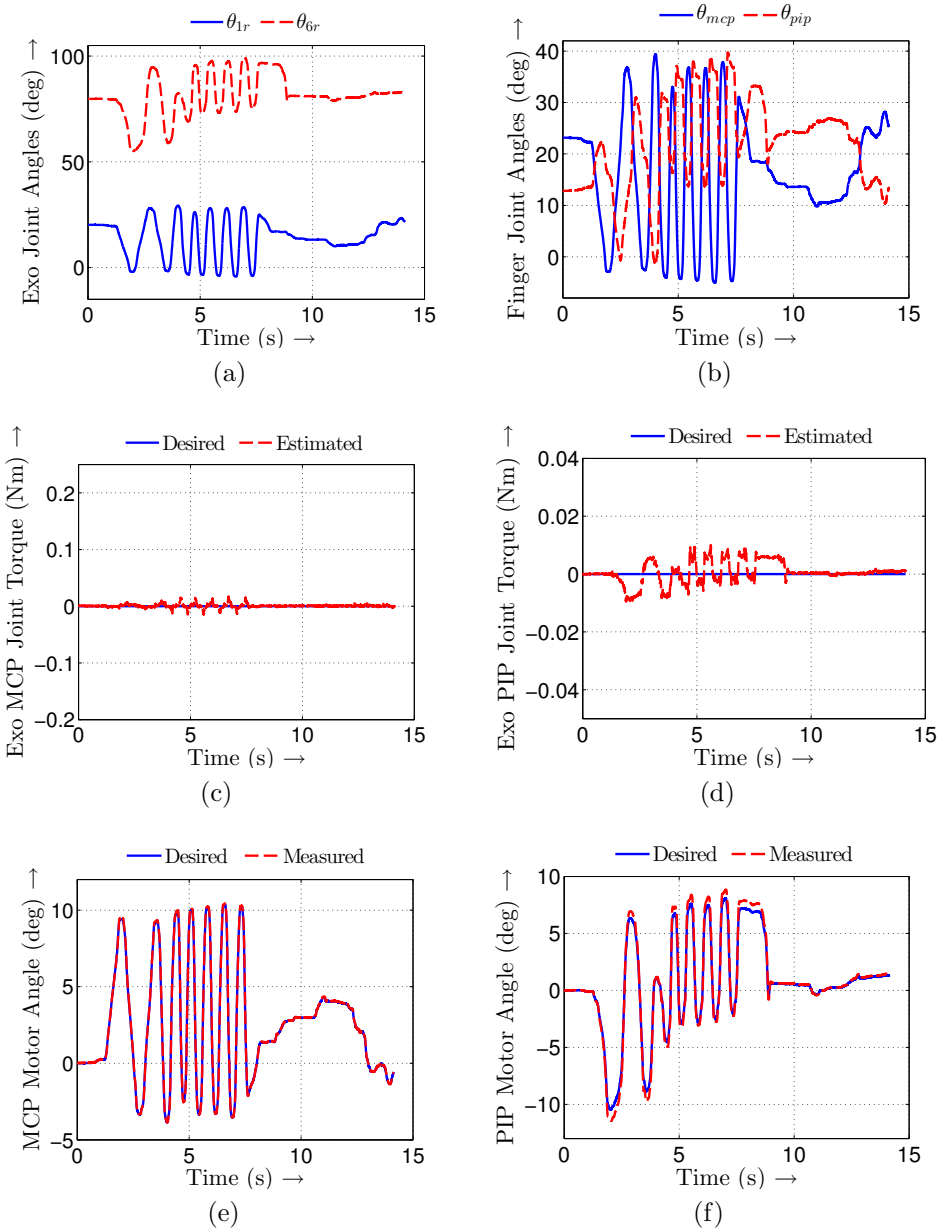

Figure 2.26: The dynamic transparency test results as obtained from the index finger exoskeleton prototype. (a) Exoskeleton joint angle trajectories, (b) estimated finger joint angle trajectories, (c) exoskeleton MCP joint torque trajectories, (d) exoskeleton PIP joint torque trajectories, (e) MCP joint motor angle trajectories and (f) PIP joint motor angle trajectories.

linear, (iii) the losses due to friction at the exoskeleton joints was assumed to be negligible and (iv) the inertial torque was not accurately modeled.

The experiments for kinematic characterization showed that the device fits well to the hands of the subjects and was easily adjustable. It was also observed that the relative attachment of the exoskeleton to the finger phalanges affected the achievable range of finger flexion-extension angle by the exoskeleton. So, by adjusting the exoskeleton attachment relative to the finger, different regions of the finger ROM can be exercised. However, there were a few limitations of the methodology used to evaluate the kinematic performance of the device. First, the motion capture data were assumed to be the ground truth for the actual motion of a subject's finger; however, there was some noise in the data, especially, due to the close proximity of the markers on a subject's finger. Second, the subjects were asked to move the finger without significant adduction-abduction motion, however, some motion was observed ($< 12°$) as it was difficult for the subjects to avoid it during a timed trial. Any out of plane rotation due to the adduction-abduction motion will result in an over-estimation of the joint angles. Overall the prototype manufactured using SLS was strong and light in weight. We envision that, given the pervasiveness of 3D printing technology in the future, rapid customization of the interfacing components in the design to a specific patient in a clinical setting will become a reality, thereby improving both the ergonomics and performance of the device.

2.3 Thumb Module of the Exoskeleton

In this section, we present the details of the test, control and experimentation carried out with the thumb exoskeleton module of the hand exoskeleton.

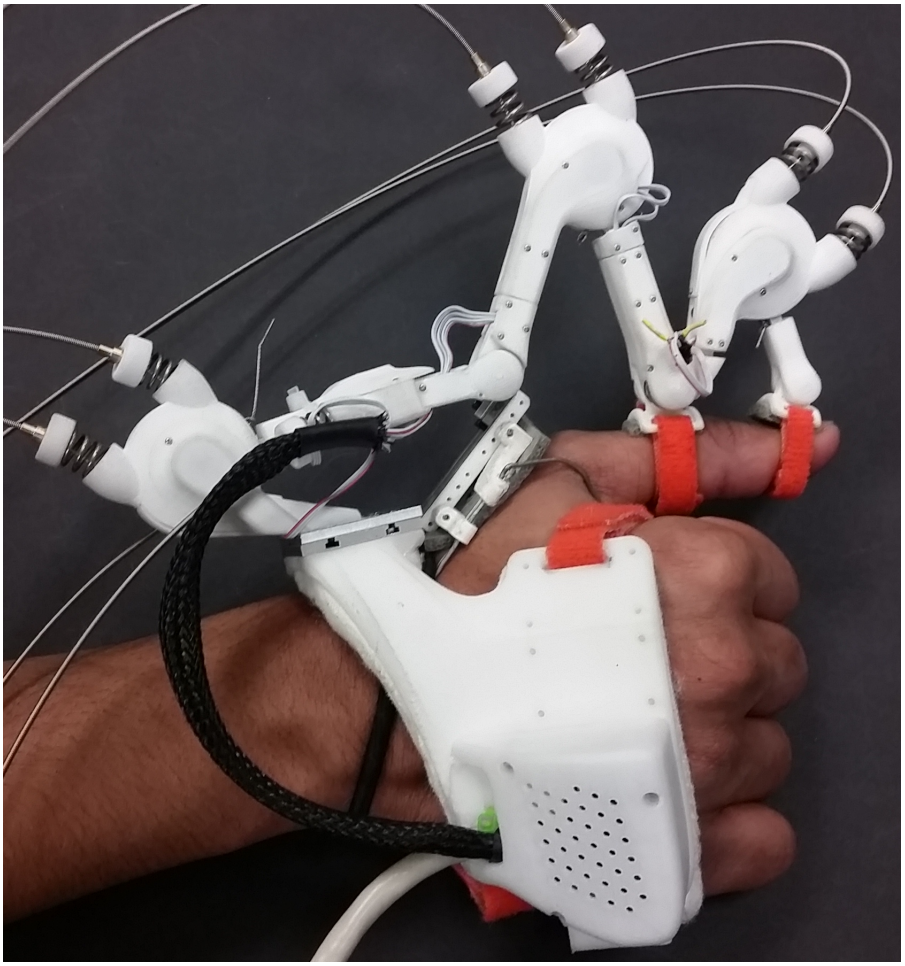

Figure 2.27: Thumb exoskeleton prototype mounted on a subject's hand for experimentation.

2.3.1 Design

In this section, we present the underlying mechanism of the proposed design, the kinematics of the coupled thumb-exoskeleton system, kinematic optimization carried out to improve the range of motion of the design, details of the actuation mechanism for torque control and finally, the developed prototype.

2.3.1.1 Mechanism

The human thumb consists of primarily four DOFs, namely, carpometacarpal flexion-extension (CMC FE), carpometacarpal abduction-adduction (CMC AA), metacarpophalangeal flexion-extension (MCP FE) and interphalangeal flexion-extension (IP FE). The mechanism for the thumb exoskeleton consists of three closed-loop chains to actively actuate these four DOFs while avoiding the exoskeleton-human joint axes misalignment problem (Figure 2.28). The CMC chain consists of four revolute and one prismatic joint forming closed-loop chain with the thumb carpometacarpal bone allowing for two DOFs in the chain. The use of a sliding joint as the interaction interface between the exoskeleton and the thumb ensures that only normal forces are applied on the phalanx. One of the revolute joints allows for the thumb abduction-adduction motion. Both the MCP and IP chains consist of four revolute joints which provides 1 DOF to each chain.

2.3.1.2 Kinematics

To solve for the kinematics of the CMC, MCP and IP chains, each of these chains is considered as a four-bar mechanism. A more detailed 3D kinematic model of the coupled thumb-exoskeleton could have been developed. However, a number of unknown and difficult to measure kinematic parameters (e.g. location and orientation of the CMC FE and CMC AA axes, orientation of the exoskeleton links with respect to the thumb joints etc.) makes it challenging to capture the kinematics of the coupled system accurately using such a model. Furthermore, reliable estimation of these unknown subject-specific parameters using redundant sensor data proved to be significantly challenging due to the highly nonlinear nature of the motion in 3D space. Hence, in lieu of a more detailed but uncertain 3D kinematic model, an approximate more reliable 2D model is developed.

For the CMC chain, since the motion at the CMC abduction-adduction joint is out of plane, an equivalent four-bar mechanism is realized that takes into account the changing length of the link AC due to abduction-adduction motion. The loop-closure equation for the proximal (CMC) chain of the thumb exoskeleton (Figure 2.28) is then given by (2.30).

$$l_{AC}(\theta_2)e^{i\theta_1} + l_{CE}e^{i\theta_3} + r_4 e^{i(\theta_5-\pi)} = x_G + iy_G \tag{2.30}$$

where $l_{AC}(\theta_2)$ is the effective length of the link AC in the CMC four-bar chain, which is function of θ_2. l_{CE} is the length of line segment CE. r_4 represents the sliding length in CMC chain at a given configuration. θ's and θ_r's represent

the absolute and relative joint angles between the links participating in a joint, respectively. (x_G, y_G) represents the coordinate of the human CMC joint (point G) in the coordinate frame located at the exoskeleton joint at A. Similarly, the loop closure equations for the middle (MCP) and distal (IP) chains are expressed.

The forward kinematics deals with evaluating the thumb CMC, MCP and IP joint angles (θ_5, θ_9, θ_{13}) and the exoskeleton passive joint displacements (r_4, θ_6, θ_{10}) given the exoskeleton relative joint angles (θ_{1r}, θ_{7r}, θ_{11r}). The relative joint angle is the angle measured by the joint angle sensor mounted at the joint. The kinematics of the system is solved using the standard four-bar kinematics solution [113] in the order–CMC, MCP and IP. When the loop closure equation (2.30) resulted in significant residual due to error in geometric parameter measurement, we evaluated the least-squares solution of the equation. The final solution can be expressed as in (2.31).

$$\mathbf{X} = \mathbf{X}(\mathbf{\Theta_r}) \tag{2.31}$$

where $\mathbf{X} = \begin{bmatrix} r_4 & \theta_5 & \theta_9 & \theta_{13} \end{bmatrix}^T$ and $\mathbf{\Theta}_r = \begin{bmatrix} \theta_{1r} & \theta_{2r} & \theta_{7r} & \theta_{11r} \end{bmatrix}^T$.

2.3.1.3 Kinematics Optimization

A thumb exoskeleton that allows for large range of motion for different hand sizes could be used to serve different target population with minimal customization. To this end, we carry out an optimization study to maximize the range of motion by varying the kinematics of the design. A design that

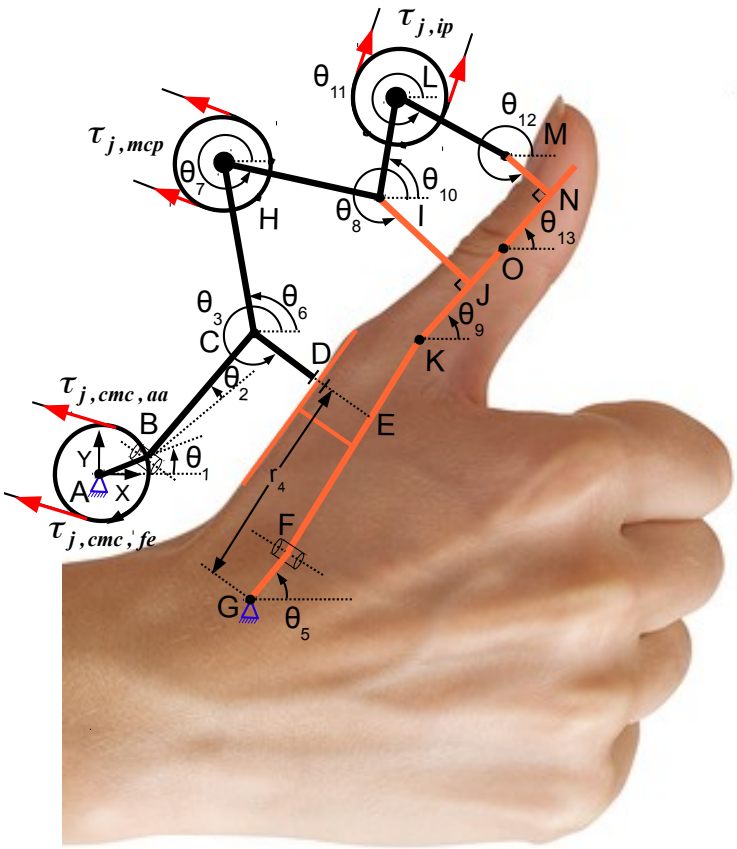

Figure 2.28: Nomenclature for the kinematic model of the designed thumb exoskeleton. All angles are measured in counterclock-wise direction. The arrows in red color depict forces acting on the system. The arrows in black represent kinematic variables. (Best viewed in color.)

also results in increased mechanical advantage from the exoskeleton joint to the human joint would reduce the torque requirement at the exoskeleton joint and thus, help in minimizing the size of the transmission mechanism. We carried out such a study for the thumb exoskeleton module to both increase its range of motion and ensure kinematic robustness of the design against hand size variation.

In order to determine the mechanical advantage for CMC flexion-extension motion, we take the differential of the kinematic equation of the CMC chain (2.30) and solve for $\delta\theta_1$ and δr_4, which results in (2.32).

$$\begin{aligned}&\begin{bmatrix}-l_{AC}(\theta_2)\sin\theta_1 & \cos\theta_5\\ l_{AC}(\theta_2)\cos\theta_1 & \sin\theta_5\end{bmatrix}\begin{bmatrix}\delta\theta_1\\ \delta r_4\end{bmatrix}\\ &=\begin{bmatrix}l_{CE}\sin\theta_3 + r_4\sin\theta_5\\ -l_{CE}\cos\theta_3 - r_4\cos\theta_5\end{bmatrix}\delta\theta_5\end{aligned} \tag{2.32}$$

The mechanical advantage in flexion-extension at CMC joint is then evaluated as $\eta = \delta\theta_1/\delta\theta_5$. An optimization study is then set up to maximize the range of motion at the CMC chain while also maximizing the mechanical advantage. Also, since CMC joint has higher extension range of motion than flexion, we constraint the lower and upper limits of the angle.

$$\begin{aligned}&\max_{\mathbf{P}}\,(\theta_{5,max}(\mathbf{P}) - \theta_{5,min}(\mathbf{P}), \eta(\mathbf{P}))\\ &\text{s.t. } \theta_{5,max} \geq \theta_{5,u}\\ &\qquad \theta_{5,min} \leq \theta_{5,l}\\ &\qquad r_{4,l} \leq r_4 \leq r_{4,u}\\ &\qquad \mathbf{P}_l \leq \mathbf{P} \leq \mathbf{P}_u\end{aligned} \tag{2.33}$$

where $\theta_{5,max}$ and $\theta_{5,min}$ refers to the maximum and minimum CMC flexion angle. $\theta_{5,u}$ and $\theta_{5,l}$ are the upper and lower limit, respectively, of θ_5 that a feasible solution must achieve. $r_{4,u}$ and $r_{4,l}$ are the upper and lower bound, respectively, of r_4 that a feasible solution must satisfy. $\mathbf{P} = \begin{bmatrix}x_G & y_G & l_{AC} & l_{CD}\end{bmatrix}^T$ are the design variables to be determined that satisfies the optimization criteria.

Since (2.33) is a multi-objective optimization problem with non-linear objective functions, we use a parametric study to determine the best feasible solution for the problem. We varied the various design variables in the design space and evaluated the range of motion for small and large hand sizes for each design configuration. We gave preference to solutions that resulted in larger range of motion. For solutions that resulted in the same range of motion, we chose the ones that maintained the range of motion across all hand sizes.

The parametric study resulted in several different solutions with different upper and lower limits on the CMC flexion-extension angle (Figure 2.29). Results showed that solutions with higher range of motion tends to have lower mechanical advantage. For all solutions the range of motion reduces as the CMC abduction-adduction angle increases. However, the CMC flexion-extension range of motion of the human thumb also decreases as the CMC abduction-adduction angle increases. Also, the range of motion is adversely affected as the size (thickness) of the thumb metacarpal bone increases while keeping the available sliding length constant. Furthermore, solutions that are better in terms of range of motion were also more robust to changes in thumb thickness variation. The results also showed that the range of motion in the CMC chain is particularly sensitive to dimension l_{CD}. Smaller values of l_{CD} resulted in larger ranges of motion for hands of different thicknesses both in unabducted and abducted positions. We chose the solution that maximized the range of motion over the one that maximized mechanical advantage as reduced range of motion limit functionality whereas reduced mechanical ad-

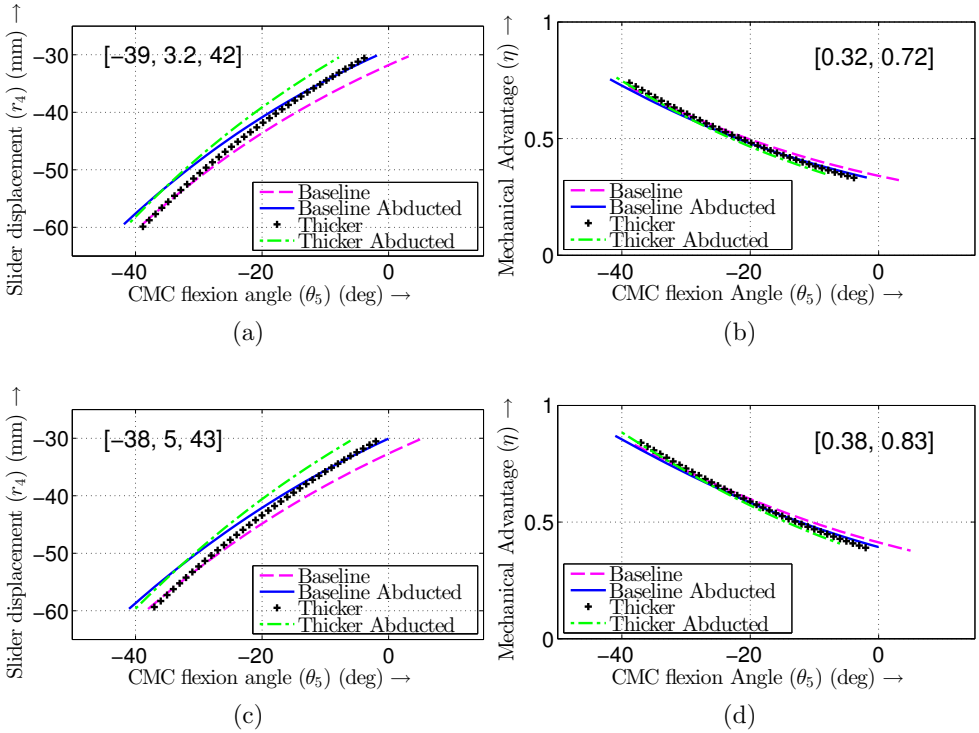

Figure 2.29: The three best solutions from the parametric study carried out to maximize the range of motion and mechanical advantage for flexion-extension motion at CMC joint. The plots in the left and right columns show the slider displacement, which determines the flexion-extension range of motion at the CMC joint and the corresponding mechanical advantage, respectively. Baseline and thicker refers to a thinner and thicker hand metacarpal bone, respectively. Abducted refers to the solution in a fully abducted thumb position ($\theta_2 = 25°$). The values in square brackets in the left column show the minimum value, maximum value and range of motion, respectively, of the flexion angle at the CMC joint for the baseline configuration of the solution. The values in square brackets in the right column show the minimum and maximum values, respectively, of the mechanical advantage for the baseline configuration of the solution.

vantage just increases the forces and torques acting in the system by a small magnitude. For the MCP and IP chains, there were several feasible solutions

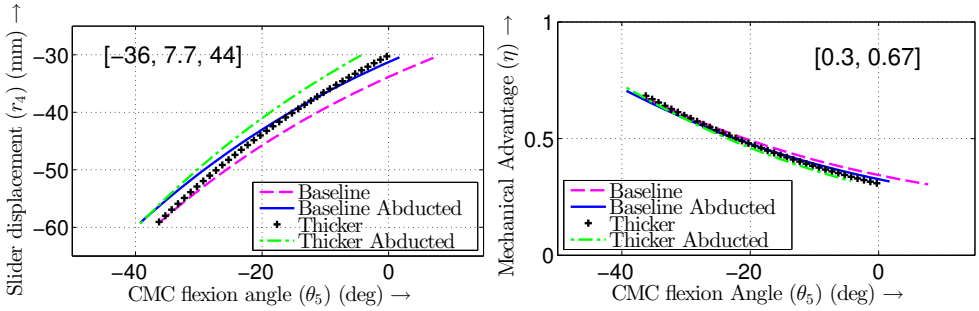

(e) (f)

Figure 2.29: The three best solutions from the parametric study carried out to maximize the range of motion and mechanical advantage for flexion-extension motion at CMC joint. The plots in the left and right columns show the slider displacement, which determines the flexion-extension range of motion at the CMC joint and the corresponding mechanical advantage, respectively. Baseline and thicker refers to a thinner and thicker hand metacarpal bone, respectively. Abducted refers to the solution in a fully abducted thumb position ($\theta_2 = 25°$). The values in square brackets in the left column show the minimum value, maximum value and range of motion, respectively, of the flexion angle at the CMC joint for the baseline configuration of the solution. The values in square brackets in the right column show the minimum and maximum values, respectively, of the mechanical advantage for the baseline configuration of the solution. (contd.)

which could be easily obtained without explicitly setting up any optimization study. So, we chose the links lengths for those chains manually and solve for the kinematics while satisfying the design constraints.

2.3.1.4 Prototype

The optimized kinematic mechanism of the thumb exoskeleton presented in Sections 2.3.1.1 and 2.3.1.3 is realized in the form of a prototype (Figure 2.30). The SEA referred to in Section 2.1 are implemented at each

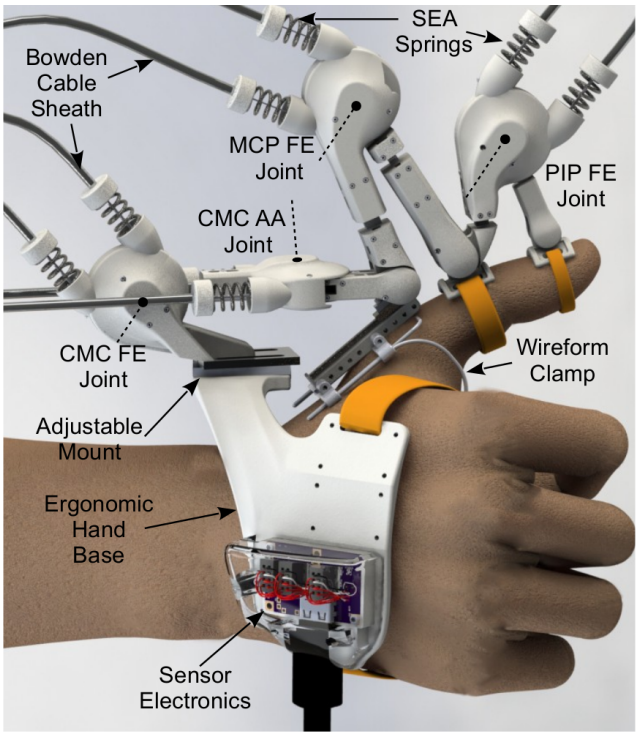

Figure 2.30: CAD model of the designed thumb exoskeleton prototype.

of the actuated joints of the exoskeleton. The CMC joint required multi-axis SEA to actuate both the flexion-extension and the abduction-adduction joint. The SEA for the CMC AA joint is mounted on the output of the SEA for the CMC FE joint to achieve this. Since, our SEA is small enough (44 mm $\times$ 35 mm $\times$ 17 mm) this was possible. Each joint has a bearing to reduce the friction at the joints. Each link is adjustable to allow for quick customization of the device for a specific subject. Also, we use a magneto-resistive angle sensor (KMA210, NXP Semiconductors) with a diametrically magnetized ring magnet to measure the exoskeleton joint angles (enclosed in casings). Due to the close proximity of the CMC FE and CMC AA joint axes, we do not use

a magnetoresistive sensor at the CMC AA joint to avoid interference in the measurements from the two sensors. Instead, we use a sliding contact type miniature rotary potentiometer to sense the joint angle.

The thumb exoskeleton chain is mounted on a hand base through an adjustable mount that allows for changing the angular and linear position of the chain to accommodate for the variability in different hand sizes. Also, the wires for the sensors are routed internally to ensure durability of the sensors and connected to the sensor board mounted on the hand base. The various parts of the exoskeleton are manufactured using Selective Laser Sintering[4] (SLS) to keep the overall design light in weight. Some of the load bearing parts (e.g. SEA pulleys, adjustable mount) are machined our of metal to ensure durability of the device.

One of the challenges in thumb exoskeleton design has been to apply bidirectional forces on the thumb metacarpal. This is because it is difficult to hold on to the metacarpal bone of the thumb as there is no circumferential access to it and the bellies of the Thenar eminence muscles change in shape as the thumb moves around. We designed an ergonomic wire-form structure with galvanized steel wire to address this issue. The structure has a ring around the MCP joint with four protruded legs placed so as to have minimal interference with any deformation of the muscles. The structure rests closely against the metacarpal, cages the metacarpal bone and provides stability to transfer and

[4]See http://en.wikipedia.org/wiki/Selective_laser_sintering

distribute the forces applied by the exoskeleton on the metacarpal. The slider in the CMC chain is attached with an adjustable mount to the wire-form structure to allow for the transmission of the forces from the exoskeleton to the metacarpal. The structure is kept in place with the help of an elastic band (not shown in figure), which prevents it from slipping forward when the forces are applied. This wire-form design is a lightweight and comfortable solution to the challenging problem of exoskeleton attachment to the thumb.

2.3.2 Controls

A torque controller was implemented to track the desired torque trajectories at the exoskeleton SEA joints (Figure 2.31). The output of the system is the torque ($\hat{\mathbf{y}}$) generated at the exoskeleton joints through SEA as estimated using (2.34).

$$\hat{\mathbf{y}} = \begin{bmatrix} \tau_{j,cmc,fe} \\ \tau_{j,cmc,aa} \\ \tau_{j,mcp} \\ \tau_{j,ip} \end{bmatrix} = 2\mathbf{K}r_j\left(r_m\mathbf{\Theta_m} - r_j(\mathbf{\Theta_r} - \mathbf{\Theta_{r0}})\right) \tag{2.34}$$

where

$$\mathbf{K} = \begin{bmatrix} k_{j,cmc,fe} & 0 & 0 & 0 \\ 0 & k_{j,cmc,aa} & 0 & 0 \\ 0 & 0 & k_{j,mcp} & 0 \\ 0 & 0 & 0 & k_{j,ip} \end{bmatrix}$$

$$\mathbf{\Theta_m} = \begin{bmatrix} \theta_{m,cmc,fe} \\ \theta_{m,cmc,aa} \\ \theta_{m,mcp} \\ \theta_{m,ip} \end{bmatrix}$$

$k_{j,cmc,fe}$, $k_{j,cmc,aa}$, $k_{j,mcp}$ and $k_{j,ip}$ represent the magnitude of the effective stiffness at the exoskeleton CMC F/E, CMC A/A, MCP and IP joints, respectively.

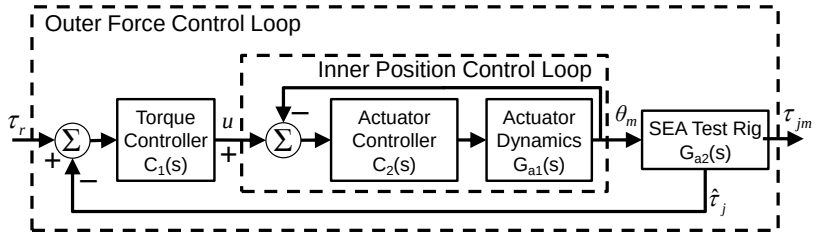

Figure 2.31: The schematic of the torque controller implemented for the SEAs. The inner position control loop represents the position control implemented in the motor driver. The outer force control loop refers to the control loop implemented for output torque tracking.

$\theta_{m,cmc,fe}$, $\theta_{m,cmc,aa}$, $\theta_{m,mcp}$ and $\theta_{m,ip}$ are the CMC F/E, CMC A/A, MCP and IP motor angles, respectively. The feed-forward PID controller is then given by (2.35).

$$\begin{aligned}
\mathbf{e} =& \mathbf{y}_d - \hat{\mathbf{y}} \\
\dot{\mathbf{e}} =& \dot{\mathbf{y}}_\mathbf{d} - \dot{\hat{\mathbf{y}}} \\
\mathbf{u} =& \frac{1}{r_m}\left(\frac{\mathbf{K}^{-1}\mathbf{y_d}}{2r_j} + r_j\left(\mathbf{\Theta_r} - \mathbf{\Theta_{r0}}\right)\right) + \mathbf{K_p}\mathbf{e} + \\
& \mathbf{K_d}\dot{\mathbf{e}} + \mathbf{K_i}\int \mathbf{e}dt
\end{aligned} \tag{2.35}$$

where $\mathbf{e}$ is the vector containing exoskeleton joint torque errors, $\mathbf{y}_d$ is the vector containing the desired torque at the two exoskeleton joints and $\mathbf{u}$ is the control input vector (desired motor position) for the four exoskeleton joints. $\mathbf{K_p}$, $\mathbf{K_d}$ and $\mathbf{K_i}$ represent the diagonal proportional, derivative and integral gain matrices for the PID controller.

2.3.3 Experimentation

To validate the effectiveness of the designed thumb exoskeleton in achieving our design goals, we carry out experiments with the prototype to assess (i) workspace of thumb with and without the exoskeleton, (ii) kinematic transparency of the device to understand how the natural motion of the thumb is affected by the device and (iii) torque control of the device. Four healthy subjects (three males and one female, ages 20-33 years) with no history of any neuromuscular injury voluntarily participated in the experiments, after they provided their informed consent (The University of Texas at Austin institutional review board amended study number 2013-05-0126). The subjects donned the device and the link lengths and neutral position of the exoskeleton were adjusted so that the device is comfortable for each subject. For the workspace and kinematic transparency experiments, motion capture data were recorded using an active marker motion capture system (PhaseSpace Inc.) at 480 Hz. The location of the motion capture markers was chosen to ensure minimal interference with exoskeleton attachment interface (Figure 2.32) and maintain similar experimental conditions without and with the device. Three markers were placed on the wrist to establish a coordinate frame to account for any movement of the hand. The remaining four markers were placed at each of three joints and tip of the thumb. The hand of the subjects was supported to ensure minimal motion at the wrist joint. Since, these experiments were aimed at characterizing only the kinematics of device, the Bowden-cable-based SEAs were not connected during this experimentation.

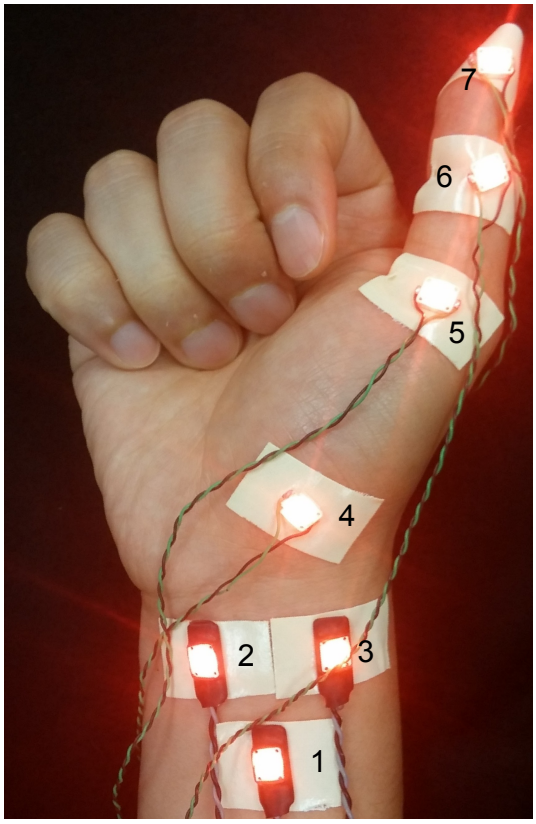

Figure 2.32: The motion capture marker set used to carry out the kinematic experiments with the thumb exoskeleton. The number next to each marker represents the marker number used to refer the marker.

2.3.3.1 Workspace Analysis

In order to quantify the volume of the workspace of the thumb with human subjects, we carry out experiments using the motion capture system. We asked the subjects to move there thumb to reach full achievable range of motion at each joint. In order to accurately capture the curvature of the workspace boundary several repetitions of the motion were performed. These experiments were carried out both without and with the exoskeleton. The

collected data is then processed to correct for any overall hand movement using the three ground markers on the wrist. A convex hull is fitted to the data for markers 4, 5, 6, and 7 to evaluate the volume of the region the thumb was able to reach. The percentage volume of the workspace of the thumb with the exoskeleton with respect to without exoskeleton is given in (2.36), which gives a measure of the volumetric range of motion preserved with the exoskeleton.

$$\eta = \frac{V_{we}}{V_{ne}} \times 100\% \tag{2.36}$$

2.3.3.2 Kinematic Transparency

Kinematic transparency tests were carried out to quantify the similarity of the motion without and with the thumb exoskeleton. We used the following protocol to perform the kinematic transparency experiments. The motion capture markers are placed on the thumb and the subjects were asked to perform four different motions at four different speeds: (i) CMC, MCP and IP joints articulation through full active range of motion (AROM) in flexion-extension while maintaining the abduction-adduction angle at the CMC joint, (ii) full AROM abduction-adduction motion at the CMC joint while maintaining the position of the other joint angles, (iii) full AROM flexion-extension and abduction-adduction motion in a circular pattern at the CMC joint and (iv) full AROM flexion-extension motion at the MCP and IP joint while maintaining the position of the other joints. The rationale behind choosing motion (i) rather than isolated motion at the CMC joint was that it was difficult to

achieve the full AROM by the subjects without flexing the MCP joint. The subjects were asked to wear the device and the link lengths were adjusted to ensure that the subjects can reach their full AROM with the device. Care was taken to ensure that the motion capture markers did not move while wearing the device. Some initial time was provided to the subject to get comfortable with the device and practice each motion for a certain duration. The subjects are then asked to perform the same motions with the exoskeleton. The experiments were performance at four different speeds–(i) 0.25 Hz, (ii) 0.5 Hz, (iii) 0.75 Hz and (iv) 1 Hz. An audio cue with the help of a metronome was provided to the subjects to help them maintain the required finger frequency. The motion capture data was resampled at 1/10 frequency (48 Hz).

The motion capture data is processed to evaluate the angle of each phalanx with respect to the ground reference frame established using the markers placed on the wrist. The orientation of the ground reference frame is first calculated using Gram-Schmidt orthonormalization [30] as given in (2.37).

$$\begin{aligned} \mathbf{u}_x &= \mathbf{p}_3 - \mathbf{p}_2 & \hat{\mathbf{e}}_x &= \frac{\mathbf{u}_x}{||\mathbf{u}_x||} \\ \mathbf{u}_y &= \mathbf{p}_3 - \mathbf{p}_1 - \hat{\mathbf{e}}_x.(\mathbf{p}_3 - \mathbf{p}_1) & \hat{\mathbf{e}}_y &= \frac{\mathbf{u}_y}{||\mathbf{u}_y||} \\ \mathbf{e}_z &= \hat{\mathbf{e}}_x \times \hat{\mathbf{e}}_y \end{aligned} \tag{2.37}$$

where $\mathbf{p}_i$ is the 3d position of the ith marker in the reference frame of the motion capture system. $\mathbf{e}_x$, $\mathbf{e}_y$ and $\mathbf{e}_z$ refer to the unit vectors in the ground reference frame along the X, Y and Z axis, respectively. $\mathbf{u}_x$ and $\mathbf{u}_y$ are the vectors evaluated to calculate the unit vectors. The rotation angles of the metacarpal phalanx in 3D is calculated with respect to the evaluated reference

frame using direction cosines as given in (2.38). Similarly the angles for the middle and distal phalanges are calculated using their respective markers.

$$\begin{aligned}
\theta_{cmc,x} &= \cos^{-1}\left(\frac{(\mathbf{p}_5 - \mathbf{p}_4)\,.\hat{\mathbf{e}}_x}{||\,(\mathbf{p}_5 - \mathbf{p}_4)\,||}\right) \\
\theta_{cmc,y} &= \cos^{-1}\left(\frac{(\mathbf{p}_5 - \mathbf{p}_4)\,.\hat{\mathbf{e}}_y}{||\,(\mathbf{p}_5 - \mathbf{p}_4)\,||}\right) \\
\theta_{cmc,z} &= \cos^{-1}\left(\frac{(\mathbf{p}_5 - \mathbf{p}_4)\,.\hat{\mathbf{e}}_z}{||\,(\mathbf{p}_5 - \mathbf{p}_4)\,||}\right)
\end{aligned} \tag{2.38}$$

2.3.3.3 Torque Control

The torque control experiments are carried out to ensure if the device is able to track a desired torque trajectory using the controller proposed in Section 2.3.2. The four subjects participated in this experiment. In the first phase of the experiment, the subjects were asked to avoid any voluntary contraction of the muscle and let the exoskeleton actively move their thumb around. In the second phase, the subjects were asked to block the motion to validate if the device still tracks the desired torque trajectory. We use a mean and phase-shifted sinusoidal trajectory as the desired torque trajectory at each joint of the thumb exoskeleton as given in (2.39).

$$\begin{aligned}
\tau_{j,i} &= \tau_{A,i}\left(\sin\left(2\pi f t + \phi_{\tau,i}\right) + D_{\tau,i}\right) \times S(t) \\
S(t) &= \frac{1}{1 + e^{-(t-5)}}
\end{aligned} \tag{2.39}$$

where S(t) is sigmoid function, which is multiplied to gradually increase the torque levels from zero to their respective value to ensure that any phase and amplitude relationship between the thumb torques can be achieved.

2.3.4 Results

In this section, we present the results from the workspace analysis, kinematic transparency tests and torque control of the device.

2.3.4.1 Workspace Analysis

Table 2.7: Thumb workspace analysis results without and with the device for the different subjects.

Subject #	V_{ne} (cm^3)	V_{we} (cm^3)	η
I	707.31	560.25	79.21 %
II	1152.54	1049.86	91.09 %
III	729.38	570.73	78.25 %
IV	701.32	658.16	93.84 %
	Average		85.59 %

Results showed that the device is able to retain around 85.59 % workspace on average with the exoskeleton (Table 2.7). Also, some variability was observed in the percent reachable workspace from subject to subject. This variability might be due to the significant natural variation that exists in thumb anatomy which has been shown to support the idea of non-existence of a single generic biomechanical model that can represent the entire population [126]. A comparison of the workspace in XY, YZ and XZ plane without and with the exoskeleton for Subject III shows that the major portion of the workspace can be reached with the exoskeleton (Figure 2.33).

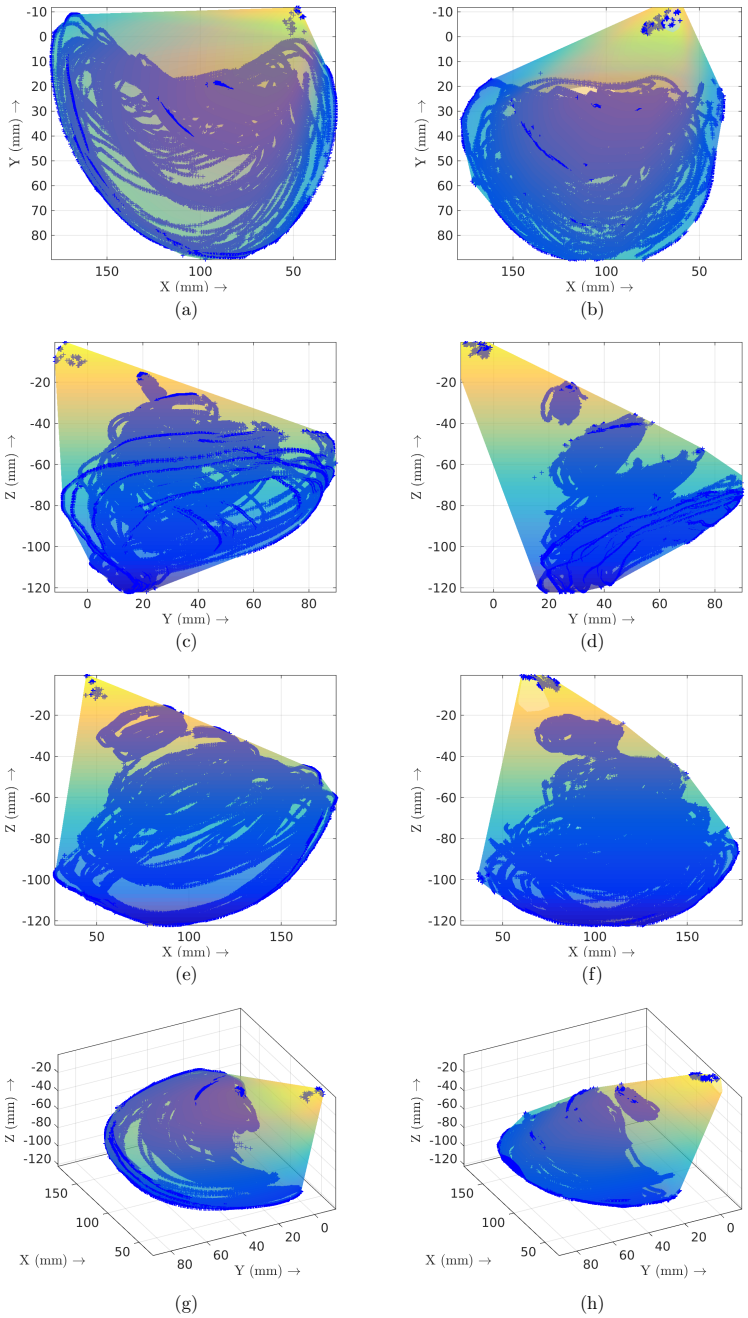

Figure 2.33: Workspace results without and with the exoskeleton for subject III. The left and right columns represent the plots of the thumb workspace without and with the thumb exoskeleton, respectively. The dark trajectories are the plotted marker data as captured using the motion capture system.

2.3.4.2 Kinematic Transparency

A comparison of the thumb phalanx angles in 3D without and with the exoskeleton is carried out for the different motions. Pearsons product moment correlation coefficient averaged over three repetitions is calculated to quantify the degree of similarity between the angle trajectories without and with the exoskeleton. Correlation is used as a measure of transparency instead of RMS error as it is difficult for a subject to exactly replicate the same motion consistently with or without the device.

Table 2.8: Pearson's product moment correlation coefficient averaged over 3 repetitions as obtained from the kinematic transparency tests. The p-value was coumputed using a Student's t distribution. The correlation is calculated only for those trajectories where significant motion was observed either in with or without exoskeleton trajectory.

Motion type	CMC			MCP			IP		
	X	Y	Z	X	Y	Z	X	Y	Z
(i)	0.9122 ($p <$ 0.01)	0.9201 ($p <$ 0.01)	0.5368 ($p <$ 0.01)	0.9397 ($p <$ 0.01)	0.7997 ($p <$ 0.01)	0.4796 ($p <$ 0.01)	0.9132 ($p <$ 0.01)	0.6073 ($p <$ 0.01)	0.5990 ($p <$ 0.01)
(ii)	0.9077 ($p <$ 0.01)	0.8874 ($p <$ 0.01)	0.6727 ($p <$ 0.01)	0.9414 ($p <$ 0.01)	0.9071 ($p <$ 0.01)	0.8293 ($p <$ 0.01)	0.9383 ($p <$ 0.01)	0.9277 ($p <$ 0.01)	0.8375 ($p <$ 0.01)
(iii)	0.9024 ($p <$ 0.01)	0.8324 ($p <$ 0.01)	0.6200 ($p <$ 0.01)	0.9442 ($p <$ 0.01)	0.6228 ($p <$ 0.01)	0.6880 ($p <$ 0.01)	0.9441 ($p <$ 0.01)	0.5149 ($p <$ 0.01)	0.7932 ($p <$ 0.01)
(iv)	–	–	–	0.9658 ($p <$ 0.01)	0.9582 ($p <$ 0.01)	–	0.9677 ($p <$ 0.01)	0.8852 ($p <$ 0.01)	0.8139 ($p <$ 0.01)

Results of motion (i) at 0.25 Hz showed that most of the thumb phalanx angle trajectories without and with the exoskeleton (Figure 2.34) are strongly

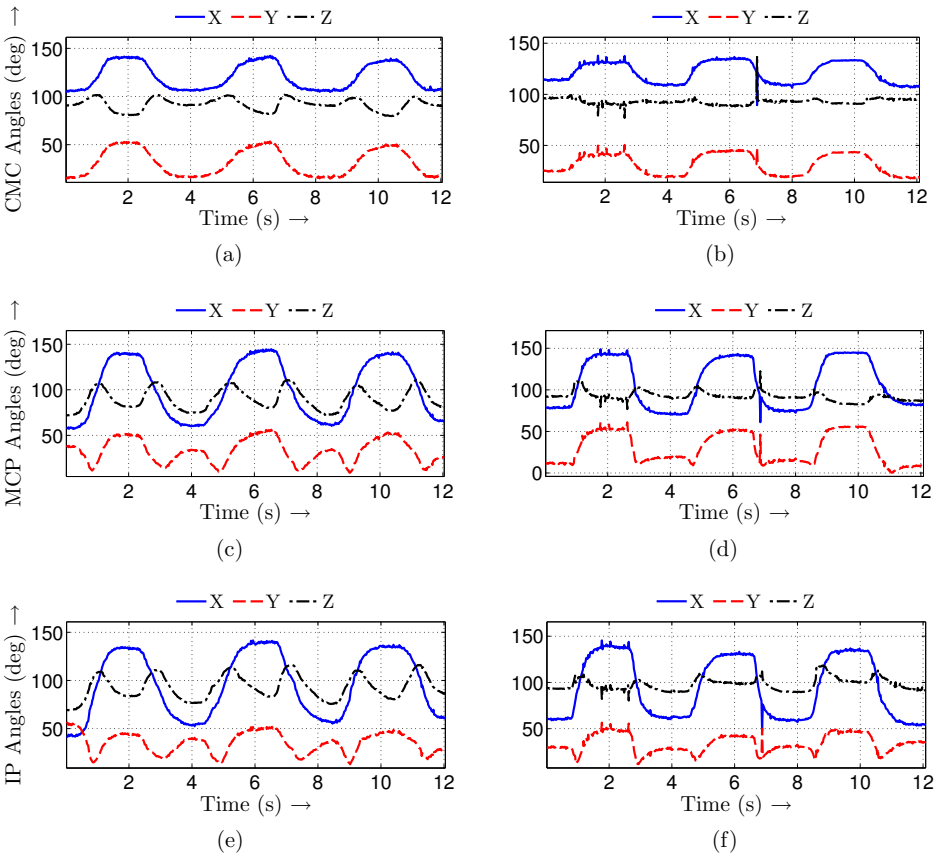

Figure 2.34: Kinematic transparency results without and with the exoskeleton for motion (i) at 0.25 Hz with subject I. The left and right columns represent the plots of the various thumb phalanx angles with respect to the reference frame without and with the thumb exoskeleton, respectively.

correlated (Table 2.8) for the two phalanges and metacarpal of the thumb. Some deviation was observed in the trajectory of the angles about the Z axis for the phalanges. However, the range of motion about Z axis is relatively smaller as compared to the other two axes. Results of motion (ii) at 0.5 Hz also showed that the two sets of angle trajectories (Figure 2.35) are strongly correlated (Table 2.8). The range of motion at the CMC joint is relatively

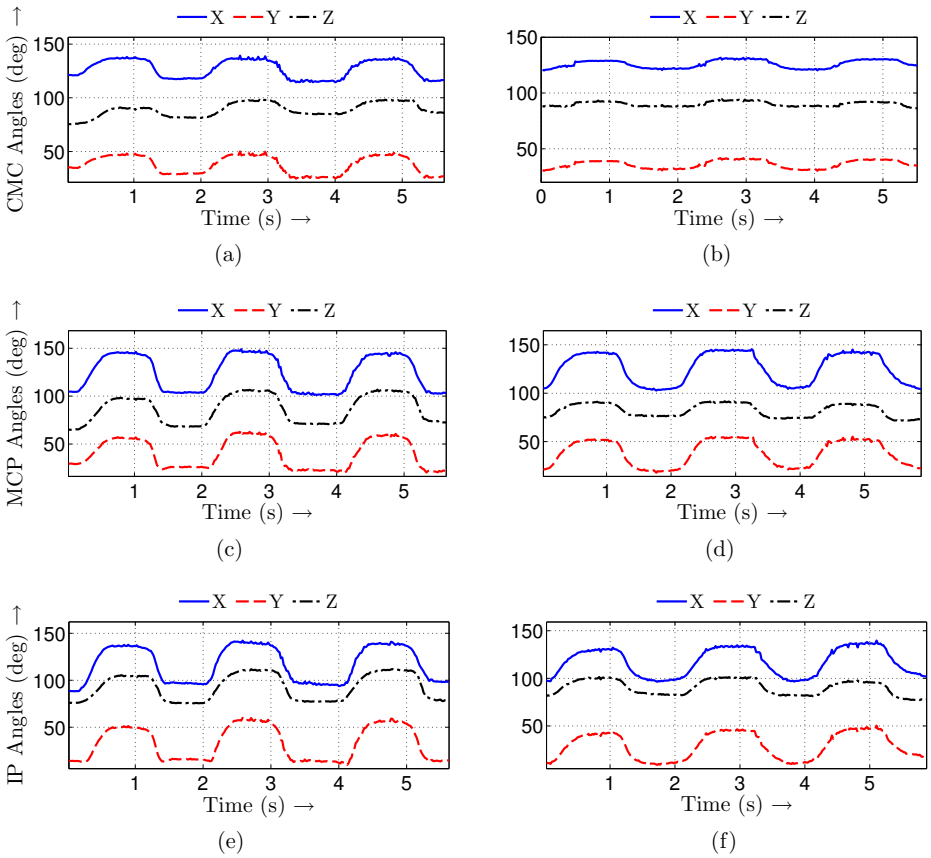

Figure 2.35: Kinematic transparency results without and with the exoskeleton for motion (ii) at 0.5 Hz with subject I. The left and right columns represent the plots of the various thumb phalanx angles with respect to the reference frame without and with the thumb exoskeleton, respectively.

reduced with the exoskeleton than without it. This is because the wireform structure and the velco strap to hold the exoskeleton base on the hand occupies some space, which reduces the effective range. However, the nature of motion is preserved showing that the exoskeleton has not affected the motion adversely. The two sets of angle trajectories (Figure 2.36) are also strongly correlated (Table 2.8) for motion (iii) at 0.75 Hz. The peaks of the motion with

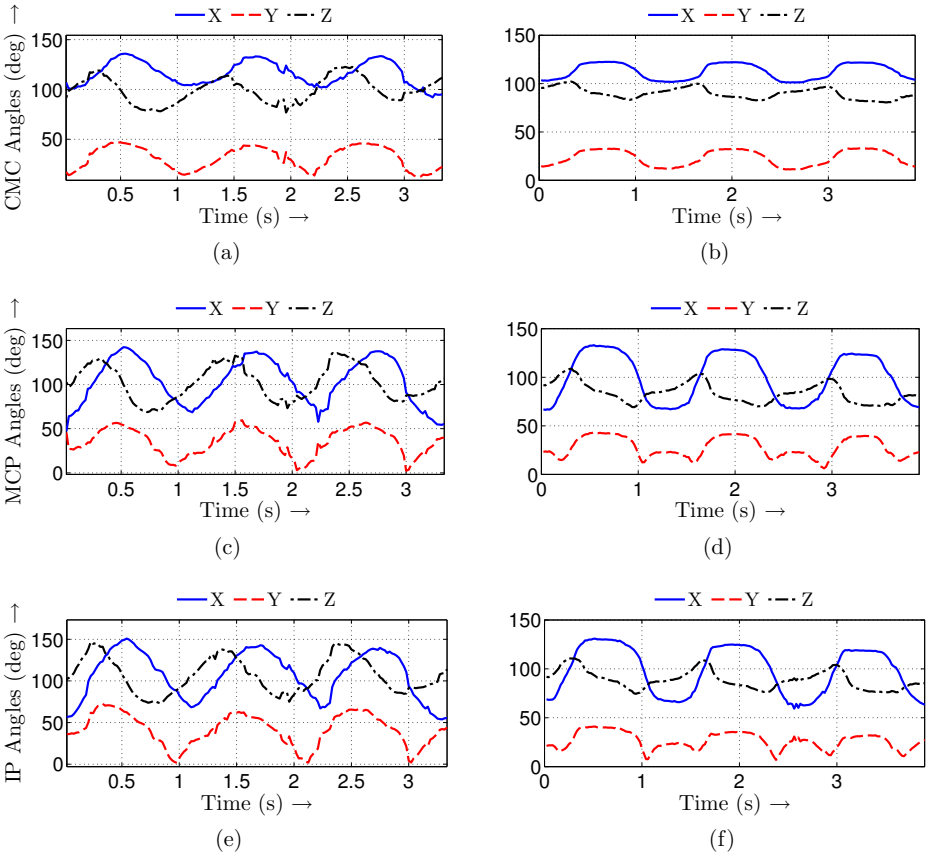

Figure 2.36: Kinematic transparency results without and with the exoskeleton for motion (iii) at 0.75 Hz with subject I. The left and right columns represent the plots of the various thumb phalanx angles with respect to the reference frame without and with the thumb exoskeleton, respectively.

the exoskeleton are plateaued for some of the trajectories. Also, some deviation was observed in the metacarpal trajectory about the Z axis, proximal and distal phalanges about the Y and Z axes for this motion. Finally, trajectories for motion (iv) at 1 Hz also showed significant correlation (Table 2.8). Since, this motion involved only moving the MCP and IP joint in flexion-extension, small motion was observed at the CMC joint both without and with the ex-

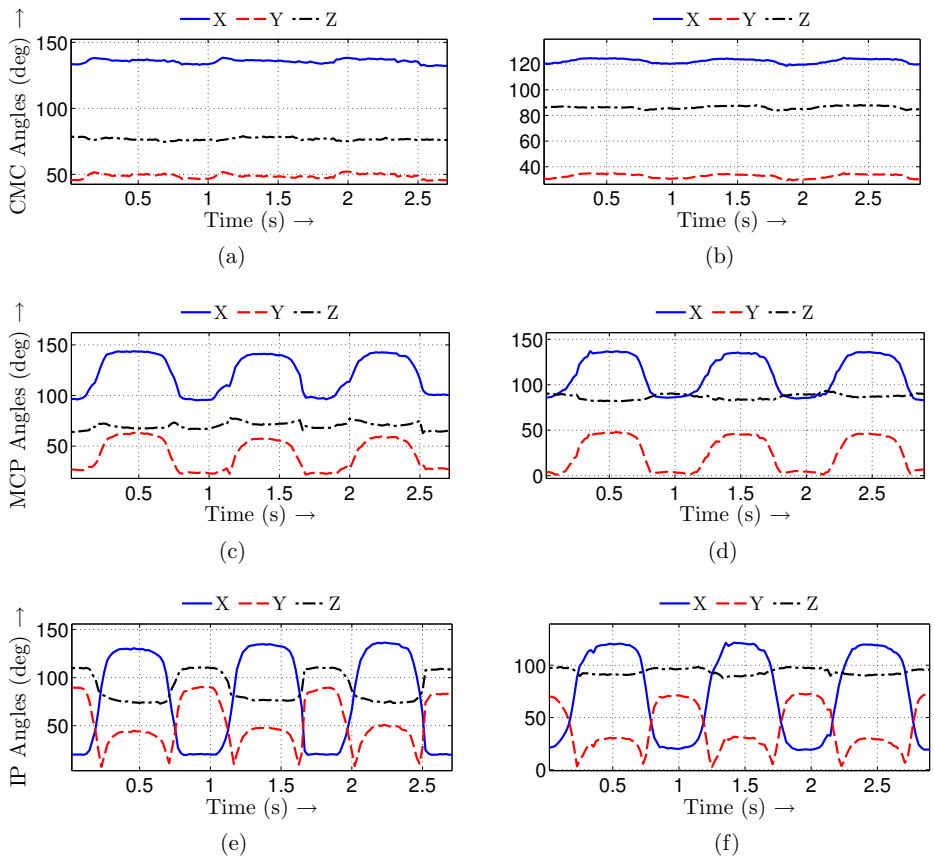

Figure 2.37: Kinematic transparency results without and with the exoskeleton for motion (iv) at 1 Hz with subject I. The left and right columns represent the plots of the various thumb phalanx angles with respect to the reference frame without and with the thumb exoskeleton, respectively.

oskeleton (Figures 2.37a and 2.37b). This shows that the subject were able to move the MCP and IP joints with minimal motion at the CMC joint both without and with the exoskeleton. Some deviation was observed for the distal phalanx joint angle about Z axis for this motion. Also, it was observed that it took slightly longer for the subject to complete the motion with the exoskeleton than without it, especially at higher frequencies. However, the

nature of the trajectories is not significantly affected as the speed of motion increases, showing that the device does not alter the coordinated motion of the phalanges even at higher speeds. Thus, these experiments demonstrate that overall the device preserves the natural motion of the thumb. Similar results were obtained for the other subjects.

2.3.4.3 Torque Control

Results from the first phase of the experiment showed that the joint torque controller is able to track the desired torque at the thumb exoskeleton joints with an RMS error of 4.16% (0.0151 Nm), 13.07% (0.0294 Nm), 6.6% (0.0132 Nm) and 10.53% (0.0084 Nm) at the CMC FE, CMC AA, MCP and IP joint, respectively (Figure 2.38). A relatively noisier torque output is observed at the CMC AA joint as a sliding-contact type potentiometer was used at that joint for joint angle sensing (Section 2.3.1.4). Furthermore, the torque at each joint increase gradually as expected due to the Sigmoid function in (2.39). The torque envelop and mean torque required to move the four thumb joints were also obtained for the four subjects (Figure 2.39).

Results from the second phase of the experiment showed that even when significant external disturbance is applied at the exoskeleton joints, which resulted in considerable changes in the exoskeleton joint angles (Figure 2.40(a)), the controller is able to maintain the desired torque level (Figure 2.40(b)). Thus, the device can perform torque control irrespective of the impedance of

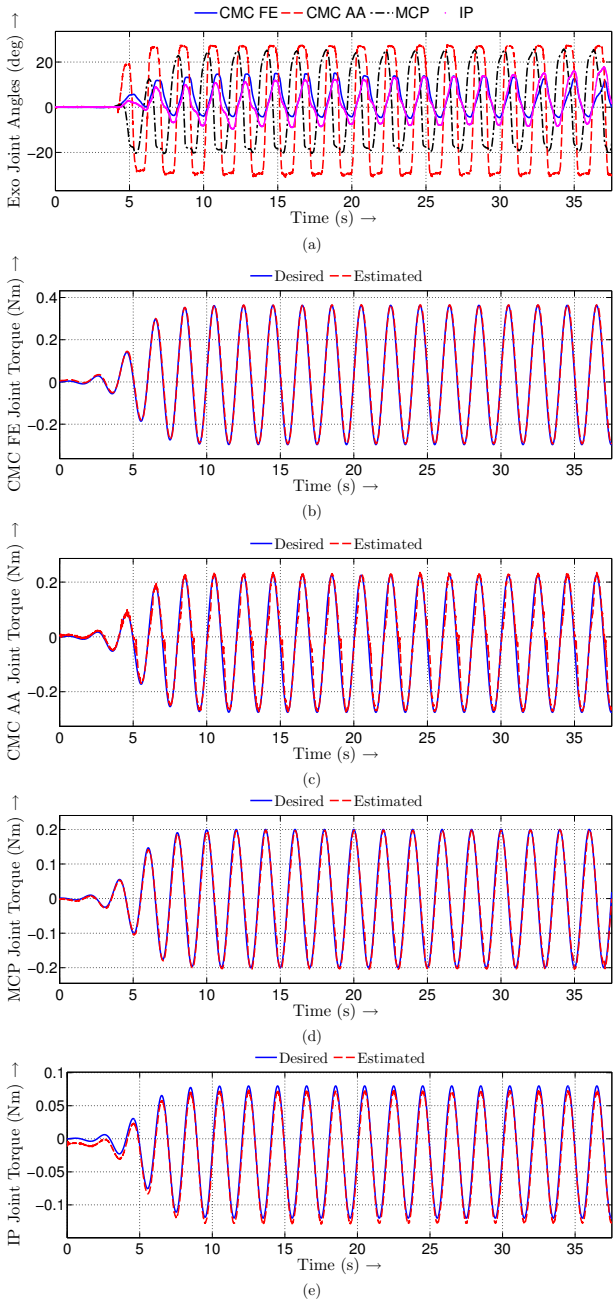

Figure 2.38: The joint torque tracking performance at the thumb exoskeleton joints for Subject 1. (a) Exoskeleton joint angles (b) torque at exoskeleton CMC FE joint, (c) torque at exoskeleton CMC AA joint, (d) torque at exoskeleton MCP joint and (e) torque at exoskeleton IP joint.

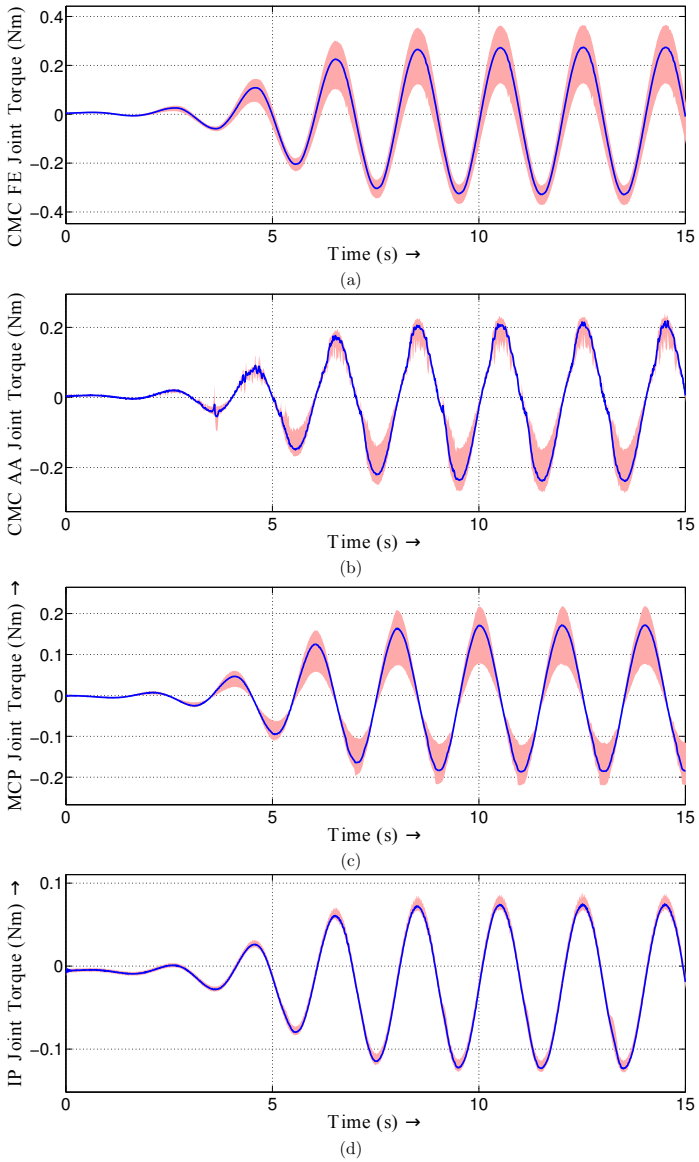

Figure 2.39: The joint torque envelope (shaded region) and mean joint torque (solid line) trajectory at the thumb exoskeleton joints for the four subjects. (a) Torque at exoskeleton CMC FE joint, (b) torque at exoskeleton CMC AA joint, (c) torque at exoskeleton MCP joint and (d) torque at exoskeleton IP joint. The joint torque envelope refers to the area between the maximum and minimum joint torque trajectory considering the torque trajectories of the four subjects.

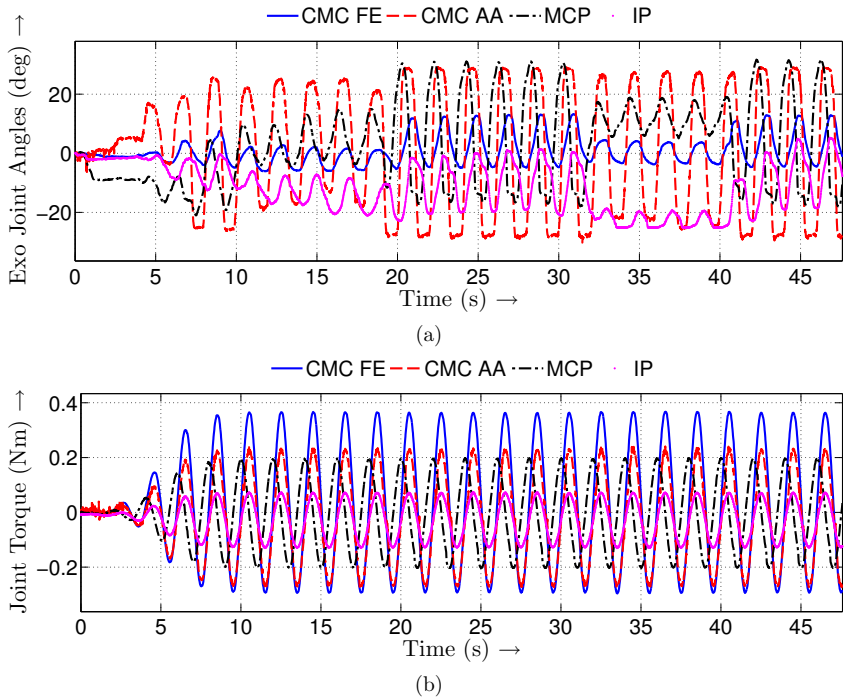

Figure 2.40: The joint torque tracking performance at the thumb exoskeleton joints when external disturbance is applied on the system for Subject 1. (a) Exoskeleton joint angles (b) torque at the four exoskeleton joints.

the external environment with which the exoskeleton is interacting.

2.3.5 Discussion

We presented a novel thumb exoskeleton with Bowden-cable-based SEAs that accomplishes the stated design objectives of accurate and stable bidirectional torque control of each thumb joint individually, kinematically compatible motion at the four thumb joints, large workspace with thumb and low weight with capability for free movement of the hand during the operation of the device. Experiments with multiple human subjects showed that the de-

vice is capable of bidirectional torque control at each thumb joint individually. The kinematic transparency tests showed that the device is compatible with the natural motion at the four thumb joints. The experiments for evaluation of the workspace showed that the device provides a large workspace with the thumb (retains on average 85% of the thumb workspace). Finally, the Bowden cable based actuation mechanism with the use of SLS for manufacturing the prototype makes the design light in weight ($\sim$136 g), while also allowing for free motion of the hand with minimal resistance.

During the kinematic transparency tests, even though the subjects were asked to keep there wrist joint stationary, some observable motion was present, especially for motions where the CMC joint movement is involved as it was difficult for subjects to absolutely limit motion at the wrist joint in a timed trial. Any movement of the wrist joint would increase the range of motion as the ground coordinate frame is determined using the markers on the wrist. This motion was more constrained with the exoskeleton as an elastic band surrounded their wrist to keep the wireform structure in place. This might have also contributed to the slight reduction in the joint angles at the various joints during these experiments. The reduced range of motion with the exoskeleton in some regions is also partly due to the attachment interface that connects the exoskeleton to the thumb. The wireform structure though provides a good way to transfer the forces to the thumb metacarpal, restricts the motion at the CMC joint toward the palm to some extent. The velcro straps at the middle and distal phalanx are close to each other and therefore, reduces the

range of motion at the distal joint. Also, the velcro strap which connects the exoskeleton base to the hand reduces the abduction-adduction range of motion to some extent.

The torque control experiments showed that the device is able to control the torque even under significant external disturbance. Some reduction in range of motion was also observed due to the deformation of the flesh over the metacarpal on the palmar side with the application of force on the wireform structure. Overall, the subjects reported that the interaction with the device felt comfortable and it was effective in exercising their thumb. The variation in torque between the subjects was partly due to the inherent differences in the requirement of torque for their thumbs and partly because the device was fitted to their hand at slightly shifted locations based on their hand contour.

2.4 Hand Exoskeleton: Maestro

We named the hand exoskeleton as Maestro. The final design consists of identical index and middle finger modules and a thumb module to actively assist the three digits of the hand (Figure 2.41). There are total 8 actuators to actively assist the MCP and PIP joints of the index and middle finger and CMC, MCP and IP joints of the thumb. We target the rehabilitation of these digits as amputation of either index or middle finger is considered to result in a 20% loss of hand function, whereas the loss of ring or little finger reduces the functional capacity of the hand by only 10% [149]. Furthermore, there is an estimated 40% loss in the functional capacity of hand with the amputation of

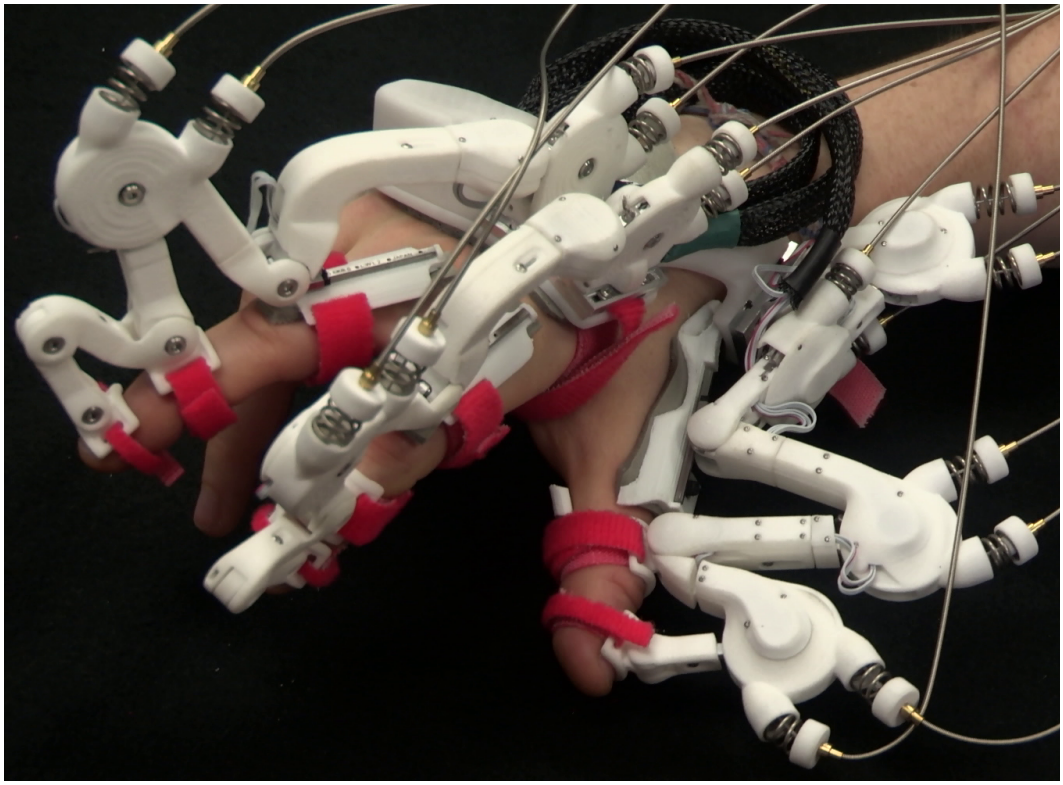

Figure 2.41: Hand exoskeleton prototype donned by a subject for experimentation.

thumb. These percentages agree with the observation that most manual tasks can be accomplished with three or four digits, provided that one of these digits is the thumb [74]. [80] evaluated the percentage contribution of static grip force to total grip force for the index, middle, ring and little fingers to be 42%, 27.4%, 17.6% and 12.9%, respectively. Furthermore, they reported that these percentages remained relatively constant as the weight of an object increased from 200 to 800 g. This suggests that the heavier the weight being lifted, the larger the contributions of the index and middle finger to grip force. As the grip

mode changed from five to four to three fingers, the total grip force increased, but the contribution of the index finger remained fairly constant at around 43% and so the force produced by the little and ring finger are generated by the middle finger. Considering all these facts, we focus on the rehabilitation of the index and middle fingers and thumb using our hand exoskeleton.

Chapter 3

Advanced Control

In this chapter, we present two different types of controllers that are based on learning subject-specific models of the exoskeleton joint torques required to control the device.

3.1 Learned Force-field Control

The goal of this controller is to assist the subject in flexion-extension motion of the index finger with a coordinated motion at the finger MCP and PIP joints. Force-field control creates a tunnel like force-field around the target path, which guides the limb motion along the desired joint angle trajectory [23, 71]. One important aspect of this controller is that the reference trajectory and therefore, the control input torque is only a function of the current state of the system and not of time explicitly. In this work, we propose the use of neural network to learn the assistance along the path and then use the trained network to provide the assistance needed at any location in the joint angle space (Fig. 3.1). Such a controller accurately learns the specific needs of a subject and reproduces accurate torque while assisting the subject.

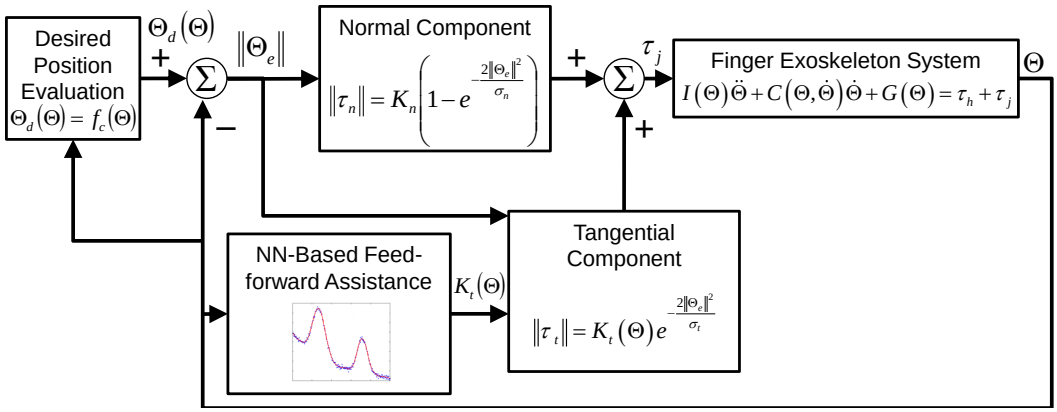

Figure 3.1: Overview of the learned force-field control implemented on the index finger exoskeleton.

3.1.1 Subject-specific Data

To obtain the exoskeleton joint torques variation with respect to the exoskeleton joint angles needed for a specific subject (Fig. 3.2(e)), we control the exoskeleton using impedance control [2], with the goal of executing sinusoidal motion at the finger joints, which closely represents the finger joint motion during different tasks [78], by gradually increasing impedance. The exoskeleton torque varies in a closed contour as the exoskeleton joint angle varies, both at the exoskeleton MCP and PIP joints (Fig. 3.2(c)). This is because the finger joint torque shows hysteresis due to viscous and frictional dissipation [46]. Also, the target trajectory in joint angle space is a line segment for the sinusoidal motion at the finger joints (Fig. 3.2(d)).

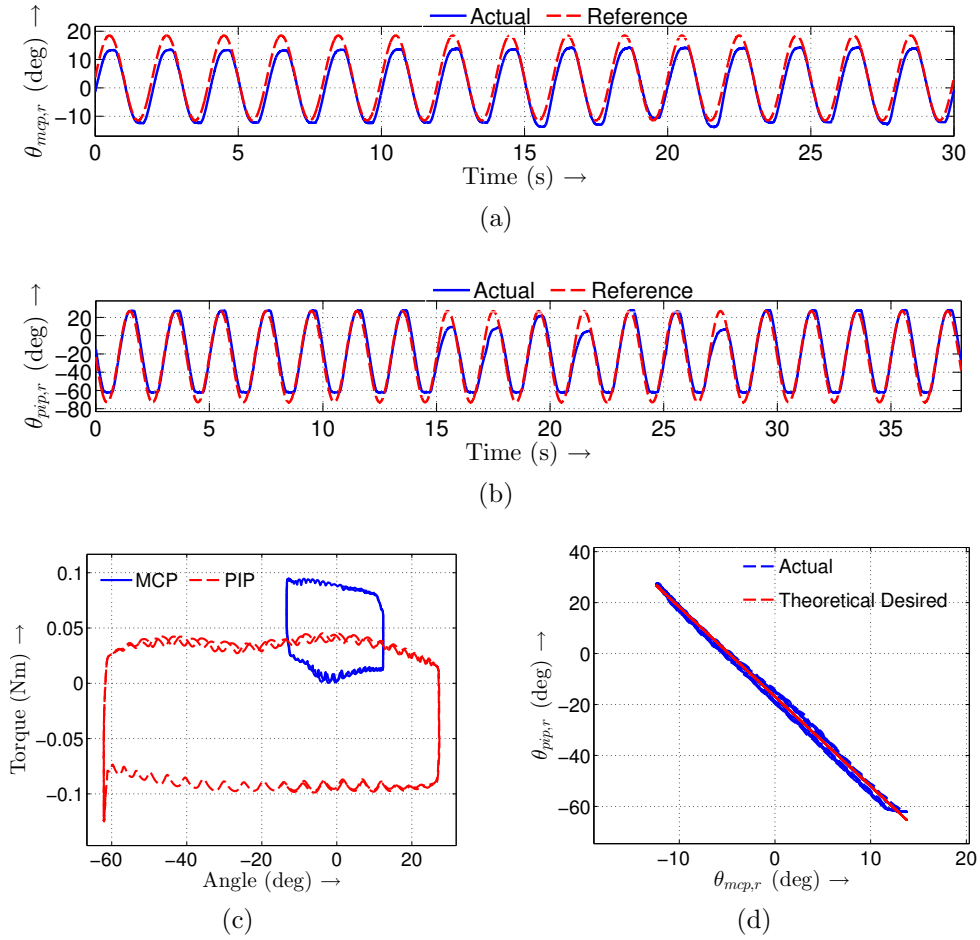

Figure 3.2: Results from the impedance control of the index finger exoskeleton with sinusoidal desired trajectories at the exoskeleton MCP and PIP joints. (a) Exoskeleton MCP joint relative angle tracking, (b) exoskeleton PIP joint relative angle tracking, (c) exoskeleton joint torque variation with respect to the respective exoskeleton joint angle at the MCP and PIP joints and (d) exoskeleton MCP joint angle variation with respect to the exoskeleton PIP joint angle.

3.1.2 Learning System Dynamics

A neural network with one hidden layer having three perceptrons is used to learn the required applied torques at the two actuated exoskeleton joints

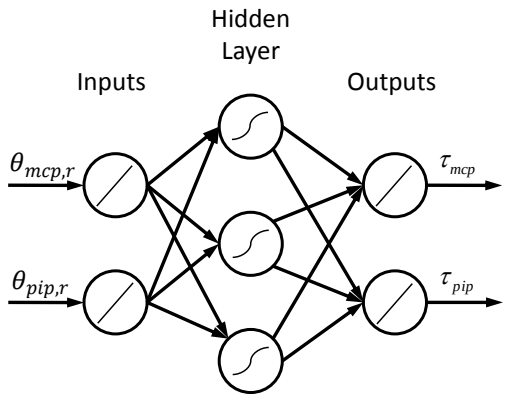

Figure 3.3: The single hidden layer neural network having three perceptrons for predicting the exoskeleton joint torques given the exoskeleton joint angles for learned force-field control.

given the angular position of the two exoskeleton joints (Fig. 3.3). Since, the torque-angle trajectory is a closed curve, two different networks are learned, one for flexion and the other for extension motion. We use linear transfer function for the input and output layers and a hyperbolic tangent sigmoid transfer function for the perceptrons in the hidden layer. We use hyperbolic tangent sigmoid as the transfer function, as some studies have shown that the networks with these functions are more generalizable [169] and perform better than the networks with other types of transfer functions [77, 108].

3.1.3 Force-field Control

The high level force-field controller generates a torque vector (τ) that has a normal ($\tau_{\mathbf{n}}$) and a tangential ($\tau_{\mathbf{t}}$) torque component. The torque vector (τ) contains the torques applied at the exoskeleton MCP and PIP joints (Eq. (3.1)). The normal component is responsible for pushing the finger towards the

desired trajectory and the tangential component assists in tracking the desired trajectory. We learn the gain for the tangential component of the force field assistance ($\mathbf{K_t}(\mathbf{\Theta})$) using the neural network to guide the finger motion along the desired joint angle trajectory.

$$\tau = \tau_{\mathbf{n}} + \tau_{\mathbf{t}} \tag{3.1}$$

$$\begin{aligned} \|\tau_{\mathbf{n}}\| &= \mathbf{K_n}\left(1 - e^{-\frac{2\|\mathbf{\Theta}_{\boldsymbol{e}}\|^2}{\sigma_n}}\right) \\ \|\tau_{\mathbf{t}}\| &= \mathbf{K_t}(\mathbf{\Theta})e^{-\frac{2\|\mathbf{\Theta}_{\boldsymbol{e}}\|^2}{\sigma_t}} \end{aligned} \tag{3.2}$$

where $\mathbf{K_n}$ and $\mathbf{K_t}(\mathbf{\Theta})$ are the gain vectors for the normal and tangential force field assistance, respectively and $\mathbf{\Theta}$ is the current angular joint position vector of the exoskeleton joints. $||\mathbf{\Theta}_{\boldsymbol{e}}||$ is the distance between the current exoskeleton joints position and the closest point on the desired joint space trajectory. Two force field tunnels with diameters σ_n and σ_t are created around the desired trajectory in the joint angle space by Eq. (3.2). The magnitude of the normal component increases to $\mathbf{K_n}$ outside of the tunnel and gradually reduces to zero as one approaches the desired trajectory inside the tunnel. The magnitude of the tangential component, on the other hand, is close to zero outside the tunnel and gradually increases to $\mathbf{K_t}(\mathbf{\Theta})$ as one approaches the desired trajectory inside the tunnel. An analytical expression is obtained for $\mathbf{\Theta}_{\boldsymbol{e}}$ by projecting the current exoskeleton joint angle state on the desired line segment contour ($\mathcal{C}$) (Eq. (3.3)).

$$\|\boldsymbol{\Theta_e}\| = \min_{\boldsymbol{\Theta_d} \in \mathcal{C}} \|\boldsymbol{\Theta} - \boldsymbol{\Theta_d}\| \tag{3.3}$$

Since, two different networks are learned for flexion and extension motion, a switching between the two networks is performed based on whether the upper ($\boldsymbol{\Theta}_{ub}$) or lower ($\boldsymbol{\Theta}_{lb}$) exoskeleton joint angle limit is crossed (Eq. (3.4)).

$$\mathbf{K_t}(\boldsymbol{\Theta}) = \begin{cases} \mathbf{K_{tf}}(\boldsymbol{\Theta}), & \text{if } \boldsymbol{\Theta} \leq \boldsymbol{\Theta}_{lb} \\ \mathbf{K_{te}}(\boldsymbol{\Theta}), & \text{if } \boldsymbol{\Theta} \geq \boldsymbol{\Theta}_{ub} \end{cases} \tag{3.4}$$

where $\mathbf{K_{tf}}(\boldsymbol{\Theta})$ and $\mathbf{K_{te}}(\boldsymbol{\Theta})$ are the gain vectors for the tangential component of the force field assistance for the flexion and extension motion, respectively, as learned using neural network.

One major limitation of the learned force-field control is that the NN mapping is static. Torque requirement is not updated with changes in the trajectory motion frequency or inherent changes in the required finger torque due to the increased assistance provided by the subject with improvement in motor capabilities or changes in finger passive properties. So, next we implement an assist-as-needed controller, which is adaptive in nature and modifies the feed-forward assistance based on the trajectory tracking error.

3.2 Adaptive-assistance-based Control

Adaptive assist-as-needed control learns a dynamic model of the coupled finger-exoskeleton system and patient's ability and effort in real-time for a specific subject [172] (Fig. 3.4).

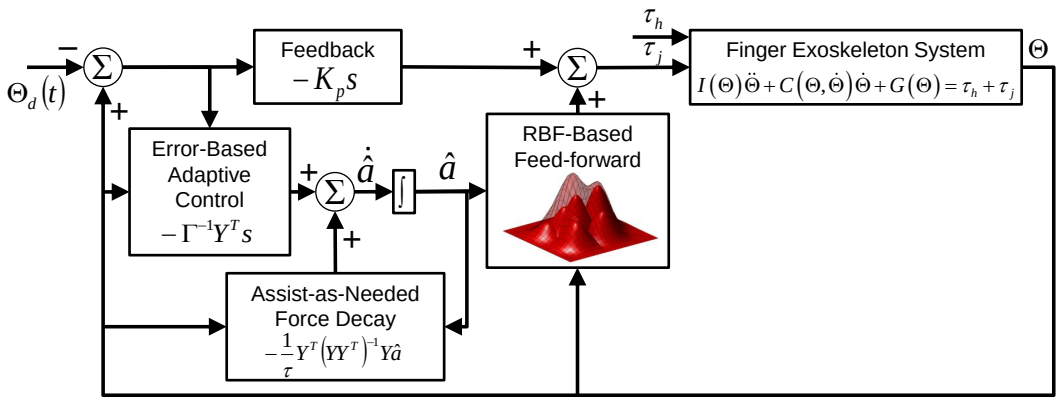

Figure 3.4: Overview of the adaptive-assistance-based control implemented on the index finger exoskeleton.

3.2.1 Adaptive Controller for Learning Coupled System Dynamics

The coupled dynamics of the finger exoskeleton system can be expressed as in Eq. (3.5).

$$\mathbf{I}(\mathbf{\Theta})\ddot{\mathbf{\Theta}} + \mathbf{C}(\mathbf{\Theta}, \dot{\mathbf{\Theta}})\dot{\mathbf{\Theta}} + \mathbf{G}(\mathbf{\Theta}) = \tau_{\mathbf{j}} + \tau_{\mathbf{h}} \tag{3.5}$$

where $\mathbf{\Theta}$ is the 2×1 vector of exoskeleton MCP and PIP joint angular position, $\boldsymbol{I}(\mathbf{\Theta})$ is the inertia matrix, $\boldsymbol{C}(\mathbf{\Theta}, \dot{\mathbf{\Theta}})$ is the matrix representing Coriolis and centrifugal terms, $\mathbf{G}$ is the vector representing gravitational terms, $\tau_{\mathbf{j}}$ is the 2×1 vector representing the torques applied by the actuated exoskeleton MCP and PIP joints and $\tau_{\mathbf{h}}$ is the 2×1 vector representing the torques applied by the human subject at the exoskeleton MCP and PIP joints.

For the joint angle tracking, a sliding surface ($\mathbf{s}$) can be defined as in Eq. (3.6).

$$\mathbf{s} = \dot{\tilde{\mathbf{\Theta}}} + \Lambda\tilde{\mathbf{\Theta}} = (\dot{\mathbf{\Theta}} - \dot{\mathbf{\Theta}}_d) + \Lambda(\mathbf{\Theta} - \mathbf{\Theta}_d) \tag{3.6}$$

where $\tilde{\mathbf{\Theta}} = \mathbf{\Theta}(t) - \mathbf{\Theta}_{\boldsymbol{d}}(t)$ is the tracking error with $\mathbf{\Theta}_{\boldsymbol{d}}(t)$ as the desired joint angle trajectory. Λ is a 2×2 constant, positive definite and symmetric matrix.

Since, for the finger-exoskeleton system the contribution of inertial effects is small, we only consider the position-dependent terms in the system dynamics Eq. (3.5) and define a position-dependent regressor matrix. Since, the system dynamics is linear in terms of the system parameters, the estimated system dynamics can be expressed as a product of the unknown system parameters ($\hat{\mathbf{a}}$) and the regressor matrix ($\mathbf{Y}(\mathbf{\Theta})$) (Eq. (3.7)).

$$\hat{\mathbf{G}}(\mathbf{\Theta}) - \hat{\tau}_{\mathbf{h}} = \mathbf{Y}(\mathbf{\Theta})\hat{\mathbf{a}} \tag{3.7}$$

The torque control law for the system is then given by Eq. (3.8)

$$\tau_{\mathbf{j}} = \mathbf{Y}(\mathbf{\Theta})\hat{\mathbf{a}} - \mathbf{K_p}s \tag{3.8}$$

where $\mathbf{K_p}$ is a symmetric positive definite feedback gain matrix.

We approximate the arbitrary torque surface with respect to the exoskeleton joint angles using radial basis function (RBF) defined in Eq. (3.9).

$$\phi_n = e^{-\dfrac{\|\mathbf{\Theta} - \mu_{\mathbf{n}}\|^2}{2\sigma^2}} \tag{3.9}$$

We use 25 RBFs to approximate the torque-angle relationship throughout the workspace by partitioning the rotational DOF into five equally spaced intervals at both the MCP and PIP joints of the exoskeleton. The regressor matrix is then given by Eq. (3.10).

$$\mathbf{Y}^{2\times 50} = \begin{bmatrix} \mathbf{\Phi}^T & \mathbf{0} \\ \mathbf{0} & \mathbf{\Phi}^T \end{bmatrix} \tag{3.10}$$

where $\mathbf{\Phi} = [\phi_1 \ \phi_2 \ \ldots \phi_{25}]$. The regressor matrix takes into account both the joint angles to determine the torque at each joint. The parameter update law is given by Eq. (3.11) and it can be shown using Lyapunov stability analysis that the controller is uniformly ultimately bounded with this update law [117].

$$\dot{\hat{\mathbf{a}}} = -\mathbf{\Gamma}^{-1}\mathbf{Y}^T\mathbf{s} \tag{3.11}$$

3.2.2 Assist-as-needed Controller Modification

Experiments have shown that subjects slack when full assistance is provided through the controller, which inhibits rehabilitation [172]. To account for this effect, the parameter update law is modified as in Eqs. (3.12) and (3.13) to decay the applied torques when errors are small as proposed in [172].

$$\frac{\partial}{\partial t}\left(\mathbf{Y}\hat{\mathbf{a}}\right) = \mathbf{Y}\dot{\hat{\mathbf{a}}} = -\frac{1}{\tau}\mathbf{Y}\hat{\mathbf{a}} \tag{3.12}$$

$$\dot{\hat{\mathbf{a}}} = -\Gamma^{-1}\mathbf{Y}^T\mathbf{s} - \frac{1}{\tau}\mathbf{Y}^T\left(\mathbf{Y}\mathbf{Y}^T\right)^{-1}\mathbf{Y}\hat{\mathbf{a}} \tag{3.13}$$

where τ is the time constant for the parameter decay.

3.3 Experiments

Index finger flexion-extension motion experiments were carried out to validate the developed controllers and to understand the advantages and disadvantages of the two. A healthy subject (male, age 29 years) participated in the study. While carrying out these experiments, the motion of the subject's finger is occasionally impeded to assess the reaction of the controller and how safe is the device with each.

3.3.1 Learned Force-field Control

In this experiment, a subject's torque-angle relationship is learned using the developed neural network and the trained subject-specific network is then used for force-field control of the index finger with the desired target trajectory in the joint angle space. The subject is asked to keep the finger passive while the torque data is collected for training the neural network. Once, the model is learned, the subject is asked to follow the motion, while the controller is assisting the subject with the applied force-field.

3.3.2 Adaptive-assistance-based Control

In this experiment, the performance of the controller in terms of adapting to the requirement of the subject and thereby, resulting in improved joint angle trajectory tracking performance is assessed. Sinusoidal joint angle trajectory is used as the desired motion at the two joints.

3.3.2.1 Healthy Subject Experiments

First, two experiments with the unaltered index finger module are carried out to understand if the system adapts as per the needs of the subject. For the first experiment, the subject is asked to keep the finger passive and the controller adapted to the joint torque requirement of the subject. For the second experiment, the subject was asked to impede the motion of the exoskeleton to assess how quickly the controller reacted to the changed torque requirement.

3.3.2.2 Stiffened Exoskeleton Subject Experiments

Stiffening of the finger PIP joint is a common phenomenon observed in several hand impairments [57, 61, 84]. To validate the effectiveness of the adaption algorithm, an exoskeleton stiffened at the PIP joint with rubber bands is used for the experiment. For this experiment, the subject was asked to keep the finger passive and an assessment of whether the controller is able to adapt to the changed system configuration is carried out.

3.4 Results

In this section, we present the neural network fitting statistics and the performance of the two controllers as assessed through the experiments.

3.4.1 Learned Force-field Control

The controller performance for the learned force-field control depends on how closely the neural network is able to predict the required exoskeleton joint torques given the exoskeleton joint angles.

3.4.1.1 Neural Network Fitting Results

The fitting results show that the mean squared error for the trained network is of the order of 10^{-6} for both flexion and extenion networks under training, validation and testing (Table 3.1). The neural network fitting shows that the neural network is able to predict the exoskeleton joint torques given the exoskeleton joint angles accurately (Fig. 3.5).

Table 3.1: Model fitting statistics (mean squared error) for the neural networks learned to represent the torque-angle relationship for the flexion and extension motions.

Motion	Training ($\times 10^{-6}$)	Validation ($\times 10^{-6}$)	Testing ($\times 10^{-6}$)	Overall ($\times 10^{-6}$)
Flexion	3.64	3.87	3.47	3.65
Extension	5.88	8.90	4.38	6.11

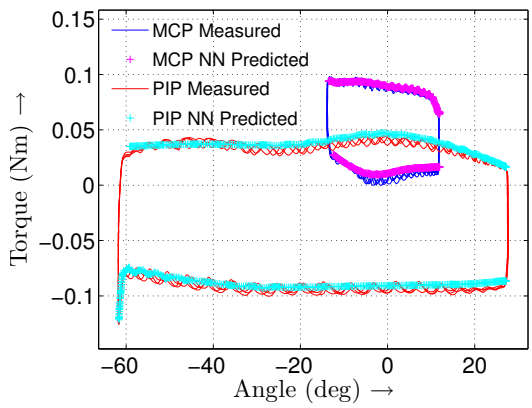

Figure 3.5: Comparison of the learned neural-network-based predicted exoskeleton joint torques with those estimated by the series elastic actuator controller in real-time (labeled as measured). (Best viewed in color)

3.4.1.2 Hand Exoskeleton Control

Results show that the system is able to trace the desired trajectory in the exoskeleton joint space with low error (Fig. 3.6(e)). The large deviation in few trials from the theoretical desired trajectory is due to external blocking of the finger motion to assess how the controller reacts to external disturbance, which may be present due to the nature of finger impairment (Section 1.2.3).

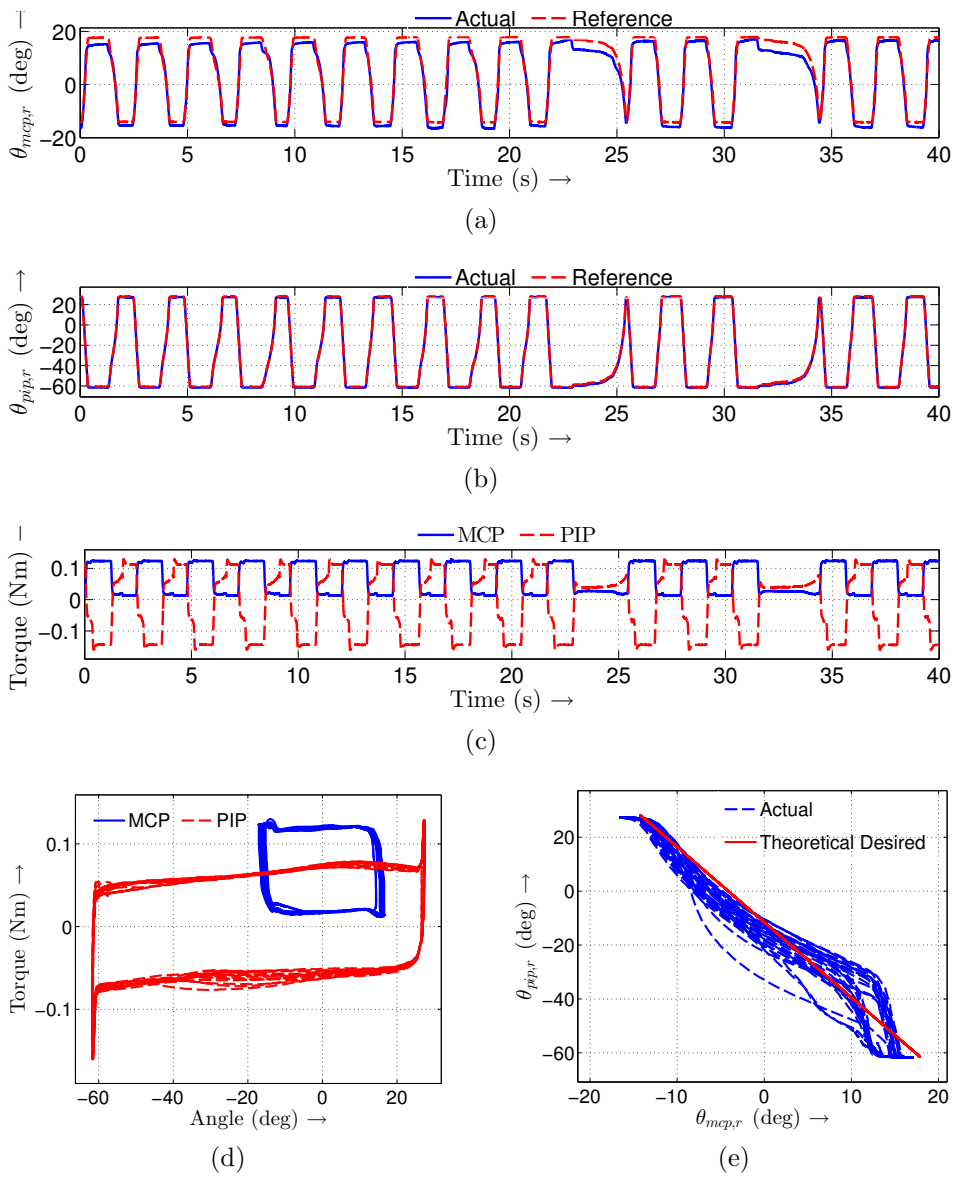

Figure 3.6: Results from force-field control of the index finger exoskeleton with a linear relationship between MCP and PIP joint angles as the desired trajectory (a) Exoskeleton MCP joint relative angle tracking, (b) exoskeleton PIP joint relative angle tracking, (c) exoskeleton joint torque with respect to the respective relative joint angle and (d) exoskeleton relative PIP joint angle with respect to relative MCP joint angle.

Also, force-field control does not apply excessive torques when the motion is stalled at time 22 sec and 31 sec (Figs. 3.6(a),(b) and (c). However, the velocity with which the trajectory is traced is not accurately controlled (Figs. 3.6(a) and (b)). Force-field control allows for coordinating between joints and is good for training for the tasks that only need joint angle coordination, while not reacting to any uncertain external torques that might act on the system.

3.4.2 Adaptive-assistance-based Control

Both the healthy subject and stiffened exoskeleton experiments demonstrate the effectiveness of adaptive-assistance-based control.

3.4.2.1 Healthy Subject Experiments

For the first experiment, results show that the system is able to adapt to the torque requirement of the subject. The feed-forward component of the torque increases gradually, while the feedback component reduces both at the MCP and the PIP joints (Figs. 3.7(a) and (b)). The variation of unknown learned parameters show that the parameters tend to converge to their desired values (Figs. 3.7(c) and (d)). The root mean square (RMS) tracking error for the initial and final 10 seconds show that the error reduced from 5° to 3° at the MCP joint and from 3.5° to under 2° at the PIP joint showing that the learned model assisted in improving the tracking performance (Figs. 3.7(g) and (h)).

For the second experiment, the results show that when the finger motion is impeded by the subject, the controller reacted by increasing the applied

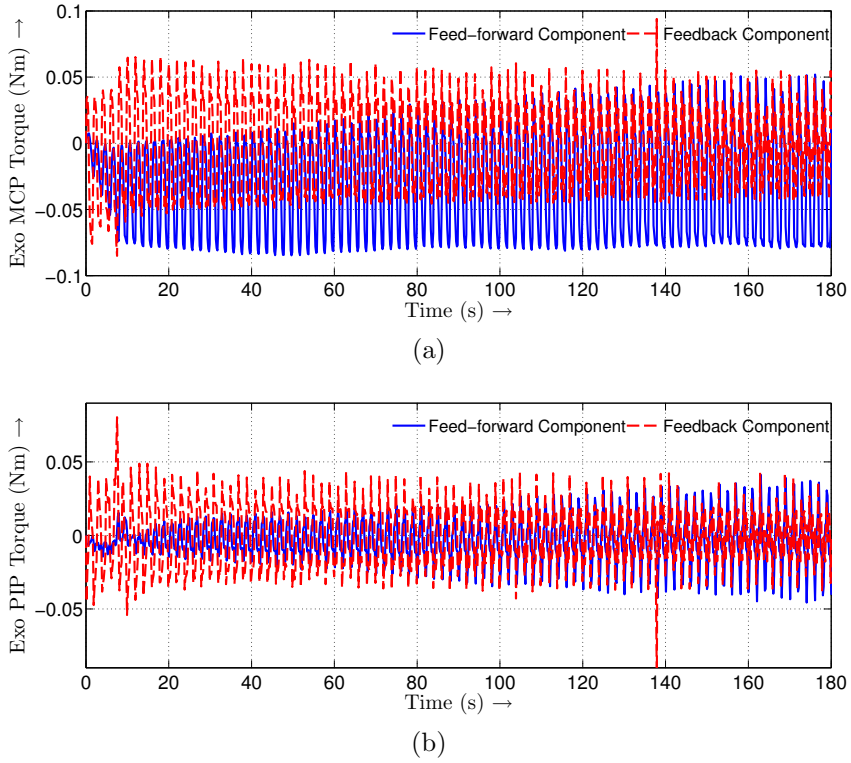

Figure 3.7: Results from adaptive assist-as-needed control experiments of the index finger exoskeleton with a healthy subject. (a) Exoskeleton MCP joint feed-forward and feedback torque component, (b) exoskeleton PIP joint feed-forward and feedback torque component, (c) parameter adaptation results for 5 out of 25 parameters ($\mu_{\mathbf{n}} = [\mu(n) \ -70°]^T$) that contributed to the MCP joint torque (d) parameter adaptation results for 5 out of 25 parameters ($\mu_{\mathbf{n}} = [-30° \ \mu(n)]^T$) that contributed to the PIP joint torque, (e) exoskeleton joint torque variation with respect to the joint angles, (f) exoskeleton MCP angle with respect to the PIP joint angle, (g) MCP joint tracking error for the initial and final 10 seconds and (h) PIP joint tracking error for the initial and final 10 seconds. (Best viewed in color)

torque (at time 66 sec and 86 sec in Fig. 3.8). Also, as soon as the externally applied torque is removed the controller torque returned to the original value demonstrating that the controller is quite reactive and can quickly adapt to

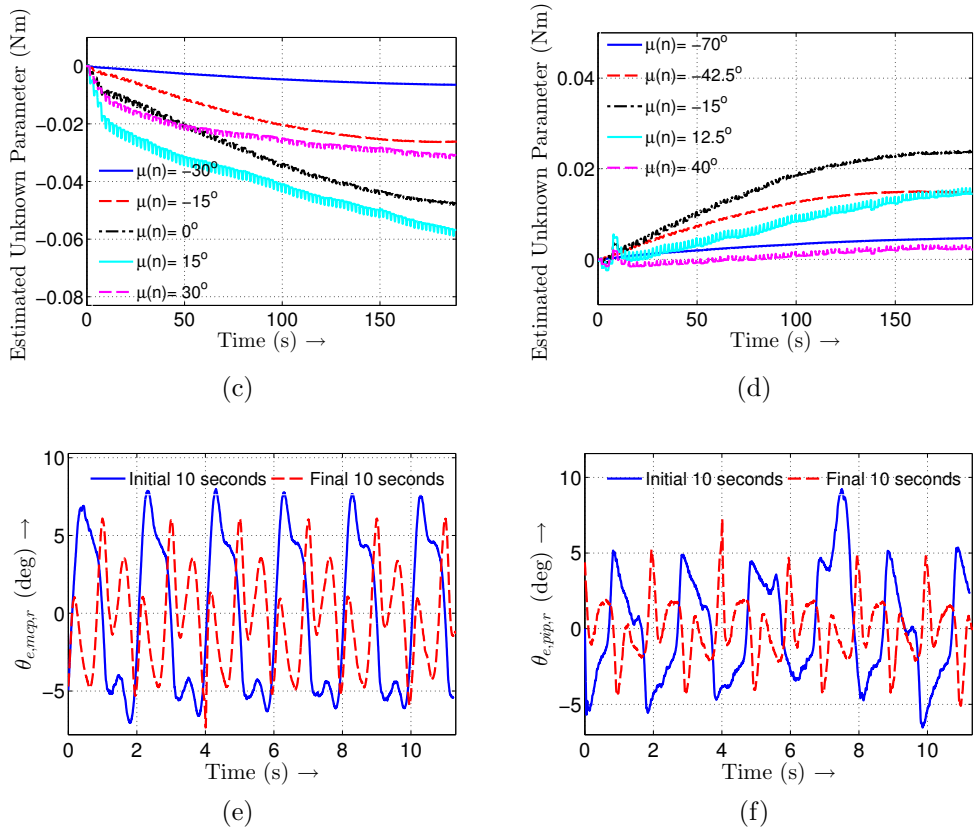

Figure 3.7: Results from adaptive assist-as-needed control experiments of the index finger exoskeleton with a healthy subject. (a) Exoskeleton MCP joint feed-forward and feedback torque component, (b) exoskeleton PIP joint feed-forward and feedback torque component, (c) parameter adaptation results for 5 out of 25 parameters ($\mu_{\mathbf{n}} = [\mu(n) \ -70°]^T$) that contributed to the MCP joint torque (d) parameter adaptation results for 5 out of 25 parameters ($\mu_{\mathbf{n}} = [-30° \ \mu(n)]^T$) that contributed to the PIP joint torque, (e) exoskeleton joint torque variation with respect to the joint angles, (f) exoskeleton MCP angle with respect to the PIP joint angle, (g) MCP joint tracking error for the initial and final 10 seconds and (h) PIP joint tracking error for the initial and final 10 seconds. (Best viewed in color) (contd.)

the changing requirements of a subject. However, when the finger motion is impeded using an external disturbance the system exhibited increased magni-

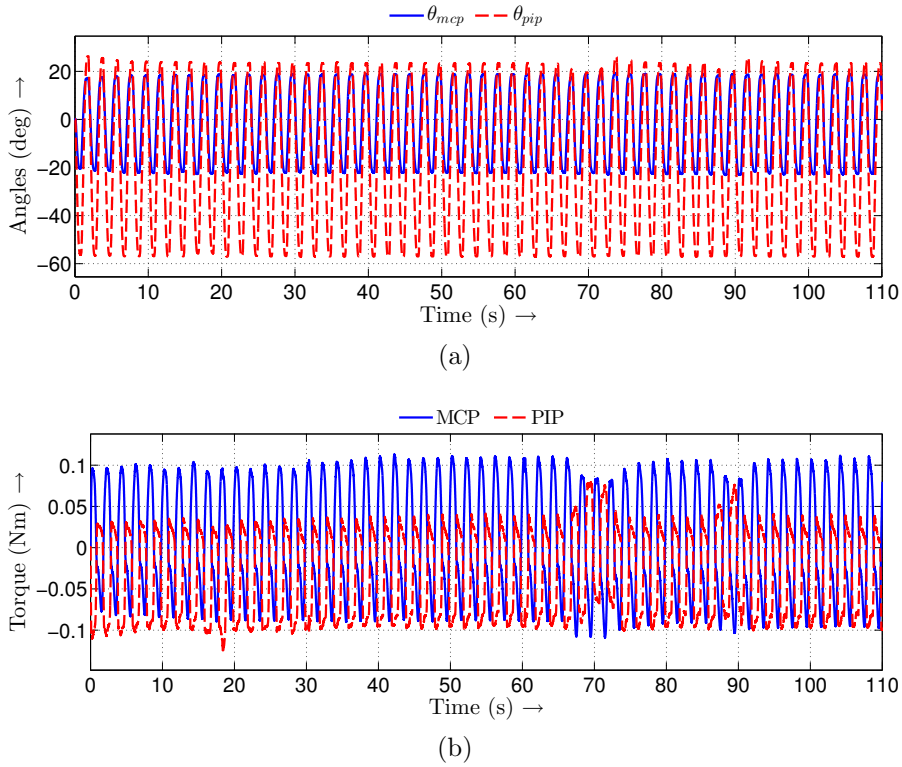

Figure 3.8: Adaptive assist-as-needed control experiment with impeded finger motion at time 66 sec and 86 sec. (a) MCP and PIP exoskeleton joint angle with respect to time and (b) MCP and PIP joint torques with respect to time. The joint torque magnitude increases when the finger motion is impeded.

tude of torques both at the MCP and PIP joints, which might not be safe in case of accidental locking of a joint.

3.4.2.2 Stiffened Exoskeleton Subject Experiments

Experiments with the stiffened exoskeleton also showed similar results (Figs. 3.9). An altered and increased magnitude of the required torque is observed at the MCP and PIP joint, respectively, due to stiffening of the

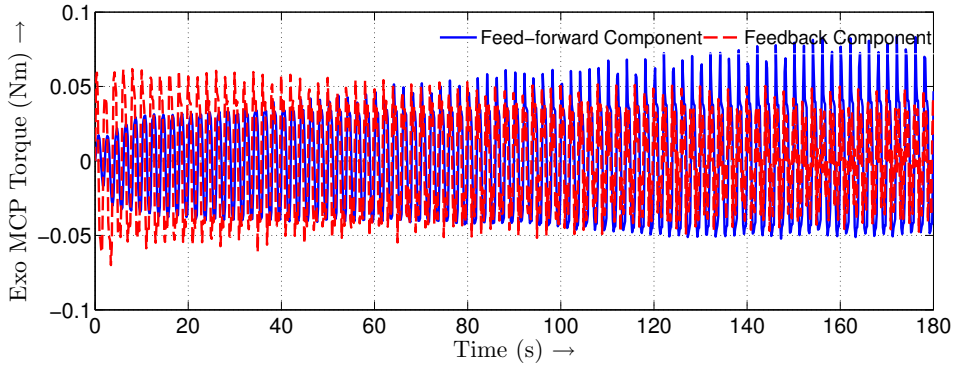

(a)

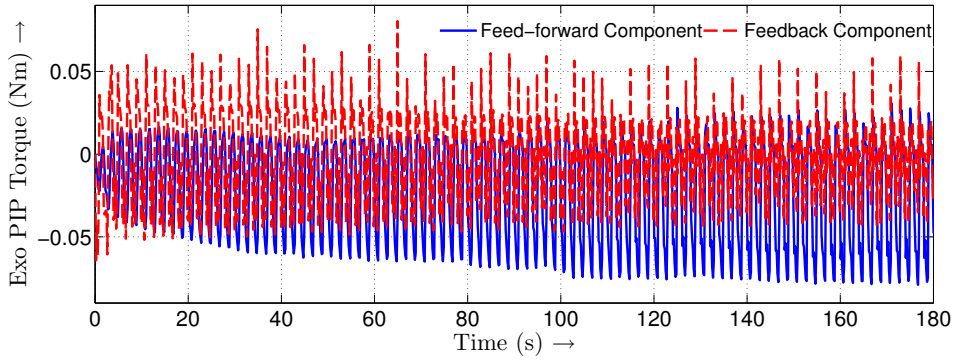

(b)

Figure 3.9: Results from adaptive assist-as-needed control experiments of the index finger exoskeleton with stiffened exoskeleton joints. (a) Exoskeleton MCP joint feed-forward and feedback torque component, (b) exoskeleton PIP joint feed-forward and feedback torque component, (c) parameter adaptation results for 5 out of 25 parameters ($\mu_{\mathbf{n}} = [\mu(n) \ \ -70°]^T$) that contributed to the MCP joint torque (d) parameter adaptation results for 5 out of 25 parameters ($\mu_{\mathbf{n}} = [-30° \ \ \mu(n)]^T$) that contributed to the PIP joint torque, (e) exoskeleton joint torque variation with respect to the joint angles, (f) exoskeleton MCP angle with respect to the PIP joint angle, (g) MCP joint tracking error for the initial and final 10 seconds and (h) PIP joint tracking error for the initial and final 10 seconds. (Best viewed in color)

exoskeleton PIP joint showing that the system adapted to the changed configuration (Figs. 3.9(a) and (b)). RMS error for this case reduced from 5°

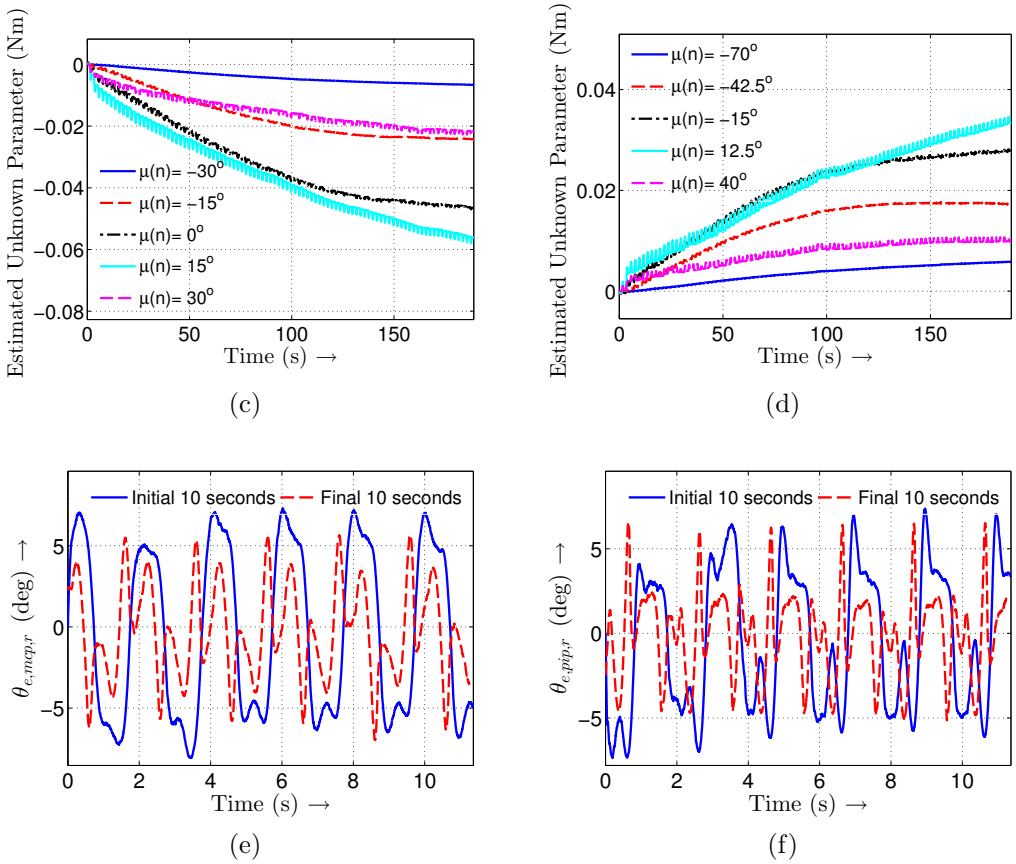

Figure 3.9: Results from adaptive assist-as-needed control experiments of the index finger exoskeleton with stiffened exoskeleton joints. (a) Exoskeleton MCP joint feed-forward and feedback torque component, (b) exoskeleton PIP joint feed-forward and feedback torque component, (c) parameter adaptation results for 5 out of 25 parameters ($\mu_{\mathbf{n}} = [\mu(n) \ \ -70°]^T$) that contributed to the MCP joint torque (d) parameter adaptation results for 5 out of 25 parameters ($\mu_{\mathbf{n}} = [-30° \ \mu(n)]^T$) that contributed to the PIP joint torque, (e) exoskeleton joint torque variation with respect to the joint angles, (f) exoskeleton MCP angle with respect to the PIP joint angle, (g) MCP joint tracking error for the initial and final 10 seconds and (h) PIP joint tracking error for the initial and final 10 seconds. (Best viewed in color) (contd.)

to under 3° for the MCP joint and from over 4° to 2.5° for the PIP joint (Figs. 3.9(g) and (h)).

Chapter 4

Development of a Framework for Rehabilitation

Stroke often leads to a persistent impairment of the upper or lower limbs or both for a majority of the survivors [111]. Over 82% of the stroke survivors are left severely impaired as conventional therapies for stroke rehabilitation could only provide limited recovery. Robotic devices have been developed to aid in stroke rehabilitation, however, robotic therapy have so far shown similar outcomes [29]. This is because current robot-assisted therapy makes limited use of the general motor learning and neuro-rehabilitation principles, which have been experimentally verified over the years. An understanding of what type of task, robot control algorithm and feedback would result in maximum recovery could benefit robot-assisted rehabilitation.

Our idea is to first understand the key factors that affect motor learning and neuromuscular rehabilitation and then incorporate those in the robot control algorithm to give rise to a rehabilitation environment that is optimized for each subject and is adaptively tailored based on his or her performance and needs. Challenge Point Hypothesis and also related experiments suggest that optimal learning occurs when the challenge is matched with the skill level of

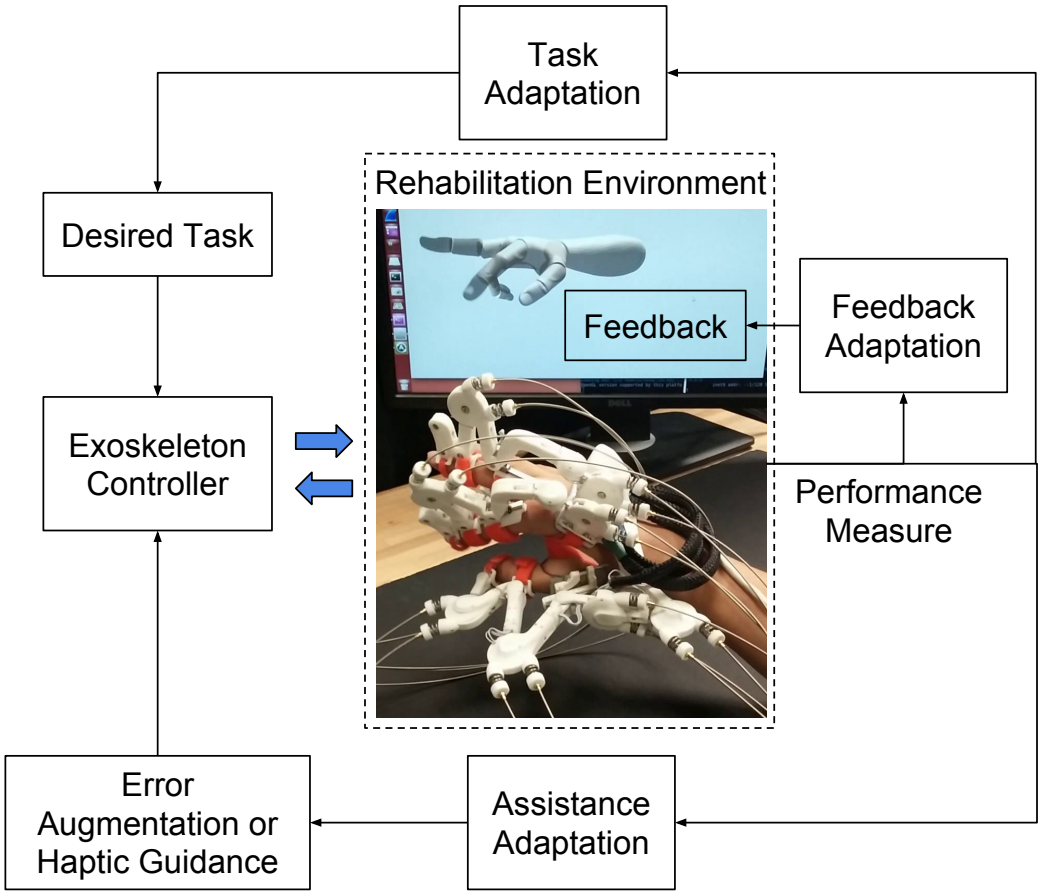

Figure 4.1: An overview of the proposed framework for robot-assisted motor (re)-learning.

the performer [55]. So far challenge in robotic rehabilitation has been modulated by only adjusting the amount of assistance provided by the robot during therapy. Experiments with this approach show that results are promising but there is limited success as just adjusting assistance may not be sufficient to affect true recovery. Task variability and augmented feedback have also been shown to affect motor learning and therefore can be used to modulate challenge

[106, 130].

We present a framework for performance-based modulation of challenge in this multi-dimensional space (task, assistance and feedback) on motor learning and re-learning during rehabilitation (Fig. 4.1). The framework is designed around the idea of providing an optimum rehabilitation environment to each subject by adapting the environment variables to provide a challenge level commensurate with the level of the skill of the subject. The rehabilitation environment consists of a human subject performing a functional task with a robotic device, while the framework provides some form of feedback (e.g. verbal, visual, or auditory). The performance on the task is assessed using measures that estimate the level of skill of the subject. The framework consists of continuous adaptation along the following three dimensions based on the performance of the subject on a functional task: (i) task adaptation to introduce sufficient variability in the task for keeping the task optimally challenging based on the skill level of the subject, (ii) assistance adaptation to provide a haptic guidance or an error augmentation training while smoothly transiting between the two based on the subject's skill level, and (iii) feedback adaptation to provide just the right amount of feedback to avoid reliance on feedback and instead encourage motor adaptation and learning.

One of the challenges in providing efficacious rehabilitation using robotic devices after a neuromuscular injury such as stroke is that how motor (re)-learning is affected by the various factors is currently unknown. To gain a better understanding of motor (re)-learning, we address the question of how

simultaneous adaptations along the three different dimensions affect motor learning using the framework. We carry out human subject experiments using the hand exoskeleton to test if simultaneous adaptation of task, assistance and feedback can modulate challenge and affect motor learning.

4.1 Limitations of Existing Control Strategies for Rehabilitation

Several robot control strategies have been developed for rehabilitation of both the upper and the lower limbs, including assistive, challenge-based, haptic simulation and coaching [102]. A majority of the work has been done on implementing assistive strategies, including impedance-, force-field- and EMG-based controllers. Some adaptive control techniques (e.g. adaptive assist-as-needed) have also been developed that provide subject-specific assistance by modifying the control parameters [3, 172]. However, clinical studies carried out on stroke subjects using these control strategies have shown only very limited to no improvement over conventional therapy [29]. We believe that one of the reasons for the limited effectiveness of the existing control strategies is that so far these are primarily focused on only one of the aspects of what constitutes a rehabilitation environment, i.e., assistance. We first seek to understand all the important factors that affect motor learning and neuromuscular rehabilitation and incorporate those in the robot control algorithm to give rise to an optimum rehabilitation environment that is subject-specific and is adaptively tailored based on his or her performance and needs. Next, we review the factors that

have been shown to affect motor learning and neuromuscular rehabilitation.

4.2 Factors Affecting Motor Learning and Neuromuscular Rehabilitation

There are three important factors that have been shown to affect motor learning and neuromuscular rehabilitation. This includes the type and variability of task, level and nature of assistance, and frequency and modality of feedback. Practice variability hypothesis states that motor learning is better when a skill is performed in a variety of ways or contexts rather than one way [43, 65, 130, 142, 162, 177]. Even though practice variability produces more error during practice and learning, several studies have shown that introducing task variability in the acquisition session improves performance in subsequent sessions [83, 140]. This is because a constant task becomes monotonous and discourages motor learning by leading to memorization of the time sequence of muscle forces rather than actual learning of the skill. Also, some studies have shown that task-related functional training leads to long-lasting and better outcomes [14, 50, 66, 87].

Another important factor that influences motor learning is error augmentation or haptic guidance. Guidance refers to a variety of techniques including assisting the learner by providing appropriate amounts of forces or torques or preventing incorrect movements by means of physical limitations on the apparatus [133]. Error augmentation, on the other hand, refers to artificially increasing movement error during practice. It has been shown in the lit-

erature that many forms of learning, including motor learning, are error-driven processes [139, 153]. Milot et al. carried out a comparison study to understand whether error augmentation or haptic guidance leads to better motor learning for a timing-based task with healthy subjects [105]. Their study showed that error augmentation training was more beneficial for the skilled subjects whereas haptic guidance training was more effective for the less skilled subjects. Patton et al. also carried out a study to understand motor adaptation in chronic stroke survivors during the execution of planar multi-joint movements that are disturbed by a force-field [114]. Their study showed that enhancing trajectory errors by the use of force fields induced better learning compared to reducing trajectory errors or providing no force field in individuals with stroke. This shows that there is a need to develop robot control algorithms that provide the right type of training based on the skill level of the subject for the task at hand and adapt as the skill level of the subject changes. This conclusion is also in line with the challenge point hypothesis, which speculates that when optimal challenge is offered to the individuals based on their skill level, greater learning is achieved [55].

Augmented feedback has also been shown to play a significant role in motor learning in several studies [69, 106, 107, 143]. This type of feedback can be provided in the form of knowledge of results (outcome), knowledge of performance (e.g. quality or type of movement) or visual information (e.g. current and desired trajectory) about performance on the task. Some studies have shown that uncertainty in visual feedback determines the speed of motor

adaptation and that noisy visual feedback reduces the rate of adaptation [146, 168]. Furthermore, guidance hypothesis predicts that augmented feedback is beneficial for motor learning when used to reduce error, but detrimental when relied upon [131]. A heavily guiding form of feedback might be detrimental for learning. Also, practice with a high relative frequency of augmented feedback would be detrimental for learning. Thus, there is a need to provide augmented feedback that adapts based on the subject-specific performance on the task and becomes easy or difficult to interpret to encourage motor learning [171].

4.3 Need for a Torque-based Task

Force-control based strategies (e.g. impedance, admittance, assist-as-needed [23]) can be more effective for rehabilitation of both the upper [16, 33, 118] and lower limbs [102] than pure position-based control [58]. However, even though force-controlled devices have been developed for both the upper and lower limbs, these devices have so far focused on training for accuracy of movement and correlating position tracking accuracy with degree of rehabilitation [76, 172]. Studies have shown that the ability to dynamically control fingertip force is critical for dexterous manipulation [21, 158, 159]. Since manipulation relies heavily on applying appropriate interaction forces on the concerned object, a training paradigm that deals with training for forces or torques could be more effective in improving the manipulation skill. There exists a few studies where the subjects deal with an isometric manipulation task [51, 86, 115]. However, a training paradigm that provides subjects an opportu-

nity to dynamically regulate finger joint torque or force could be more effective in developing the skill for dexterous manipulation. Thus, training to achieve desired torques at finger joints and assessing performance based on accuracy of torque tracking could be more effective to develop and assess manipulation skill.

4.4 Framework for Robot-assisted Motor (Re)-learning

We present a novel rehabilitation framework that combines aforementioned factors to provide an optimum rehabilitation environment with a challenge level commensurate with the level of the skill of the subject. This framework consists of a rehabilitation environment with a robotic device using which a task is performed by the subject, while the framework provides some form of feedback (Fig. 4.1). The performance on the task is measured using performance measures, which determine the level of skill of the subject. These performance measures are then used to carry out the three forms of adaption mentioned above. The role of adaptation at the task level is to introduce sufficient variability in the task to keep the task challenging based on the skill level of the subject. Adaptation in assistance is carried out to smoothly transition from a haptic guidance training to an error augmentation training based on the performance on the task. Finally, adaptation in feedback is carried out to provide just the right amount of feedback to avoid reliance on feedback and instead promote motor adaptation and learning. Different types of adaptation algorithms can be incorporated in this framework for each component. We

implement the following three types of adaptations for our experiments.

4.4.1 Task Adaptation

To model variability in task, we model a functional task using a machine learning algorithm that learns and generates arbitrarily complex movement patterns that are rhythmic and require multi-joint coordination using nonlinear dynamical systems [68]. This approach uses a canonical limit cycle oscillator with well-defined stability properties and modifies the attractor landscape of the canonical system using statistical learning methods to embed arbitrary smooth target patterns without loosing the stability properties. This learned pattern generator is an autonomous dynamical system, which can robustly deal with external perturbations that disrupt the time dependent flow of the original motion pattern. Another important aspect of this approach is that it allows for on-line modifications of the target trajectory. The variability in the learned task can be then introduced by changing the frequency and amplitude parameters of the non-linear dynamical system based on performance. This approach allows us to model any periodic task in the form of a time based trajectory (e.g. position or torque trajectory).

4.4.1.1 Modeling Task

We use a nonlinear oscillator (4.1) to create a rhythmic phase variable (ϕ) that governs the desired output trajectory (4.2) using a learned nonlinear

function (4.3).

$$\begin{aligned}\dot{x}_1 &= -\frac{\mu}{r_0}(r - r_0)x_1 - k^2 x_2 \\ \dot{x}_2 &= \frac{x_1}{(1 + \kappa_{x_2}(\mathbf{y} - \mathbf{y}_d)^T(\mathbf{y} - \mathbf{y}_d))}\end{aligned} \tag{4.1}$$

$$\dot{\mathbf{y}} = \mathbf{f} + \beta(\mathbf{y}_m - \mathbf{y}_d) + \kappa_y(\mathbf{y} - \mathbf{y}_d) \tag{4.2}$$

$$\mathbf{f} = \mathbf{\Psi}(\phi)\mathbf{w}\sqrt{r_0} \tag{4.3}$$

where x_1 and x_2 are the states of the oscillator, parameter k corresponds to the frequency of the oscillator, r_0 corresponds to the desired total energy and determines the amplitude of the oscillation, μ determines the convergence rate to the limit cycle and β is a positive constant. $\mathbf{y}_m$ is a parameter which determines the mean around which $\mathbf{y}$ oscillates. $\mathbf{y}$ and $\mathbf{y}_d$ are the measured and the desired output, respectively. κ_{x_2} and κ_y are the output feedback gains for x_2 and $\dot{\mathbf{y}}$, respectively. $\mathbf{\Psi}$ is the matrix with Gaussian kernel function given in (4.4).

$$\psi_i = e^{-\frac{(\phi - c_i)^2}{\sigma_i^2}} \tag{4.4}$$

$$\phi = \tan^{-1}\left(\frac{x_1}{kx_2}\right) \tag{4.5}$$

The non-linear oscillator has a stable limit cycle characterized by the closed trajectories as in (4.6)

$$\frac{x_1^2}{2} + \frac{k^2 x_2^2}{2} = r_0 \tag{4.6}$$

and energy at any state (x_1, x_2) as

$$r(x_1, x_2) = \frac{x_1^2}{2} + \frac{k^2 x_2^2}{2} \tag{4.7}$$

To learn the nonlinear function $\mathbf{f}$ from a given desired trajectory ($\mathbf{y}_d$), we solve a nonlinear function approximation problem to find the parameters $\mathbf{w}$ in (4.3). Given the sampled trajectory data ($\mathbf{y}_d$), we obtain the target function using (4.8)

$$\mathbf{f}_{target} = \dot{\mathbf{y}}_d - \beta(\mathbf{y}_m - \mathbf{y}_d) \tag{4.8}$$

We use an incremental radial basis function network to learn the target function, which has been shown to be more robust and generate compact networks [175]. Such a learning algorithm can allocate resources as needed while dealing with the bias-variance dilemma in a systematic way.

4.4.1.2 Incorporating Variability in Learned Task

We model the amplitude and frequency of the learned task as a function of performance on the task as in (4.9). We consider the error over N time steps to assess performance instead of instantaneous performance to take into account the averaged performance, which gives a more accurate estimate of the skill level of the subject.

$$\begin{aligned} \text{Amplitude: } r_0 &= e^{-\kappa_r \frac{1}{N} \sum_{i=1}^{N} (\mathbf{y}_i - \mathbf{y}_{i,d})^T (\mathbf{y}_i - \mathbf{y}_{i,d})} \\ \text{Frequency: } k &= k_0 e^{-\kappa_k \frac{1}{N} \sum_{i=1}^{N} (\mathbf{y}_i - \mathbf{y}_{i,d})^T (\mathbf{y}_i - \mathbf{y}_{i,d})} \end{aligned} \tag{4.9}$$

where κ_r and κ_k are the parameters associated with amplitude and frequency, respectively. k_0 is the maximum desired frequency and n refers to the number

of output trajectories being tracked. $\mathbf{y}_i$ and $\mathbf{y}_{i,d}$ represent the actual and the desired joint torque vector for ith. According to this model as the error increases the relative amplitude of the motion reduces from one towards zero and the frequency of the motion reduces from k_0 towards zero.

4.4.2 Assistance Adaptation

Incorporating both performance-based error augmentation or haptic guidance training requires a controller that could seamlessly transition from haptic guidance regimen to an error-augmentation one. We incorporate performance-based error augmentation or haptic guidance in the control algorithm using adaptive impedance control as given by (4.10).

$$\begin{aligned} \theta_{m,j,ff} &= k_{j,ff}\frac{1}{r_m}\left(\frac{y_{j,d}}{2k_j r_j}\right) \\ k_{j,ff} &= \text{mtanh}\left(\frac{1}{N}\sum_{i=1}^{N}\left(y_{j,i}-y_{j,i,d}\right)^2\right) \end{aligned} \tag{4.10}$$

where $\theta_{m,j,ff}$ represents the feed-forward motor position for the jth exoskeleton joint, which is calculated using the desired joint torque ($y_{j,d}$), exoskeleton SEA joint stiffness (k_j) and joint and motor pulley radii (r_j and r_m). $k_{j,ff}$ is the gain for the jth joint that determines the amount of assistance provided by the exoskeleton based on the torque tracking performance of the subject on the task. $y_{j,i}$ and $y_{j,i,d}$ represent the actual and the desired torque of the jth joint of the exoskeleton for ith sample, respectively. In this type of control both gain and trajectory adaptations take place. The gain is adapted such that the controller gain becomes negative (error augmentation training) as the error

becomes very low and increases (haptic guidance) as the error becomes large. We use modified hyperbolic tangent function for gain adaptation to realize such an adaptation.

4.4.3 Visual Feedback Adaptation

We incorporate performance-based visual feedback by changing the transparency of the visual feedback based on the performance on the task as in (4.11).

$$t_{j,r} = k_{j,t} \left(1 - e^{-\kappa_{j,t} \sum_{i=1}^{N} (y_{j,i} - y_{j,i,d})^2} \right) \tag{4.11}$$

where $t_{j,r}$, $k_{j,t}$ and $\kappa_{j,t}$ represent the degree of transparency, transparency gain and the parameter governing the rate at which the transparency changes with change in torque tracking error, respectively, corresponding to the jth joint. The visual feedback becomes less transparent, i.e., less visible, as the performance over the task improves, making the task more challenging for the subject.

4.5 Experimentation

We carry out experimentation to evaluate first the functionality of the framework and then use the framework to test a hypothesis on motor learning of healthy subjects using our previously developed hand exoskeleton [4].

4.5.1 Task Modeling

For the task to be learnable for healthy subjects, we chose the simultaneous tracking of torque trajectories at the two joints of index finger exoskeleton as the task for our experiments. We limit the task to two joints as a visual feedback is associated with the task and simultaneously observing more than two trajectories is very challenging for the subjects. In order to develop a torque-based task that is closer to the natural finger motion, we first run the index finger exoskeleton in zero-torque mode and perform a finger flexion-extension task with a healthy subject. During this motion, we collect the exoskeleton joint angle trajectories and learn a model using the approach presented in Section 4.4.1.1. In order to generate the torque trajectory associated with this task, we then run the device in impedance control mode to track the learned trajectories. The recorded exoskeleton joint torque trajectories are then again learned using the learning from demonstration approach. Finally, the torque task is generated using the learned dynamic model.

4.5.2 Task, Assistance and Visual Feedback Adaptation

The three adaptations presented in Section 4.4 are then introduced in the modeled torque tracking task. We tested the functioning of the framework by letting a subject perform the torque tracking task and observing the variation in task amplitude and frequency, joint impedance and transparency of visual feedback.

4.5.3 Hypothesis Testing

There is a wide spectrum of training paradigms that could be designed using our framework. The training paradigm could vary from one where no adaptation takes place in task, assistance or feedback to the one where simultaneous adaptation of task, assistance and feedback takes place. As a first step towards understanding of how these training paradigms could affect motor learning, we propose a hypothesis and carry out human subject studies to examine the same.

We carry out a human subjects study with the goal of understanding: (i) if the subjects could learn the task when trained in the presence of three types of adaptations as incorporated in the framework and (ii) if the three types of adaptations could modulate the level of challenge i.e. the three adaptations affect the motor learning rate as compared to a training where the task, assistance and feedback do not adapt. 10 healthy subjects (seven male and three female, ages 19-32) with no history of any neuromuscular injury, voluntarily participated in the experiments, after they provided their informed consent. The subjects were randomly distributed among two groups, one is trained with an adaptive training paradigm and the other with a non-adaptive training. The study was approved by The University of Texas at Austin institutional review board.

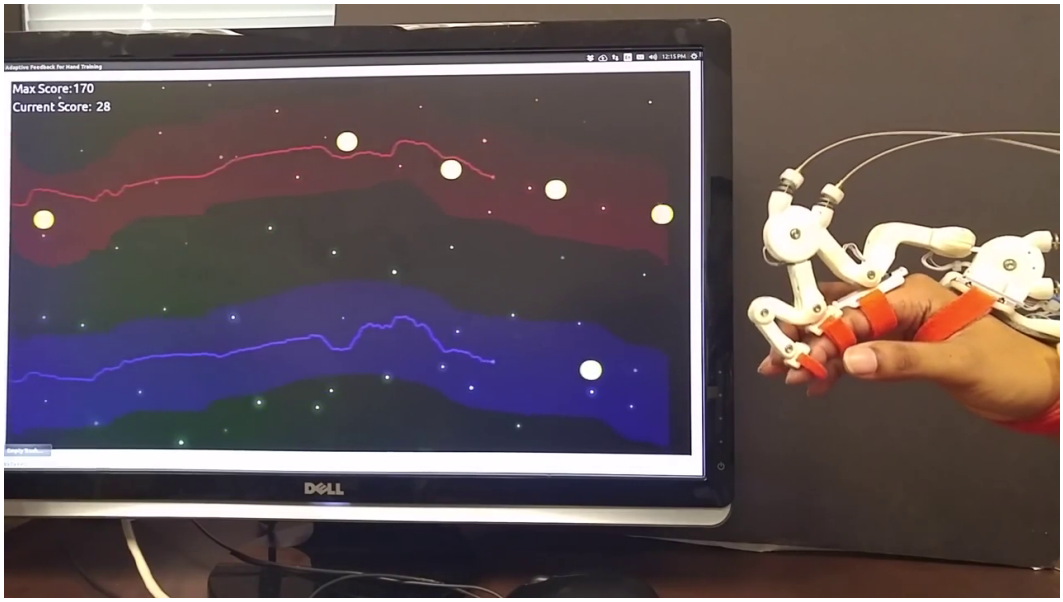

Figure 4.2: The index finger exoskeleton module and the graphical user interface presented to the subject for the motor learning study.

4.5.3.1 Hypothesis

Training using simultaneous adaptation of task, assistance and feedback based on performance can modulate challenge and affect motor learning of healthy human subjects on a torque-based task.

4.5.3.2 Training Task

The torque tracking task was presented to the subject in the form of an engaging game (Fig. 4.2). The graphical user interface for the game consists of two torque tunnels corresponding to the two joints of the index finger. The subjects are asked to build appropriate levels of torques at the two exoskeleton joints such that they could travel in the two tunnels as far as possible without

hitting the boundaries of either tunnel. The current torque level is shown to the subject in the form of a visual feedback whose visual transparency is governed based on the performance on the task. Rewards in the form of coins are presented at the center of the tunnel, which corresponds to the desired torque trajectory and the subjects are encouraged to collect as many coins as possible while navigating the tunnels to score higher in the game. The game becomes progressively more difficult as the width of each tunnel reduces linearly as subjects travel farther in the tunnels. The total score consists of the sum of how long a subject could survive in the game and how many coins the subject collects on his or her way. A higher score in the game reflects a subject's capability to dynamically generate desired level of torque at the two finger joints under uncertain visual feedback. Both the current and maximum scores are also shown to encourage active participation of the subjects in the task. For adaptive training, the task, assistance and feedback is varied as described in Section 4.4. For non-adaptive training, the task, assistance and feedback is kept constant during training.

4.5.3.3 Evaluation Task

To assess the skill level of the subject, an evaluation task was presented to the subjects in the form of a challenging game. For the evaluation task, the task frequency and amplitude (4.13), resistive feed-forward assistance gain (4.14) and visual feedback transparency (4.15) were varied with three different random variables ($\chi_k, k = \{1, 2, 3\}$) uniformly distributed between 0 and 1

(4.12). This ensures that the level of challenge for the evaluation task remains consistent for each subject.

$$\chi_k \sim U([0,1]), k = \{1,2,3\} \tag{4.12}$$

$$\begin{aligned} \text{Amplitude: } r_0 &= e^{-\kappa_r \chi_1} \\ \text{Frequency: } k &= k_0 e^{-\kappa_k \chi_1} \end{aligned} \tag{4.13}$$

$$k_{j,ff} = \text{mtanh}\left(\chi_2\right) \tag{4.14}$$

$$\text{Transparency: } t_r = k_{j,t}\left(1 - e^{-\kappa_t \chi_3}\right) \tag{4.15}$$

where $U([a,b])$ represents a uniform distribution between a and b.

4.5.3.4 Protocol

The study consisted of five training and three evaluation sessions for each training group. In each training session the subjects played the game with the training task for at least 15 minutes. Each training session was conducted on a separate day to ensure that subjects could learn and retain the task from session to session. For evaluation, each subject was presented with 10 trials of the evaluation task to assess the level of skill of the subject. Each subject was evaluated before, in the middle of and after training to assess any improvement in performance on the task. In the first session, each subject was tested on the evaluation task to assess the pre-training performance. The subjects were then trained for three sessions using the adaptive or non-adaptive training task and the performance is assessed again using the evaluation task at the end of third session. Finally, the subjects were trained for two sessions and their performance was again assessed at the end of fifth training session. The

post-, mid- and pre-training performance were then compared to understand if statistically significant improvement in performance is observed. During experiments the subjects were not informed whether they are being trained or evaluated or which training paradigm they are being trained with. Since, it is difficult to perform consistently in each trial, we consider top 5 scores in 10 trials in each evaluation session for statistical analysis to assess the performance of each subject.

4.6 Results

4.6.1 Task Modeling

Results show that the exoskeleton joint angle task trajectories are reproduced by the learned dynamic model for both the joints (Fig. 4.3(c)). The states and phase of the nonlinear oscillator which governs the generation of the joint angle trajectory show periodic motion (Figs. 4.3(a) and (b)). Also, the exoskeleton joint torques generated using the learned dynamic model reproduce the torque trajectories measured from the device as obtained using impedance control (Fig. 4.3(d)).

4.6.2 Task, Assistance and Visual Feedback Adaptation

Results show that the three types of performance-based adaptations are captured by the framework and are reflected while performing the task. The task amplitude reduces as the torque root mean square (RMS) error increases and vice versa (Fig. 4.4(b)). The feed-forward assistance gain varies as per

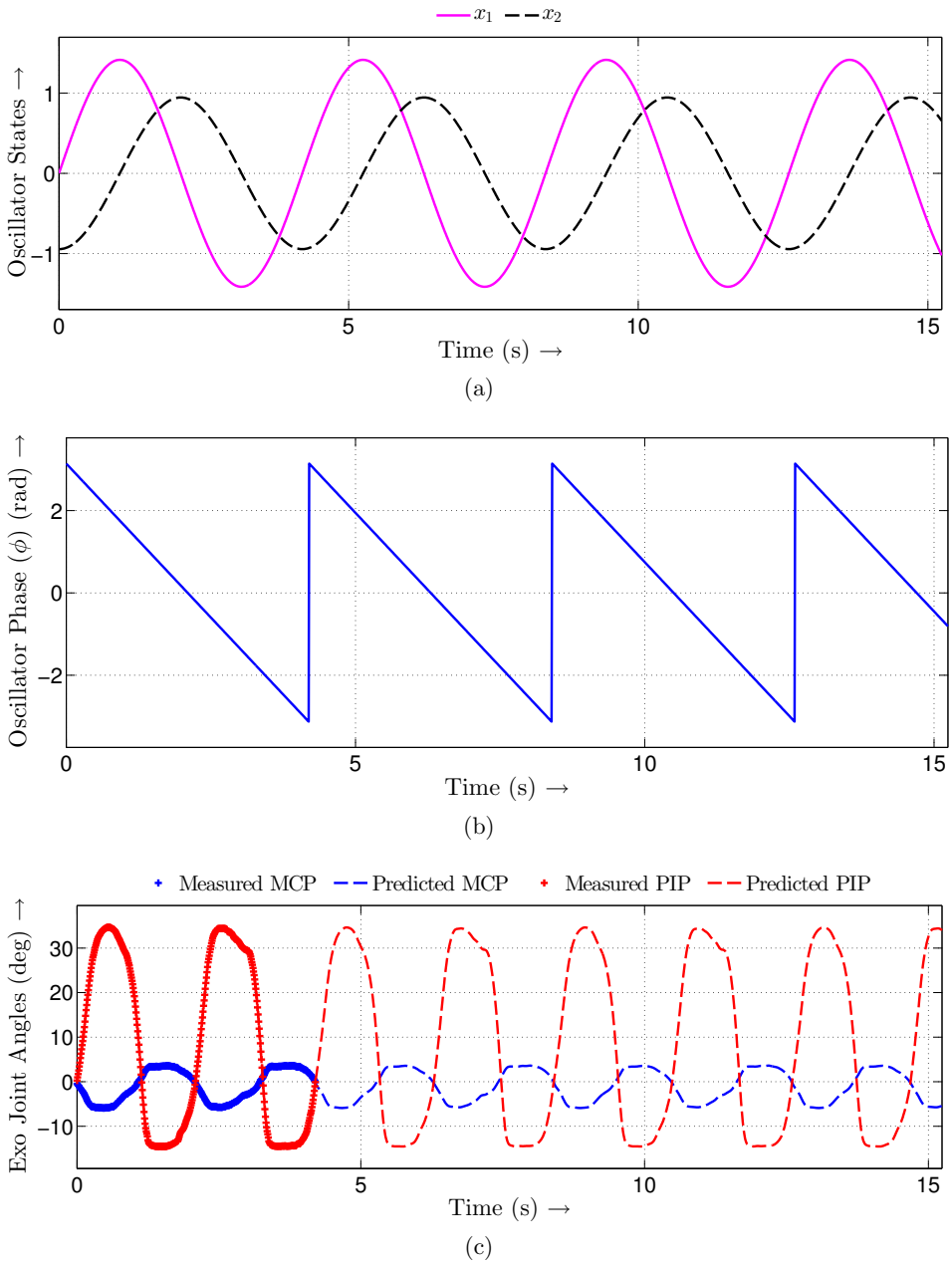

Figure 4.3: The finger flexion-extension task as modeled using the learning from demonstration approach. (a) The states and (b) phase angle of the nonlinear oscillator corresponding to the exoskeleton joint angle trajectories, (c) measured and generated exoskeleton joint angle trajectories for the two exoskeleton joints and (d) measured and generated exoskeleton joint torques. (contd.)

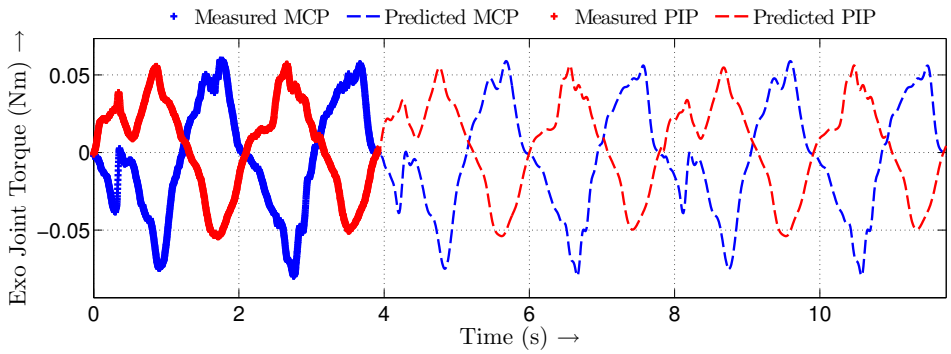

(a)

Figure 4.3: The finger flexion-extension task as modeled using the learning from demonstration approach. (a) The states and (b) phase angle of the nonlinear oscillator corresponding to the exoskeleton joint angle trajectories, (c) measured and generated exoskeleton joint angle trajectories for the two exoskeleton joints and (d) measured and generated exoskeleton joint torques.

(4.10) as the torque RMS error changes (Fig. 4.4(c)). The transparency of the visual feedback decreases, i.e., the trajectory becomes less visible as the torque tracking error reduces making the task more challenging. Thus, the three adaptations ensure that the task is consistently challenging for the subject even when the skill level of the subject changes.

4.6.3 Hypothesis Testing

4.6.3.1 Total Score

Results from the human subjects study showed that the performance of 4 out of 5 subjects and all 5 subjects improve in the evaluation session with the adaptive and non-adaptive training paradigm, respectively (Fig. 4.5). Higher scores were observed with non-adaptive training than with adaptive training. A few different learning trends were also observed. Some subjects showed

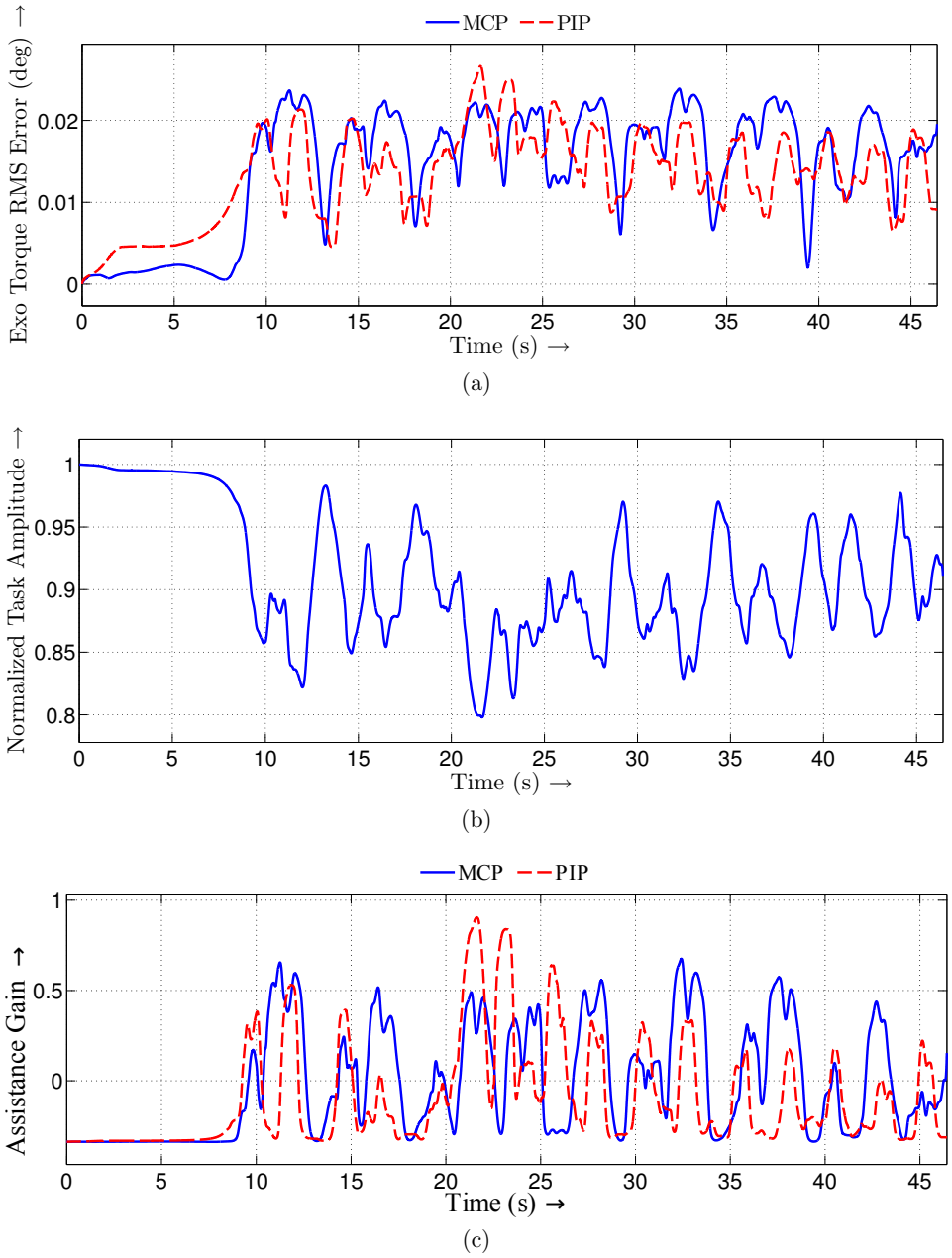

Figure 4.4: The three types of adaptations as implemented in the framework for the torque tracking task. (a) Exoskeleton joint torque RMS error trajectories, (b) normalized task amplitude and frequency trajectories, (c) exoskeleton feed-forward assistance gain trajectories and (d) visual feedback transparency trajectories for the two exoskeleton joints. (contd.)

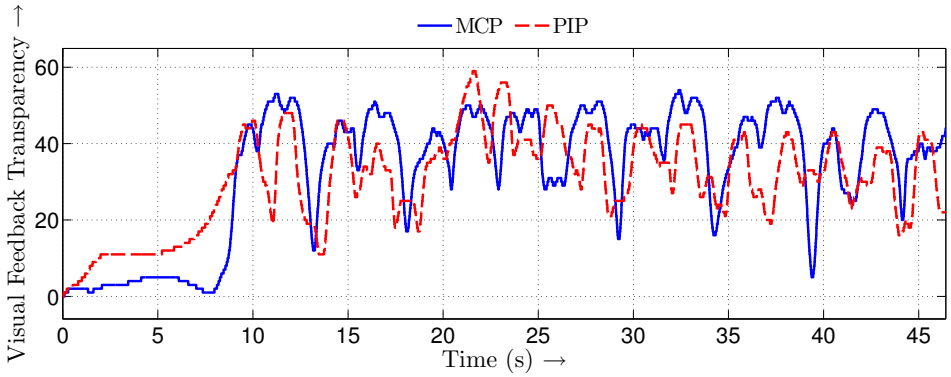

(a)

Figure 4.4: The three types of adaptations as implemented in the framework for the torque tracking task. (a) Exoskeleton joint torque RMS error trajectories, (b) normalized task amplitude and frequency trajectories, (c) exoskeleton feed-forward assistance gain trajectories and (d) visual feedback transparency trajectories for the two exoskeleton joints.

a steady improvement in performance from pre- to post-training evaluation. While some form of saturation in performance was visible in the performance of others. Only one subject showed an improvement from pre- to mid-training session and a decline in performance from mid- to post-training evaluation with adaptive training. Thus, training using adaptations does modulate challenge and affects motor learning of the subjects.

4.6.3.2 Time- and Tracking-based Scores

Since the total score consists of time- and tracking-based scores, we also analyze these scores individually. Time-based score indicates for how long a subject could survive as they are trained. Tracking-based score at the two exoskeleton is a measure of how well the subject could track the desired

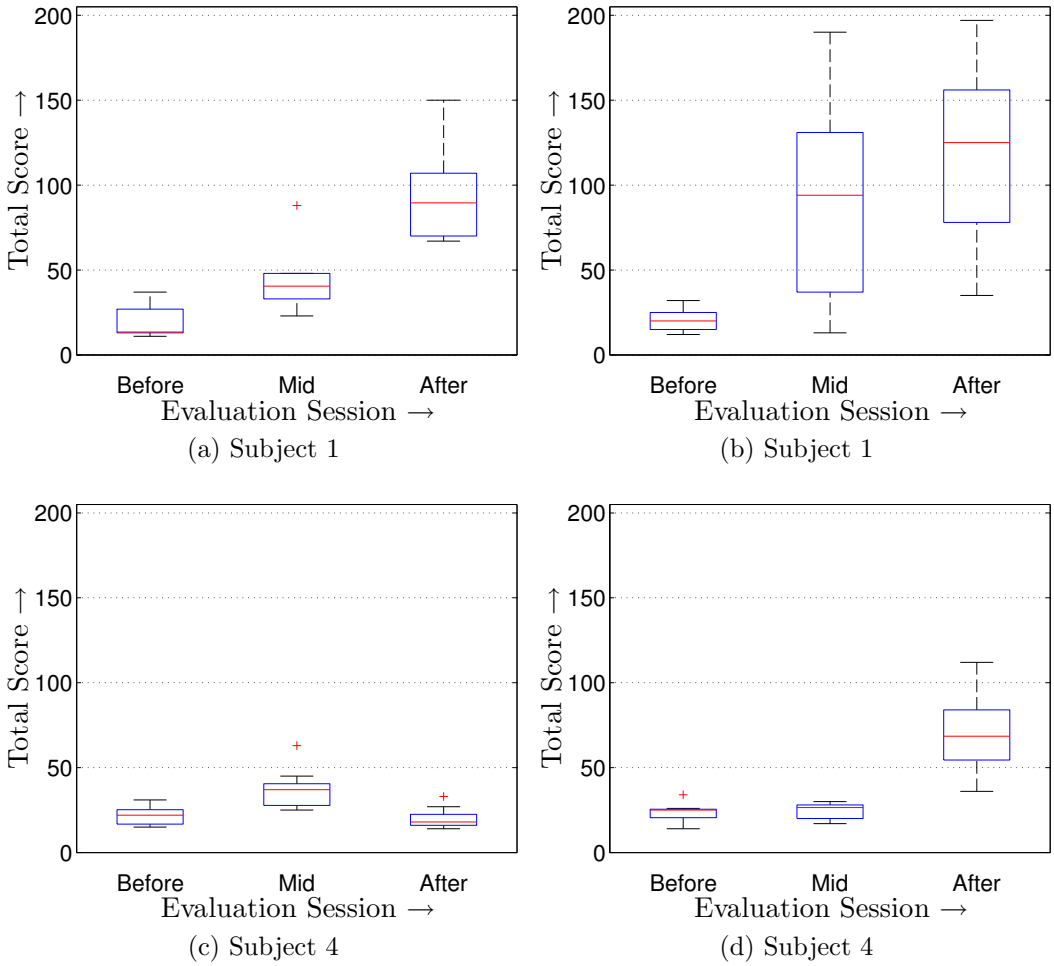

Figure 4.5: The box plot of the total score for subjects 1 and 4 in the evaluation sessions conducted before, in the middle of and after training with and without the adaptive training. The left side plots show training with all three adaptations and the right side plots show training without the adaptations. The central mark represents the median, the edges of the box are the 25th and 75th percentiles, the whiskers extend to the most extreme data points not considered outliers and the outliers are plotted individually.

torque trajectories. 4 out of 5 and all 5 subjects showed some improvement in time- and tracking-based scores at both the MCP and PIP joints with the

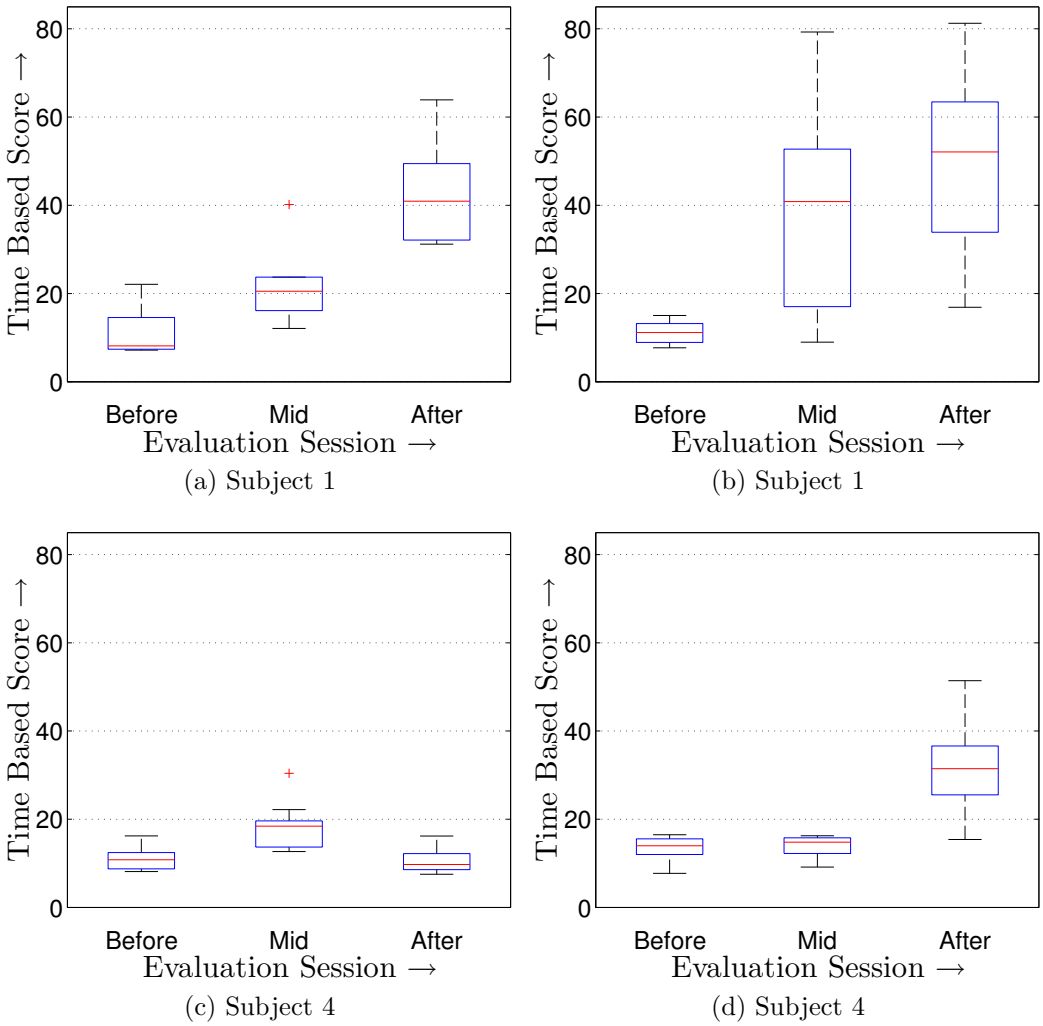

Figure 4.6: The box plot of the time-based score for subjects 1 and 4 in the evaluation sessions conducted before, in the middle of and after training with and without the adaptations. The left side plots show training with all three adaptations and the right side plots show training without the adaptations.

adaptive and non-adaptive training, respectively (Figs. 4.6,4.7,4.8). However, higher improvements in score were observed with non-adaptive training than with adaptive training indicating that adaptations do influence motor learning.

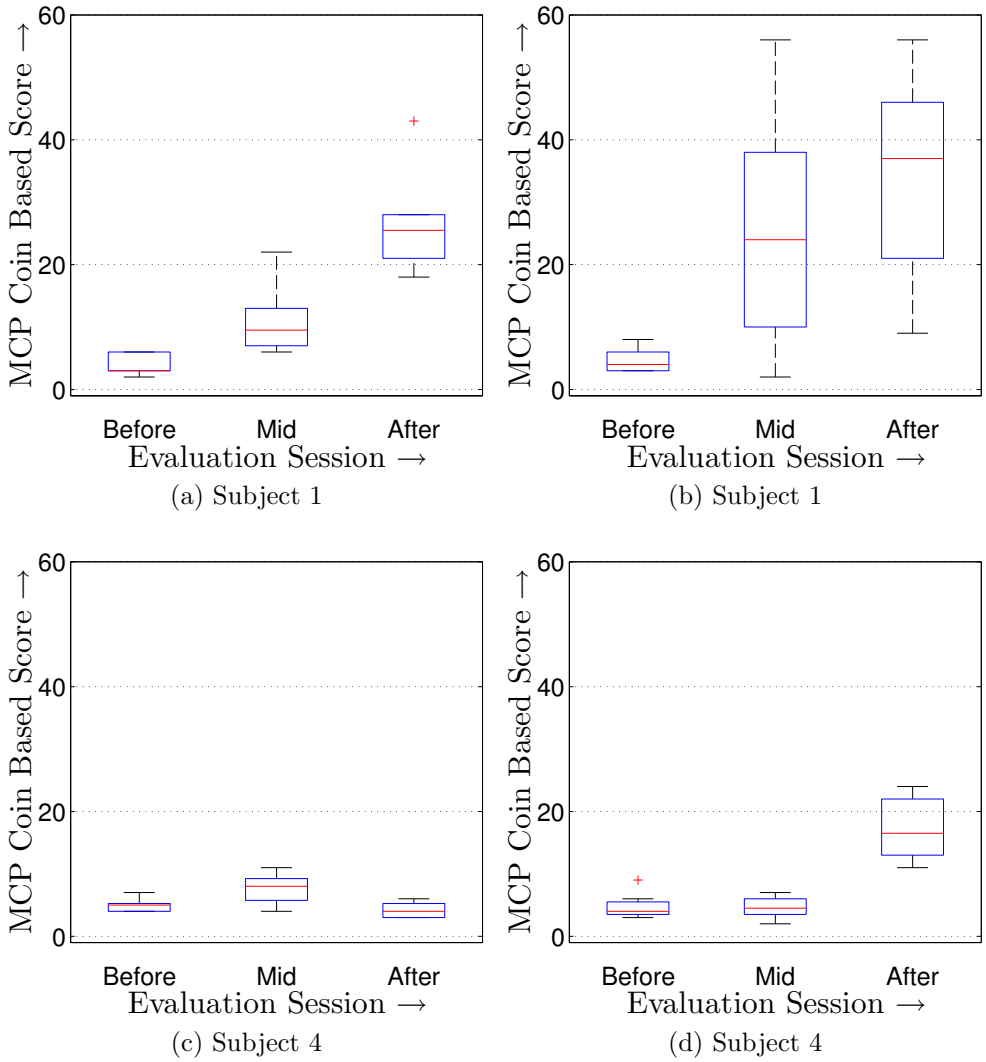

Figure 4.7: The box plot of the MCP torque-tracking-based score for subjects 1 and 4 in the evaluation sessions conducted before, in the middle of and after training with and without the adaptations. The left side plots show training with all three adaptations and the right side plots show training without any adaptation.

4.6.3.3 Tracking Performance per unit Time

Another important way to assess the improvement in the skill of the subjects is to determine how accurately a subject played as they could survive

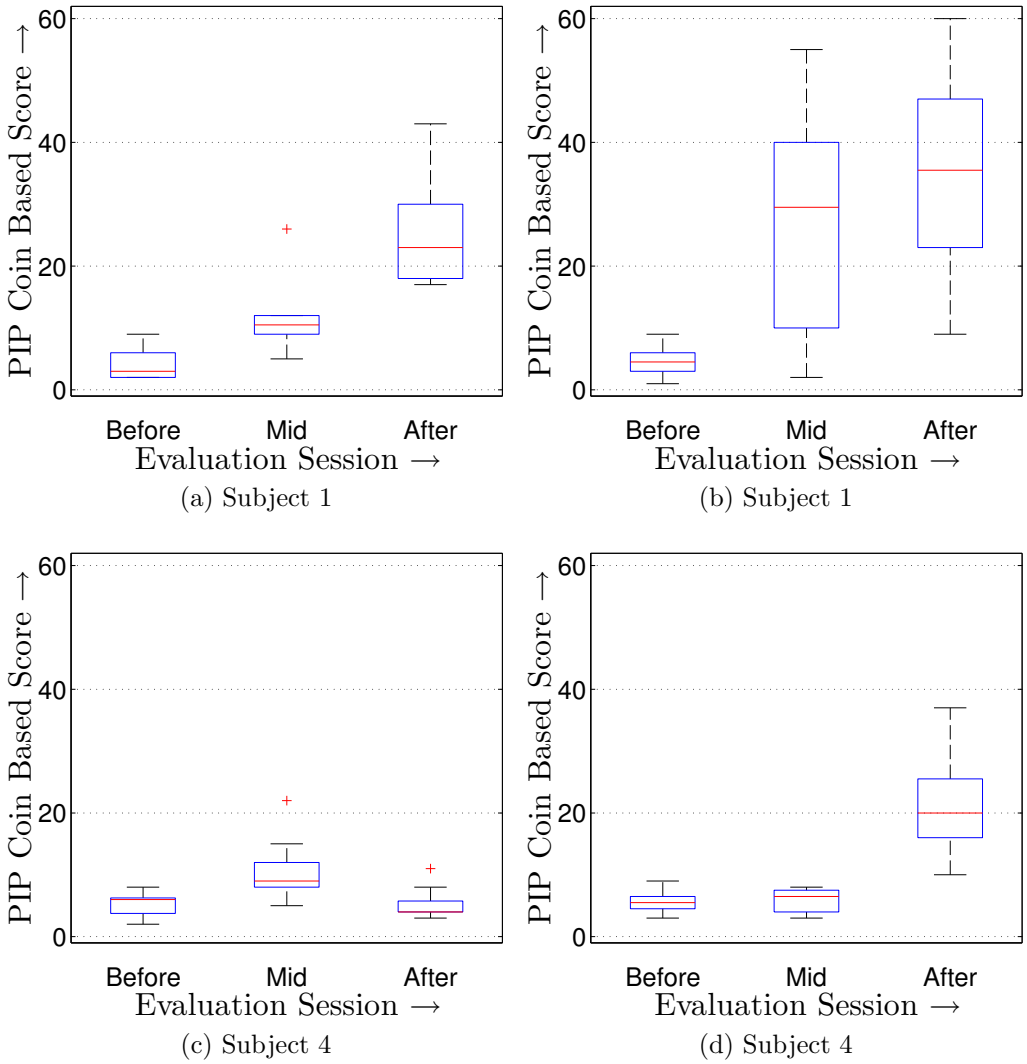

Figure 4.8: The box plot of the PIP torque-tracking-based score for subjects 1 and 4 in the evaluation sessions conducted before, in the middle of and after training with and without the adaptations. The left side plots show training with all three adaptations and the right side plots show training without any adaptation.

for a longer duration from session to session. We evaluated tracking performance per unit time metric to assess this improvement in the skill. Since the coins are located on the desired trajectory, the number of coins collected by a subject indicates the tracking performance of the subject. Thus, coins collected per unit time is a measure of the skill level of the subject. Results showed that tracking performance per unit time improves for 4 out of 5 subjects and all 5 subjects with the adaptive and non-adaptive training, respectively (Fig. 4.9). Thus, subjects not only could survive longer as they are trained, they also get better at playing the game. Higher improvement in tracking performance per unit time is observed in non-adaptive training than with adaptive training suggesting adaptations do affect motor learning.

4.6.3.4 Smoothness

The normalized mean RMS torque tracking error which is an indicator of the smoothness of the torque trajectory also improved from 41.57 % to 21.79% of peak torque at MCP joint and from 40.90% to 31.01% of peak torque at PIP joint for Subject 1 with an adaptive training paradigm. For a training paradigm with no adaptations, the normalized mean RMS torque tracking error improved from 38.89 % to 15.43% of peak torque at MCP joint and from 44.04% to 17.70% of peak torque at PIP joint for Subject 1. Thus, both training paradigms improved the quality of movement of the subjects with an adaptive training paradigm being more challenging for the subjects for motor learning.

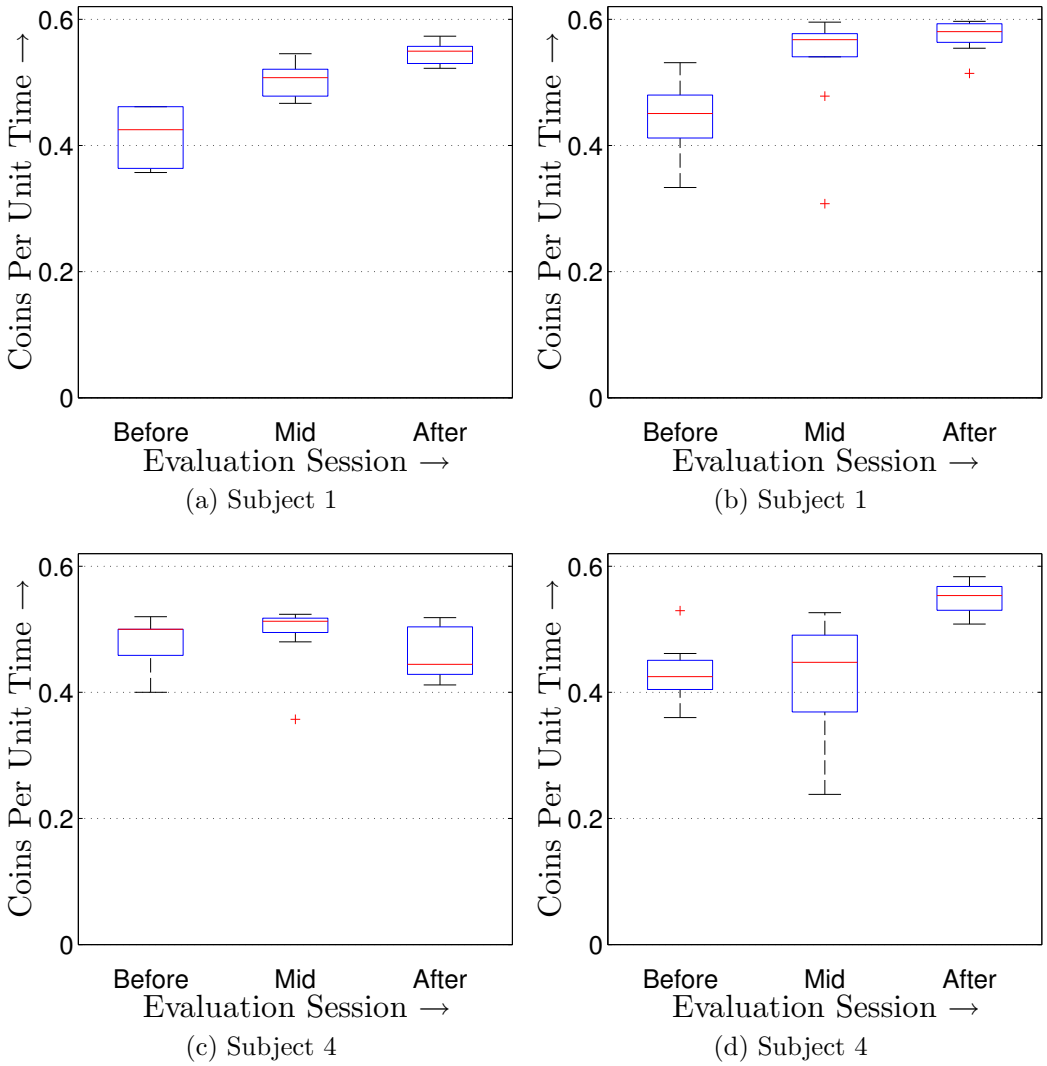

(a) Subject 1 (b) Subject 1

(c) Subject 4 (d) Subject 4

Figure 4.9: The box plot of the coins collected per unit time for subjects 1 and 4 in evaluation sessions conducted before, in the middle of and after training with and without the adaptations. The left side plots show training with all three adaptations and the right side plots show training without any adaptation.

4.6.3.5 Statistical Analysis

Both the median and mean scores in the evaluation sessions improved with training considering scores of all subjects for both the adaptive and non-adaptive training (Figs. 4.10 (a) and (b). Higher increase in scores were observed with non-adaptive training than with adaptive training. This shows that a task with all three types of adaptations was more challenging for the subjects than a non-adaptive task. However, the analysis showed that the variance of score also increase with both types of training. Thus, as subjects get better at playing the game they also become less consistent at achieving the same score. While a consistent increase in variance is observed with an adaptive training, the variance tend to diminish with more training in a non-adaptive paradigm (Figs. 4.10 (c) and (d)).

A paired-samples t-test was conducted to compare the evaluation scores of all subjects before and after adaptive training. There was a significant difference in scores before (M=22.0, SD=7.0) and after training (M=68.8, SD=39.2); $t(24)=-5.1$, $p<0.0001$. A post hoc power analysis revealed that on the basis of the mean, before and after comparison effect size observed in the study with adaptive training, an n of approximately 3 would be needed to obtain statistical power at the 0.99 level. Another paired-samples t-test was conducted to compare the evaluation scores of all subjects before and after non-adaptive training. A significant difference in scores before (M=36.7, SD=17.4) and after training (M=131.4, SD=31.9); $t(24)=-6.2$, $p<0.0001$ is observed. Another post hoc power analysis revealed that on the basis of the

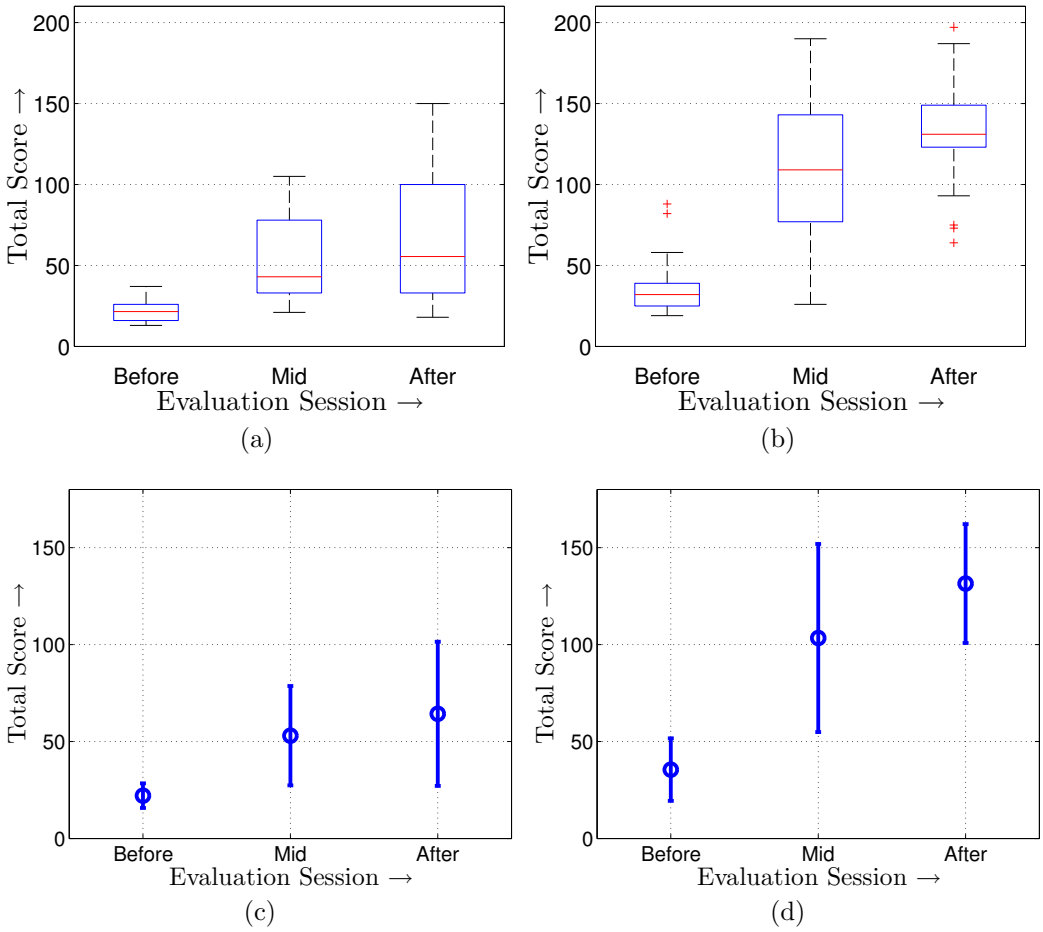

Figure 4.10: Combined total score for all subjects in evaluation sessions conducted before, in the middle of and after training with and without the adaptations. (a), (b) Box plot of the total score and (c), (d) Error bar plot of the total score. The left side plots show training with all three adaptations and the right side plots show training without any adaptation. The center in the error bar represents mean and whiskers represent two standard deviation units in length.

mean, before and after comparison effect size observed in the study with non-adaptive training, an n of approximately 3 would be needed to obtain statistical power at the 0.98 level. These results support the hypothesis that

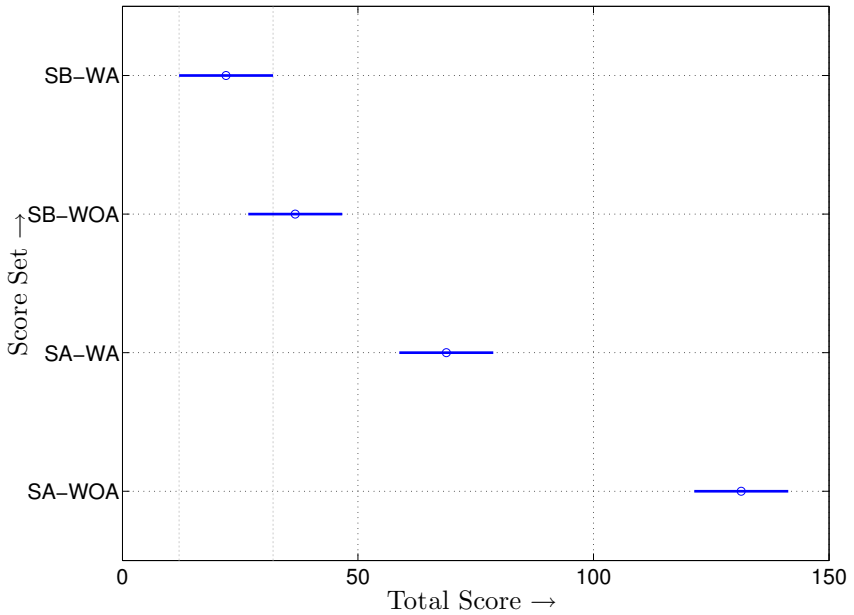

Figure 4.11: The results from multiple comparison test, where the center circle represents the group mean and the error bar represent the 95% confidence interval of the mean. SB-WA and SB-WOA represent score group before training with and without adaptations, respectively. SA-WA and SA-WOA represent score group after training with and without adaptations, respectively.

training using both adaptive and non-adaptive paradigms positively affects motor learning on a torque-based task.

To distinguish between the motor learning in the two training paradigms a Tukey-Kramer multiple comparison test [155] was carried out to examine whether the scores obtained after adaptive training (SA-WA) are statistically different from those obtained after a non-adpative training (SA-WOA) and whether these two are statistically different from their respective scores before training (SB-WA and SB-WOA, respectively). Significance was set at $p<0.05$. Results show that even when the scores of the subjects chosen for the two types

Table 4.1: The results from the multiple comparison test. SB-WA and SB-WOA represent score group before training with and without adaptations, respectively. SA-WA and SA-WOA represent score group after training with and without adaptations, respectively.

Comparison	Mean Difference	95% Confidence Interval of Difference	Significant?	Adjusted p value
SB-WA vs SB-WOA	-14.68	-34.63 to 5.27	No	0.2250
SB-WA vs SA-WA	-46.76	-66.71 to -26.81	Yes	<0.0001
SB-WA vs SA-WOA	-109.36	-129.31 to -89.41	Yes	<0.0001
SB-WOA vs SA-WA	-32.08	-52.03 to -12.13	Yes	<0.0001
SB-WOA vs SA-WOA	-94.68	-114.63 to -74.73	Yes	<0.0001
SA-WA vs SA-WOA	-62.60	-82.55 to -42.65	Yes	<0.0001

of training in the beginning are not statistically different, the scores for the two groups are statistically different after training (Fig. 4.11 and Table 4.1). This shows that the adaptive and non-adaptive training significantly affects the rate at which motor learning takes place. These results support the hypothesis that simultaneous adaptation of task, assistance and visual feedback can modulate challenge and affect motor learning on a torque-based task.

4.7 Discussion

Results showed that there are differences in the rate at which motor learning takes place based on the type of task, assistance and visual feedback provided during training. Subjects with an adaptive task, assistance and visual feedback training showed significantly different learning rates than those trained under the non-adaptive paradigm. This shows that adaptations in the space of task, assistance and visual feedback governs the rate of motor learning. We further speculate that several factors might be responsible for such differences in learning rates, which we discuss next.

Firstly, an adaptive paradigm training is more challenging for a subject to learn in. This is because as subjects learn to perform the task better, the task also becomes correspondingly challenging making it difficult for the subject to continue performing at the same level of performance. This could influence the motivation of a subject in different ways, which we believe is highly subject-specific. If the subject perceives the task to be too challenging it can discourage the subject and they can loose the motivation to learn the task.

Secondly, the rate of adaptation plays a crucial role in how the subjects learn and determine the rate of motor adaptation [25]. Tasks that adapt too fast may make it difficult for the motor system of the subjects to reach a steady state and will therefore be perceived as very challenging or unintuitive. There might exist a task with an optimum rate of adaptation that would result in best learning rate. For example, a less skilled subject would learn better

if the task is less challenging as his motor system could learn from such a task. However, a highly skilled subject would continue to learn if the task is more challenging. Thus, the rate of adaptation needs to be subject-specific for maximum learning.

Thirdly, since three types of adaptations are carried out simultaneously, it is difficult for the subjects to isolate the effect of each type of adaptation. So, adaptive training with one of the factors being adapted at a time might be better as compared to all the factors being adapted simultaneously as the motor system of the subject could better interpret the adaptations and the task becomes more intuitive for the subjects. There might even be an optimum sequence in which the three adaptations should be introduced in the training regimen for achieving the best possible rate of learning.

Fourthly, challenge even when adapted based on the level of skill of the subject, might not always encourage learning, which is in contradiction with challenge point hypothesis. Different types of adaptations could be present in the environment (i.e. task, assistance and visual feedback) and each subject could perceive these as different level of challenges and therefore, respond differently to these adaptations. May be not all forms of challenge encourage motor learning. Or may be it is not the challenge but how subjects perceive challenge is what governs motor learning. Subjects who perceive challenge as discouraging might not be benefited by a training paradigm that challenges the subjects and vice versa.

There are also several limitations of the human subject experiments car-

ried out to test the motor learning hypothesis. Firstly, though games played by each subject adapted as per the needs of the subject, same rate of adaptations were used for all the subjects. A subject-specific adaptation rate might result in better learning. However, how to determine these adaptation rates for a specific subject that maximizes learning is still an open question. Secondly, the games were based on a torque-based task which is assumed to better reflect the needs of rehabilitation than a position-based task. Clinical testing would be needed to ensure that a torque-based task is necessarily better than a position-based task. Thirdly, it is assumed that the scores are a measure of the motor learning of the subjects and reflect their true skill level. It might be difficult to capture and measure all the nuances of motor learning with such a performance measure.

4.8 Conclusion

The presented framework addresses the limitation of the existing control strategies in that it provides an evidence-based means to understand how task, assistance and feedback affects motor learning. It incorporates these three important factors and provides a subject-specific training environment as per the skill level of the subject. We carried out human subject experiments with a torque-based task to verify if training using simultaneous adaptation of task, assistance and feedback could affect motor learning of healthy subjects. Results showed that task, assistance and feedback adaptations could significantly affect the rate at which motor adaptation takes place and can modulate

challenge for the subjects. These results have implications for rehabilitation as our framework could provide subject-specific therapy regimen based on the understanding of what affects the rate of motor adaptation of a subject the most and gear the therapy as per his or her needs.

Chapter 5

Conclusions and Future Work

5.1 Summary

In this dissertation, we address the following three stated research goals: (i) design, development and testing of a hand exoskeleton, (ii) development of advanced controllers for the device and (iii) development of a framework for rehabilitation and its implementation on the hand exoskeleton.

Towards the goal of designing and developing a hand exoskeleton, we developed two miniature and compact Bowden-cable-based SEAs with linear compression and torsion springs for bidirectional torque control of small-scale robotic devices. Experiments using a SEA test rig showed that with a feed-forward PID controller the desired torque was tracked with sufficient accuracy (RMSE < 12 %) and fidelity (> 97 %) for both the actuators. Using one of the developed SEAs, we developed a hand exoskeleton capable of controlling the torques at the individual joints of the hand digits. The designed device assists the index and middle fingers and thumb, while allowing for large range of motion of the hand digits. We also carried out several different tests with both the index finger and thumb exoskeleton modules to characterize the performance of the device.

For advanced controls of the device, two subject-specific assist-as-needed controllers were developed for the index finger module of the hand exoskeleton. This is the first time that AAN controllers have been developed for a hand exoskeleton. Experiments showed that the learned force-field control is able to maintain the desired relation between the joint displacements for coordinated motion. Also, the adaptive-assistance-based control is able to quickly adapt to the changing requirements of a subject and track the desired joint angle trajectory with small RMS errors. For rehabilitation therapy where the goal is to train for time critical tasks with accurate tracking of the desired joint angle trajectory in time, adaptive assist-as-needed control would be a better choice. On the other hand, therapy where the coordination between the joints is important rather than the timeliness of the motion, learned force-field control would be more helpful. Learned force-field control is safer than the adaptive assist-as-needed control, as it does not apply increased torques if the motion is accidentally stalled.

Finally, we presented a framework for robot-assisted motor (re)-learning that incorporates subject-specific training. The framework allows for simultaneous adaptation of task, assistance and feedback based on the performance of a subject on a task to keep the task sufficiently challenging for the subject. As a part of the framework development, we presented a learning from demonstration approach to model a coordinated task to modulate the challenge level of the task in an online manner. We also presented a torque-based task that trains subject to dynamically regulate joint torques similar to that needed for

dexterous manipulation. Finally, we conducted a study with the human subjects and the results suggested that a training paradigm that simultaneously adapts the task, assistance and feedback does modulate challenge and affect motor learning of healthy humans subjects on a torque-based task.

5.2 Conclusions

This work has made several contributions to the area of stroke rehabilitation in general and hand rehabilitation more specifically. We developed a device capable of providing therapeutic exercises to hand similar to a therapist. The device could control torque applied at the individual joints of index and middle fingers and thumb while assisting them through their range of motion. The controllers developed for the device could be used to provide therapy for various hand impairments that result from stroke or spinal cord injury. We also realized during the experiments that each subject has their requirements and a specific type of control would best serve their needs. Furthermore, we developed a framework for robot-assisted rehabilitation that could help determine a subject-specific therapy regimen based on principles of motor learning. We also provided an instantiation of the framework which could be used to provide therapy to impaired subjects. Beyond the present application of the developed device as a rehabilitation tool, it can also be used as a haptic device for virtual reality applications. Furthermore, the proposed framework is more general and could be applied to train impaired subjects using other robots in a rehabilitation setting.

5.3 Future Work

There are severals ways in which the design and control of the device and the rehabilitation framework could be further improved:

1. One of the areas that still needs improvement before the device could be used in a clinical setting is the interface of the device with the hand. The current interface (especially the wireform strucutre in the thumb exoskeleton) requires some subject-specific customization before it fits to the hand of a subject at its natural position. The wearability of the device could be improved by attaching it to a glove that could help in quick doning and doffing of the device.

2. The structural design of the device including the actuator and control boxes could be further optimized to make the overall device more compact and portable.

3. Since both the learned force-field control and the adaptive assist-as-needed control have their respective limitations, new controllers that address the limitations of both the control techniques could be designed for more efficacious rehabilitation.

4. Several different hypothesis could be tested using the proposed framework to understand the role of each component and how rate of different types of adaptations influence motor learning. Also the efficacy of this multi-modal challenge modulation could be tested for different tasks.

5. We also plan to carry out human subject studies with individuals that exhibit hand pathologies to evaluate the efficacy of the device and the rehabilitation framework.

Appendix

Appendix 1

Expression for Jacobian

The expression for Jacobian ($\mathbf{J} = \dfrac{\partial \mathbf{X}}{\partial \mathbf{\Theta_r}}$) is obtained symbolically using MATLAB as expressed in (1.1).

$$
\begin{aligned}
J_{1,1} &= \frac{l_{BC}\, l_{CD}\, \cos(\theta_1 - \theta_4)}{x_3} - l_{BC}\, \sin(\theta_1 - \theta_4) \\
J_{1,2} &= 0 \\
J_{2,1} &= \frac{l_{BC}\, \cos(\theta_1 - \theta_4)}{x_3} \\
J_{2,2} &= 0 \\
J_{3,1} &= \frac{n_{3,1}}{d_{3,1}} \\
J_{3,2} &= -\frac{l_{EF}\, \cos(\theta_{HFG} + \theta_5 - \theta_8 + \theta_{6r})}{l_{EF}\, \cos(\theta_{HFG} + \theta_5 - \theta_8 + \theta_{6r}) - l_{CE}\, \cos(\theta_{HFG} + \theta_5 - \theta_8)} \\
J_{4,1} &= \frac{n_{4,1}}{d_{4,1}} \\
J_{4,2} &= \frac{l_{CE}\, l_{EF}\, \sin(\theta_{6r})}{l_{FH}\, (l_{EF}\, \cos(\theta_{HFG} + \theta_5 - \theta_8 + \theta_{6r}) - l_{CE}\, \cos(\theta_{HFG} + \theta_5 - \theta_8))}
\end{aligned}
\tag{1.1}
$$

where $J_{i,j}$ represents the $(i,j)^{th}$ entry in the Jacobian and

$$
n_{3,1} = -\frac{5\, l_{BC}\, \sin\left(\theta_{HFG} + \tan^{-1}\left(\frac{l_{AH} - x_3}{l_{CD}}\right) + \theta_1 - \theta_8\right)\, {x_3}^2}{4}
$$

$$
\begin{aligned}
&- \frac{l_{BC}\,\sin\left(\tan^{-1}\left(\frac{l_{AH}-x_3}{l_{CD}}\right) - \theta_{HFG} + \theta_1 + \theta_8\right)\,{x_3}^2}{4} \\
&+ \frac{{l_{AH}}^2\,l_{BC}\,\sin\left(\theta_{HFG} + \tan^{-1}\left(\frac{l_{AH}-x_3}{l_{CD}}\right) - \theta_1 + 2\,\theta_4 - \theta_8\right)}{2} \\
&+ \frac{l_{BC}\,\sin\left(\theta_{HFG} + \tan^{-1}\left(\frac{l_{AH}-x_3}{l_{CD}}\right) - \theta_1 - \theta_8\right)\,{x_3}^2}{4} \\
&+ \frac{l_{BC}\,\sin\left(\tan^{-1}\left(\frac{l_{AH}-x_3}{l_{CD}}\right) - \theta_{HFG} - \theta_1 + \theta_8\right)\,{x_3}^2}{4} \\
&+ \frac{{l_{AH}}^2\,l_{BC}\,\sin\left(\theta_{HFG} + \tan^{-1}\left(\frac{l_{AH}-x_3}{l_{CD}}\right) + \theta_1 - \theta_8\right)}{2} \\
&- \frac{l_{BC}\,\sin\left(\theta_{HFG} + \tan^{-1}\left(\frac{l_{AH}-x_3}{l_{CD}}\right) - \theta_1 + 2\,\theta_4 - \theta_8\right)\,{x_3}^2}{2} \\
&- \frac{11\,l_{BC}\,l_{CD}\,\cos\left(\theta_{HFG} + \tan^{-1}\left(\frac{l_{AH}-x_3}{l_{CD}}\right) + \theta_1 - \theta_8\right)\,x_3}{8} \\
&- \frac{l_{BC}\,l_{CD}\,\cos\left(\tan^{-1}\left(\frac{l_{AH}-x_3}{l_{CD}}\right) - \theta_{HFG} + \theta_1 + \theta_8\right)\,x_3}{8} \\
&- \frac{7\,l_{AH}\,l_{BC}\,\sin\left(\theta_{HFG} + \tan^{-1}\left(\frac{l_{AH}-x_3}{l_{CD}}\right) + \theta_1 - \theta_8\right)\,x_3}{4} \\
&+ \frac{l_{AH}\,l_{BC}\,\sin\left(\tan^{-1}\left(\frac{l_{AH}-x_3}{l_{CD}}\right) - \theta_{HFG} + \theta_1 + \theta_8\right)\,x_3}{4} \\
&+ l_{AH}\,l_{BC}\,l_{CD}\,\cos\left(\theta_{HFG} + \tan^{-1}\left(\frac{l_{AH}-x_3}{l_{CD}}\right)\right. \\
&\left.-\theta_1 + 2\,\theta_4 - \theta_8\right) \\
&- \frac{l_{BC}\,l_{CD}\,\cos\left(\theta_{HFG} + \tan^{-1}\left(\frac{l_{AH}-x_3}{l_{CD}}\right) - \theta_1 - \theta_8\right)\,x_3}{8} \\
&+ \frac{l_{BC}\,l_{CD}\,\cos\left(\tan^{-1}\left(\frac{l_{AH}-x_3}{l_{CD}}\right) - \theta_{HFG} - \theta_1 + \theta_8\right)\,x_3}{8}
\end{aligned}
$$

$$
\begin{aligned}
&- \frac{l_{AH}\, l_{BC}\, \sin\left(\theta_{HFG} + \tan^{-1}\left(\frac{l_{AH}-x_3}{l_{CD}}\right) - \theta_1 - \theta_8\right)\, x_3}{4} \\
&- \frac{l_{AH}\, l_{BC}\, \sin\left(\tan^{-1}\left(\frac{l_{AH}-x_3}{l_{CD}}\right) - \theta_{HFG} - \theta_1 + \theta_8\right)\, x_3}{4} \\
&+ l_{AH}\, l_{BC}\, l_{CD}\, \cos\left(\theta_{HFG} + \tan^{-1}\left(\frac{l_{AH} - x_3}{l_{CD}}\right) + \theta_1 - \theta_8\right) \\
&- \frac{l_{BC}\, l_{CD}\, \cos\left(\theta_{HFG} + \tan^{-1}\left(\frac{l_{AH}-x_3}{l_{CD}}\right) - \theta_1 + 2\,\theta_4 - \theta_8\right)\, x_3}{2} \\
&+ \frac{l_{BC}\, \sin(\theta_{HFG} + \theta_1 - \theta_8)\, {x_3}^2}{2\sqrt{\frac{(l_{AH}-x_3)^2}{{l_{CD}}^2} + 1}} \\
&+ \frac{l_{BC}\, \sin(\theta_1 - \theta_{HFG} + \theta_8)\, {x_3}^2}{2\sqrt{\frac{(l_{AH}-x_3)^2}{{l_{CD}}^2} + 1}} \\
&- \frac{l_{BC}\, l_{CD}\, \cos(\theta_{HFG} + \theta_1 - \theta_8)\, x_3}{4\sqrt{\frac{(l_{AH}-x_3)^2}{{l_{CD}}^2} + 1}} \\
&+ \frac{l_{BC}\, l_{CD}\, \cos(\theta_1 - \theta_{HFG} + \theta_8)\, x_3}{4\sqrt{\frac{(l_{AH}-x_3)^2}{{l_{CD}}^2} + 1}} \\
&- \frac{l_{AH}\, l_{BC}\, \sin(\theta_{HFG} + \theta_1 - \theta_8)\, x_3}{2\sqrt{\frac{(l_{AH}-x_3)^2}{{l_{CD}}^2} + 1}} \\
&- \frac{l_{AH}\, l_{BC}\, \sin(\theta_1 - \theta_{HFG} + \theta_8)\, x_3}{2\sqrt{\frac{(l_{AH}-x_3)^2}{{l_{CD}}^2} + 1}}
\end{aligned}
$$

$$
\begin{aligned}
d_{3,1} &= x_3\, (l_{EF}\, \cos(\theta_{HFG} + \theta_5 - \theta_8 + \theta_{6r}) \\
&\quad - l_{CE}\, \cos(\theta_{HFG} + \theta_5 - \theta_8)) \\
n_{4,1} &= \frac{l_{BC}\, l_{CE}\, \cos\left(\tan^{-1}\left(\frac{l_{AH}-x_3}{l_{CD}}\right) - \theta_1 + \theta_5\right)\, {x_3}^2}{4} \\
&\quad - \frac{l_{BC}\, l_{EF}\, \cos\left(\tan^{-1}\left(\frac{l_{AH}-x_3}{l_{CD}}\right) - \theta_1 + 2\,\theta_4 - \theta_5 - \theta_{6r}\right)\, {x_3}^2}{2}
\end{aligned}
$$

$$
\begin{aligned}
&- \frac{5\, l_{BC}\, l_{CE}\, \cos\left(\tan^{-1}\left(\frac{l_{AH}-x_3}{l_{CD}}\right) + \theta_1 - \theta_5\right)\, {x_3}^2}{4} \\
&- \frac{l_{BC}\, l_{EF}\, \cos\left(\tan^{-1}\left(\frac{l_{AH}-x_3}{l_{CD}}\right) - \theta_1 + \theta_5 + \theta_{6r}\right)\, {x_3}^2}{4} \\
&- \frac{{l_{AH}}^2\, l_{BC}\, l_{CE}\, \cos\left(\tan^{-1}\left(\frac{l_{AH}-x_3}{l_{CD}}\right) - \theta_1 + 2\,\theta_4 - \theta_5\right)}{2} \\
&+ \frac{5\, l_{BC}\, l_{EF}\, \cos\left(\tan^{-1}\left(\frac{l_{AH}-x_3}{l_{CD}}\right) + \theta_1 - \theta_5 - \theta_{6r}\right)\, {x_3}^2}{4} \\
&- \frac{l_{BC}\, l_{CE}\, {x_3}^2\, \cos\left(\tan^{-1}\left(\frac{l_{AH}-x_3}{l_{CD}}\right) - \theta_1 - \theta_5\right)}{4} \\
&+ \frac{{l_{AH}}^2\, l_{BC}\, l_{EF}\, \cos\left(\tan^{-1}\left(\frac{l_{AH}-x_3}{l_{CD}}\right) - \theta_1 + 2\,\theta_4 - \theta_5 - \theta_{6r}\right)}{2} \\
&- \frac{{l_{AH}}^2\, l_{BC}\, l_{CE}\, \cos\left(\tan^{-1}\left(\frac{l_{AH}-x_3}{l_{CD}}\right) + \theta_1 - \theta_5\right)}{2} \\
&+ \frac{l_{BC}\, l_{EF}\, \cos\left(\tan^{-1}\left(\frac{l_{AH}-x_3}{l_{CD}}\right) + \theta_1 + \theta_5 + \theta_{6r}\right)\, {x_3}^2}{4} \\
&- \frac{l_{BC}\, l_{CE}\, \cos\left(\tan^{-1}\left(\frac{l_{AH}-x_3}{l_{CD}}\right) + \theta_1 + \theta_5\right)\, {x_3}^2}{4} \\
&+ \frac{l_{BC}\, l_{CE}\, \cos\left(\tan^{-1}\left(\frac{l_{AH}-x_3}{l_{CD}}\right) - \theta_1 + 2\,\theta_4 - \theta_5\right)\, {x_3}^2}{2} \\
&+ \frac{l_{BC}\, l_{EF}\, \cos\left(\tan^{-1}\left(\frac{l_{AH}-x_3}{l_{CD}}\right) - \theta_1 - \theta_5 - \theta_{6r}\right)\, {x_3}^2}{4} \\
&+ \frac{{l_{AH}}^2\, l_{BC}\, l_{EF}\, \cos\left(\tan^{-1}\left(\frac{l_{AH}-x_3}{l_{CD}}\right) + \theta_1 - \theta_5 - \theta_{6r}\right)}{2} \\
&+ \frac{l_{AH}\, l_{BC}\, l_{EF}\, \cos\left(\tan^{-1}\left(\frac{l_{AH}-x_3}{l_{CD}}\right) - \theta_1 + \theta_5 + \theta_{6r}\right)\, x_3}{4} \\
&+ \frac{l_{BC}\, l_{EF}\, \cos(\theta_1 - \theta_5 - \theta_{6r})\, {x_3}^2}{2\sqrt{\frac{(l_{AH}-x_3)^2}{{l_{CD}}^2} + 1}}
\end{aligned}
$$

$$+\frac{l_{BC}\,l_{CD}\,l_{EF}\,\sin\left(\tan^{-1}\left(\frac{l_{AH}-x_3}{l_{CD}}\right)-\theta_1+\theta_5+\theta_{6r}\right)\,x_3}{8}$$

$$+\frac{l_{BC}\,l_{CD}\,l_{EF}\,\sin\left(\tan^{-1}\left(\frac{l_{AH}-x_3}{l_{CD}}\right)-\theta_1+2\,\theta_4-\theta_5-\theta_{6r}\right)\,x_3}{2}$$

$$+\frac{7\,l_{AH}\,l_{BC}\,l_{CE}\,\cos\left(\tan^{-1}\left(\frac{l_{AH}-x_3}{l_{CD}}\right)+\theta_1-\theta_5\right)\,x_3}{4}$$

$$-\frac{l_{AH}\,l_{BC}\,l_{CE}\,\cos\left(\tan^{-1}\left(\frac{l_{AH}-x_3}{l_{CD}}\right)-\theta_1+\theta_5\right)\,x_3}{4}$$

$$-\frac{3\,l_{BC}\,l_{CD}\,l_{CE}\,\sin\left(\tan^{-1}\left(\frac{l_{AH}-x_3}{l_{CD}}\right)+\theta_1-\theta_5\right)\,x_3}{2}$$

$$+l_{AH}\,l_{BC}\,l_{CD}\,l_{CE}\,\sin\left(\tan^{-1}\left(\frac{l_{AH}-x_3}{l_{CD}}\right)-\theta_1+2\,\theta_4-\theta_5\right)$$

$$-\frac{l_{BC}\,l_{EF}\,\cos(\theta_1+\theta_5+\theta_{6r})\,{x_3}^2}{2\sqrt{\frac{(l_{AH}-x_3)^2}{{l_{CD}}^2}+1}}$$

$$-\frac{7\,l_{AH}\,l_{BC}\,l_{EF}\,\cos\left(\tan^{-1}\left(\frac{l_{AH}-x_3}{l_{CD}}\right)+\theta_1-\theta_5-\theta_{6r}\right)\,x_3}{4}$$

$$+\frac{l_{BC}\,l_{CE}\,\cos(\theta_1+\theta_5)\,{x_3}^2}{2\sqrt{\frac{(l_{AH}-x_3)^2}{{l_{CD}}^2}+1}}$$

$$+\frac{11\,l_{BC}\,l_{CD}\,l_{EF}\,x_3\,\sin\left(\tan^{-1}\left(\frac{l_{AH}-x_3}{l_{CD}}\right)+\theta_1-\theta_5-\theta_{6r}\right)}{8}$$

$$+\frac{l_{AH}\,l_{BC}\,l_{CE}\,x_3\,\cos\left(\tan^{-1}\left(\frac{l_{AH}-x_3}{l_{CD}}\right)-\theta_1-\theta_5\right)}{4}$$

$$-l_{AH}\,l_{BC}\,l_{CD}\,l_{EF}\,\sin\left(\tan^{-1}\left(\frac{l_{AH}-x_3}{l_{CD}}\right)-\theta_1+2\,\theta_4-\theta_5-\theta_{6r}\right)$$

$$-\frac{l_{AH}\,l_{BC}\,l_{EF}\,\cos\left(\tan^{-1}\left(\frac{l_{AH}-x_3}{l_{CD}}\right)+\theta_1+\theta_5+\theta_{6r}\right)\,x_3}{4}$$

$$+l_{AH}\,l_{BC}\,l_{CD}\,l_{CE}\,\sin\left(\tan^{-1}\left(\frac{l_{AH}-x_3}{l_{CD}}\right)+\theta_1-\theta_5\right)$$

$$
\begin{aligned}
&- \frac{l_{BC}\, l_{CD}\, l_{EF}\, \sin\left(\tan^{-1}\left(\frac{l_{AH}-x_3}{l_{CD}}\right) + \theta_1 + \theta_5 + \theta_{6r}\right)\, x_3}{8} \\
&+ \frac{l_{AH}\, l_{BC}\, l_{CE}\, \cos\left(\tan^{-1}\left(\frac{l_{AH}-x_3}{l_{CD}}\right) + \theta_1 + \theta_5\right)\, x_3}{4} \\
&- \frac{l_{AH}\, l_{BC}\, l_{EF}\, \cos\left(\tan^{-1}\left(\frac{l_{AH}-x_3}{l_{CD}}\right) - \theta_1 - \theta_5 - \theta_{6r}\right)\, x_3}{4} \\
&- \frac{l_{BC}\, l_{CE}\, {x_3}^2\, \cos(\theta_1 - \theta_5)}{2\sqrt{\frac{(l_{AH}-x_3)^2}{{l_{CD}}^2} + 1}} \\
&- \frac{l_{BC}\, l_{CD}\, l_{CE}\, \sin\left(\tan^{-1}\left(\frac{l_{AH}-x_3}{l_{CD}}\right) - \theta_1 + 2\,\theta_4 - \theta_5\right)\, x_3}{2} \\
&+ \frac{l_{BC}\, l_{CD}\, l_{EF}\, \sin\left(\tan^{-1}\left(\frac{l_{AH}-x_3}{l_{CD}}\right) - \theta_1 - \theta_5 - \theta_{6r}\right)\, x_3}{8} \\
&- l_{AH}\, l_{BC}\, l_{CD}\, l_{EF}\, \sin\left(\tan^{-1}\left(\frac{l_{AH}-x_3}{l_{CD}}\right) + \theta_1 - \theta_5 - \theta_{6r}\right) \\
&- \frac{l_{AH}\, l_{BC}\, l_{EF}\, \cos(\theta_1 - \theta_5 - \theta_{6r})\, x_3}{2\sqrt{\frac{(l_{AH}-x_3)^2}{{l_{CD}}^2} + 1}} \\
&+ \frac{l_{BC}\, l_{CD}\, l_{EF}\, \sin(\theta_1 - \theta_5 - \theta_{6r})\, x_3}{4\sqrt{\frac{(l_{AH}-x_3)^2}{{l_{CD}}^2} + 1}} \\
&+ \frac{l_{AH}\, l_{BC}\, l_{EF}\, \cos(\theta_1 + \theta_5 + \theta_{6r})\, x_3}{2\sqrt{\frac{(l_{AH}-x_3)^2}{{l_{CD}}^2} + 1}} \\
&+ \frac{l_{BC}\, l_{CD}\, l_{EF}\, \sin(\theta_1 + \theta_5 + \theta_{6r})\, x_3}{4\sqrt{\frac{(l_{AH}-x_3)^2}{{l_{CD}}^2} + 1}} \\
&- \frac{l_{AH}\, l_{BC}\, l_{CE}\, \cos(\theta_1 + \theta_5)\, x_3}{2\sqrt{\frac{(l_{AH}-x_3)^2}{{l_{CD}}^2} + 1}} + \frac{l_{AH}\, l_{BC}\, l_{CE}\, x_3\, \cos(\theta_1 - \theta_5)}{2\sqrt{\frac{(l_{AH}-x_3)^2}{{l_{CD}}^2} + 1}} \\
d_{4,1} = {} & l_{FH}\, x_3\, (l_{EF}\, \cos(\theta_{HFG} + \theta_5 - \theta_8 + \theta_{6r}) \\
& - l_{CE}\, \cos(\theta_{HFG} + \theta_5 - \theta_8))
\end{aligned}
$$

The derivative of the Jacobian is evaluated numerically using (1.2).

$$\dot{\mathbf{J}}(t) = \frac{\mathbf{J}(t) - \mathbf{J}(t - \Delta t)}{\Delta t} \tag{1.2}$$

Bibliography

[1] Sergei V. Adamovich, Alma S. Merians, Rares Boian, Jeffrey A. Lewis, Marilyn Tremaine, Grigore S. Burdea, Michael Recce, and Howard Poizner. A virtual reality-based exercise system for hand rehabilitation post-stroke. *Presence: Teleoperators and Virtual Environments*, 14(2):161–174, 2005.

[2] Priyanshu Agarwal and Ashish D. Deshpande. Impedance and force-field control of the index finger module of a hand exoskeleton for rehabilitation. In *IEEE International Conference on Rehabilitation Robotics*, pages 85–90, 2015.

[3] Priyanshu Agarwal, Benito R. Fernandez, and Ashish D. Deshpande. Assist-as-needed controllers for index finger module of a hand exoskeleton for rehabilitation. In *ASME Dynamic Systems and Control Conference*, page V003T42A002, 2015.

[4] Priyanshu Agarwal, Jonas Fox, Youngmok Yun, Marcia K. O'Malley, and Ashish D. Deshpande. An index finger exoskeleton with series elastic actuation for rehabilitation: Design, control and performance characterization. *The International Journal of Robotics Research*, 34(14):1747–1772, 2015.

[5] Priyanshu Agarwal, Arnold Hechanova, and Ashish D. Deshpande. Kinematics and dynamics of a biologically inspired index finger exoskeleton. In *ASME 2013 Dynamic Systems and Control Conference*, page V002T28A001, 2013.

[6] Priyanshu Agarwal, Pei-Hsin Kuo, Richard R. Neptune, and Ashish D. Deshpande. A novel framework for virtual prototyping of rehabilitation exoskeletons. In *IEEE International Conference on Rehabilitation Robotics*, pages 1–6, 2013.

[7] Gabriel Aguirre-Ollinger, J. Edward Colgate, Michael A. Peshkin, and Ambarish Goswami. Active-impedance control of a lower-limb assistive exoskeleton. In *IEEE International Conference on Rehabilitation Robotics*, pages 188–195, 2007.

[8] Manuel Aiple and Andre Schiele. Pushing the limits of the cybergrasp for haptic rendering. In *IEEE International Conference on Robotics and Automation*, pages 3541–3546, 2013.

[9] Jock Anderson. Examination and diagnosis of musculoskeletal disorders. *Australasian Radiology*, 46(2):216–217, 2002.

[10] Carlo Alberto Avizzano, F. Bargagli, Antonio Frisoli, and Massimo Bergamasco. The hand force feedback: analysis and control of a haptic device for the human-hand. In *IEEE International Conference on Systems, Man, and Cybernetics*, volume 2, pages 989–994, 2000.

[11] Sivakumar Balasubramanian, Ruihua Wei, Richard Herman, and Jiping He. Robot-measured performance metrics in stroke rehabilitation. In *IEEE International Conference on Complex Medical Engineering*, pages 1–6, 2009.

[12] C. H. Barnett and A. F. Cobbold. Effects of age upon the mobility of human finger joints. *Annals of the Rheumatic Diseases*, 27(2):175–177, 1968.

[13] E. Basafa, M. Sheikholeslami, A. Mirbagheri, F. Farahmand, and G. R. Vossoughi. Design and implementation of series elastic actuators for a haptic laparoscopic device. In *Proceedings of the international conference of the IEEE/EMBS*, pages 2–6, 2009.

[14] Nestor A. Bayona, Jamie Bitensky, Katherine Salter, and Robert Teasell. The role of task-specific training in rehabilitation therapies. *Topics in stroke rehabilitation*, 2015.

[15] Michael Bernhardt, Martin Frey, Gery Colombo, and Robert Riener. Hybrid force-position control yields cooperative behaviour of the rehabilitation robot lokomat. In *IEEE International Conference on Rehabilitation Robotics*, pages 536–539, 2005.

[16] Amy A. Blank, James A. French, Ali Utku Pehlivan, and Marcia K. OMalley. Current trends in robot-assisted upper-limb stroke rehabilitation: promoting patient engagement in therapy. *Current physical medicine and rehabilitation reports*, 2(3):184–195, 2014.

[17] Mourad Bouzit, Grigore Burdea, George Popescu, and Rares Boian. The Rutgers Master II-new design force-feedback glove. *IEEE/ASME Transactions on Mechatronics*, 7(2):256–263, 2002.

[18] Matthew W. Brault. *Americans with disabilities: 2010*. US Department of Commerce, Economics and Statistics Administration, US Census Bureau, 2012.

[19] E. B. Brokaw, I. Black, R. J. Holley, and P. S. Lum. Hand spring operated movement enhancer (HandSOME): a portable, passive hand exoskeleton for stroke rehabilitation. *IEEE Transactions on Neural Systems and Rehabilitation Engineering*, 19(4):391–399, 2011.

[20] Grigore Burdea and Jiachen Zhuang. Dextrous telerobotics with force feedback–an overview: Part 2. control and implementation. *Robotica*, 9(3):291–298, 1991.

[21] Magnus K. O. Burstedt, J. Randall Flanagan, and Roland S. Johansson. Control of grasp stability in humans under different frictional conditions during multidigit manipulation. *Journal of neurophysiology*, 82(5):2393–2405, 1999.

[22] R. H. Byrd, M. E. Hribar, and J. Nocedal. An interior point algorithm for large-scale nonlinear programming. *SIAM Journal on Optimization*, 9(4):877–900, 1999.

[23] Lance L. Cai, Andy J. Fong, Chad K. Otoshi, Yongqiang Liang, Joel W. Burdick, Roland R. Roy, and V. Reggie Edgerton. Implications of assist-as-needed robotic step training after a complete spinal cord injury on intrinsic strategies of motor learning. *The Journal of Neuroscience*, 26(41):10564–10568, 2006.

[24] Giorgio Carpino, Dino Accoto, Fabrizio Sergi, Nevio Luigi Tagliamonte, and Eugenio Guglielmelli. A novel compact torsional spring for series elastic actuators for assistive wearable robots. *Journal of Mechanical Design*, 134(12):121002, 2012.

[25] Luis Nicolas Gonzalez Castro, Alkis M. Hadjiosif, Matthew A. Hemphill, and Maurice A. Smith. Environmental consistency determines the rate of motor adaptation. *Current Biology*, 24(10):1050–1061, 2014.

[26] Besir Celebi, Mustafa Yalcin, and Volkan Patoglu. Assiston-knee: A self-aligning knee exoskeleton. In *IROS*, pages 996–1002, 2013.

[27] Marco Cempini, Mario Cortese, and Nicola Vitiello. A powered finger–thumb wearable hand exoskeleton with self-aligning joint axes. *IEEE/ASME Transactions on Mechatronics*, 20(2):705–716, 2015.

[28] Richmond B. Chan and Dudley S. Childress. On information transmission in human-machine systems: channel capacity and optimal filtering. *IEEE Transactions on Systems, Man and Cybernetics*, 20(5):1136–1145, 1990.

[29] Won Hyuk Chang and Yun-Hee Kim. Robot-assisted therapy in stroke rehabilitation. *Journal of stroke*, 15(3):174–181, 2013.

[30] Ward Cheney and David Kincaid. *Linear algebra: Theory and applications*. Jones and Bartlett, 2009.

[31] Shawn A. Chillag and Stephen Greenberg. An Unusual Cause of Trigger Finger. *New England Journal of Medicine*, 365(7), 2011.

[32] Azzurra Chiri, Nicola Vitiello, Francesco Giovacchini, Stefano Roccella, Fabrizio Vecchi, and Maria Chiara Carrozza. Mechatronic design and characterization of the index finger module of a hand exoskeleton for post-stroke rehabilitation. *IEEE/ASME Transactions on Mechatronics*, 17(5):884–894, 2012.

[33] Roberto Colombo, Fabrizio Pisano, Silvestro Micera, Alessandra Mazzone, Carmen Delconte, M. Chiara Carrozza, Paolo Dario, and Giuseppe Minuco. Robotic techniques for upper limb evaluation and rehabilitation of stroke patients. *IEEE Transactions on Neural Systems and Rehabilitation Engineering*, 13(3):311–324, 2005.

[34] William P. Cooney, Michael J. Lucca, E. Y. Chao, and R. L. Linscheid. The kinesiology of the thumb trapeziometacarpal joint. *The Journal of Bone & Joint Surgery*, 63(9):1371–1381, 1981.

[35] Agostino De Santis, Bruno Siciliano, Alessandro De Luca, and Antonio Bicchi. An atlas of physical human–robot interaction. *Mechanism and*

Machine Theory, 43(3):253–270, 2008.

[36] Ashish D. Deshpande, Nick Gialias, and Yoky Matsuoka. Contributions of intrinsic visco-elastic torques during planar index finger and wrist movements. *IEEE Transactions on Biomedical Engineering*, 59(2):586–594, 2012.

[37] Matthew DiCicco, Lenny Lucas, and Yoky Matsuoka. Comparison of control strategies for an emg controlled orthotic exoskeleton for the hand. In *IEEE International Conference on Robotics and Automation*, volume 2, pages 1622–1627, 2004.

[38] Myron A. Diftler, J. S. Mehling, Muhammad E. Abdallah, Nicolaus A. Radford, Lyndon B. Bridgwater, Adam M. Sanders, Roger Scott Askew, D. Marty Linn, John D. Yamokoski, F. A. Permenter, et al. Robonaut 2-the first humanoid robot in space. In *ICRA*, pages 2178–2183, 2011.

[39] E. Dionysian, J. M. Kabo, F.J. Dorey, and R. A. Meals. Proximal interphalangeal joint stiffness: measurement and analysis. *The Journal of Hand Surgery*, 30(3):573–579, 2005.

[40] Aaron M Dollar. Classifying human hand use and the activities of daily living. In *The Human Hand as an Inspiration for Robot Hand Development*, pages 201–216. Springer, 2014.

[41] Ludovic Dovat, Olivier Lambercy, Berna Salman, Vineet Johnson, Theodore Milner, Roger Gassert, Etienne Burdet, and Teo C. Leong. A technique

to train finger coordination and independence after stroke. *Disability & Rehabilitation: Assistive Technology*, 5(4):279–287, 2010.

[42] Alex W. Dromerick. Clinical features of spasticity and principles of treatment. In *Clinical Evaluation and Management of Spasticity*, pages 13–26. Springer, 2002.

[43] Thomas A. Eidson and Robert E. Stadulis. Effects of variability of practice on the transfer and performance of open and closed motor skills. *Adapted physical activity quarterly*, 8(4):342–3556, 1991.

[44] Jorhabib Eljaik, Zhibin Li, Marco Randazzo, Alberto Parmiggiani, Giorgio Metta, Nikos G. Tsagarakis, and Francesco Nori. Quantitative evaluation of standing stabilization using stiff and compliant actuators. In *Robotics: science and systems*, 2013.

[45] Ergonomics for Schools. Hand tools. http://www.ergonomics4schools.com/lzone/tools.htm, 2008.

[46] A. Esteki and J. M. Mansour. An experimentally based nonlinear viscoelastic model of joint passive moment. *Journal of biomechanics*, 29(4):443–450, 1996.

[47] Ronald C. Evans. *Illustrated orthopedic physical assessment*. Elsevier Health Sciences, 2008.

[48] Robert Feeney. Specific anthropometric and strength data for people with dexterity disability. *Consumer and Competition Policy Directorate: Department of Trade and Industry*, 2002.

[49] Marco Fontana, Salsedo Fabio, Simone Marcheschi, and Massimo Bergamasco. Haptic hand exoskeleton for precision grasp simulation. *Journal of Mechanisms and Robotics*, 5(4):041014, 2013.

[50] Beverley French, Lois Thomas, Michael Leathley, Christopher Sutton, Joanna McAdam, Anne Forster, Peter Langhorne, Christopher Price, Andrew Walker, and Caroline Watkins. Does repetitive task training improve functional activity after stroke? a cochrane systematic review and meta-analysis. *Journal of rehabilitation medicine*, 42(1):9–15, 2010.

[51] Nizan Friedman, Vicky Chan, Andrea N. Reinkensmeyer, Ariel Beroukhim, Gregory J. Zambrano, Mark Bachman, and David J. Reinkensmeyer. Retraining and assessing hand movement after stroke using the musicglove: comparison with conventional hand therapy and isometric grip training. *Journal of neuroengineering and rehabilitation*, 11(1):1, 2014.

[52] Nadia Garcia-Hernandez, Ioannis Sarakoglou, Nikos Tsagarakis, and Darwin Caldwell. Under-actuated hand exoskeleton with novel kinematics for potential use in rehabilitation. In *EuroHaptics*, pages 463–465, 2014.

[53] Hugues Garnier, Michel Mensler, and Alain Richard. Continuous-time

model identification from sampled data: implementation issues and performance evaluation. *International Journal of Control*, 76(13):1337–1357, 2003.

[54] Marwan A. Gharaybeh and Grigore C. Burdea. Investigation of a shape memory alloy actuator for dextrous force-feedback masters. *Advanced robotics*, 9(3):317–329, 1994.

[55] Mark A. Guadagnoli and Timothy D. Lee. Challenge point: a framework for conceptualizing the effects of various practice conditions in motor learning. *Journal of motor behavior*, 36(2):212–224, 2004.

[56] Dr Guilherme N. DeSouza, Patrick Aubin, Kelsey Petersen, Hani Sallum, Conor Walsh, Annette Correia, and Leia Stirling. A pediatric robotic thumb exoskeleton for at-home rehabilitation: The isolated orthosis for thumb actuation (IOTA). *International Journal of Intelligent Computing and Cybernetics*, 7(3):233–252, 2014.

[57] Douglas H. Harrison. The stiff proximal interphalangeal joint. *The Hand*, 9(2):102–108, 1977.

[58] William S. Harwin, Tariq Rahman, and Richard A. Foulds. A review of design issues in rehabilitation robotics with reference to north american research. *IEEE Transactions on Rehabilitation Engineering*, 3(1):3–13, 1995.

[59] Yasuhisa Hasegawa, Yasuyuki Mikami, Kosuke Watanabe, and Yoshiyuki Sankai. Five-fingered assistive hand with mechanical compliance of human finger. In *IEEE International Conference on Robotics and Automation*, pages 718–724, 2008.

[60] Vincent Hayward and Oliver R. Astley. Performance measures for haptic interfaces. In *Robotics Research*, pages 195–206. Springer, 1996.

[61] Basil H. Helal. Extra-articular causes of proximal interphalangeal joint stiffness in rheumatoid arthritis. *The Hand*, 7(1):37–40, 1975.

[62] P. Heo, G.M. Gu, S. Lee, K. Rhee, and J. Kim. Current hand exoskeleton technologies for rehabilitation and assistive engineering. *International Journal of Precision Engineering and Manufacturing*, 13(5):807–824, 2012.

[63] Neville Hogan. Impedance control: An approach to manipulation: Part II–Implementation. *Journal of Dynamic Systems, Measurement, and Control*, 107(1):8–16, 1985.

[64] Neville Hogan, Hermano I Krebs, Brandon Rohrer, Jerome J. Palazzolo, Laura Dipietro, Susan E. Fasoli, Joel Stein, Richard Hughes, Walter R. Frontera, Daniel Lynch, et al. Motions or muscles? Some behavioral factors underlying robotic assistance of motor recovery. *Journal of Rehabilitation Research and Development*, 43(5):605, 2006.

[65] Courtney L. Holladay and Miguel A. Quinones. Practice variability and transfer of training: the role of self-efficacy generality. *Journal of applied psychology*, 88(6):1094, 2003.

[66] Isobel J. Hubbard, Mark W. Parsons, Cheryl Neilson, and Leeanne M. Carey. Task-specific training: evidence for and translation to clinical practice. *Occupational therapy international*, 16(3-4):175–189, 2009.

[67] C. H. Hwang, J. W. Seong, and D. S. Son. Individual finger synchronized robot-assisted hand rehabilitation in subacute to chronic stroke: a prospective randomized clinical trial of efficacy. *Clinical Rehabilitation*, 26(8):696–704, 2012.

[68] Auke Jan Ijspeert, Jun Nakanishi, Heiko Hoffmann, Peter Pastor, and Stefan Schaal. Dynamical movement primitives: learning attractor models for motor behaviors. *Neural computation*, 25(2):328–373, 2013.

[69] Tsuyoshi Ikegami, Masaya Hirashima, Rieko Osu, and Daichi Nozaki. Intermittent visual feedback can boost motor learning of rhythmic movements: evidence for error feedback beyond cycles. *The Journal of Neuroscience*, 32(2):653–657, 2012.

[70] HyunKi In and Kyu-Jin Cho. Analysis of the forces on the finger joints by a joint-less wearable robotic hand, snu exo-glove. In *Converging Clinical and Engineering Research on Neurorehabilitation*, pages 93–97. Springer, 2013.

[71] Xin Jin, Xiang Cui, and Sunil K. Agrawal. Design of a cable-driven active leg exoskeleton (C-ALEX) and gait training experiments with human subjects. In *IEEE International Conference on Robotics and Automation*, pages 5578–5583, 2015.

[72] Inseong Jo and Joonbum Bae. Design and control of a wearable hand exoskeleton with force-controllable and compact actuator modules. In *IEEE International Conference on Robotics and Automation*, pages 5596–5601, 2015.

[73] C. L. Jones, Furui Wang, R. Morrison, N. Sarkar, and D. G. Kamper. Design and development of the cable actuated finger exoskeleton for hand rehabilitation following stroke. *IEEE/ASME Transactions on Mechatronics*, 19(1):131–140, 2014.

[74] Lynette A. Jones and Susan J. Lederman. *Human hand function*. Oxford University Press, 2006.

[75] Makoto Kaneko, M. Wada, H. Maekawa, and K. Tanie. A new consideration on tendon-tension control system of robot hands. In *IEEE International Conference on Robotics and Automation*, pages 1028–1033, 1991.

[76] Pei-Chun Kao, Shraddha Srivastava, Sunil K. Agrawal, and John P. Scholz. Effect of robotic performance-based error-augmentation versus error-reduction training on the gait of healthy individuals. *Gait & posture*, 37(1):113–120, 2013.

[77] Bekir Karlik and A. Vehbi Olgac. Performance analysis of various activation functions in generalized mlp architectures of neural networks. *Int. J. Artificial Intell. Expert Syst*, 1(4):111–122, 2011.

[78] Nareen Karnati, Benjamin A. Kent, and Erik D. Engeberg. Bioinspired sinusoidal finger joint synergies for a dexterous robotic hand to screw and unscrew objects with different diameters. *IEEE/ASME Transactions on Mechatronics*, 18(2):612–623, 2013.

[79] Haruhisa Kawasaki, Hiroki Kimura, Satoshi Ito, Yutaka Nishimoto, Hiroyuki Hayashi, and Hirohumi Sakaeda. Hand rehabilitation support system based on self-motion control, with a clinical case report. In *World Automation Congress*, pages 1–6, 2006.

[80] Hiroshi Kjnoshita, Satoru Kawai, and Komei Ikuta. Contributions and co-ordination of individual fingers in multiple finger prehension. *Ergonomics*, 38(6):1212–1230, 1995.

[81] Julius Klein, Steven J. Spencer, and David J. Reinkensmeyer. Breaking it down is better: Haptic decomposition of complex movements aids in robot-assisted motor learning. *IEEE Transactions on Neural Systems and Rehabilitation Engineering*, 20(3):268–275, 2012.

[82] Kyoungchul Kong, Joonbum Bae, and Masayoshi Tomizuka. Control of rotary series elastic actuator for ideal force-mode actuation in human–robot interaction applications. *IEEE/ASME Transactions on Mechatronics*, 14(1):105–118, 2009.

[83] John W. Krakauer. Motor learning: its relevance to stroke recovery and neurorehabilitation. *Current opinion in neurology*, 19(1):84–90, 2006.

[84] K. Kuczynski. The proximal interphalangeal joint anatomy and causes of stiffness in the fingers. *Journal of Bone & Joint Surgery, British Volume*, 50(3):656–663, 1968.

[85] Pei-Hsin Kuo and Ashish D. Deshpande. Muscle-tendon units provide limited contributions to the passive stiffness of the index finger metacarpophalangeal joint. *Journal of Biomechanics*, 45(15):2531–2538, 2012.

[86] Gregorij Kurillo, Matjaž Mihelj, Marko Munih, and Tadej Bajd. Multi-fingered grasping and manipulation in virtual environments using an isometric finger device. *Presence*, 16(3):293–306, 2007.

[87] Gert Kwakkel, Boudewijn J. Kollen, and Robert C. Wagenaar. Therapy impact on functional recovery in stroke rehabilitation: a critical review of the literature. *Physiotherapy*, 85(7):377–391, 1999.

[88] Claude Lagoda, Alfred C. Schouten, Arno H. A. Stienen, Edsko E. G. Hekman, and Herman van der Kooij. Design of an electric series elastic actuated joint for robotic gait rehabilitation training. In *IEEE RAS and EMBS International Conference on Biomedical Robotics and Biomechatronics*, pages 21–26, 2010.

[89] Olivier Lambercy, David Schröder, Sven Zwicker, and Roger Gassert. Design of a thumb exoskeleton for hand rehabilitation. In *Proceedings*

of the 7th International Convention on Rehabilitation Engineering and Assistive Technology, page 41. Singapore Therapeutic, Assistive & Rehabilitative Technologies (START) Centre, 2013.

[90] Kyung-Sun Lee and Myung-Chul Jung. Ergonomic evaluation of biomechanical hand function. *Safety and Health at Work*, 2014.

[91] Daniele Leonardis, Michele Barsotti, Claudio Loconsole, Massimiliano Solazzi, Marco Troncossi, Claudio Mazzotti, Vincenzo Parenti Castelli, Caterina Procopio, Giuseppe Lamola, Carmelo Chisari, et al. An EMG-controlled robotic hand exoskeleton for bilateral rehabilitation. *IEEE Transactions on Haptics*, 8(2):140–151, 2015.

[92] Pamela K. Levangie and Cynthia C. Norkin. *Joint structure and function: a comprehensive analysis*. FA Davis, 2011.

[93] Jiting Li, Ruoyin Zheng, Yuru Zhang, and Jianchu Yao. iHandRehab: An interactive hand exoskeleton for active and passive rehabilitation. In *IEEE International Conference on Rehabilitation Robotics*, pages 1–6, 2011.

[94] Zong-Ming Li and Jie Tang. Coordination of thumb joints during opposition. *Journal of Biomechanics*, 40(3):502–510, 2007.

[95] Neal Y. Lii, Zhaopeng Chen, Benedikt Pleintinger, Christoph H. Borst, Gerd Hirzinger, and Andre Schiele. Toward understanding the effects of visual-and force-feedback on robotic hand grasping performance for

space teleoperation. In *IEEE/RSJ International Conference on Intelligent Robots and Systems*, pages 3745–3752, 2010.

[96] Hwai-Ting Lin, Li-Chieh Kuo, Hsin-Yi Liu, Wen-Lan Wu, and Fong-Chin Su. The three-dimensional analysis of three thumb joints coordination in activities of daily living. *Clinical Biomechanics*, 26(4):371–376, 2011.

[97] Lennart Ljung. Informative experiments. In *System identification: theory for the user*, pages 361–369. Prentice Hall Inc. and System Sciences Series, New Jersey, 1999.

[98] Martin Lotze, Christoph Braun, Niels Birbaumer, Silke Anders, and Leonardo G. Cohen. Motor learning elicited by voluntary drive. *Brain*, 126(4):866–872, 2003.

[99] Lenny Lucas, Matthew DiCicco, and Yoky Matsuoka. An EMG-controlled hand exoskeleton for natural pinching. *Journal of Robotics and Mechatronics*, 16:482–488, 2004.

[100] Peter S. Lum, Charles G. Burgar, Peggy C. Shor, Matra Majmundar, and Machiel Van der Loos. Robot-assisted movement training compared with conventional therapy techniques for the rehabilitation of upper-limb motor function after stroke. *Archives of Physical Medicine and Rehabilitation*, 83(7):952–959, 2002.

[101] Paxton Maeder-York, Tyler Clites, Emily Boggs, Ryan Neff, Panagiotis Polygerinos, Dónal Holland, Leia Stirling, Kevin Galloway, Catherine Wee, and Conor Walsh. Biologically inspired soft robot for thumb rehabilitation. *Journal of Medical Devices*, 8(2):020933–1–3, 2014.

[102] Laura Marchal-Crespo and David J. Reinkensmeyer. Review of control strategies for robotic movement training after neurologic injury. *Journal of Neuroengineering and Rehabilitation*, 6(1):20, 2009.

[103] Matthew T. Mason. Compliance and force control for computer controlled manipulators. *IEEE Transactions on Systems, Man and Cybernetics*, 11(6):418–432, 1981.

[104] Wei Meng, Quan Liu, Zude Zhou, Qingsong Ai, Bo Sheng, and Shengquan S. Xie. Recent development of mechanisms and control strategies for robot-assisted lower limb rehabilitation. *Mechatronics*, 31:132–145, 2015.

[105] Marie-Hélène Milot, Laura Marchal-Crespo, Christopher S. Green, Steven C. Cramer, and David J. Reinkensmeyer. Comparison of error-amplification and haptic-guidance training techniques for learning of a timing-based motor task by healthy individuals. *Experimental brain research*, 201(2):119–131, 2010.

[106] Anat Mirelman, Paolo Bonato, and Judith E. Deutsch. Effects of training with a robot-virtual reality system compared with a robot alone on the gait of individuals after stroke. *Stroke*, 40(1):169–174, 2009.

[107] Birgit I. Molier, Edwin HF Van Asseldonk, Hermie J. Hermens, and Michiel J. A. Jannink. Nature, timing, frequency and type of augmented feedback; does it influence motor relearning of the hemiparetic arm after stroke? a systematic review. *Disability and rehabilitation*, 32(22):1799–1809, 2010.

[108] John Moody and Christian J. Darken. Fast learning in networks of locally-tuned processing units. *Neural computation*, 1(2):281–294, 1989.

[109] James M. Moran, John H. Hemann, and A. Seth Greenwald. Finger joint contact areas and pressures. *Journal of Orthopaedic Research*, 3(1):49–55, 1985.

[110] John B. Morrell and J. Kenneth Salisbury. Parallel-coupled micro-macro actuators. *The International Journal of Robotics Research*, 17(7):773–791, 1998.

[111] Dariush Mozaffarian, Emelia J. Benjamin, Alan S. Go, Donna K. Arnett, Michael J. Blaha, Mary Cushman, Sarah de Ferranti, Jean-Pierre Despres, Heather J. Fullerton, Virginia J. Howard, et al. Heart disease and stroke statistics-2015 update: a report from the american heart association. *Circulation*, 131(4):e29, 2015.

[112] Marcello Mulas, Michele Folgheraiter, and Giuseppina Gini. An EMG-controlled exoskeleton for hand rehabilitation. In *IEEE International Conference on Rehabilitation Robotics*, pages 371–374, 2005.

[113] Robert L. Norton. *Design of machinery: an introduction to the synthesis and analysis of mechanisms and machines*. WCB McGraw-Hill, 1999.

[114] James L. Patton, Mary Ellen Stoykov, Mark Kovic, and Ferdinando A. Mussa-Ivaldi. Evaluation of robotic training forces that either enhance or reduce error in chronic hemiparetic stroke survivors. *Experimental brain research*, 168(3):368–383, 2006.

[115] Sabrina Tiago Pedão, José Angelo Barela, Kauê Carvalho de Almeida Lima, and Paulo Barbosa De Freitas. Grip and load force coordination in cyclical isometric manipulation task is not affected by the feedback type. *Journal of neuroengineering and rehabilitation*, 10(1):1, 2013.

[116] Alessandra Pedrocchi, Simona Ferrante, Emilia Ambrosini, Marta Gandolla, Claudia Casellato, Thomas Schauer, Christian Klauer, Javier Pascual, Carmen Vidaurre, Margit Gföhler, et al. MUNDUS project: MUltimodal Neuroprosthesis for daily Upper limb Support. *Journal of Neuroengineering and Rehabilitation*, 10:66, 2013.

[117] Ali Utku Pehlivan, Fabrizio Sergi, and Marcia K. O'Malley. A subject-adaptive controller for wrist robotic rehabilitation. *IEEE/ASME Transactions on Mechatronics*, 20(3):1338–1350, 2015.

[118] Ali Utku Pehlivan, Fabrizio Sergi, and Marcia K. O'Malley. A subject-adaptive controller for wrist robotic rehabilitation. *IEEE/ASME Transactions on Mechatronics*, 20(3):1338–1350, 2015.

[119] Monica A. Perez, Bjarke K. S. Lungholt, Kathinka Nyborg, and Jens B. Nielsen. Motor skill training induces changes in the excitability of the leg cortical area in healthy humans. *Experimental Brain Research*, 159(2):197–205, 2004.

[120] Gill A. Pratt and Matthew M. Williamson. Series elastic actuators. In *IROS*, pages 399–406, 1995.

[121] Yupeng Ren, Hyung-Soon Park, and Li-Qun Zhang. Developing a whole-arm exoskeleton robot with hand opening and closing mechanism for upper limb stroke rehabilitation. In *IEEE International Conference on Rehabilitation Robotics*, pages 761–765, 2009.

[122] L. Nortron Robert. *Machine Design An Integrated Approach*. Pearson Prentice Hall Publishers, USA, 2006.

[123] David William Robinson. *Design and analysis of series elasticity in closed-loop actuator force control*. PhD thesis, Massachusetts Institute of Technology, 2000.

[124] David Rollinson, Steven Ford, Ben Brown, and Howie Choset. Design and modeling of a series elastic element for snake robots. In *ASME Dynamic Systems and Control Conference*, 2013.

[125] J. Kenneth Salisbury. Active stiffness control of a manipulator in Cartesian coordinates. In *IEEE Conference on Decision and Control includ-*

ing the Symposium on Adaptive Processes, volume 19, pages 95–100, 1980.

[126] Veronica J. Santos and Francisco J. Valero-Cuevas. Reported anatomical variability naturally leads to multimodal distributions of denavit-hartenberg parameters for the human thumb. *IEEE Transactions on Biomedical Engineering*, 53(2):155–163, 2006.

[127] Ioannis Sarakoglou, Nikolaos G. Tsagarakis, and Darwin G. Caldwell. Occupational and physical therapy using a hand exoskeleton based exerciser. In *IEEE/RSJ International Conference on Intelligent Robots and Systems*, volume 3, pages 2973–2978, 2004.

[128] C. N. Schabowsky, S. B. Godfrey, R. J. Holley, and P. S. Lum. Development and pilot testing of HEXORR: Hand exoskeleton rehabilitation robot. *Journal of NeuroEngineering and Rehabilitation*, 7(1):1–16, 2010.

[129] Andre Schiele, Pierre Letier, Richard Van Der Linde, and Frans Van Der Helm. Bowden cable actuator for force-feedback exoskeletons. In *IROS*, pages 3599–3604, 2006.

[130] Richard A. Schmidt. A schema theory of discrete motor skill learning. *Psychological review*, 82(4):225, 1975.

[131] Richard A. Schmidt. Motor learning principles for physical therapy. In *Contemporary management of motor control problems: Proceedings*

of the II STEP Conference. Alexandria, VA: Foundation for Physical Therapy, pages 49–62, 1991.

[132] Richard A. Schmidt and Robert A. Bjork. New conceptualizations of practice: Common principles in three paradigms suggest new concepts for training. *Psychological science*, 3(4):207–217, 1992.

[133] Richard A. Schmidt and Tim Lee. *Motor control and learning*. Human kinetics, 1988.

[134] Jonathon W. Sensinger and R. F. Weir. User-modulated impedance control of a prosthetic elbow in unconstrained, perturbed motion. *IEEE Transactions on Biomedical Engineering*, 55(3):1043–1055, 2008.

[135] Luis Sentis, Josh Petersen, and Roland Philippsen. Experiments with balancing on irregular terrains using the dreamer mobile humanoid robot. In *Robotics: Science and Systems*, 2012.

[136] Luis Sentis, Josh Petersen, and Roland Philippsen. Implementation and stability analysis of prioritized whole-body compliant controllers on a wheeled humanoid robot in uneven terrains. *Autonomous Robots*, 35(4):301–319, 2013.

[137] Fabrizio Sergi, Dino Accoto, Giorgio Carpino, Nevio Luigi Tagliamonte, and Eugenio Guglielmelli. Design and characterization of a compact rotary series elastic actuator for knee assistance during overground walk-

ing. In *IEEE RAS & EMBS International Conference on Biomedical Robotics and Biomechatronics*, pages 1931–1936, 2012.

[138] Fabrizio Sergi, Melissa M. Lee, and Marcia K. O'Malley. Design of a series elastic actuator for a compliant parallel wrist rehabilitation robot. In *IEEE International Conference on Rehabilitation Robotics*, pages 1–6, 2013.

[139] Reza Shadmehr, Maurice A. Smith, and John W. Krakauer. Error correction, sensory prediction, and adaptation in motor control. *Annual review of neuroscience*, 33:89–108, 2010.

[140] Charles H. Shea and Robert M. Kohl. Composition of practice: Influence on the retention of motor skills. *Research quarterly for exercise and sport*, 62(2):187–195, 1991.

[141] T. B. Sheridan and W. R. Ferrell. *Man-Machine Systems: Introductory Control and Decision Models of Human Performance*. Cambridge, MA: MIT Press, 1974.

[142] David E. Sherwood and Timothy D. Lee. Schema theory: critical review and implications for the role of cognition in a new theory of motor learning. *Research quarterly for exercise and sport*, 74(4):376–382, 2003.

[143] Roland Sigrist, Georg Rauter, Robert Riener, and Peter Wolf. Augmented visual, auditory, haptic, and multimodal feedback in motor learning: A review. *Psychonomic bulletin & review*, 20(1):21–53, 2013.

[144] W. Paul Smutz, Apichai Kongsayreepong, Richard E. Hughes, Glen Niebur, William P. Cooney, and Kai-Nan An. Mechanical advantage of the thumb muscles. *Journal of Biomechanics*, 31(6):565–570, 1998.

[145] P. N. Soucacos. Indications and selection for digital amputation and replantation. *Journal of Hand Surgery (British and European Volume)*, 26(6):572–581, 2001.

[146] Ian H. Stevenson, Hugo L. Fernandes, Iris Vilares, Kunlin Wei, and Konrad P. Krding. Bayesian integration and non-linear feedback control in a full-body motor task. *PLoS Comput Biol*, 5(12):e1000629, 12 2009.

[147] Arno H. A. Stienen, Edsko E. G. Hekman, Huub ter Braak, Arthur MM Aalsma, Frans C. T. van der Helm, and Herman van der Kooij. Design of a rotational hydroelastic actuator for a powered exoskeleton for upper limb rehabilitation. *IEEE Transactions on Biomedical Engineering*, 57(3):728–735, 2010.

[148] James S. Sulzer, Ronald A. Roiz, Michael A. Peshkin, and James L. Patton. A highly backdrivable, lightweight knee actuator for investigating gait in stroke. *IEEE Transactions on Robotics*, 25(3):539–548, 2009.

[149] Alfred B. Swanson, Carl Göran-Hagert, and Genevieve de Groot Swanson. Evaluation of impairment in the upper extremity. *The Journal of hand surgery*, 12(5):896–926, 1987.

[150] Hossein Taheri, Justin B. Rowe, David Gardner, Vicki Chan, Kyle Gray, Curtis Bower, David J. Reinkensmeyer, and Eric T. Wolbrecht. Design and preliminary evaluation of the finger rehabilitation robot: controlling challenge and quantifying finger individuation during musical computer game play. *Journal of Neuroengineering and Rehabilitation*, 11(1):10, 2014.

[151] Motoki Takagi, Kie Iwata, Yoshiyuki Takahashi, S-i Yamamoto, Hiroyuki Koyama, and Takashi Komeda. Development of a grip aid system using air cylinders. In *IEEE International Conference on Robotics and Automation*, pages 2312–2317, 2009.

[152] C. D. Takahashi, L. Der-Yeghiaian, V. Le, R. R. Motiwala, and S. C. Cramer. Robot-based hand motor therapy after stroke. *Brain*, 131(2):425–437, 2008.

[153] Ken Takiyama, Masaya Hirashima, and Daichi Nozaki. Prospective errors determine motor learning. *Nature communications*, 6, 2015.

[154] K. Y. Tong, S. K. Ho, P. M. K. Pang, X. L. Hu, W. K. Tam, K. L. Fung, X. J. Wei, P. N. Chen, and M. Chen. An intention driven hand functions task training robotic system. In *Annual International Conference of the IEEE Engineering in Medicine and Biology Society*, pages 3406–3409, 2010.

[155] Larry E. Toothaker. *Multiple comparison procedures*. Sage, 1993.

[156] Kiminori Toya, Toyomi Miyagawa, and Yuji Kubota. Power-assist glove operated by predicting the grasping mode. *Journal of System Design and Dynamics*, 5(1):94–108, 2011.

[157] Satoshi Ueki, Haruhisa Kawasaki, Satoshi Ito, Yutaka Nishimoto, Motoyuki Abe, Takaaki Aoki, Yasuhiko Ishigure, Takeo Ojika, and Tetsuya Mouri. Development of a hand-assist robot with multi-degrees-of-freedom for rehabilitation therapy. *IEEE/ASME Transactions on Mechatronics*, 17(1):136–146, 2012.

[158] Francisco J. Valero-Cuevas. Predictive modulation of muscle coordination pattern magnitude scales fingertip force magnitude over the voluntary range. *Journal of Neurophysiology*, 83(3):1469–1479, 2000.

[159] Francisco J. Valero-Cuevas, Felix E. Zajac, and Charles G. Burgar. Large index-fingertip forces are produced by subject-independent patterns of muscle excitation. *Journal of biomechanics*, 31(8):693–703, 1998.

[160] Heike Vallery, Alexander Duschau-Wicke, and Robert Riener. Optimized passive dynamics improve transparency of haptic devices. In *IEEE International Conference on Robotics and Automation*, pages 301–306, 2009.

[161] Heike Vallery, Jan Veneman, Edwin Van Asseldonk, Ralf Ekkelenkamp, Martin Buss, and Herman Van Der Kooij. Compliant actuation of reha-

bilitation robots. *IEEE Robotics & Automation Magazine*, 15(3):60–69, 2008.

[162] Jacques H. A. Van Rossum. Schmidt's schema theory: The empirical base of the variability of practice hypothesis: A critical analysis. *Human Movement Science*, 9(3):387–435, 1990.

[163] Jan F. Veneman, Ralf Ekkelenkamp, Rik Kruidhof, Frans C. T. van der Helm, and Herman van der Kooij. A series elastic-and bowden-cable-based actuation system for use as torque actuator in exoskeleton-type robots. *The International Journal of Robotics Research*, 25(3):261–281, 2006.

[164] Furui Wang, Milind Shastri, Christopher L. Jones, Vikash Gupta, Christian Osswald, Xuan Kang, Derek G. Kamper, and Nilanjan Sarkar. Design and control of an actuated thumb exoskeleton for hand rehabilitation following stroke. In *IEEE International Conference on Robotics and Automation*, pages 3688–3693, 2011.

[165] Shuang Wang, Jiting Li, Ruoyin Zheng, Zhongyuan Chen, and Yuru Zhang. Multiple rehabilitation motion control for hand with an exoskeleton. In *IEEE International Conference on Robotics and Automation*, pages 3676–3681, 2011.

[166] A. Wege and G. Hommel. Development and control of a hand exoskeleton for rehabilitation of hand injuries. In *IEEE/RSJ International Conference on Intelligent Robots and Systems*, pages 3046–3051, 2005.

[167] Andreas Wege, Konstantin Kondak, and Guenter Hommel. Force control strategy for a hand exoskeleton based on sliding mode position control. In *IEEE/RSJ International Conference on Intelligent Robots and Systems*, pages 4615–4620, 2006.

[168] Kunlin Wei and Konrad Körding. Uncertainty of feedback and state estimation determines the speed of motor adaptation. *Frontiers in computational neuroscience*, 4, 2010.

[169] Dietrich Wettschereck and Thomas Dietterich. Improving the performance of radial basis function networks by learning center locations. In *NIPS*, volume 4, pages 1133–1140, 1991.

[170] Matthew M. Williamson. Series elastic actuators. Master's thesis, Massachusetts Institute of Technology, 1995.

[171] Carolee J. Winstein, Patricia S. Pohl, and Rebecca Lewthwaite. Effects of physical guidance and knowledge of results on motor learning: support for the guidance hypothesis. *Research quarterly for exercise and sport*, 65(4):316–323, 1994.

[172] Eric T. Wolbrecht, Vicky Chan, David J. Reinkensmeyer, and James E. Bobrow. Optimizing compliant, model-based robotic assistance to promote neurorehabilitation. *IEEE Transactions on Neural Systems and Rehabilitation Engineering*, 16(3):286–297, 2008.

[173] John Z. Wu, Kai-Nan An, Robert G. Cutlip, Kristine Krajnak, Daniel Welcome, and Ren G. Dong. Analysis of musculoskeletal loading in an index finger during tapping. *Journal of Biomechanics*, 41(3):668–676, 2008.

[174] Gordon Wyeth. Demonstrating the safety and performance of a velocity sourced series elastic actuator. In *ICRA*, pages 3642–3647, 2008.

[175] Hao Yu, Philip D. Reiner, Tiantian Xie, Tomasz Bartczak, and Bogdan M. Wilamowski. An incremental design of radial basis function networks. *IEEE transactions on neural networks and learning systems*, 25(10):1793–1803, 2014.

[176] Damiano Zanotto, Paul Stegall, and Sunil K. Agrawal. Adaptive assist-as-needed controller to improve gait symmetry in robot-assisted gait training. In *IEEE International Conference on Robotics and Automation*, pages 724–729, 2014.

[177] Eleni Zetou, Leonidas Papadakis, Nikolaos Vernadakis, Vassiliki Derri, Evangelos Bebetsos, and Filippos Filippou. The effect of variable and stable practice on performance and learning the header skill of young athletes in soccer. *Procedia-Social and Behavioral Sciences*, 152:824–829, 2014.

[178] Jilin Zhou, François Malric, and Shervin Shirmohammadi. A new hand-measurement method to simplify calibration in cyberglove-based virtual

rehabilitation. *IEEE Transactions on Instrumentation and Measurement*, 59(10):2496–2504, 2010.

Vita

Priyanshu Agarwal received his Bachelor of Technology (B.Tech) degree in Mechanical Engineering from Motilal Nehru National Institute of Technology, Allahabad, India in 2007. He worked for two years in the Research and Development division of an automobile manufacturer Bajaj Auto Ltd., Pune, India. He received his Master of Science (M.S.) degree in Mechanical Engineering from The State University of New York at Buffalo (SUNY Buffalo), Buffalo, New York in 2012. Since then, he has been pursuing his Ph.D. degree in ReNeu Robotics Lab at The University of Texas at Austin, Austin, Texas.

Email: mail2priyanshu@utexas.edu

This dissertation was typeset with LaTeX[†] by the author.

[†]LaTeX is a document preparation system developed by Leslie Lamport as a special version of Donald Knuth's TeX Program.